

**Novel Lewis acidic zeolites as  
heterogeneous catalysts for  
liquid phase chemistry**

**By**

**Abbas Al-Nayili**

**Submitted to the Department of Chemistry  
In Partial Fulfilment of the Requirements  
for the Degree of Doctor Philosophy in  
Chemistry**

**at the**

**Cardiff Catalysis Institute (CCI)**

**Supervisor: Dr. CERI HAMMOND**

**2017**

## Declaration

This work has not been submitted in substance for any other degree or award at this or any other university or place of learning, nor is being submitted concurrently in candidature for any degree or other award.

Signed..... (candidate)                      Date .....

### **Statement 1**

This thesis is being submitted in partial fulfilment of the requirements for the degree of .....PhD..... (insert MCh, MD, MPhil, PhD, etc, as appropriate).

Signed ..... (candidate)                      Date .....

### **Statement 2**

This thesis is the result of my own independent work/investigation, except where otherwise stated, and the thesis has not been edited by a third party beyond what is permitted by Cardiff University's Policy on the Use of Third Party Editors by Research Degree Students. Other sources are acknowledged by explicit references. The views expressed are my own.

Signed ..... (candidate)                      Date .....

### **Statement 3**

I hereby give consent for my thesis, if accepted, to be available online in the University's Open Access repository and for inter-library loan, and for the title and summary to be made available to outside organisations.

Signed ..... (candidate)                      Date .....

### **Statement 4: Previously Approved Bar on Access.**

I hereby give consent for my thesis, if accepted, to be available online in the University's Open Access repository and for inter-library loans **after expiry of a bar on access previously approved by the Academic Standards and Quality Committee.**

Signed ..... (candidate)                      Date .....

## Acknowledgements

First of all, I'd like to present my sincere Praise and thanks to Almighty Allah without whose help this thesis would not have been completed.

Particular thanks I'd like to express to my main advisor Dr. Ceri Hammond, Head of Research Group (Catalysis Engineering) and Dr. Nikolaos Dimitratos for their constant support, valuable insight and encouragement which strongly motivated me throughout conducting research at Cardiff Catalysis Institute (CCI).

I am grateful to the Iraqi government, the Embassy of Iraq in the UK and Al-Qadisiya University in Iraq for supporting and funding this research project and for giving me the opportunity to fulfil my ambition.

Also, I want to thank Dr. David Apperley, Dr. Fraser Markwell and Dr. Eric Hughes of the ESPRC UK National Solid-State NMR Service at Durham University for performing the MAS NMR experiments, and for their valuable remarks. Thanks are extended to Dr. Peter Wells (University College London/UK Catalysis Hub) for his help in the measurement of the XAS spectra and for his useful discussions. Diamond Light Source and the Research Complex at Harwell for the provision of beamtime (SP8071).

My thanks are honestly expressed to the members of catalysis engineering group, Daniele Padovan and Keiko Yakabi for their encouragement, support and wonderful atmosphere in the lab throughout the years of my PhD. I wish them good luck and profound success. My warm thanks are also due to the brilliant people with whom I have very advantaged interaction namely Felipe, Khaled, Guillermo, Giulia, Davide, Manuel and Stefano.

I also acknowledge the technical support team in CCI for their kind assistance during the experimental programs.

Last but certainly not least, I would like to thank my family members my dear wife Areej and my children Manar, Huda, Suroor and Mohammed for their support and patience until the end of my study.

## Abstract

Porous Lewis acids are rapidly emerging heterogeneous catalysts, particularly for the upgrading of biorenewable feedstocks, due to their ability to coordinate lone-electron pairs from oxygen atom, hence inducing molecular rearrangements and cleavage. As such, this study tackles one of the most important challenges in liquid phase catalytic chemistry, namely the design of novel Lewis acidic zeolites to act as heterogeneous catalysts for liquid phase applications.

Lewis acidic (Sn-BEA) zeolites are typically synthesised by highly complicated hydrothermal synthesis procedures, which have significant downsides preventing industrial application. In addition to technical difficulties, some drawbacks minimize the effectiveness of Sn-BEA in industrial interest. Amongst these limitations are 1) long crystallization time (40 days), 2) the large crystallite sizes obtained via typical hydrothermal synthesis, resulting in mass-transfer issues, and 3) the low Sn amount (typically < 2 wt.%), resulting in low space-time yield. Furthermore, a relatively amount of undesirable HF is required to induce crystallisation. Therefore, much academic and industrial research is currently devoted to the development of new methodologies for preparing Lewis-acid zeolite catalysts with higher or similar activity.

The broad context at this doctoral dissertation is to investigate the potential of acid leaching (i.e., demetallation) of commercial (Al-containing) BEA zeolite as a simple, versatile, and scalable method to introduce different amounts of active centers (Sn) in zeolites, using solid-state incorporation (SSI). To evaluate the activity of the synthesized catalysts, the study focused firstly on the Meerwein-Ponndorf-Verley (MPV) transfer hydrogenation of carbonyl compounds and isomerization of glucose.

Owing to the low activity of Sn-BEA micropores catalyst for the activation of bulky molecules, mesopores are subsequently created via top-down alkaline treatment to synthesis hierarchical Lewis-acid porous zeolite (Sn-h<sup>\*</sup>-BEA), by employing the post-synthetic demetallation route. This catalyst, was evaluated in reactions that involve bulky molecules, such as cyclooctanone (C<sub>8</sub>) and cyclododecanone (C<sub>12</sub>). Sn-h<sup>\*</sup>-BEA was found to be active, selective and more stable for continuous operation than its purely microporous analogue.

Subsequent work focused on the catalytic valorisation of bio-renewable feedstock, which often relies upon multi-stage processing of highly-functionalised substrates, resulting in selectivity and process engineering challenges. Later parts of this thesis therefore report the synthesis of a novel acid-base bifunctional catalyst [Sn-Al] BEA which contains Sn-related Lewis acid sites and Al-related Brønsted acid sites. This bifunctional catalyst has been tested, as a catalyst for the cascade catalytic transfer hydrogenation and etherification of furfural, under batch as well as continuous flow reaction condition. With this catalyst, furfural was first converted by Lewis acid Sn(IV) framework sites to form furfural alcohol via transfer hydrogenation from the solvent. Subsequently, furfuryl alcohol etherification with the solvent is catalysed by the Brønsted acid (Al) framework to produce corresponding alkyl furfuryl ether. Such ethers are highly desirable as bio renewable fuel additives.

## List of abbreviations

BEA	Zeolite-Beta, Three-dimensional with 12-ring channel system
BET	Brunauer, Emmett, Teller
CD <sub>3</sub> CN	deuterated acetonitrile (probe molecules)
°C	degree celsius
2D	two-dimensional
3D	three-dimensional
EXAFS	extended X-ray absorption fine structure
FTIR	fourier transform infrared spectroscopy.
G	gram
GC	gas chromatography
h	hour
HT	hydrogen transfer
ICP-MS	Inductively coupled plasma mass spectrometry
LA	Lewis acid
λ	wavelength
MAS-NMR	magic angle spinning nuclear magnetic resonance
rpm	revolutions per minute
SiO <sub>2</sub> /Al <sub>2</sub> O <sub>3</sub> = X	X moles of SiO <sub>2</sub> to 1 mole of Al <sub>2</sub> O <sub>3</sub> in a specific zeolite
SDA	Structural directing agents
Sn-BEA	tin incorporated in zeolite Beta.
TGA	thermogravimetric analysis
TOF	turnover frequency
TON	turnover number
UV-Vis	Ultraviolet-visible spectroscopy
wt. %	weight percentage of total mass
2, 5, 8 and 10 wt. % Sn-BEA	weight percentage of Sn in terms of final catalyst loading
XRD	X-ray powder diffraction
XANES	X-ray absorption near edge spectroscopy

---

# Table of Contents

## Chapter 1 Introduction

1.1	Zeolites .....	1
1.1.1	Structure .....	1
1.1.2	General properties of zeolites .....	4
1.1.3	Application of zeolite in catalysis .....	9
1.1.4	Modification of zeolites .....	11
1.1.4.1	Ultra-large pore zeolites .....	11
1.1.4.2	Nano-crystal zeolites .....	12
1.1.4.3	Hierarchical porous zeolites .....	12
1.2	Lewis-acid zeolites .....	15
1.3	Stannosilicate zeolites are liquid phase catalysts .....	17
1.4	Synthesis of Sn-BEA .....	19
1.4.1	Hydrothermal synthesis approach .....	19
1.4.2	Dry-Gel Conversion techniques .....	21
1.4.3	Post-synthetic methods for preparing Lewis-acid zeolites ....	22
1.5	Solid acid-base bifunctional catalysts .....	25
1.6	Catalyst deactivation .....	27
1.7	Objectives of the thesis .....	31
1.8	References .....	32

## Chapter 2 Experimental and Characterization

2.1	Reagents .....	40
2.2	Definition .....	41
2.2.1	Conversion .....	41
2.2.2	Selectivity .....	41
2.2.3	Turnover frequency (TOF) .....	41
2.3	Catalysts synthesis .....	41
2.4	Kinetic studies .....	42
2.5	Analytical methods .....	42
2.5.1	Gas chromatography (GC) .....	42
2.5.2	High performance liquid chromatography (HPLC) .....	43
2.6	Characterisation techniques .....	44
2.6.1	Gas adsorption .....	45

2.6.2	X-Ray powder diffraction (XRD) .....	47
2.6.3	X-Ray absorption spectroscopy (XAS) .....	49
2.6.4	Fourier-transform Infrared absorption spectroscopy (FT-IR) .....	51
2.6.5	Scanning electron microscopy (SEM) .....	53
2.6.6	Transmission electron microscopy (TEM) .....	55
2.6.7	Magic angle spinning nuclear magnetic resonance (MAS NMR) .....	56
2.6.8	Thermogravimetric analysis (TGA) .....	59
2.6.9	Ultraviolet-Visible spectroscopy (UV-Vis) .....	59
2.7	References .....	61

### **Chapter 3 Identification of Active and Spectator Sn Sites in Sn-BEA Following Solid-State Stannation, and Consequences for Lewis Acid Catalysis**

3.1	Introduction .....	65
3.2	Results and Discussion .....	67
3.2.1	Catalyst synthesis and characterization .....	67
3.2.2	Catalytic tests .....	75
3.2.2.1	MPV reduction of cyclohexanone .....	75
3.2.2.2	Glucose isomerization .....	78
3.2.3	Insight into the Sn-BEA activity .....	81
3.2.4	Magic-Angle Spinning (MAS) NMR spectroscopy .....	83
3.2.5	X-ray absorption spectroscopy .....	85
3.2.6	FTIR using a probe molecules .....	94
3.3	Conclusions .....	97
3.4	Experimental .....	98
3.4.1	Catalyst synthesis and pre-treatment .....	98
3.4.2	Catalyst characterization .....	98
3.4.3	Kinetic evaluation and analytical methods .....	100
3.5	References .....	101

### **Chapter 4 Hierarchically porous BEA stannosilicates as unique catalysts for bulky ketone conversion and continuous operation**

4.1	Introduction .....	105
4.2	Results and discussion .....	108
4.2.1	Generation of hierarchical zeolite BEA .....	108

4.2.2	Preparation and characterisation of 2Sn-h <sup>+</sup> BEA, following solid state stannation .....	117
4.2.3	Magic-Angle Spinning (MAS) NMR Spectroscopy .....	120
4.2.4	X-ray absorption spectroscopy .....	122
4.2.5	Catalytic test .....	124
4.2.6	Deactivation studies .....	131
4.3	Conclusions .....	135
4.4	Experimental .....	136
4.4.1	Catalyst synthesis .....	136
4.4.1.1	Synthesis 2Sn-h <sup>+</sup> -BEA .....	136
4.4.1.2	Synthesis 2Sn-MCM-41.....	137
4.4.2	Plug flow reactor conditions .....	137
4.4.3	Catalyst characterisation .....	138
4.4.4	Kinetic evaluation and analytical methods .....	139
4.5	References .....	140
<b>Chapter 5 Bifunctional Lewis and Brønsted acidic zeolites permit the continuous production of bio-renewable furanic ethers</b>		
5.1	Introduction .....	145
5.2	Results and discussion .....	147
5.2.1	Lewis acid only system .....	147
5.2.2	Catalytic etherification .....	154
5.2.3	Bifunctional catalytic systems .....	157
5.2.4	Optimisation of physical mixture .....	157
5.2.5	Preparation and characterisation of bifunctional [Sn, Al]-BEA....	159
5.2.6	Meerwein-Ponndorf-Verley of Furfural by bifunctional .....	164
5.2.7	Continuous performance of physical mixtures and bifunctional catalysts .....	169
5.2.8	Bifunctional [Sn, Al]-BEA prepared by solid state incorporation	174
5.3	Conclusions .....	182
5.4	Experimental .....	183

5.4.1	Catalyst synthesis .....	183
5.4.2	Catalyst characterisation .....	183
5.4.3	Kinetic evaluation and analytical methods .....	184
5.5	References .....	186
<b>Chapter 6 Conclusions, Outlooks and pertaining challenges</b>		
6.1	Conclusions .....	190
6.2	Outlook and pertaining challenges .....	192
<b>Chapter 7 Appendix</b>		
7.1	GC chromatogram .....	196
7.2	HPLC chromatogram .....	197
7.3	Calibration curves .....	197
7.4	Experimental data for chapter 3 .....	203
7.5	Experimental data for chapter 4 .....	205
7.6	Conference contributions .....	207
7.7	References .....	207

## Introduction

### 1.1 Zeolites

#### 1.1.1 Structure

Zeolites are crystalline porous aluminosilicate materials which consist of a network of  $[\text{SiO}_4]^{4-}$  and  $[\text{AlO}_4]^{5-}$  tetrahedral  $\text{TO}_4$  (where  $\text{T}=\text{Si}, \text{Al}$ ), that are connected to each other by bridging oxygen atoms. The concentration often results in a three-dimensional structure with regular framework topology of uniform channels (pores) and cages (cavities) with dimensions of ( $0.3 < \text{diameter} < 1.2 \text{ nm}$ ).<sup>1</sup> While silicon tetrahedral is neutral, the Al tetrahedral conveys a negative charge on the zeolite framework, which is balanced by cations, such as:  $\text{K}^+$ ,  $\text{Mg}^{2+}$ ,  $\text{Na}^+$ , etc., which are located close to the adjacent cavity or channel. Proton from zeolites (H-Zeolite), materials display strong Brønsted acidity, whose strength can be comparable to that of 100%  $\text{H}_2\text{SO}_4$  (see Figure 1.1).<sup>2</sup>

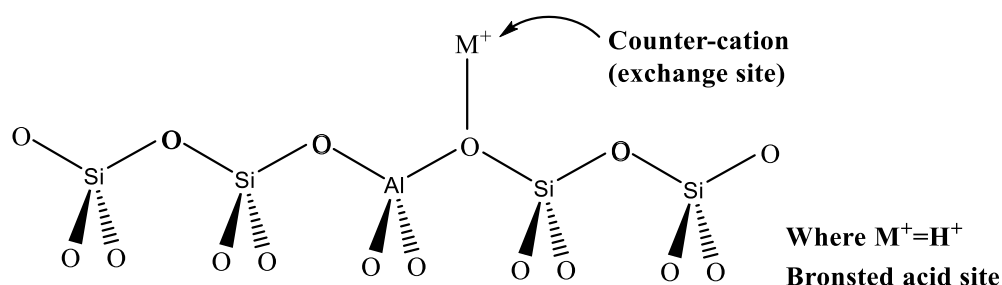


**Figure 1.1** Structural representation of zeolite materials, and how Brønsted acidity arises due to the incorporation of Al into the framework.

The framework density for zeolite materials is lower than 21 T-atom nm<sup>-3</sup>, in which the values of the density range from 2.1 to 2.2 g cm<sup>-3</sup>. Zeolites have the following general properties.<sup>3</sup>

- Large surface area.
- High adsorption ability.
- High ion-exchange capacity.
- Strong acidity/basicity.
- High hydro(thermal) stabilities.
- Tuneable hydrophilicity/hydrophobicity.
- Capacity to behave act as host-guest systems by hosting various molecules in the framework.
- Environmentally friendly materials.

The International Union of Pure and Applied Chemistry (IUPAC) has classified the porosity of materials into three categories according to pore diameter sizes as follows:<sup>4</sup>

- Microporous (below 2 nm).
- Mesoporous (from 2 to 50 nm).
- Macroporous (more than 50 nm).

Zeolites are members of the microporous category because their pore size is typically below 2 nm. Microporous zeolites can be further classified on the basis of their maximum pore aperture, which puts them into three categories as follows:

- Narrow-pore (8 T-atoms per pore, diameter ± 0.30-0.45 nm) e.g. LTA
- Medium-pore (10 T-atoms per pore, diameter ± 0.45-0.60 nm) e.g. MFI
- Large-pore (12 T-atoms per pore, diameter ± 0.60-0.80 nm) e.g. BEA, FAU (Figure 1.2).<sup>5</sup>

Recently zeolites with 14-member pore ring have been produced with crystallographic diameter up to 1 nm, e.g. UTD-1.

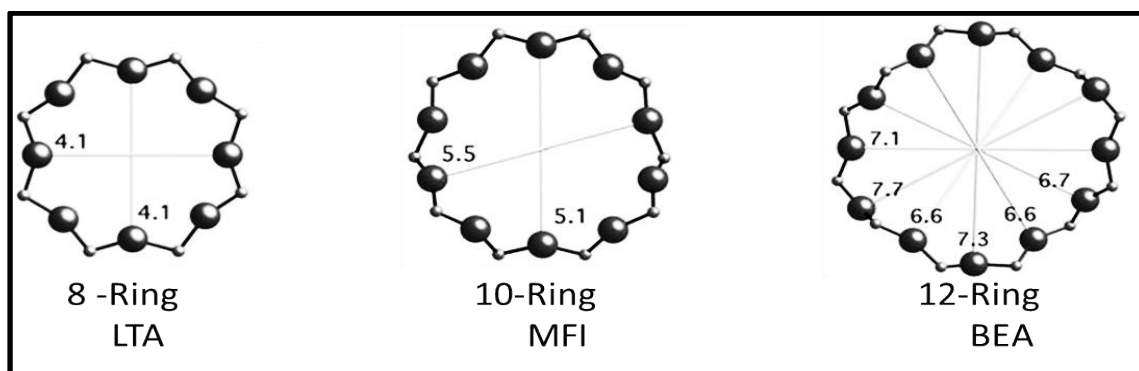


**Figure 1.2** Typical examples of pore openings in 8-,10- and 12-ring zeolites.<sup>6</sup>

Various zeolite framework/structures with varied pore structure and framework density can be prepared by careful selection of reaction formulation and conditions such as temperature, Si/Al ratio, template type, etc.. Figure 1.3 gives typical examples of different zeolite pore structure.

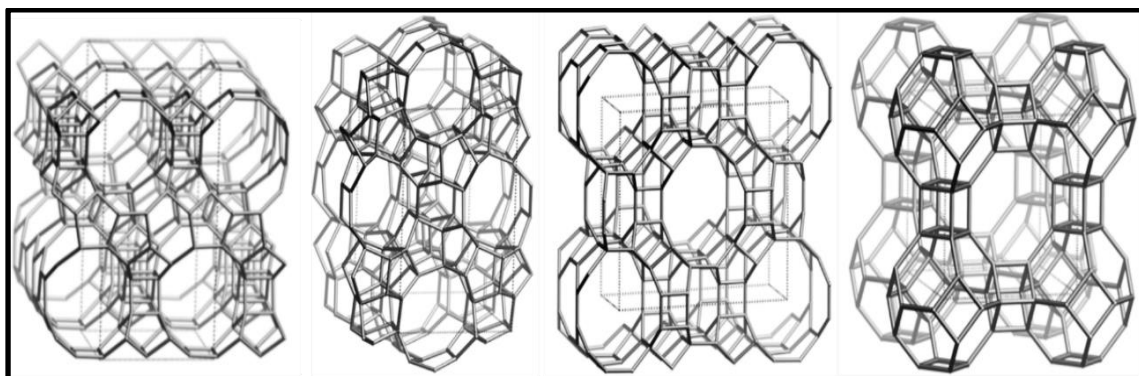


**Figure 1.3** 2D drawings of varied zeolite structure.<sup>6</sup>

The chemical structure of zeolites is built from the crystallographic unit cell represented by the following formula:<sup>7</sup>



Where M is the exchangeable extraframework cations,  $y/x$  corresponds to the Si/Al ratio, which ought to be higher than 1 ( $\text{SiO}_2/\text{Al}_2\text{O}_3 > 2$ ),  $W$  represents the

number of water molecules per unit cell, and the charge-balancing cations and water molecules are positioned in the cavities and channels.<sup>5</sup> The hydrophilicity/hydrophobicity and the acidity - including the acid strength and density- of zeolites can be modified by altering the Si/Al ratio of the zeolite. Due to these flexibilities offered by zeolites, they are used in a wide range of industrial applications. Notable examples include their use as heterogeneous catalysts, ion-exchange materials and adsorbents. A specific attention was given, in this study, to the Lewis and Brønsted acid sites of zeolites, which have the capability of performing H<sup>+</sup> mediated catalysis, leading to their extensive use in several petroleum refining reactions.<sup>8</sup>

### 1.1.2 General properties of zeolites

In general, the zeolites are found in the Na<sup>+</sup> form or with other alkaline ions as framework charge balancing cations. The exchange of the alkaline cations with NH<sub>4</sub><sup>+</sup> followed by heat treatment (calcination at 300 to 500 °C) is responsible for the introduction of H<sup>+</sup>. The residual H<sup>+</sup> retained after calcination is the source of Brønsted acidity in zeolites. Figure 1.4 illustrates the introduction of acidity to zeolite. Typical reaction requiring zeolite acidity includes catalytic cracking reactions.<sup>9,10</sup>

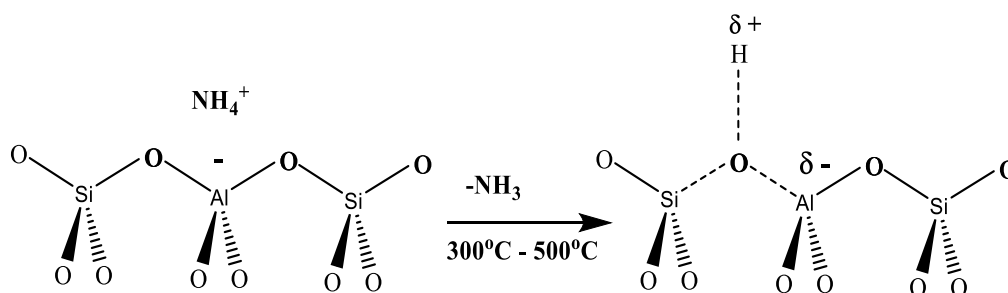


**Figure 1.4** Formation of the Brønsted acid sites (bridging hydroxyl groups) by calcinating NH<sub>4</sub><sup>+</sup> form of the zeolite at elevated temperatures.<sup>7</sup>

Figure 1.4 refers to the connecting bond between the zeolite framework and proton. It is clear that each oxygen atom makes three various bonds and has a negative charge. The transformation of electronic density from the hydrogen to the oxygen atom is due to the fact that hydrogen is less electronegative than oxygen. Hence, the hydrogen is responsible for the positive charge and it is the OH bond which possesses the main ionic character. Thus, this particular bond is easily broken making the proton largely mobile over the zeolite framework, and producing a highly active Brønsted acid site, as presented in Figure 1.5.<sup>10</sup>

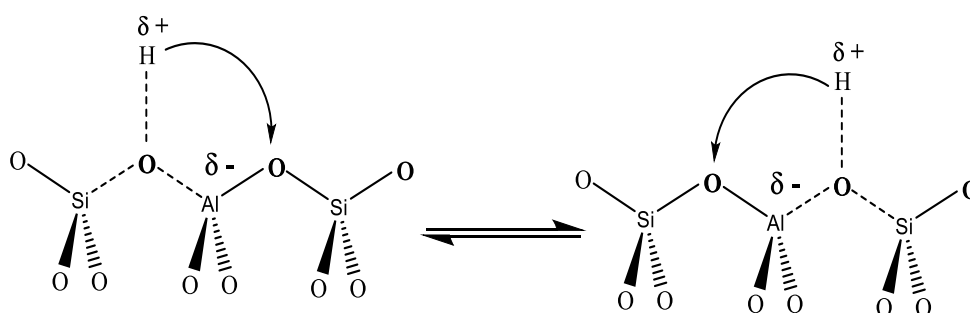


**Figure 1.5** Mobility of the proton in bridging hydroxyl groups.

Since the highest theoretical number of protonic sites equals the number of tetrahedral Al atoms in the zeolite structure, the Brønsted acidity of a zeolite is also directly related to the framework Si/Al ratio of zeolite. Yet the number of protonic sites is always lower than the theoretical number because of incomplete ion exchange and due to dehydroxylation and dealumination in the process of activating the zeolite at relatively high temperatures which can lead to the creation of extraframework Al species (EFAl).<sup>9,10</sup> The extraframework Al species and the tri-coordinated Al account for zeolites structural defects and motivate the availability of Lewis acid sites, which are capable of hosting a pair of electrons in the zeolites. A variety of Lewis acid sites can be available in zeolites examples of which include:  $\text{Al}^{3+}$ ,  $\text{AlO}^+$ ,  $\text{Al}(\text{OH})^{2+}$  (cationic Al),  $\text{Al}(\text{OH})_3$ ,  $\text{AlO}(\text{OH})$ ,  $\text{Al}_2\text{O}_3$  (neutral Al), and  $\equiv\text{Si}^+$  (silicate species).<sup>11,12</sup> Kühl<sup>13</sup> proposes the formation of Lewis acid sites in a two-step model. Figure 1.6 illustrates an in sample of a possible scheme

of dealumination. In the first step, dehydroxylation take place (Figure 1.6) at adjacent bridging hydroxyl groups. While in the second step, the system, in a metastable position, passes into a more stable state, helped by an adjacent framework Al site. After that the Al is easily released from the structure of the zeolite in the presence of the closest neighbouring Al atoms, which turns the Al atoms to be less stable. The second step is very simply performed on zeolites enriched by Al (low Si/Al ratio), like zeolite Y, and is less preferable in zeolites with high Si/Al ratio, in which the entire Brønsted acid sites are mostly isolated.<sup>11,14,15</sup>

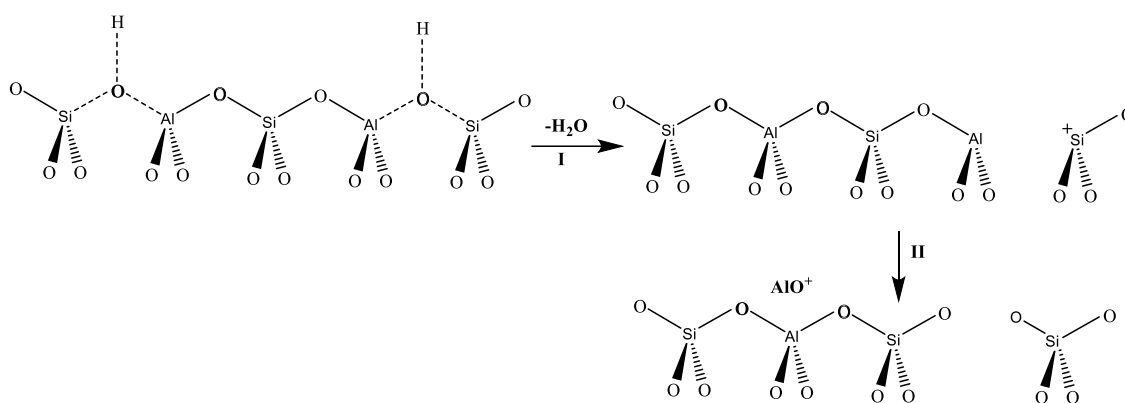


**Figure 1.6** Two-step mechanism for the formation of extraframework Al species: I) dehydroxylation and II) dealumination.<sup>10</sup>

In general, zeolite acidity is dependent on the strength and concentration of Brønsted sites. There are some factors that influence the acidic strength of the Brønsted sites, such as:

**T-O-T bond angle:** The acidic strength of the connected proton is dependent on the T-O-T bond. Consequently, the protonic sites of H-Faujasite with bond angle in the range of 138-147° are weaker than those of H-Mordenite with bond angle of 143-180°.<sup>10</sup>

---

**Ionic exchange degree:** The acidic strength of the protonic sites intensifies according to the degree of ionic exchange.<sup>9</sup>

**The acidic sites proximity:** The number of the neighbouring Al atoms limits the strength of an acidic site.<sup>9</sup> The acidic strength of a certain site intensified when the number of tetrahedral Al that reinforces the acid site is minimal, and it would be in the maximum at zero Al in the neighbouring position. This behaviour is related to the higher electronegativity of silicon atom in comparison with Al atom. In fact, there is a greater electron density transfer from the oxygen atom to the silicon atom and, thus, from the hydrogen atom to the oxygen atom, than with the Al atom, which intensifies the ionic character of the hydroxyl bond as well as the acid strength.

**Interaction with Lewis acid sites:** The strength of Brønsted acid sites can be reinforced by their interaction with neighbouring extraframework Al species (Lewis acid sites) because of their inductive impact.<sup>16-18</sup> This impact is responsible for the rise of the activity of some zeolites.<sup>10</sup> Nevertheless, extraframework Al species can have some disadvantages properties: i) they might hinder the access to the active acid sites, and ii) the neutralization of the charge in the framework, which can decrease the number of Brønsted acid sites.<sup>19</sup> The concentration of framework Al in the zeolite mainly dictates its acidity. In essence, one potential acid site is generated from each Al atom in the framework and thus, the zeolite's acidic strength depends on its SiO<sub>2</sub>/Al<sub>2</sub>O<sub>3</sub> ratio. The SiO<sub>2</sub>/Al<sub>2</sub>O<sub>3</sub> ratio influences many zeolitic properties and it can be considerably manipulated by adjusting the proportions of Al and silicon sources in the synthesis gel. Since the Al atoms influence the acidic sites directly, the SiO<sub>2</sub>/Al<sub>2</sub>O<sub>3</sub> ratio has a considerable effect on the zeolite acidity.<sup>20,21</sup> The impact of the Al atoms incorporated into, for example, H-ZSM-5 zeolite is not only related to creating new acid sites, but also modifying the acidic strength of the originally existed sites. As the SiO<sub>2</sub>/Al<sub>2</sub>O<sub>3</sub> ratio decreases, the concentration of the acid site increases, yet the acidic power decreases in the residual protons because the highly proliferated Al content in the framework that contains abundant associated protons compensates for the highly positive charge. If the Al atoms decrease in

the framework content, the lower positive charge should be neutralized so that the acidic power of the residual zeolite protons would increase. In this way, the acid site density and its acidic strength are vital elements to decide the zeolite activity and selectivity. Hence, in any acid site reaction, determining the  $\text{SiO}_2/\text{Al}_2\text{O}_3$  ratio is an essential factor. For instance, to prohibit extravagant polymerisation, the highly potent acid sites should be abolished and the total acidity must remain sufficient. For this purpose, the most appropriate solution is ZSM-5 zeolite whose  $\text{SiO}_2/\text{Al}_2\text{O}_3$  ratio is in the range of 10-40.<sup>22</sup> The proliferation of Al content in zeolites determines their capacity for exchangeable cations, and increases its hydrophilic character. The opposite is true in the more siliceous zeolites with a lower charge imbalance and thus lower cation exchange capability are obtained; however, the zeolite still shows a more hydrophobic character.<sup>7</sup> As the  $\text{SiO}_2/\text{Al}_2\text{O}_3$  ratio differs, some differences are observed in the zeolite properties such as presented in Table 1.1 below. In the naturally existing aluminosilicate, 5.5 is the highest recorded  $\text{SiO}_2/\text{Al}_2\text{O}_3$  ratio, which is located in mordenite. Yet, in the industrially synthesised zeolites, the  $\text{SiO}_2/\text{Al}_2\text{O}_3$  ratio can be extended up infinitely to yield materials which are very close to the composition of pure  $\text{SiO}_2$ . For instance, the  $\text{SiO}_2/\text{Al}_2\text{O}_3$  ratio reaches infinity in the ZSM-5 zeolite analogue, Silicate-1.

**Table 1.1** The influence of  $\text{SiO}_2/\text{Al}_2\text{O}_3$  ratio on zeolite properties.

High $\text{SiO}_2/\text{Al}_2\text{O}_3$ ratio	Low $\text{SiO}_2/\text{Al}_2\text{O}_3$ ratio
Increment of: <ul style="list-style-type: none"> <li>• Hydrophobicity.</li> <li>• Acid resistance.</li> <li>• Thermal stability.</li> </ul>	Increment of: <ul style="list-style-type: none"> <li>• Hydrophilicity.</li> <li>• Cation exchange capacity.</li> </ul>
Lowering of: <ul style="list-style-type: none"> <li>• Affinity for polar adsorption.</li> <li>• Cation exchange capacity</li> </ul>	

### 1.1.3 Applications of zeolite in catalysis

An essential branch of heterogeneous catalysis is zeolite, which consists of nanoporous crystalline materials composed of silicon and oxygen and distinguished by thermal stability, large surface area, and most importantly to add catalytic functionality in their framework. Catalytic functionality can be added to zeolites by several means such as the incorporation of acidic and oxidation metal sites. Table 1.2 lists some industrially employed zeolite catalysts and their typical applications.

**Table 1.2** The most important applications of zeolites as catalysts.<sup>7,23</sup>

Zeolite type	Catalytic application
FAU (X- and Y- zeolite)	Catalytic cracking, aromatic transalkylation and alkylation, acylation, NO <sub>x</sub> reduction and separation
BEA (Beta zeolite)	Baeyer-Villiger reaction, FCC additive, Benzene alkylation
MOR (Mordenite)	Olefin oligomerisation, hydro-isomerisation, hydro-cracking, aromatic alkylation
MFI(ZSM-5, TS-1)	Xylene isomerisation, production of ethylbenzene and styrene, ammoxidation, Beckmann rearrangement, methanol to gasoline, toluene disproportionation and alkylation, aromatisation.
MWW (MCM-22)	Benzene alkylation
FER (Ferrierite)	n-Butene skeletal isomerisation
LTL (KL-type zeolite)	Catalytic aromatisation
ERI (Erionite)	hydro-cracking, Selective reforming
CHA (SAPO-34)	Methanol to olefins (MTO)
TON (ZSM-22, Theta-1)	Long-chain paraffin isomerisation
AEL (SAPO-11)	Dewaxing (long chain alkane hydro-isomerisation)

Two special zeolite frameworks are the 10-membered ring MFI zeolite and the 12-membered ring BEA zeolite. Characteristically, BEA zeolite possesses a 3D intersecting pore framework with high 0.65 nm pores, which assists in the transport of reaction molecules to the catalytic sites. Figure 1.7 illustrates the framework dimensions of the BEA structure which is the main zeolite utilised in the present thesis.

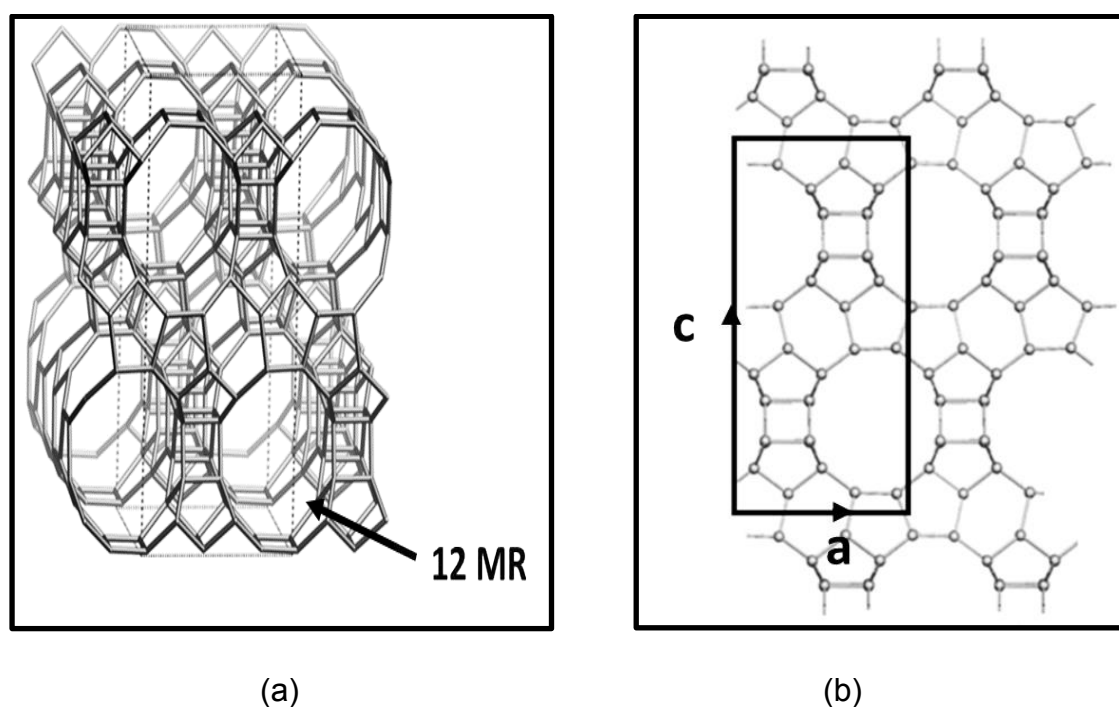


**Figure 1.7** Framework structure of BEA zeolite viewed along [010] (a) and unit cell (b).<sup>5</sup>

Other than the conventional heterogeneous catalysis, zeolites are also used in other fields due to their physico-chemical features and their ability to act as host-guest materials. Other areas where zeolites have found new applications are the following:

- Biomedicine (drug-release,<sup>24,25</sup> immobilisation of cell/enzymes,<sup>26,27</sup> disinfection).<sup>28,29</sup>
- Bio-catalysis.<sup>26</sup>

- 
- Bio-chemistry.<sup>27</sup>
  - Energetics.<sup>30,31</sup>
  - Solid ionic conductors.<sup>32,33</sup>

As mentioned in section 1.1.1, the zeolites are considerably applied in catalysis, due to the large surface area, uniform pore size, ion-exchange capacity, strong acidity and shape-selective feature. Yet, in several notable cases, the co-presence of micropores and relatively small pores (0.3-1.5 nm) urges mass-transport limitations on the processing rate, showing low exploitation of the zeolite. It was repeatedly proved<sup>8,34</sup> that the diffusion limitation in zeolite bulk crystals performs an essential part in industrial application. Due to their small micropore sizes, zeolites have a limited role in adsorption and catalysis with bulky molecular species (> 1 nm). Therefore, zeolites can be modified in different ways to improve molecular transport properties.

#### 1.1.4 Modification of zeolites

No more than 5% of the 200 known zeolite architectures are practically employed for industrial purposes, like MOR, FER, FAU, CHA and MFI types of zeolites.<sup>35</sup> This demands high conversion and fast diffusion required for bulky substrates, intermediates and products. The activity of microporous materials can be largely improved by lowering the intracrystalline diffusion limitations in small channels and cavities.<sup>36,37</sup> To cope with the diffusion problems that often lead to the loss of activity and a reduced lifetime as well as loss of selectivity in zeolites,<sup>36</sup> some potential solutions have been proposed such as forming of zeolites with large pores, and zeolites with nano-crystals, as well as hierarchical zeolites.

##### 1.1.4.1 Ultra-large pore zeolites

Since the 1990s, extra-large micropore zeolites of more than 12 member rings, which could minimise the diffusion limitation; such as ITQ-40,<sup>8</sup> VPI-5<sup>38</sup> and other extra-large pore zeolites have been developed.<sup>39</sup> However, the modest

framework stability and acidity of these catalysts, as well as the high price of the organic templates used in their synthesis have limited the industrial applications for these zeolites.<sup>40</sup>

### 1.1.4.2 Nano-crystal zeolites

Reducing the crystal size of zeolites particles from micron-sized crystals to nano-crystals can help to alleviate the diffusion path and enlarge the external surface area. Such zeolite nano particles acquire colloidal features due to their small crystal size.<sup>41</sup> This property has resulted in the use of nano-crystal zeolites in the manufacturing of zeolite films and membranes.

Nevertheless, the nano-crystals zeolites still face some essential problems as the use of considerable amounts of toxic and expensive templates is required in their synthesis. Moreover, at nano-crystalline size, the diffusional path of molecules (reactant and product) are shorted excluding or reducing undesired diffusional limitations of the reaction rate.<sup>7</sup> Hence, nano-size zeolite crystals are far from commercial realisation.

### 1.1.4.3 Hierarchical porous zeolites

The microporous crystalline structures of zeolites provides them with excellent molecular sieving capability and hydrothermal stability for different catalytic reactions. However, the catalytic vitality of zeolite catalysts can be hindered by slow molecular diffusion in their microporous structures; particularly when large molecules are involved. A new generation of porous materials are called hierarchical zeolites, which consist of mesoscale porosity superimposed on crystalline microporous structures offering both molecular sieving capability and fast mass transport.<sup>42,43,44</sup> The speed of molecular mass transport in hierarchical zeolites helps molecules to reach the active sites in micropores quickly and shorten the residence time of molecules in the catalysts, which would immediately result in the enhancement of reaction rates and slowing deactivation through fouling i.e. pore blocking.<sup>45,46</sup> To combine micropores with meso/macropores in a single material is one of the proposed solutions to overcome the problem of

diffusion in zeolites. The resulting material includes highly accessible catalytic sites and elevated diffusion rate.<sup>37</sup> Different approaches have been employed to generate secondary porosity in zeolites framework which can be broadly categorised into six different strategies as listed in the following:<sup>47,48</sup>

- (i) Elimination of framework atoms by:
  - (a) Dealumination,
  - (b) Desilication
- (ii) Binary templating with surfactants.
- (iii) Hard-templating approaches such as:
  - (a) Polymeric templates.
  - (b) Carbonaceous templates.
  - (c) Other solids as templates.
- (iv) Zeolitization of a preformed solids.
- (v) Methods based on silanisation such as:
  - (a) the crystallisation of silanised protozeolitic nanounits,
  - (b) crystallisation by using silylated polymers or amphiphilic organosilanes.
- vi) Miscellaneous methods.

The extraction of silicon (desilication method) from zeolite crystals by treating it in an alkaline aqueous medium under controlled conditions has been proved as the most preferable method for producing mesoporosity in the crystals compared to other methods.

The remarkable improvement of mesoporosity and silicon extraction are highly dependent on the ratio of Si/Al in the zeolites.<sup>49,50,51</sup> The tetrahedrally coordinated Al in the zeolite adjusts the extent of silicon extraction and shape of mesopore as in Figure 1.8.<sup>52</sup> The impact of Si/Al ratio on the mesopores shape in the commercial H-ZSM-5 with a framework Si/Al ratio in the range of 15-1000 in alkaline solution was investigated, and the favourable Si/Al range for the optimal desilication was found to be between 25 and 50.<sup>53</sup> Higher framework Al (lower Si/Al ratio) results in enormous stability of the surrounding silicon atoms, resulting

in only minimal desilication leading to small pores. However, in low framework Al concentration, i.e. high Si/Al ratio, excessive leaching takes place, leading to the macropores (>50 nm) formation and eventually total structural collapse.

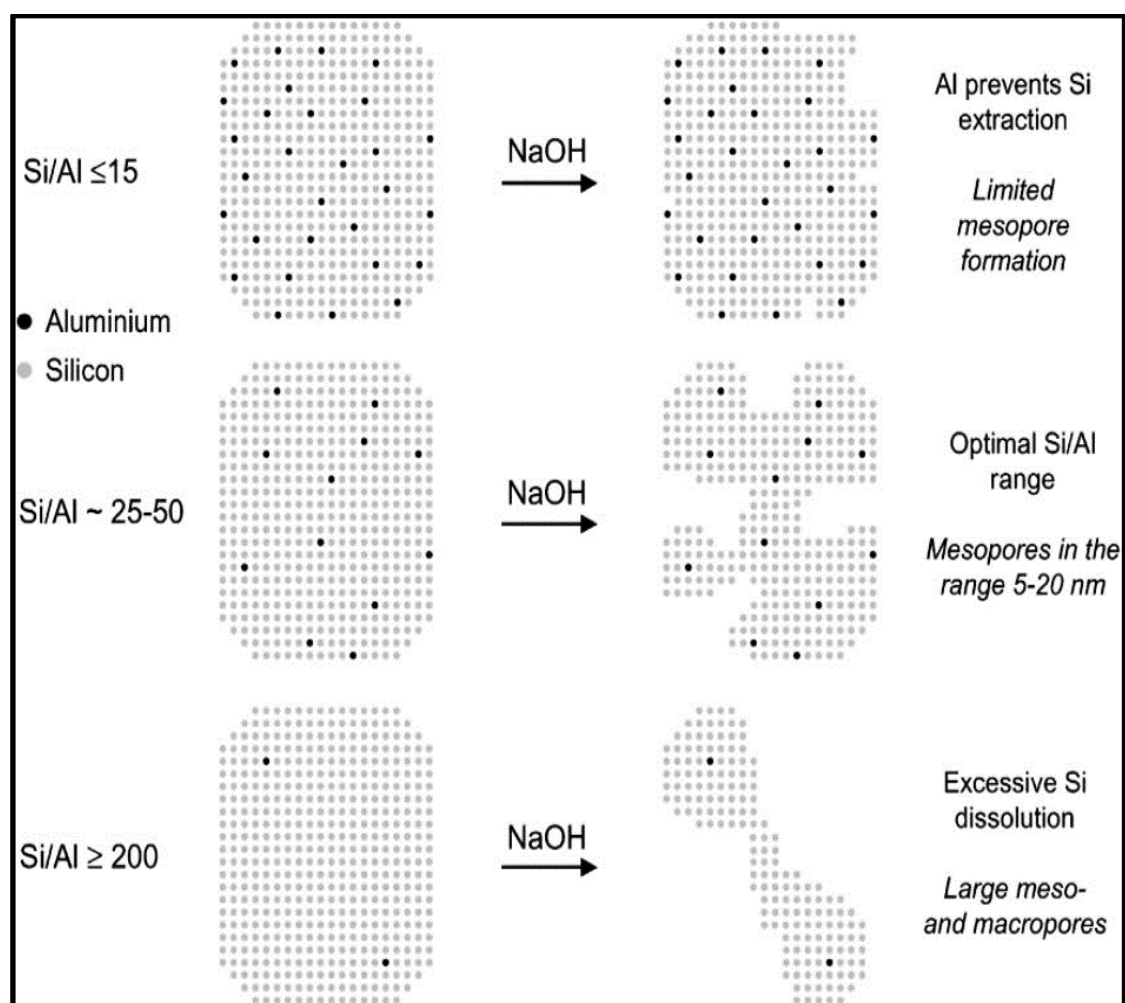


**Figure 1.8** Schematic representation of the effect of Al content in desilication treatment of MFI zeolites by NaOH solution from Groen et al.<sup>52</sup>

An important factor in the design of zeolite catalyst with superior lifetime is minimising deactivation. It is often thought that the external acid sites resulting from mesoporosity will strongly affect external coke formation, and thus increase the catalyst lifetime. Srivastava et al.<sup>54</sup> reported that the hierarchical MFI zeolite

presented a very high resistance to deactivation in different acid-catalysed reactions, which is related to the facile molecular diffusion of coke precursors away from the catalyst active region through the mesopores. Similarly, Groen et al.,<sup>55</sup> contrasted a hierarchical mordenite (MOR) catalyst acquired by desilication of a commercial sample in the liquid phase benzene alkylation with ethylene. The mesoporous mordenite displayed higher activity than the commercial sample. The improved catalytic performance of the mesoporous mordenite was related to the enhanced mass transport of the substrates to the active sites. Furthermore, the mesoporous sample showed lower retention time of products in the micropores, which can result in the formation of less secondary coke product.<sup>56</sup> However, no studies to date have clearly demonstrated the benefits of hierarchical materials when it comes to improved stability in liquid phase catalytic applications.

## 1.2 Lewis-acid zeolites

Due to the disadvantages of extraframework Al species (see section 1.1.2), much research over recent decades has targeted the generation of zeolites with exclusive Lewis acidic character exclusively, i.e. Lewis acidity without the co-presence of Brønsted acidity. The remarkable performance of titanium silicalite-1 (TS-1) as proven 30 years ago by Taramasso,<sup>57</sup> is attributed to the presence of Lewis acid sites, which arise from isolated tetrahedral  $Ti^{4+}$  atoms in framework positions that are located in a hydrophobic environment. Unlike traditional zeolites, TS-1 possesses Lewis acidity in the absence of Brønsted acidity, which makes this material a highly selective Lewis acid catalyst. The Lewis acidity of TS-1 is highly hydrophobic while the Lewis acidity of aluminosilicates strongly hydrophilic because of the co-presence of framework  $Al^{+3}$ . This makes TS-1 perform as a Lewis acidic catalyst even in highly protic and polar solvents like water and methanol. TS-1 is an ideal catalyst material to oxidize the hydrophobic species like alkanes because it does not have a negative framework charge when the dipole-dipole interaction between the polar oxygenated products and zeolite

are not spotted. This would guarantee that no partially oxygenated products are gained in the zeolite pores to avoid the potential sequential oxidation reactions. One of TS-1 disadvantages is its comparatively small pores, as it is composed of 10-membered MFI rings (Figure 1.9). This characteristic limits the catalyst to comparatively small molecules, leads to internal mass transfer restrictions, and increases the deactivation rates. On the other hand, the main channel of the BEA structure consists of 12-membered-rings, which means it has larger pores than the MFI analogue that has traditional pore size growing from  $\pm 5.5^\circ\text{A}$  (MFI) to  $\pm 6.7^\circ\text{A}$  (BEA).

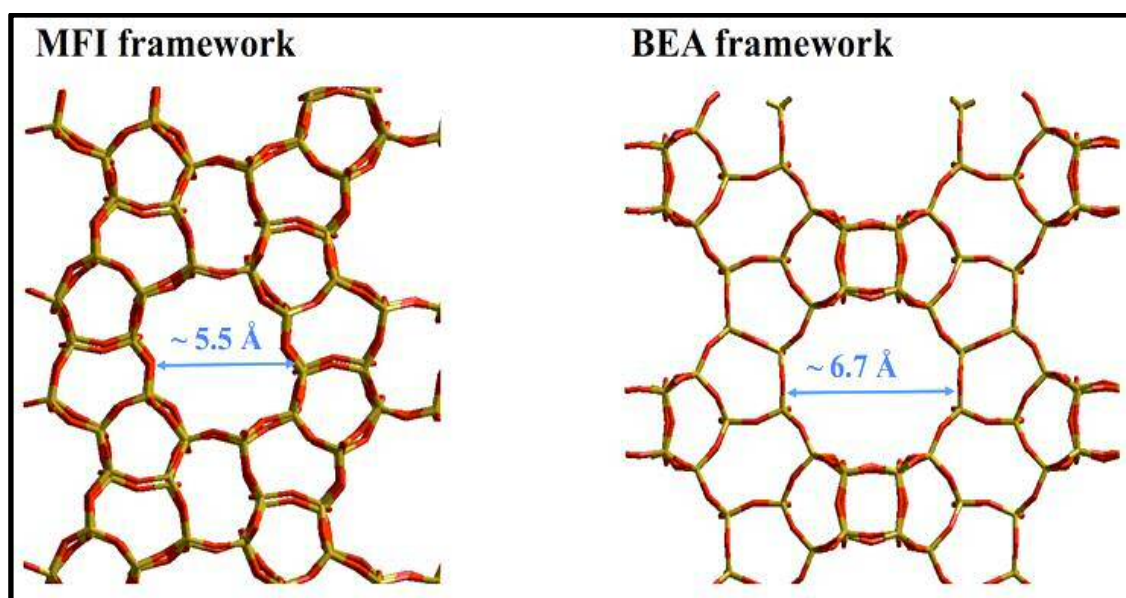


**Figure 1.9** Structure of (Left) zeolite MFI, and (Right) zeolite BEA, possessing 10- and 12- membered main rings respectively.

Historically, zeolite catalysis, although widely employed in industry, are only really used for vapour/gas phase reactions at high temperatures.<sup>58</sup> However, there are extensive oxygenate-containing reactions that require working in the liquid phase at low temperatures. This makes water-tolerant Lewis acid an appropriate solution for such reactions where the waste resulted from the use of

homogeneous catalysts is also avoided. The Lewis acid's ability to catalyse heterogeneously in the presence of water provides great industrial potentials.

### 1.3 Stannosilicate zeolites as liquid phase catalysts

The successful catalytic results obtained with Ti- containing zeolites have paved the way for the production of new zeolites and mesoporous materials having different Lewis acidic centres: such as tin (Sn), niobium (Nb), tantalum (Ta) and zirconium (Zr) in framework position. These elements were successfully grafted into the framework of zeolite BEA, and show distinct catalytic properties that are different from Ti-based zeolite. Lewis acid zeolites such as Sn-BEA have more remarkable efficiency than amorphous porous materials like Sn-MCM-41 in relevant trioses and hexoses conversion, particularly in aqueous media.<sup>59</sup> It is widely believed that the superior activity of Sn-BEA stems from the availability of isolated Lewis-acid Sn centres which are hosted in a non-defective, and hence highly hydrophobic silica matrix (e.g., Si-O- or Si-OH).<sup>60,61</sup> However, it is worth noticing that the effect of site speciation and crystallinity cannot be eliminated. The incorporation of Sn into the framework of porous silicate structures have resulted into environmental-friendly solid Lewis acid catalysts for sustainable chemistry.<sup>62,63</sup> Zeolites with the BEA topology that includes Sn metal centres in the framework (Sn-BEA) were successfully used in a number of very important reactions; such as Meerwein-Ponndor-Verely reductions,<sup>64</sup> Baeyer- Villiger oxidation<sup>65,66</sup> and ring-opening hydration of epoxides<sup>67</sup> to prepare fine chemicals (Figure 1.10).

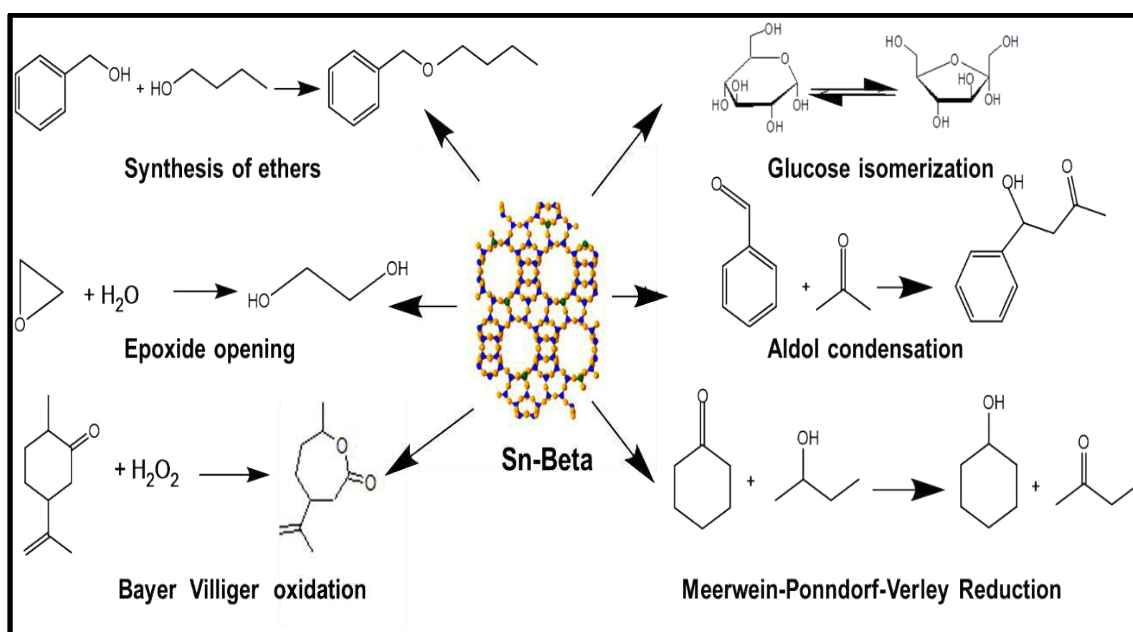


**Figure 1.10** Some examples of Lewis acid (Sn-BEA) catalysed reactions.

They were also used for their remarkable activity in preparing bio-based chemicals. The most currently utilised Sn-based zeolite is Sn-BEA, which shows excellent performance in the isomerisation of glucose to fructose and mannose,<sup>68,69,59</sup> xylose to xylulose<sup>70</sup> and lactose to lactulose,<sup>71</sup> as well as the conversion of various pentoses and hexoses into methyl lactates<sup>72</sup> and hydroxymethylfurfural into furan derivatives.<sup>73</sup> In spite of the fact that the enzymatic process is highly selective, the industrial use of enzyme for isomerization is very expensive, involving the periodic replacement of the enzyme due to irreversible deactivation, strict control over reaction temperature, reactant purity and solvent pH. Aldose epimerization products are also observed with Sn-BEA zeolite catalysts for glucose to xylose and mannose isomerisation. In each of these reactions, the framework Sn atoms behave as Lewis-acid sites. Roman-Leshkov et al.<sup>74</sup> used <sup>13</sup>C and <sup>1</sup>H NMR spectroscopy to study the mechanism of glucose isomerization using Sn-BEA as the catalyst in water. The results indicate the glucose isomerization reaction with a solid Lewis acid catalyst in pure water proceeds by means of an intramolecular hydrogen transfer from C-2 to C-1 and

from O-2 to O-1 of an  $\alpha$ -hydroxy aldehyde to create the  $\alpha$ -hydroxy ketone (Figure 1.11).

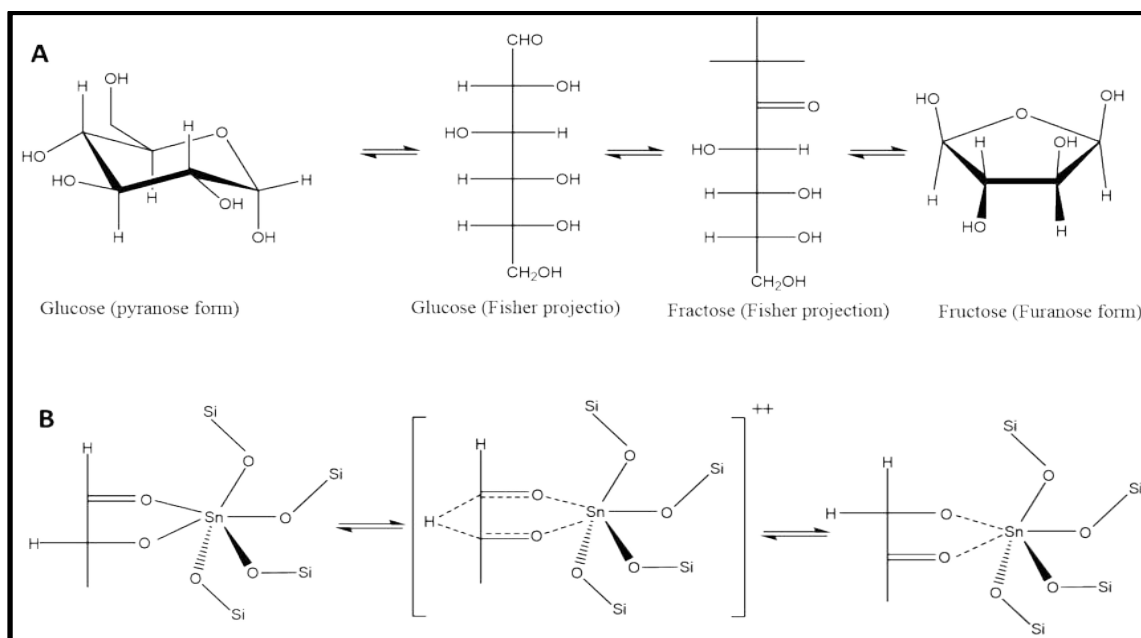


**Figure 1.11** (A) Scheme for the isomerization of glucose to fructose, and (B) scheme for the metal-catalysed proton shift.

The industrial applications of Sn-BEA are still restricted to a certain extent due to complexities in its synthesis. Consequently, current researches concentrate their aim on developing new methods for preparing metal-containing Lewis-acid BEA zeolites.

## 1.4 Synthesis of Sn-BEA

### 1.4.1 Hydrothermal synthesis approach.

The evolution of Lewis-acid zeolites is very much associated with the discovery of the titanium silicalite-1, and with the confirmation that the entirety of silica zeolites can be crystallised by using fluoride ions as mineralising agent<sup>75</sup> in

---

neutral conditions which paved the way to using metal precursors that are insoluble or poorly soluble in basic media. Although zeolites with different Lewis-acid metal; such as Sn, Hf, and Zr were prepared, the focus of this study will be on Sn-substituted zeolites. Moliner and Corma<sup>61</sup> have recently reviewed the hydrothermal synthesis of Ti-containing porous materials, and they proved that Sn-containing zeolites are the most active Lewis-acid catalysts. Corma et al. showed that pure stannosilicate material prepared by this route have improved physical properties; such as higher hydrophobicity, better hydrothermal stability, and increased crystallinity. Each of these features highly influences the performance of the catalyst.<sup>75</sup>

In spite of its activity, this synthesis method is not without some shortcomings that are related to its long preparation time, scalability and technical difficulties. This method requires up to 40 days to crystallize the catalyst appropriately. Moreover, crystallisation requires very high temperatures (160-200 °C) and pressures. Figure (1.12) presents the synthesis procedure for the preparation of stannosilicates via hydrothermal conditions. The long crystallization time comes from the presence of the Sn precursor as has been proved by Tolberg et al.<sup>76</sup> who say that a longer crystallization time is required up to 60 days with increase in the Sn content (from 0 – 1.8 wt. % Sn). Recently, a modified seeding synthesis method that uses a shorter hydro-thermal synthesis time was reported, but this method still needs the use of environmentally undesirable HF as mineralising agent. It should be noted that the crystallisation with F<sup>-</sup> yield less defective and more hydrophobic zeolite crystallites, with relatively large zeolite crystals, that may contribute to mass transfer limitation when relatively bulky molecules are converted. Another limitation of the fluoride-assisted synthesis is that its framework contains low Sn amount (typically < 2 wt. %) with high formation of extra-framework Sn species (EFSn),<sup>77</sup> which could be in the form of bulk Sn oxides and scattered intrazeolite Sn species. It is widely thought that these extra-framework Sn species minimize the effectiveness of Sn-BEA in carbohydrate-isomerization reaction.<sup>78,79</sup> All these disadvantages in the synthesis method makes the current form of Sn-BEA less successful in industrial scales. Thus,

more developed Sn-BEA preparation methods are sought in academic and industrial research. These efforts result in new approaches that can be divided into two categories: bottom-up (hydrothermal approaches designed for rapid synthesis) and top-down (post-synthetic approaches). Along with the conventional hydrothermal synthesis approach, another widely studied bottom-up method is the Dry-Gel Conversion.

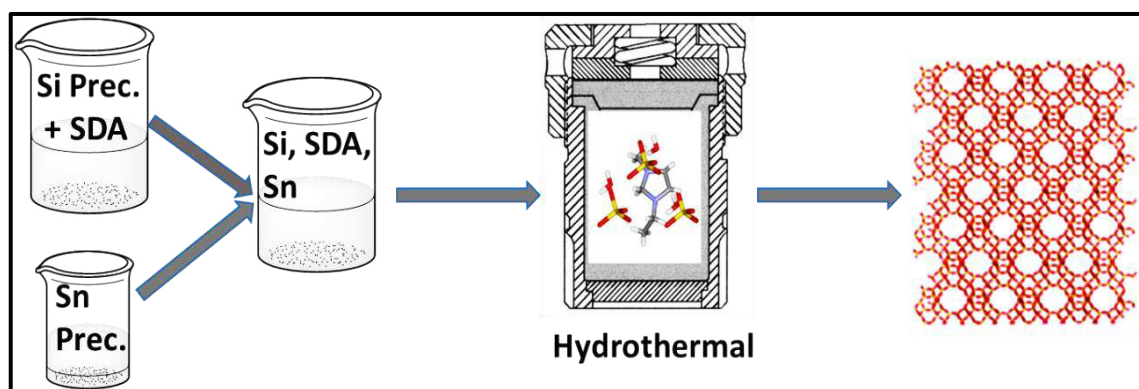


**Figure 1.12** Schematic illustration synthesis strategies for the synthesis stannosilicates via hydrothermal conditions.

#### 1.4.2 Dry-Gel Conversion (DGC) techniques.

This synthesis approach depends on the crystallisation of a dry and amorphous metallo-silicate gel in the presence of vapour streams. This technique can be further categorised into two methods: the vapour phase transport (VPT) and the steam assisted crystallisation (SAC) (Figure 1.13), which has also been used to synthesis other aluminosilicate zeolites, such as BEA, MOR and FAU. Niphadkar et al.<sup>80</sup> studied the SAC of Sn-MFI. They showed that shorter crystallisation time and less structure-directing agent were needed in SAC in comparison with the traditional hydrothermal synthesis route to prepare the same zeolite with similar catalytic properties and Si/Sn ratio. The SAC method also showed other advantages, such as increasing the solid yield and decreasing the waste generated. Instead of the lengthy hydrothermal synthesis method, Sn-BEA was

recently prepared by Kang et al.<sup>81</sup> using the SAC where only 5 hours were needed to transform the amorphous stannosilicate gel with Si/Sn=125 into an entirely crystalline Sn-BEA. However, HF is still required, and this approach was ineffective in synthesising a fully crystalline Sn-BEA zeolites from stannosilicate gels with (Si/Sn<75) even after 200 hours.

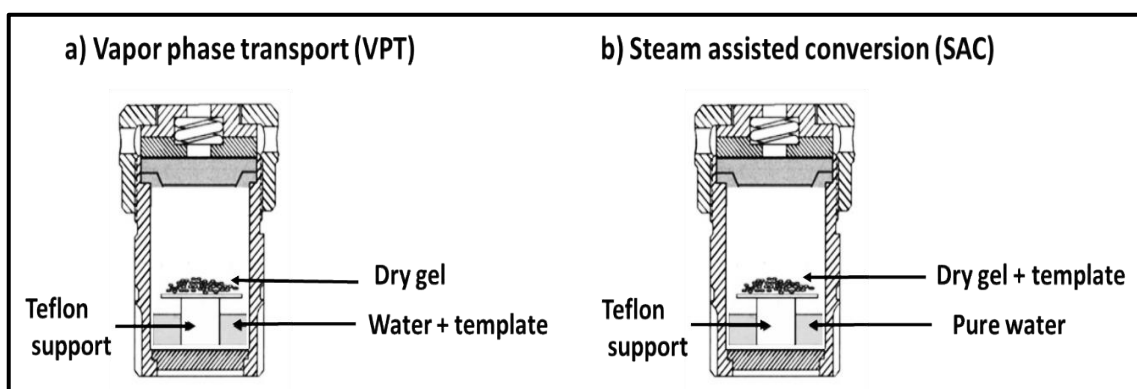


**Figure 1.13** Schematic illustration the comparison of the vapor phase transport (a) and the steam assisted conversion method (b).<sup>82</sup>

Due to all these limitations, the development of more-facile methods for preparing Sn-BEA catalysts became a vital prerequisite; specifically, developing indirect/postsynthesis methods (top-down methods). The post-synthesis method has gained profound importance over the bottom-up routes (i.e., dry-gel)<sup>83</sup> due to their simplicity, scalability and rapid synthesis time.

### 1.4.3 Post-synthetic methods for preparing Lewis-acid zeolites

The atom-planting technique was limited by the amount of metal that can be integrated into the solid zeolite. Hence, researchers adopted a different approach known as the demetallation-metalation technique. In this method, the process begins with a metallosilicate material rather than a fully siliceous material,

---

followed by a (solvo) thermal treatment process that would create vacant sites in the solid prior to metalation. This two-step method was first introduced in 1988 by Kraushaar and van Hoof.<sup>84</sup> Applying this method, they prepared a titanium-silicalite by a triple acid treatment of a ZSM-5 zeolite with Si/Al of =50 in 1M hydrochloric acid at 353 K, followed by a gas-phase treatment of the resulting zeolite (Si/Al=2000) with  $\text{TiCl}_4$ . Although, the authors did not give the amount of the grafted metal, the integration of Ti in the tetrahedral positions was proved by XRD, MAS NMR, and FTIR spectroscopy. The same post-synthetic approach was applied to MOR zeolites by calcination at 973 K and treatment in nitric acid under reflux conditions followed by exposure to different metal halide (Ga, Sb, and Ti) vapour at 475-875 K.<sup>85,86</sup> Notably, the 'demetallation-metallation' method is based on the dealumination of parent BEA zeolite followed by the solid-liquid-gas-phase incorporation of the metal in the created vacant sites. For instance, Li et al.<sup>87</sup> prepared BEA zeolite that contain up to 6.2 wt.% Sn by treating the zeolite in a 6M nitric acid solution (353 K, 8 h) followed by a gas-phase metalation with  $\text{SnCl}_4$  vapours at 770 K. The catalyst prepared in this way displays the same performance in the isomerization of glucose to fructose, compared to the Sn-BEA catalyst acquired by the bottom-up approach in fluoride media.<sup>88</sup> A better employment of Sn was accomplished by Jin et al.<sup>89</sup> who, following the same approach, aimed at lower Sn loading (1.2 wt.%), and produced Sn which is almost exclusively isomorphously substituted.

Other than the gas-phase metalation method, there are studies which focused on incorporating Lewis-acid metal in zeolite by a solid- or liquid-phase reaction. Hammond et.al.<sup>78</sup> treated a dealuminated BEA zeolite with Sn(II) acetate. They experimented with a solid-state ion- exchange (SSIE) route by dealuminating and incorporating Sn(II)-acetate without using HF media. The solid-state ion-exchange technique provides a possible strategy for preparing Sn-BEA zeolite with high Sn loading up to 10 wt. % which is devoid of bulk  $\text{SnO}_2$ . Moreover, the preparation of Sn-BEA zeolite, by using acetate precursor will avoid producing large volume of HCl that may lead to serious environmental problems. Another advantage of using the acetate precursor is avoiding the washing step to remove

the Cl<sup>-</sup> ions from the catalyst. The new solid-state ion-exchange method (Figure 1.14) to synthesize Sn-BEA zeolite is faster, less expensive and easier than other synthesis methods. Furthermore, the avoidance of HF makes this method a more environmentally green approach. Among its other advantages is that the solid-state ion-exchange technique allows the synthesis of a material with high metal content, smaller crystallite size, and more favourable catalytic properties. The same research group reported in later works that the solid-state ion-exchange method can be extended to inserting zirconium into BEA zeolite using Zr(IV) ethoxide as a precursor.<sup>90</sup>

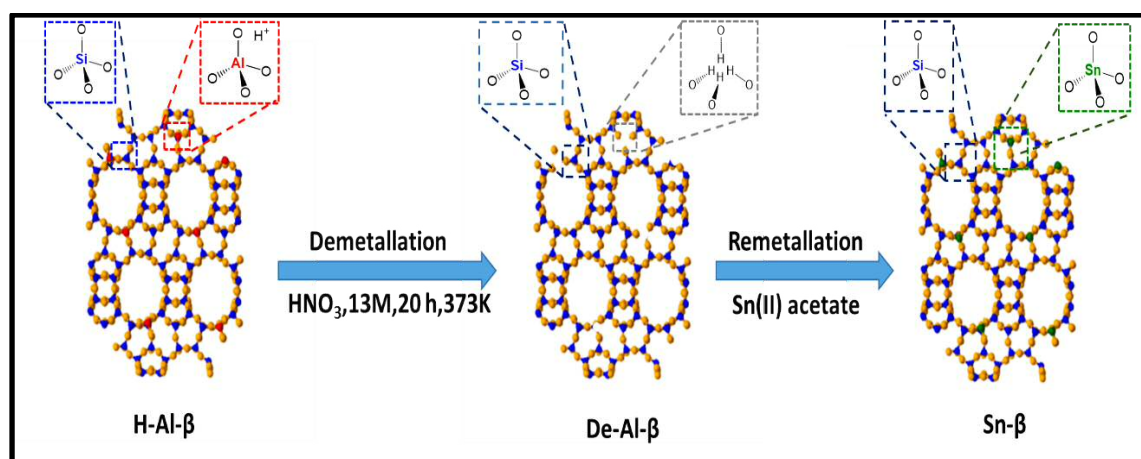


**Figure 1.14** Dealumination approach for the preparation Sn-BEA zeolite Lewis acid by SSI approach.

Tang and co-workers<sup>67</sup> successfully used Sn-BEA prepared by the solid-state ion-exchange for the first time in the ring opening hydration of epoxides to the corresponding 1,2-diol. High catalytic performance and high 1,2-diol selectivity were achieved in the reaction. Similarly, many studies have shown that the Sn-BEA as an active catalyst for epimerization and isomerization<sup>91</sup> with methanol and water as the reaction medium, respectively. The conversions of mono- and disaccharides into methyl lactate<sup>92</sup> are other reactions where Sn-BEA has been found effective. Particularly, the Sn-BEA catalyst demonstrated great stability

because it did not show evidences of deactivation after calcination or multiple cycles; i.e. no leaching of Sn was identified by elemental analysis. This study extends the research of Sn-BEA prepared by solid-state ion-exchange for isomerization of glucose to fructose and epimerization to mannose. Apart from the solid-state ion-exchange, the liquid-phase metalation has also been explored. For example, Dijkmans et al.<sup>93</sup> inserted 0.03 to 0.75 mmol of Sn into dealuminated BEA by refluxing the dealuminated zeolite in an isopropanol solution, using Sn(IV) chloride pentahydrate for 7 h. Materials with less than 1 wt.% Sn loadings are neatly obtained in tetrahedral form, but those with higher Sn loadings are characterised by the co-presence of bulk SnO<sub>2</sub> species.

To sum up, top-down strategies are more advantageous than bottom-up methodologies for the former is accompanied by the absence of HF, faster synthesis time, higher Sn loading (up to 10 wt. %), and generating Sn-BEA materials, which have relatively smaller crystallites. The most important advantage is that top-down strategies provide the opportunity of synthesising bifunctional catalysts by the remetallation of a partial dealumination sample.

### 1.5 Solid acid-base bifunctional catalysts.

In the last forty years, homogenous catalysts were regularly replaced by heterogeneous ones, which set a promising future in the catalysts industry. Heterogeneous solid acid-base bifunctional catalysts are those with double sites-metal and acid sites or reduction and oxidation sites where each site is capable of catalysing a different reaction, and both complement each other for the entire reaction. The activity and selectivity of the bifunctional catalyst can be determined by making a deliberate choice of the metal and the acid sites that show the wanted properties and characteristics. The tenability of the bifunctional sites makes bifunctional catalysts very useful in modern industries particularly in the production of liquid fuels and additives from biomass. The acid-base bifunctional solid catalysts are considered to be much better than the traditional liquid Brønsted, Lewis, and base catalysts. They show significant advantages in terms

---

of activity and selectivity, and they offer longer catalyst lifetime. They can also be repeatedly used and their separation from liquid product is much easier, in addition to being environmentally benign and non-corrosive.

An important example of an area where bifunctional materials offer high potential is biomass upgrading. For instance, an attractive top platform chemical is using ethers from 5-(hydroxymethyl)furfural (HMF) and HMF derivatives, which are extremely significant due to their high energy densities and usefulness as fuel blend.<sup>94</sup> Most of HMF etherification reactions include functionalizing the hydroxyl group of HMF to manufacture a monoether derivative.<sup>95,68,96,97</sup> In spite of the fact that catalytic synthesis of the diether is more eligible,<sup>98</sup> it is more challenging as it requires hydrogenating the carbonyl group into an alcohol before the etherification process. Balakrishnan et al.<sup>99</sup> proved that the combination of Amberlyst-15 and Pt/Al<sub>2</sub>O<sub>3</sub> can be used to catalyse the conversion of HMF into 2-5-bis(alkoxymethyl)furan in an alcoholic medium and under hydrogen pressure.<sup>99</sup> On the other hand, Gruter investigated a two-step process in which Pt/C catalyst and molecular hydrogen was used for the consecutive hydrogenation and etherification of HMF. In the first step, HMF was hydrogenated to 2,5-bis(hydroxymethyl)furan (BHMF) over the Pt/C catalyst at 5 bar of hydrogen pressure, followed by the etherified to 2,5-bis(ethoxymethyl)furan at 75 °C in the absence of hydrogen.<sup>98</sup> The hydrogenation of HMF to BHMF often requires the use of noble metal catalyst; such as Pt<sup>99</sup> or Ru<sup>100</sup> under high hydrogen pressure (> 5 bar). However, performing both the hydrogenation and etherification requires using two catalysts (metal and acid catalysts), which could increase the process setup cost. To overcome this disadvantage, the Meerwein-Ponndorf-Verley (MPV) reaction supplies an alternative approach to reduce the carbonyl groups. Instead of using molecular hydrogen, the MPV reaction uses sacrificial alcohols as hydrogen donors.<sup>101,73</sup> Since the formulation of ether requires using alcohols, a one-step process in which the alcohol works as a hydrogenation and as an etherification agent is required. According to Corma et al.,<sup>101</sup> zeolite BEA with framework Sn and Zr are solid Lewis acids, and they can actively catalyse the transfer hydrogenation and etherification reactions.<sup>101,73</sup>

The starting material used in this study is furfural, which can be produced by several well-established methods from hemicellulose. In the first step, furfural was transformed into furfuryl alcohol through a transfer hydrogenation over a Sn-BEA Lewis acid catalyst and 2-butanol as the hydrogen donor. In the second step, furfuryl alcohol was transformed into butyl furfuryl ether in the presence of a Brønsted acid (Al) and 2-butanol (Figure 1.15). The bifunctional solid acid-base catalysts, solvents, and mild reaction conditions, which were employed in this study, make it an appropriate strategy for the transfer hydrogenation /etherification processes without using costly metals or high pressures of molecular H<sub>2</sub>.

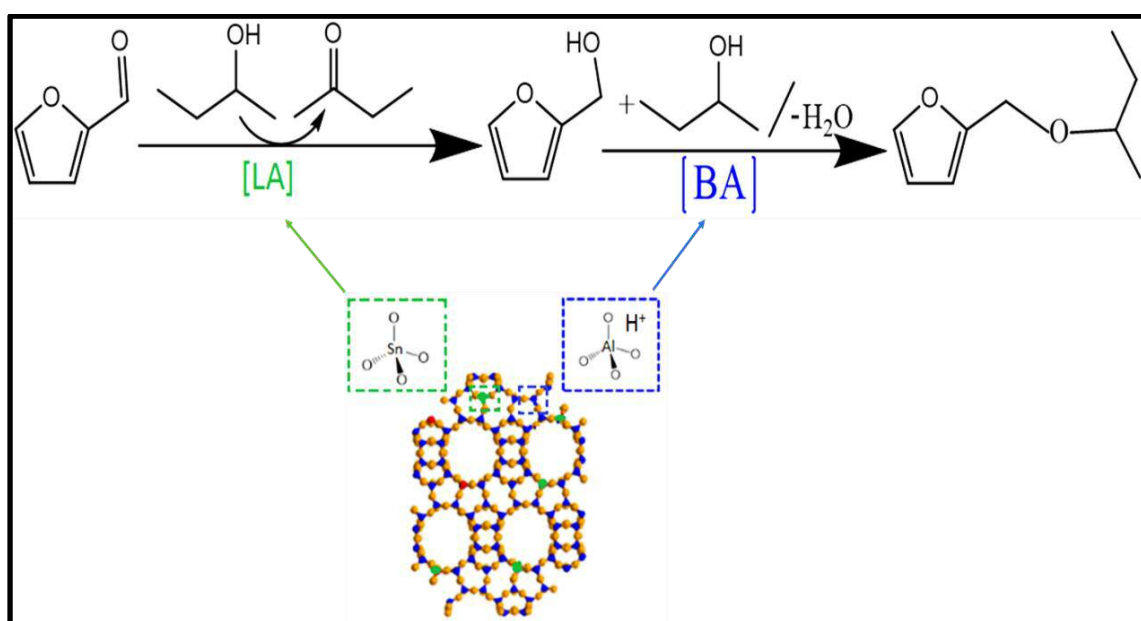


**Figure 1.16** Furfural and 2-butanol reaction pathways.

## 1.6 Catalyst Deactivation

A common problem in industrial catalytic processes is the loss of catalytic activity and selectivity with time. Every year, a large amount of time, resources and money are lost by manufacturers due to the requirement for catalyst replacement. Hence, prolonging the catalyst lifetime is a pivotal requirement in addition to

determining activity and selectivity.<sup>102</sup> All catalysts have a limited life span, and will eventually be deactivated irrespective of the rate at which this happens. The catalyst activity is highly influenced by the reaction conditions; such as pressure, temperature, and the reactant composition.<sup>103</sup> Thus, studying deactivation is essential to develop, design and operate the catalyst commercially. The catalyst deactivation can be the result of chemical, mechanical or thermal degeneration. Bartholomew,<sup>103</sup> summed up five main mechanisms of deactivation, which are: fouling or coking, poisoning, vapour-solid and/or solid-solid reactions, thermal degradation and attrition or crushing. Catalyst poisoning can occur when strong chemisorption of reactants, products and/or impurities occurs on the catalyst active sites, thereby leading to blockage of the adsorption sites, and a drastic change in the electronic properties and geometry of the catalyst surface.<sup>103</sup> Many reactions; such as hydrogenation and cracking may involve poisoning, which may either be reversible or irreversible depending on the strength of the adsorbed poison. It is preferable to avoid catalyst poisoning by removing the poison to purify the reactant stream using scrubber or guard beds.<sup>104</sup>

Catalyst aging or sintering happens as a result of long exposure to elevated liquid-phase temperatures, which results in loss of active surface area. In fact, sintering can be defined as thermally generated deactivation of catalysts that leads into the following consequences:

- a) Loss of catalyst surface area because of its crystallite expansion.
- b) Loss of the support area because of support breakdown .
- c) Loss of catalyst surface area because of pore breakdown upon crystallites of the active phase.<sup>105</sup>

Catalyst sintering often happens with high temperature reaction (typically beyond 775 K). However, it is generally accelerated in the presence of water or solvent vapour. Accordingly, even though the reactions studied in this thesis are conducted at lower temperatures (< 200 °C), sintering and (hydro)thermal damage to the material is very not likely. The catalyst mechanical failure happens in different forms, such as catalyst crushing as a result of attrition or load (reducing size or collapse of catalyst to produce fines).<sup>103</sup>

Coking or fouling is the most well-established cause of deactivation in heterogeneous catalysis especially for porous materials like zeolites.<sup>106</sup> It can be defined simply as the physical deposition of species – typically carbonaceous species on top of the catalyst surface or within the catalyst pores, from the fluid phase.<sup>103</sup> Coke is formed by decomposing or condensing hydrocarbons into catalyst surface, and its chemical framework changes with catalyst and reaction type as well as reaction conditions.<sup>107</sup> Coke usually includes heavy polymerised hydrocarbons and could range from high molecular weight hydrocarbons to elementary carbons like graphite.<sup>107</sup> The catalyst loses its activity with coke deposition due to pore blocking and/or active sites.<sup>108</sup> The rate of coke accumulation in any reaction differs considerably with catalyst structure and support, as well as the nature of the reactants and products of the reaction.<sup>109</sup> The rate of coke formation also varies with the operating conditions like temperature and pressure. In general, the rate of coke formation and deposition increases with reaction temperatures and pressures. Higher temperature leans towards side reactions that result in coke formation,<sup>109</sup> and higher pressure leans towards constructing higher molecular weight olefins.<sup>110</sup>

According to Menon,<sup>111</sup> catalyst reactions can be either coke-sensitive or coke-insensitive. In coke-sensitive reactions; such as catalytic cracking and hydrogenolysis, the unreactive coke precipitates on active sites leading to loss of activity. While, in coke-insensitive reactions; such as methanol synthesis and catalytic reforming, relatively reactive coke species are synthesised on the active centres and are taken out by using gasifying agents like hydrogen.

In order to have an adequate assessment of the catalyst stability and deactivation, the catalytic experiments should be performed in a continuous reactor. Using continuous Plug Flow Reactor (PFR, Figure 1.16) is highly advantageous in several ways including:<sup>112</sup>

- a) Better process and safety control
- b) Better levels of mass- and heat-transfer
- c) Faster reaction times

- d) Reduced reactor volumes
- e) Better degree of scalability, and
- f) Higher space-time yields,

Another advantage of the continuous Plug Flow Reactor is that it can operate at steady-state, hence, giving more accurate deactivation profile.

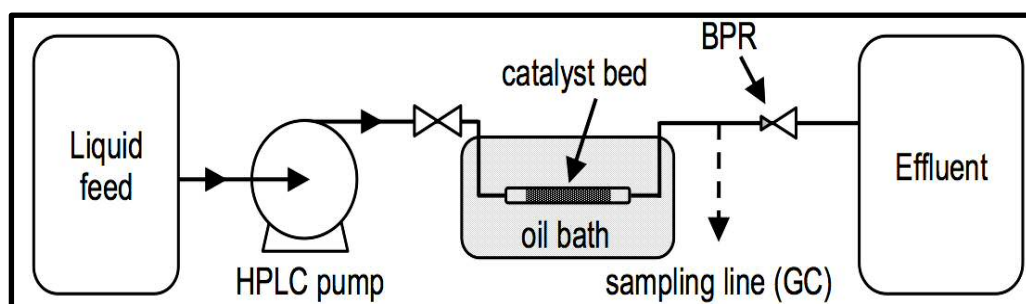


**Figure 1.16** Schematic of a Plug Flow Reactor. Reactants are fed to the reactor via the inlet flow and converted to products in the reactor.

Recently, this continuous approach was used by Lewis et al.<sup>113</sup> to assess the stability of Lewis acids (Sn, Zr and HF) containing BEA zeolites in hydrogenation transfer and etherification of HMF. It was also used by both Koehle et al.<sup>114</sup> to study the reduction of furfural to furfuryl alcohol in MPV reaction, and Van de Vyver et al.<sup>115</sup> to convert 1,3-dihydroxyacetone (DHA) and formaldehyde to  $\alpha$ -hydroxy- $\gamma$ -butyrolactone (HBL) by using Sn-BEA. In these studies, the main factors that determine the stability of Sn-BEA in operation are highlighted. Selecting a suitable zeolite pore structure is very important in limiting the coke formation and minimizing its deactivation impact. High coking ratio and high toxicity of coke molecules are attached with zeolites that have monodimensional pore system or zeolite that have trap cages; i.e., big cages with tiny openings. In fact, these pore systems prefer to seize the coke precursor, which leads to deactivation by blocking the pore. Nevertheless, these disadvantages can be

reduced by various ways; particularly, by mesopores creation in post-synthesis treatment; i.e., dealumination and preferably desilication.

## 1.7 Objectives of the thesis

The major target of this work is to develop new Lewis acidic zeolite catalysts for a variety of liquid phase catalytic transformation. In addition to identifying new materials of potentially higher levels of activity and selectivity, two major targets are to 1) overcome the inefficient procedures of synthesizing Lewis acidic zeolites in order to develop the utilizing potentialities of these important materials, and 2) develop Lewis acidic zeolites that are more resistant to catalyst deactivation. To achieve these aims, the thesis investigates a more facile preparation method of Sn(IV)-containing zeolite BEA, which is shorter and more selective, by applying solid-state incorporation (SSI) method that incorporate more Sn into the framework than by direct hydrothermal synthetic method. On the other hand, to overcome the pore size limitations to the applicability of Lewis acidic zeolites; particularly, in terms of catalysing the conversion of bulky molecules and in suffering slower rates of deactivation, the thesis aims to prepare Lewis acid containing zeolites possessing modified hierarchical BEA structures, combining microporosity and mesoporosity, which can intercede the catalytic conversion of bulky ketone substrates. Furthermore, the work seeks to design a bifunctional zeolitic materials that have both Lewis and Brønsted acid sites in a single catalytic materials, which results in high levels of activity, selectivity and stability. Finally, the thesis deals with the impact of different catalyst pore structures on the catalyst lifetime by using continuous Plug Flow Reactor.

---

## 1.9 References:

- 1 C. S. Cundy and P. A. Cox, *Chem. Rev.*, 2003, **103**, 663.
- 2 J. F. Haw, J. B. Nicholas, T. Xu, L. W. Beck and D. B. Ferguson, *Acc. Chem. Res.*, 1996, **29**, 259.
- 3 A. Corma, *J. Catal.*, 2003, **216**, 298.
- 4 K. S. W. Sing, D. H. Everett, R. a. W. Haul, L. Moscou, R. a. Pierotti, J. Rouquérol and T. Siemieniewska, *Pure Appl. Chem.*, 1982, **54**, 2201.
- 5 C. Baerlocher, L. McCusker and D. Olson, *Atlas of zeolite framework types*, 2007, vol. 12.
- 6 <http://www.iza-structure.org/databases/>.
- 7 J. Weitkamp, *Solid State Ionics*, 2000, **131**, 175.
- 8 A. Corma, *Chem. Rev.*, 1997, **97**, 2373.
- 9 M. Guisnet and J.-P. Gilson, *Zeolites for cleaner technologies*, 2002, vol. 3.
- 10 A. Corma, *Chem. Rev. (Washington, D C )*, 1995, **95**, 559.
- 11 T. Chen, A. Men, P. Sun, J. Zhou, Z. Yuan, Z. Guo, J. Wang, D. Ding and H. Li, *Catal. Today*, 1996, **30**, 189.
- 12 M. Elanany, M. Koyama, M. Kubo, E. Broclawik and A. Miyamoto, *Appl. Surf. Sci.*, 2005, **246**, 96.
- 13 G. H. Kuhl, *J. Phys. Chem. Solids*, 1977, **38**, 1259.
- 14 M. Hunger, D. Freude and H. Pfeifer, *J. Chem. Soc. Faraday Trans.*, 1991, **87**, 657.
- 15 D. Ma, F. Deng, R. Fu, X. Han and X. Bao, *J. Phys. Chem. B*, 2001, **105**, 1770.
- 16 B. A. Williams, S. M. Babitz, J. T. Miller, R. Q. Snurr and H. H. Kung,

- 
- Appl. Catal. A Gen.*, 1999, **177**, 161.
- 17 N. Katada, Y. Kageyama, K. Takahara, T. Kanai, H. A. Begum and M. Niwa, *J. Mol. Catal. A Chem.*, 2004, **211**, 119.
- 18 D. B. C. Mirodatos, *J. Chem. Soc. Chem. Commun.*, 1981, **2**, 39.
- 19 T. F. Narbeshuber, A. Brait, K. Seshan and J. A. Lercher, *Appl. Catal. A Gen.*, 1996, **146**, 119.
- 20 D. Barthomeuf, *J. Phys. Chem.*, 1979, **83**, 249.
- 21 B. Beagley, J. Dwyer, F. R. Fitch, R. Mann and J. Walters, *J. Phys. Chem.*, 1984, **88**, 1744.
- 22 A. Auroux, P. C. Gravelle, J. C. Vedrine and M. Rekas, in *5th Int. Conf. On Zeolites, (Heyden, London)*, 1980, p. 443.
- 23 M. Stöcker, *Microporous Mesoporous Mater.*, 2005, **82**, 257.
- 24 K. A. Fisher, K. D. Huddersman and M. J. Taylor, *Chem. – A Eur. J.*, 2003, **9**, 5873.
- 25 G. Cerri, M. de Gennaro, M. C. Bonferoni and C. Caramella, *Appl. Clay Sci.*, 2004, **27**, 141.
- 26 A. Corma, V. Fornes and F. Rey, *Adv. Mater.*, 2002, **14**, 71.
- 27 Å. Dahm and H. Eriksson, *J. Biotechnol.*, 2004, **111**, 279.
- 28 M. Rivera-Garza, M. T. Olguín, I. García-Sosa, D. Alcántara and G. Rodríguez-Fuentes, *Microporous Mesoporous Mater.*, 2000, **39**, 431.
- 29 V. Wernert, O. Schaf, H. Ghobarkar and R. Denoyel, *Microporous Mesoporous Mater.*, 2005, **83**, 101.
- 30 H. Takagi, H. Hatori, Y. Soneda, N. Yoshizawa and Y. Yamada, *Mater. Sci. Eng. B*, 2004, **108**, 143.
- 31 V. Eroshenko and R. . Regis, *J. Am. Chem. Soc.*, 2001, **28**, 8129.

- 
- 32 N. Yamamoto and T. Okubo, *Microporous Mesoporous Mater.*, 2000, **40**, 283.
- 33 S. D. Mikhailenko, S. Kaliaguine and E. Ghali, *Microporous Mater.*, 1997, **11**, 37.
- 34 M. Hartmann, *Angew. Chemie - Int. Ed.*, 2004, **43**, 5880.
- 35 V. Valtchev, G. Majano, S. Mintova and J. Pérez-Ramírez, *Chem. Soc. Rev.*, 2013, 263.
- 36 J. Pérez-Ramírez, C. H. Christensen, K. Egeblad, C. H. Christensen and J. C. Groen, *Chem. Soc. Rev.*, 2008, **37**, 2530.
- 37 L. Chen, X. Li, J. C. Rooke, Y. Zhang, X. Yang, Y. Tang, F. Xiao and B. Su, *J. Mater. Chem.*, 2012, **22**, 17381.
- 38 M. E. Davis, C. Saldarriaga, C. Montes, J. Garces and C. Crowdert, *Nature*, 1988, **331**, 698.
- 39 M. Stöcker, *Microporous Mesoporous Mater.*, 1999, **29**, 3.
- 40 A. Cybulski and M. M. R. A. S. Moulijn, J.A.Sharma, 2001, p. 59.
- 41 L. Tosheva and V. P. Valtchev, *Chem. Mater.*, 2005, **17**, 2494.
- 42 J. Čejka and S. Mintova, *Catal. Rev. Sci. Eng.*, 2007, **49**, 457.
- 43 C. Fernandez, I. Stan, J. P. Gilson, K. Thomas, A. Vicente, A. Bonilla and J. Pérez-Ramírez, *Chem. - A Eur. J.*, 2010, **16**, 6224.
- 44 K. Egeblad, C. H. Christensen, M. Kustova and C. H. Christensen, *Chem. Mater.*, 2008, **20**, 946.
- 45 J. Pérez-Ramírez, C. H. Christensen, K. Egeblad, C. H. Christensen and J. C. Groen, *Chem. Soc. Rev.*, 2008, **37**, 2530.
- 46 K. Na, C. Jo, J. Kim, K. Cho, J. Jung, Y. Seo, R. J. Messinger, B. F. Chmelka and R. Ryoo, *Science (80-. )*, 2011, **333**, 328.
- 47 D. P. Serrano, J. M. Escola and P. Pizarro, *Chem. Soc. Rev.*, 2013, **42**,

- 4004.
- 48 S. Lopez-Orozco, A. Inayat, A. Schwab, T. Selvam and W. Schwieger, *Adv. Mater.*, 2011, **23**, 2602.
- 49 K. Möller and T. Bein, *Chem. Soc. Rev.*, 2013, **42**, 3689.
- 50 J. C. Groen, L. A. A. Peffer, J. A. Moulijn and J. Pérez-Ramírez, *Chem. - Eur. J.*, 2005, **11**, 4983.
- 51 D. Verboekend and J. Pérez-Ramírez, *Chem. - A Eur. J.*, 2011, **17**, 1137.
- 52 J. C. Groen, J. C. Jansen, J. A. Moulijn and J. Pérez-Ramírez, *J. Phys. Chem. B*, 2004, **108**, 13062.
- 53 L. Xu, L. Duan, Z. Liu, J. Guan and Q. Kan, *Bull. Mater. Sci.*, 2013, **36**, 1291.
- 54 R. Srivastava, M. Choi and R. Ryoo, *Chem. Commun.*, 2006, **41**, 4489.
- 55 J. C. Groen, T. Sano, J. A. Moulijn and J. Pérez-Ramírez, *J. Catal.*, 2007, **251**, 21.
- 56 J. Li, X. Li, G. Zhou, W. Wang, C. Wang, S. Komarneni and Y. Wang, *Appl. Catal. A Gen.*, 2014, **470**, 115.
- 57 M. Taramasso, S. Milanese, G. Perego, Milan and B. Notari, 1982, 1.
- 58 J. N. Chheda, G. W. Huber and J. A. Dumesic, *Angew. Chemie - Int. Ed.*, 2007, **46**, 7164.
- 59 Y. Roman-Leshkov and M. E. Davis, *ACS Catal.*, 2011, **1**, 1566.
- 60 R. Gounder, *Catal. Sci. Technol.*, 2014, **4**, 2877.
- 61 M. a. Cambor, A. Corma and S. Valencia, *Chem. Commun.*, 1996, 2365.
- 62 T. Ennaert, J. Van Aelst, J. Dijkmans, R. De Clercq, W. Schutyser, M. Dusselier, D. Verboekend and B. F. Sels, *Chem. Soc. Rev.*, 2016, **45**, 584.

- 
- 63 M. Boronat, P. Concepción, A. Corma and M. Renz, *Catal. Today*, 2007, **121**, 39.
- 64 A. Corma, M. E. Domine, L. Nemeth and S. Valencia, *J. Am. Chem. Soc.*, 2002, **124**, 3194.
- 65 A. Corma, L. T. Nemeth, M. Renz and S. Valencia, *Nature*, 2001, **412**, 423.
- 66 K. Yakabi, K. Milne, A. Buchard and C. Hammond, *ChemCatChem*, 2016, **8**, 3490.
- 67 B. Tang, W. L. Dai, G. J. Wu, N. J. Guan, L. D. Li and M. Hunger, *ACS Catal.*, 2014, **4**, 2801.
- 68 C. M. Lew, N. Rajabbeigi and M. Tsapatsis, *Ind. Eng. Chem. Res.*, 2012, **51**, 5364.
- 69 E. Nikolla, Y. Román-Leshkov, M. Moliner and M. E. Davis, *ACS Catal.*, 2011, **1**, 408.
- 70 V. Choudhary, A. B. Pinar, S. I. Sandler, D. G. Vlachos and R. F. Lobo, *ACS Catal.*, 2011, **1**, 1724.
- 71 R. Gounder and M. E. Davis, *J. Catal.*, 2013, **308**, 176.
- 72 E. Taarning, S. Saravanamurugan, M. S. Holm, J. Xiong, R. M. West and C. H. Christensen, *ChemSusChem*, 2009, **2**, 625.
- 73 J. Jae, E. Mahmoud, R. F. Lobo and D. G. Vlachos, *ChemCatChem*, 2014, **6**, 508.
- 74 Y. Román-Leshkov, M. Moliner, J. A. Labinger and M. E. Davis, *Angew. Chemie - Int. Ed.*, 2010, **49**, 8954.
- 75 T. Blasco, M. a Cambor, A. Corma, P. Esteve, J. M. Guil, A. Martí, S. Valencia, A. Martínez and J. a Perdigon-Melon, *J. Phys. Chem. B*, 1998, **102**, 75.
- 76 S. Tolborg, A. Katerinopoulou, D. D. Falcone, I. Sádaba, C. M.

- 
- Osmundsen, R. J. Davis, E. Taarning, P. Fristrup and M. S. Holm, *J. Mater. Chem. A*, 2014, **2**, 20252.
- 77 S. R. Bare, S. D. Kelly, W. Sinkler, J. J. Low, F. S. Modica, S. Valencia, A. Corma and T. L. and Nemeth, *J. Am. Chem. Soc.*, 2005, **127**, 12924.
- 78 C. Hammond, S. Conrad and I. Hermans, *Angew. Chemie - Int. Ed.*, 2012, **51**, 11736.
- 79 R. Bermejo-Deval, R. Gounder and M. E. Davis, *ACS Catal.*, 2012, **2**, 2705.
- 80 P. S. Niphadkar, M. S. Kotwal, S. S. Deshpande, V. V. Bokade and P. N. Joshi, *Mater. Chem. Phys.*, 2009, **114**, 344.
- 81 Z. Kang, X. Zhang, H. Liu, J. Qiu and K. L. Yeung, *Chem. Eng. J.*, 2013, **218**, 425.
- 82 J. Weitkamp and M. Hunger, *Stud. Surf. Sci. Catal.*, 2005, **5**, 1.
- 83 C.-C. Chang, H. J. Cho, Z. Wang, X. Wang and W. Fan, *Green Chem.*, 2015, **17**, 2943.
- 84 B. Kraushaar and J. H. C. Van Hooff, *Catal. Letters*, 1988, **1**, 81.
- 85 P. Wu, T. Yashima, T. Yashima, S. Nakata and H. Shoji, *Microporous Mater*, 1997, **12**, 25.
- 86 P. Wu, T. Komatsu and T. Yashima, *J. Phys. Chem.*, 1996, **100**, 10316.
- 87 P. Li, G. Liu, H. Wu, Y. Liu, J. G. Jiang and P. Wu, *J. Phys. Chem. C*, 2011, **115**, 3663.
- 88 M. Liu, S. Jia, C. Li, A. Zhang, C. Song and X. Guo, *Chinese J. Catal.*, 2014, **35**, 723.
- 89 J. Jin, X. Ye, Y. Li, Y. Wang, L. Li, J. Gu, W. Zhao and J. Shi, *Dalton Trans.*, 2014, **43**, 8196.
- 90 P. Wolf, C. Hammond, S. Conrad and I. Hermans, *Dalton Trans.*, 2014,

- 43**, 4514.
- 91 R. Bermejo-Deval, M. Orazov, R. Gounder, S. J. Hwang and M. E. Davis, *ACS Catal.*, 2014, **4**, 2288.
- 92 M. S. Holm, S. Saravanamurugan and E. Taarning, *Science*, 2010, **328**, 602.
- 93 J. Dijkmans, D. Gabriels, M. Dusselier, F. de Clippel, P. Vanelderren, K. Houthoofd, A. Malfliet, Y. Pontikes and B. F. Sels, *Green Chem.*, 2013, **15**, 2777.
- 94 S. P. Teong, G. Yi and Y. Zhang, *Green Chem.*, 2014, **16**, 2015.
- 95 G. a. Kraus and T. Guney, *Green Chem.*, 2012, **14**, 1593.
- 96 M. Mascal and E. B. Nikitin, *ChemSusChem*, 2009, **2**, 423.
- 97 M. Mascal and E. B. Nikitin, *ChemSusChem*, 2009, **2**, 859.
- 98 G. J. M. Gruier, *United States Pat. 8277521*, 2012, **2**.
- 99 M. Balakrishnan, E. R. Sacia and A. T. Bell, *Green Chem.*, 2012, **14**, 1626.
- 100 R. Alamillo, M. Tucker, M. Chia, Y. Pagán-Torres, J. Dumesic, Y. Pagan-Torres and J. Dumesic, *Green Chem.*, 2012, **14**, 1413.
- 101 A. Corma, F. X. Llabrés I Xamena, C. Prestipino, M. Renz and S. Valencia, *J. Phys. Chem. C*, 2009, **113**, 11306.
- 102 M. Guisnet and P. Magnoux, *Appl. Catal. A Gen.*, 2001, **212**, 83.
- 103 C. H. Bartholomew, *Appl. Catal. A Gen.*, 2001, **212**, 17.
- 104 C. H. Bartholomew, *Stud. Surf. Sci. Catal.*, 1994, **88**, 1.
- 105 C. H. Bartholomew, *Appl. Catal. A Gen.*, 2001, **212**, 17.
- 106 M. Absi-Halabi, A. Stanislaus and D. L. Trimm, *Appl. Catal.*, 1991, **72**, 193.

- 
- 107 C. H. Bartholomew, *Catal. Rev. Sci. Eng.*, 1982, **24(1)**, 67.
- 108 C. V. Satyanarayana, D. Srikant and H. R. Gurav, *Catalyst Deactivation and Regeneration*, Elsevier Inc., 2016, vol. 5.
- 109 M. Guisnet and P. Magnoux, *Catal. Today*, 1997, **36**, 477.
- 110 R. J. Quann, L. A. Green, S. A. Tabak and F. J. Krambeck, *Ind. Eng. Chem. Res.*, 1988, **27**, 565.
- 111 P. G. Menon, *J. Mol. Catal.*, 1990, **59**, 207.
- 112 D. Padovan, C. Parsons, M. Simplicio Grasina and C. Hammond, *Green Chem.*, 2016, **18**, 5041.
- 113 J. D. Lewis, S. Van De Vyver, A. J. Crisci, W. R. Gunther, V. K. Michaelis, R. G. Griffin and Y. Román-Leshkov, *ChemSusChem*, 2014, **7**, 2255.
- 114 M. Koehle and L. F. Raul, *Catal. Sci. Technol.*, 2016, **6**, 3018.
- 115 S. Van De Vyver, C. Odermatt, K. Romero, T. Prasomsri and Y. Román-Leshkov, *ACS Catal.*, 2015, **5**, 972.

# 2

## Experimental and Characterization

### 2. 1 Reagents

The following reagents were used during this project. All reagents were used as received without further purification, unless otherwise stated.

Acetonitrile-d <sub>3</sub>	99%	Aldrich
Ammonium nitrate nonahydrate	98%	Sigma-Aldrich
Biphenyl	99.5%	Sigma-Aldrich
2-Butanol	≥99%	Sigma-Aldrich
Cyclohexanone	≥99%	Sigma-Aldrich
Cyclohexanol	99%	Sigma-Aldrich
Cyclooctanone	98%	Aldrich
Cyclooctanol	98%	Alfa Aesar
Cyclododecanone	99%	Sigma-Aldrich
Cyclododecanol	99%	Alfa Aesar
D-(+)-Glucose	≥99.5%	Sigma
D-(-) Fructose	≥99%	Sigma-Aldrich
Furfural	99%	Sigma-Aldrich
Furfuryl alcohol	99%	Aldrich
Hexadecyltrimethylammonium bromide	≥99%	Sigma
D-(+)-Mannose	≥99%	Fluka
D-Mannitol	≥98%	Sigma-Aldrich
Nitric acid	70%	Sigma-Aldrich

---

Pyridine anhydrous	99%	BDH
Silica, fumed	99%	Sigma-Aldrich
Sodium hydroxide-pellets	>97%	Fisher chemical
Sn(IV)chloride pentahydrate	98%	Sigma-Aldrich
Sn(II) acetate	99%	Sigma-Aldrich
Tetramethylammonium hydroxide solution	35wt.% H <sub>2</sub> O	Sigma-Aldrich
Zeolite BEA, NH <sub>4</sub> -form, SiO <sub>2</sub> /Al <sub>2</sub> O <sub>3</sub> = 38	≥99%	Zeolyst

---

## 2.2 Definitions

### 2.2.1 Conversion

$$\text{Conversion} = \frac{\text{Moles of product formed}}{\text{Moles of reactant}} \quad 2.1$$

### 2.2.2 Selectivity

$$\% \text{Selec.} = \frac{\text{Moles of desired product}}{\text{Moles of all products}} \times 100 \quad 2.2$$

2.2.3 Turnover frequency (TOF): Moles (product formed) mole<sup>-1</sup> (total metal) hour<sup>-1</sup>

$$\text{TOF} = \frac{\text{Moles of product formed}}{\text{Moles of metal} \times \text{Time}} \quad 2.3$$

## 2.3 Catalysts synthesis

The experimental procedures used to prepare the zeolite catalysts in this thesis include two main steps:

- Post-synthesis procedures starting from commercial Al-BEA zeolite (Zeolyst, NH<sub>4</sub>-form, SiO<sub>2</sub>/Al<sub>2</sub>O<sub>3</sub> = 38).
- Hydrothermal synthesis of Sn-MCM-41.

The detailed experimental procedure for the preparation and characterisation of each catalyst is presented at the end of the chapters 3, 4 and 5 that relates to each catalyst.

### 2.4 Kinetic studies

Two main types of kinetic experiments were performed in this work, including batch and continuous flow studies. The detailed experimental descriptions of both approaches is presented at the end of the chapters that are pertinent to each technique.

### 2.5 Analytical methods

The analysis of the products in this work were performed through one or both of two important chromatography techniques: Gas Chromatography (GC) and High Performance Liquid Chromatography (HPLC).

#### 2.5.1 Gas chromatography (GC)

In Gas Chromatography technique, the unknown reaction components are injected through an injection port, vaporised in the heated GC oven, and transported through the heated column placed in the GC oven by a carrier gas such as, N<sub>2</sub>, H<sub>2</sub>, Ar, or He. The components of the unknown reaction mixtures are then separated in the column according to one of either the boiling point or ionisation characters. The separated components evolve from the column at different time, detected at the detector, which produces a signal equivalent to the concentration of each components in the mixture.

Typically, two kinds of column can be employed in this technique: the capillary and the packed column. The main difference between the two columns lies in their internal wall characteristics. While the internal walls of a capillary column are either coated or supported with a thin film of polymeric material called the

stationary phase, the packed columns consist of a high surface area support materials immobilized with a liquid phase stationary coating material. In gas chromatography, the detector responds differently to different materials, depending on their physicochemical properties. The detector's specific response to each material is measured and compared with a well-recognized internal unreactive standard material to determine the relative quantity and quality of each material in the reaction components. In this project, the Agilent GC 7820 (25 m CP-Wax 52 CB) was used to identify compounds against a biphenyl internal standard.

Calibrations were performed using biphenyl as an internal standard for the Meerwein-Ponndorf-Verley transfer hydrogenations in chapter 7, the calibration curves was used to obtain the response factors for each reagent relative to biphenyl (Appendix, Figures 7.4 - 7.11). Consequently, quantification was achieved via the response factor technique. A series of calibration solutions of different concentrations, were used to obtain response factor (RF) data for the target reactions components. Equation 2.4 gives the formula upon which the response factor was calculated. A sample gas chromatogram of the reactant and reaction products is given in (Appendix, Figures 7.1 and 7.2).

$$\text{Response Factor} = \frac{\text{Area of peak}}{\text{Concentration of peak}} \quad 2.4$$

### 2.5.2 High performance liquid chromatography (HPLC)

Another complimentary technique to the gas chromatography is the High Performance Liquid Chromatography (HPLC). Both the GC and the HPLC techniques share similar operating principles except for the mobile phases used in the techniques. The liquid mobile phase is used to transport the analytes in the HPLC whereas, gases are utilised as the carrier phase in the GC. For the HPLC analysis the analytes should be soluble in the mobile phase, and the HPLC is highly convenient to analyse sample that are heat sensitive and/or non-volatile. The analytes are injected into the liquid phase carrier, and separation is achieved

based on the selective retention/ interaction of the components of the analytes with a solid stationary column material.<sup>1</sup> Detection of analytes in HPLC can be carried out with different detectors, hence, the HPLC technique can be assembled with more than one. The most common liquid chromatography detectors are the UV-Vis and RID, which detects organic compounds. The components of the reaction mixture were separated by high performance liquid chromatography (HPLC) in Varian 330 equipped with a Ca Hi -Plex column (for the analysis of sugars, sugars alcohols and organic acids) with dimensions of 6.5 x 300 mm, 8  $\mu$ m particle size, from Agilent, which was isothermally held at 60 °C. The eluent used was 0.05 M aqueous phosphoric acid solution.

Calibrations were performed using mannitol as an internal standard for the D-glucose isomerization (Chapter 7). A series of calibration solutions, at different concentrations, were investigated to have response factor (RF) data for the target reactions (Equation 2.4), (Appendix, Figures 7.12 – 7.14). A sample HPLC chromatogram of the reactant and reaction products is given in (Appendix, Figure 7.3).

## 2.6 Characterisation techniques

To better understand the catalytic performance, and to correlate the structure of the synthesized zeolites to their activity, multiple characterisation techniques were adopted in this study. These complementary techniques were conducted to investigate the structure, morphology, active site speciation, surface area, and the nature and strength of the acid site in the catalysts used in this work. Structural analysis was done with the powder X-ray diffraction (XRD), and the morphology of each material studied with Scanning Electron Microscopy (SEM) and Transmission Electron Microscopy (TEM). A comprehensive characterisation of the active sites in each catalyst was conducted through X-ray Absorption Spectroscopy (XAS), Electron Paramagnetic Resonance and UV/Visible Spectroscopy (UV-Vis). The combination of these techniques affords a deeper understanding of the active sites involved in the reaction and provides good

evidences for reaction mechanisms. These techniques are summarized in Figure 2.1. The principles of each method are presented in the succeeding section of the chapter.

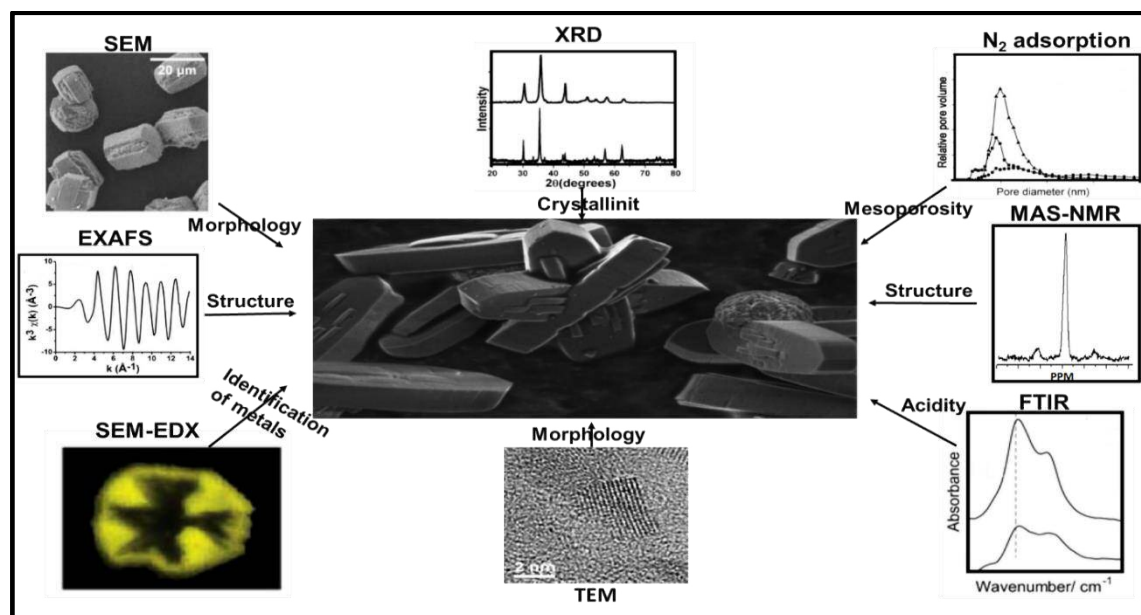


**Figure 2.1** Multi-disciplinary methods employed in this project to identify the properties of each catalyst.

### 2.6.1 Gas adsorption

This method is an essential technique for identifying the surface area and porous properties of solid materials. It is based on the gradual adsorption of a specific gas at low temperature. Commonly used gases include argon, krypton and nitrogen. Nitrogen adsorption measurement is the most popular partly due to the low cost of nitrogen and it is widely available. Nitrogen adsorption is always conducted at (77 K).

In the first step of surface area analysis, a mono-layer adsorption of gas is achieved, usually at low partial pressure, but when the nitrogen pressure increase, multi-layer formation is produced. Some very important applications of the gas adsorption technique include surface area analysis, pore characterisation and

pore volume measurements. For surface area analysis the Brunauer-Emmett-Teller (BET) method is the most widely utilised and it is based on equation 2.5,<sup>2</sup> which is accurate in the region  $P/P_o$  between 0.05 to 0.35.

$$\frac{V}{V_m} \frac{P_o}{P - P_o} = \frac{C + 1}{C - 1} \frac{P}{P_o} \quad 2.5$$

Where  $V$  = volume of adsorbed gas at a pressure  $P$ ,  $P_o$  = saturation pressure,  $V_m$  = molar volume of gas needed to make monolayer of adsorbed gas,  $C$  = BET constant.<sup>2</sup>

The physical adsorption isotherm can be described correctly, under the relative pressure range between 0.05-0.35, by using the BET equation. The pressure range for which the equation is valid varies slightly from one adsorbent-adsorbate pair to another. The BET surface area is calculated by multiplying the area occupied by one adsorbate molecule with the number of adsorbate molecules restrained in  $V_m$ , so that:

$$S_{(BET)} = V_m \cdot N_A \cdot \sigma \quad 2.6$$

Where  $S_{(BET)}$  = specific surface area,  $N_A$  = Avogadro's constant and  $\sigma$  = cross sectional area occupied by  $N_2$  molecule ( $\sigma = 0.162 \text{ nm}^2$ ). Note that  $V_m$  is obtained from equation 2.5.

The t-plot method is used to distinguish between micropores and mesopores in porous solid samples. The pore size distribution was determined by the Barrett-Joyner-Halenda (BJH) model,<sup>3</sup> adopting the adsorption branch.

The t-plot is also used to calculate the micropore volume of a solid material.<sup>4</sup> Adopting the ratio  $V_a/S$ , in which  $V_a$  represents the volume of adsorbed  $N_2$  and  $S$  is the sample's surface area, as a function of the relative pressure ( $P/P_o$ ), a common curve was given for different non-porous solids.<sup>5</sup> The density of  $N_2$  layer is a function of the relative pressure, but it does not depend on the solid. The statistical density of the adsorbed  $N_2$  multilayer is calculated by:

$$t(\text{nm}) = 0.1 \frac{V_a}{S} \quad 2.7$$

Equation 2.7 provides a convenient description of the typical t-curve when partial

pressure ranges between 0.1-0.8. The multilayer density of the adsorbed N<sub>2</sub> in a porous material can be plotted versus the adsorbed volume. The positive intercept of the linear branch is an indication of the micropore volume whilst the linear slope of this curve is proportional to the external surface area. In the presence of mesopore, two linear segments can be noticed. The first linear segment coincides with micropore volume, but the second segment with the sample's total pore volume. The difference between the total pore volume and the micropore volumes gives the mesopore volume. The BET measurements conducted in this study were utilised to gain information about the surface area, pore volume and pore size distribution of the samples. Porosimetry measurements were performed on a Quantachrome Autosorb, primarily with N<sub>2</sub> gas as adsorbate.

### 2.6.2 X-Ray powder diffraction (XRD)

The X-ray diffraction is an essential technique used to analyse the crystalline structure of materials and confirm phase purity using their diffraction patterns. The diffraction usually happens when incident beams interact with crystalline solid materials. The lattice spacing (*d*) can be obtained according to Bragg's equation 2.8.<sup>6</sup>

$$n \lambda = 2d \sin \theta$$

In which  $\lambda$  is the wavelength of the X-ray,  $\theta$  is the angle of incidence, *d* is the lattice spacing, *n* is the integral order of diffracted peaks, where X-ray constructive interference occurs, and *n* is the order of reflection. The size of the unit cell *a*<sub>0</sub> for the crystalline cubic symmetry can be measured by the following equation:

$$a_0 = \frac{a \sqrt{h^2 + k^2 + l^2}}{\sqrt{h^2 + k^2 + l^2}}$$

In which *h*, *k* and *l* refer to the Millers indices showing the lattice plane orientation. In a powdered sample, the XRD pattern is determined by fixing a stationary X-ray source and a detector to detect the intensity of the diffracted X-ray that is

functioned by the angle  $2\theta$  between the incident and diffracted beams. The framework of specimen can be determined by comparing the experimental pattern with a standard reference such as provided by the international zeolite association (IZA). Mal et al.<sup>7</sup> have used this technique recently to emphasize the effective integration of Sn into the MFI framework, and Millini et al.<sup>8</sup> evaluated the maximum amount of titanium which can be inserted into the MFI framework. The XRD measurements in this study were utilised to monitor the crystalline phase of the zeolite. This technique is rather advantageous to determine the incorporation of metals into the zeolite framework. In fact, the isomorphous replacement of Al with a bigger metal stimulates a rise in the unit cell volume, and thus producing a shift in the associated diffraction peaks. The XRD measurements are performed on a PANalytical X'Pert PRO X-ray diffractometer with a Cu K $\alpha$  radiation source (40 kv and 40 mA). Diffraction patterns were recorded between 5-55  $^{\circ}2\theta$  at a step size of 0.0167 $^{\circ}$  (time/step = 150 s, total time = 1h). The well-known XRD patterns of zeolite types are collected in "Collection of Simulated XRD Patterns for Zeolite", as well as in the IZA online database.<sup>9,10</sup> Figure 2.2 shows typical XRD patterns for parent BEA zeolite (Figure 2.2a) and after dealumination (Figure 2.2b).

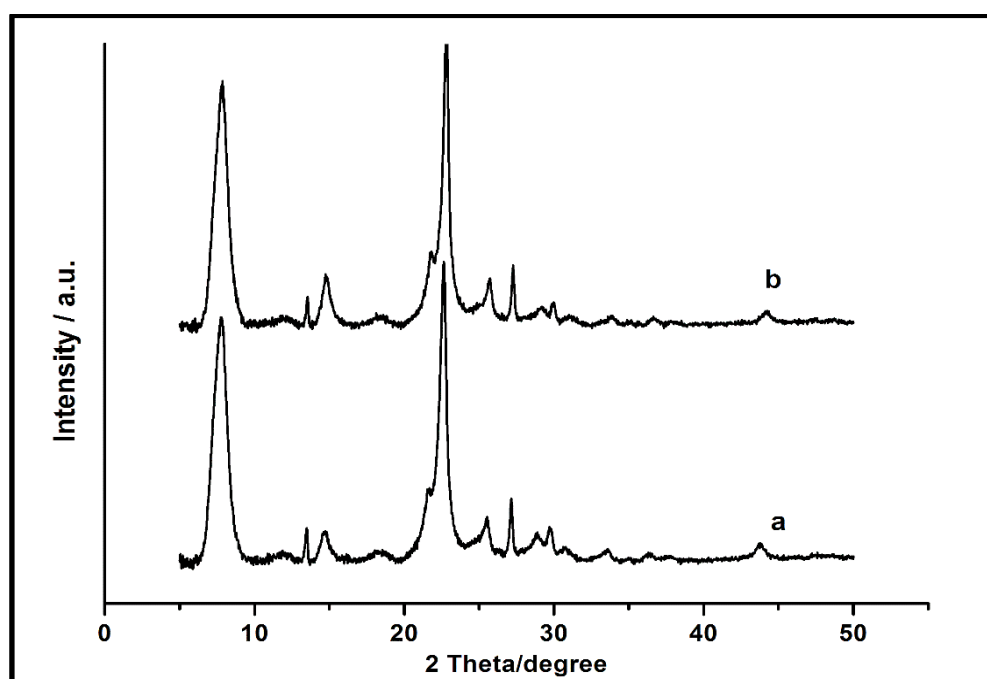


**Figure 2.2** XRD Pattern of BEA zeolite (a) before dealumination (b) post dealumination.

### 2.6.3 X-Ray absorption spectroscopy (XAS)

XAS comprises of both X-ray Absorption Near Edge Spectroscopy (XANES) and Extended X-ray Absorption Fine Structure (EXAFS). XANES spectroscopy is used to provide information about geometry and oxidation state of elements in a sample. EXAFS spectroscopy is a considerable instrument to define the exact location of the zeolites active centres in terms of T-site, which will consequently lead to define their geometry.<sup>11</sup> Although EXAFS studies on TS-1 are numerous, they were silent about identifying a preferable position of titanium in the MFI framework.<sup>12,13</sup> Bare et al.<sup>14</sup> reported that Sn is not indiscriminately located in the BEA framework during hydrothermal preparation, but it is incorporated at certain position; i.e. T5 and T6 sites inserted in the six-membered ring, their data show that Sn atoms were disseminated in pairs on opposite position of the six-membered ring. This Sn location in Sn-BEA is highly preferable, and may explain why hydrothermally synthesized Sn-BEA samples showed higher TOF than samples synthesized by post-synthetic techniques for a similar Sn content. On the other hand, it can be used to extract the details about the local atomic environment of elements, including bond distance, the number and type of neighbouring atoms, and structural disorder.<sup>15</sup> During XAS measurements, the X-ray stimulates the ejection of a core shell electron to leap up leaving a core hole, so a higher valence electron will fall down to fill up the space of the core electron hole, which would scatter the photoelectron. As a result, the scattered photoelectron energy intervenes destructively and constructively with neighbouring atoms to produce the oscillatory pattern.

XAS is an essential technique to explore chemical-structural. However, this technique requires the use of synchrotron facility - an intense light source with tuneable energy – which is expensive and not always available. Bundle of charged particles are accelerated by linear accelerators in the booster ring. The accelerated particles would reach very close to the speed of light when they get the storage ring, where the X-rays are released from the electrons for participation in the XAS process.

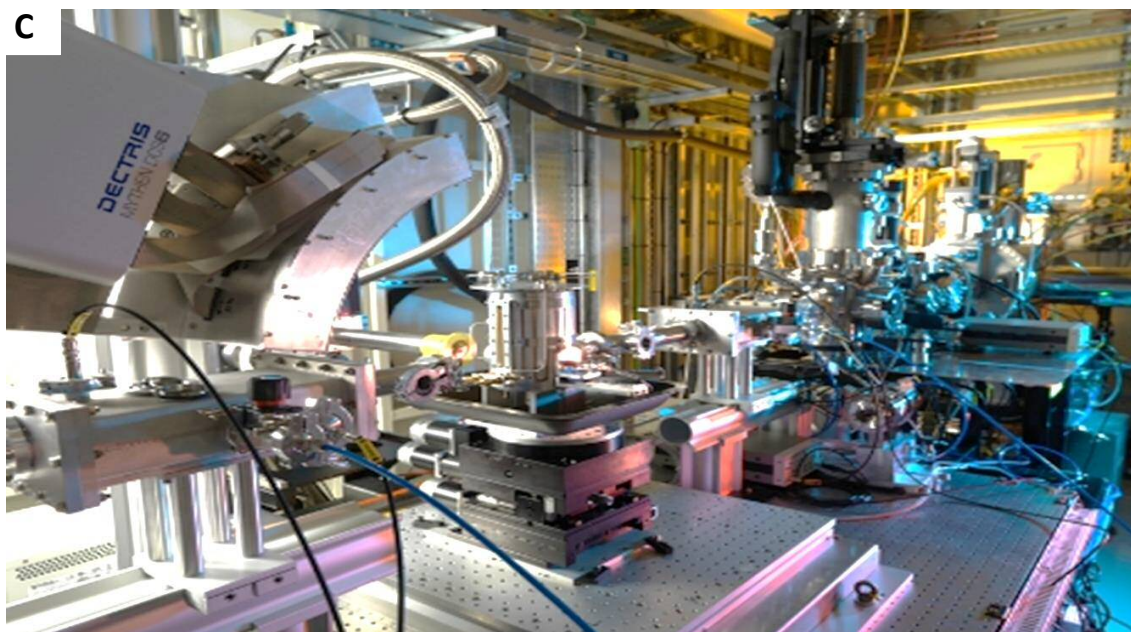
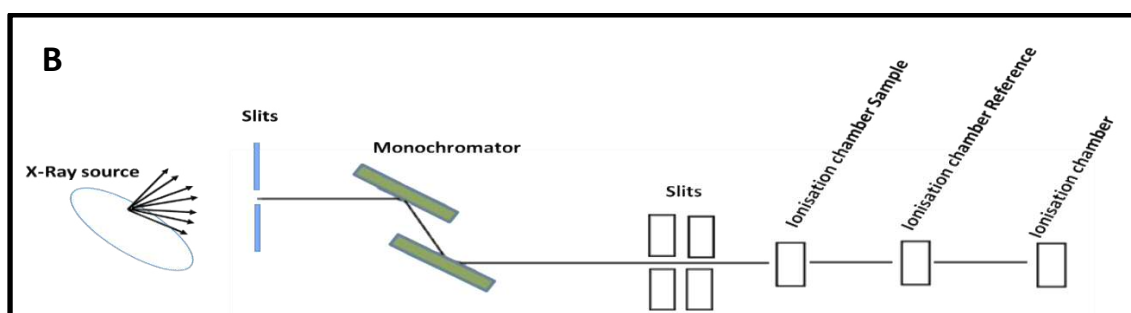
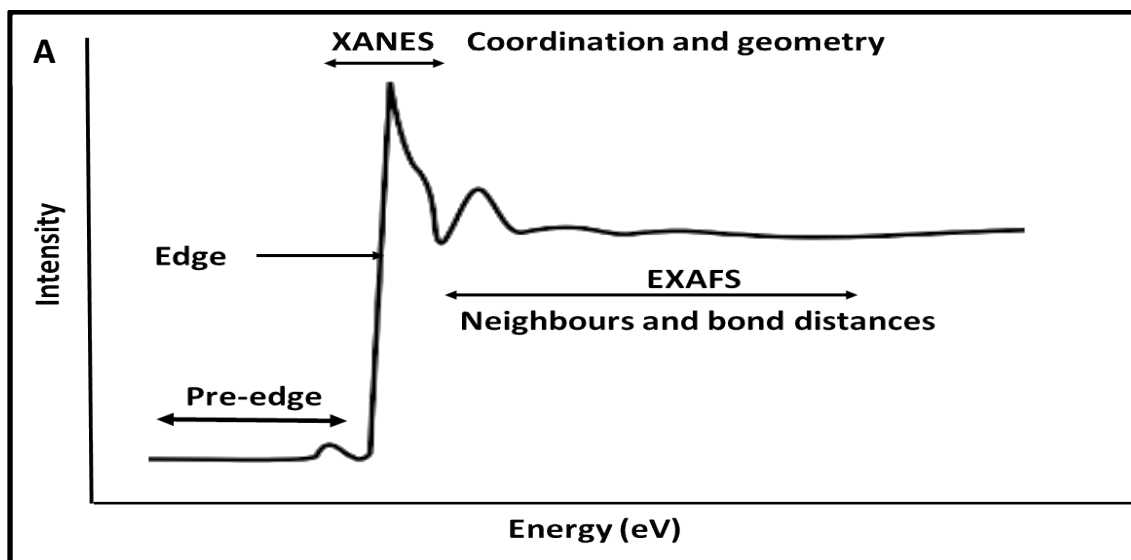


**Figure 2.3** Information obtained from a XANES/EXAFS (A),<sup>15</sup> Diagram drawing of the beamline set up for XAS analysis (B),<sup>15</sup> and actual beamline set up (C).

The EXAFS measurements in this study were used to investigate the oxidation state and coordination environment of the Sn atom. Sn K-edge XAFS studies were performed on the B18 beamline at the Diamond Light Source, Didcot, UK. The data resulting from the EXAFS procedure can be analysed by the FEFF code to find out the local environment of the absorbing atoms.

#### 2.6.4 Fourier-transform Infra-Red spectroscopy (FT-IR)

Infrared absorption spectroscopy is regarded as one of the central techniques used to characterise catalytic systems, and there are many varieties of the technique. The nature of sample and the information sought determines the type of technique used. These could include diffuse reflectance infra-red Fourier Transform spectroscopy (DRIFTS), Reflection-Absorption (RAIRS) and Transmission (TIR) infrared.<sup>16</sup> The diffuse reflectance mode is ideal for the investigation of the catalyst in powder form.<sup>17</sup> In the diffuse reflectance mode, the IR beam illuminates the catalyst sample, which is placed loosely in a small basket, the scattered ray resulting from the illumination is collected with suitable optics for analysis (Figure 2.4). The signals in DRIFTS are weak and non-trivial to collect due to the diffuse nature of the reflectance.<sup>16</sup> A better molecular information in catalytic studies can be obtained by IR spectra. The infrared absorption spectroscopy can be manipulated to distinguish between adsorbed species, measure the quantity of adsorbates coverages, and to follow their progress as a function of time in kinetic studies. Another important usage of infrared absorption spectroscopy in catalytic analysis is to identify catalytic sites on solid surfaces. The catalytic sites in solids can be examined indirectly by IR absorption spectroscopy with probe molecules. The probe molecules can be chosen to adsorb on specific sites only (e.g. acidic or basic sites), and the intensity of the IR absorption peaks indicates the quantity of their surface coverage. The IR spectra are unique to every adsorbate, highly sensitive to their bonding to the surface sites and to the local environment surrounding the molecule.<sup>6</sup> These features make IR spectroscopy an ideal method for studying both Lewis and Brønsted sites in zeolites. For the determination of acid sites, basic probe molecules such as ammonia, pyridine

and other amines are typically used; however, there are also some studies that utilised acetonitrile, carbon monoxide and molecular nitrogen for IR acid-base titration on solids.<sup>18,19,20,21,22</sup>

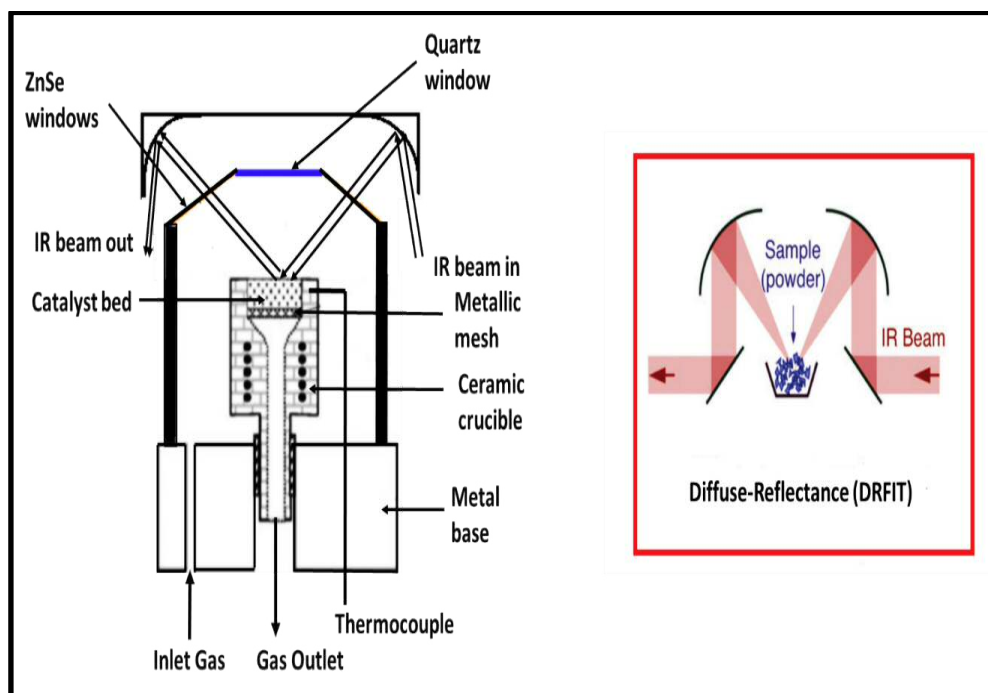


**Figure 2.4** Left: Schematic diagram representation of a high pressure/ high temperature DRIFTS cell design.<sup>23</sup> Right: setup for diffuse reflectance (DRIFTS) mode.<sup>16</sup>

The DRIFT measurements were utilised in this study to investigate the incorporation of heteroatom (Sn) into the zeolite framework and analyse the nature of the active species. Probe molecules and IR absorption spectroscopy were used in this study to identify specific acidic and basic catalytic sites, using DRIFTS signals and their variation as a function of adsorption temperature to determine the nature of catalytic sites. Hence, pyridine was used to characterize both Lewis and Brønsted sites, while acetonitrile was used to identify only the Lewis acidic sites. DRIFT analysis was performed in a Harrick praying mantis cell and spectra were recorded on a Bruker Tensor spectrometer over a range of 4000-650  $\text{cm}^{-1}$ . Figure 2.5 shows  $\text{CD}_3\text{CN}$  desorption profile for 2Sn-BEA under a dynamic vacuum at various temperature intervals, increasing from top to

bottom. Two essential adsorption features are observed at  $\tilde{\nu} = \pm 2275$  and  $\pm 2311$   $\text{cm}^{-1}$ . The first feature, at  $\tilde{\nu} = 2275$   $\text{cm}^{-1}$ , is related to physisorbed  $\text{CD}_3\text{CN}$ , weakly bound to the sample, as evidenced by its very rapid desorption upon heating treatment. The second feature, at  $\tilde{\nu} = 2311$   $\text{cm}^{-1}$ , arises from the  $\text{CD}_3\text{CN}$ -Lewis acid site interaction, upon heating treatment up to a  $200$   $^\circ\text{C}$  temperature, and both the physisorbed  $\text{CD}_3\text{CN}$  and the  $\text{CD}_3\text{CN}$  coordinated onto the Lewis acidic centres, gradually desorb.

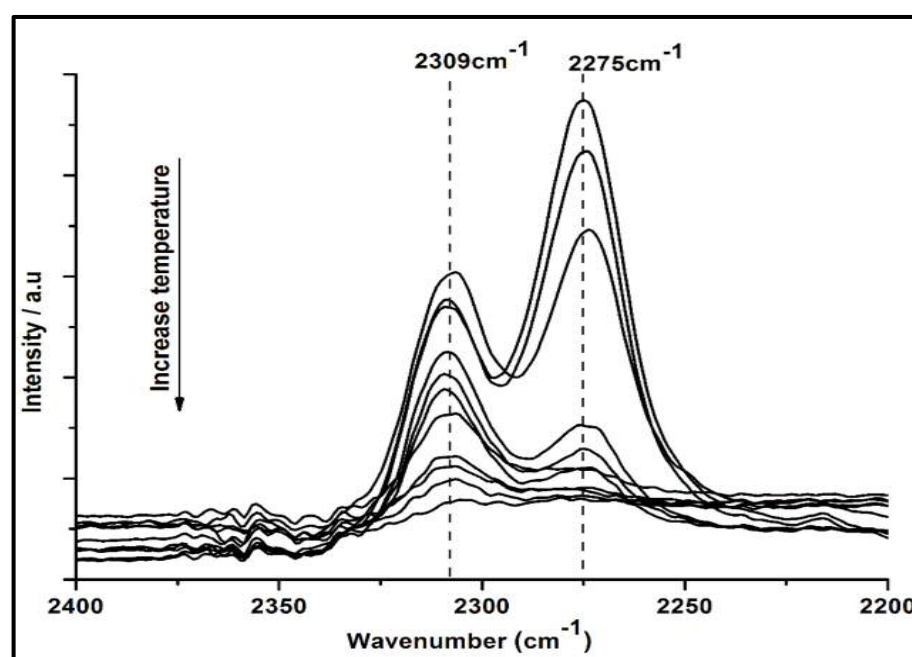


**Figure 2.5**  $\text{CD}_3\text{CN}$  desorption profile for 2Sn-BEA.

Detailed procedure used to record the DRIFT spectra are described in full at the end of chapters 3, 4, and 5.

### 2.6.5 Scanning electron microscopy (SEM)

The Scanning Electron Microscope (SEM) is very useful for the study of the morphology of solid materials. SEM images are basically obtained from the interactions between the electron beam and the specimen. These interactions

can either be elastic or inelastic.<sup>24</sup> When the incident electron is deflected by the specimen atom nucleus or by similarly energetic external shell electrons, the interaction is characterised as elastic. In this interaction, negligible energy is lost in the collision and produces wide angle of electronic scattering.<sup>24</sup> A good signal for imaging the specimen is obtained from the elastically scattered electrons that are incident and scattered in an angle of more than  $90^\circ$ , which are called backscattered electrons (BSE).<sup>6</sup> Inelastic scattering, on the other hand, happens when the interactions between the fallen electrons and the atoms and electrons of the specimen, lead to transferring essential energy to the atoms. The quantity of lost energy relies on whether the sample's electrons are excited collectively or singly and on the binding energy between electron and atom. As a result, secondary electrons (SE) would be generated from the excitation of the sample electrons during the ionization of the its atoms. These electrons are typically known to possess energies of less than 50 eV and can be applied as a useful tool to analyse or image the specimen. In addition to these signals employed to make an image, other signals would be obtained when a specimen struck by an electron beam such as Auger electrons and X-Rays. Samples were mounted on SEM plates using adhesive carbon coated disks, the samples were loaded into the electron microscopy chamber and sealed under vacuum. Scanning Electron Microscopy was utilised to have images of the particle shapes and dimensions as well as to identify any defects in the crystals. Figure 2.6 shows the schematic diagram of an SEM set-up and several possible signals generated from the interaction of an electron beam with a bulk sample.

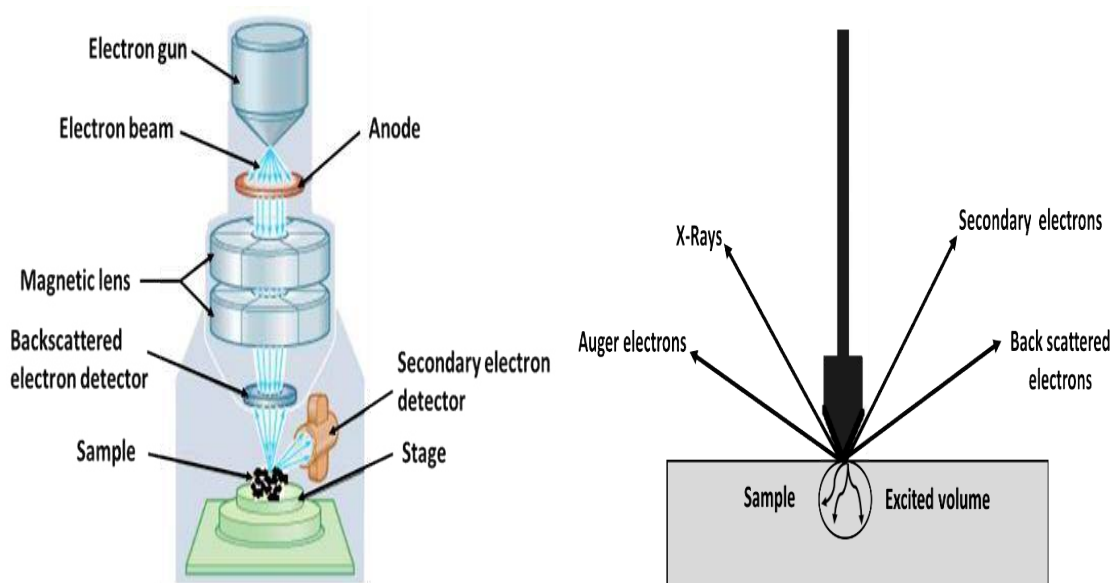


**Figure 2.6** Left Schematic diagram of SEM, Right diagram illustrates of several signals generated by the SEM interaction with sample.<sup>25</sup>

The SEM measurements in this study were used to provide direct information about morphology. It can even provide information about elemental X-ray composition maps.

### 2.6.6 Transmission electron microscopy (TEM)

Transmission Electron Microscopy is a branch of electron microscopy, which is made up of three major components including the electron gun, the lens and the recorder. The electron gun generates the electron beam, which is hits the sample, and transmitted electron are magnified by the electromagnetic lenses. The optics bring the scattered electron from the same point in the sample to the same point in the image. The image recorder transforms the electron signals into a form perceivable by the human eye.<sup>24,26</sup> While SEM works on the topological and compositional structure of a surface, TEM obtains information from the electron beam as it interferes with the mass in a two-dimensional image. A conventional Transmission Electron Microscopy can magnify x300 000 with a resolution of 0.5 nm, whereas a High-Resolution Transmission Electron Microscopy (HR-TEM)

apparatus can magnify x1000 000. The samples were prepared by dispersing the catalyst powder in high purity ethanol using ultra-sonication. 50  $\mu\text{L}$  of the suspension was dropped on to a holey carbon film supported by a 300 mesh copper TEM grid, followed by evaporation at room temperature. TEM images were obtained using a JEOL JEM-1200EX, operating at 200 kV.

### 2.6.7 Magic angle spinning nuclear magnetic resonance (MAS NMR)

The year 1960 heralds the beginning of using the Nuclear Magnetic Resonance (NMR) as a technique in the characterization of zeolites, and it has been further improved with the discovery and addition of the Magic Angle Spinning (MAS), which results in reducing line bordering.<sup>27</sup> It has become an ideal technique for the characterisation of the structural and chemical environment of atoms in zeolite catalysts. The chemical shift ( $\delta$ ) represents the magnetic field of a nucleus supplied by its specific electronic environment. The chemical shift is corresponding to the intensity of the utilized magnetic zone. Because the resonance frequency of a bare nucleus cannot be calculated directly, chemical shifts are usually determined in relation to the resonance peak of another reference compound  $V_{\text{ref}}$ . Chemical shifts can be expressed according to the following equation (2.10).

$$\delta \text{ (ppm)} = (V - V_{\text{ref}}) / (V_{\text{ref}}) \times 10^6 \quad 2.10$$

Both paramagnetic and diamagnetic contribute to the chemical shift. The chemical shift is substantiated by a tensor that represents the orientation-correspondence of the interaction of the external magnetic field with the electronic environment. In a typical NMR spectroscopy of liquids, swift molecular tumbling amounts out the average of this orientation-correspondence and creates a sharp and well defined peak at a position known as the  $\delta_{\text{iso}}$  (isotropic chemical shift) that represents the average electronic environment of the nucleus. While in the spectra of powdered solid specimen, all orientations of any given site in relation to the  $B_0$  (magnetic field) are present. These orientations possess slightly

different resonance frequencies if the local symmetry is less than cubic, which leads to a broad line-shape recognized as powder pattern from which the essential values ( $\delta_{11}$ ,  $\delta_{22}$ ,  $\delta_{33}$ ) of the chemical shift tensor can be measured (Figure 2.7). Only recently, a substitutional method was utilized by using a layout with a magic spinning probe that averages the anisotropic interactions and produces a better-defined spectra with substantially decreased line broadening.

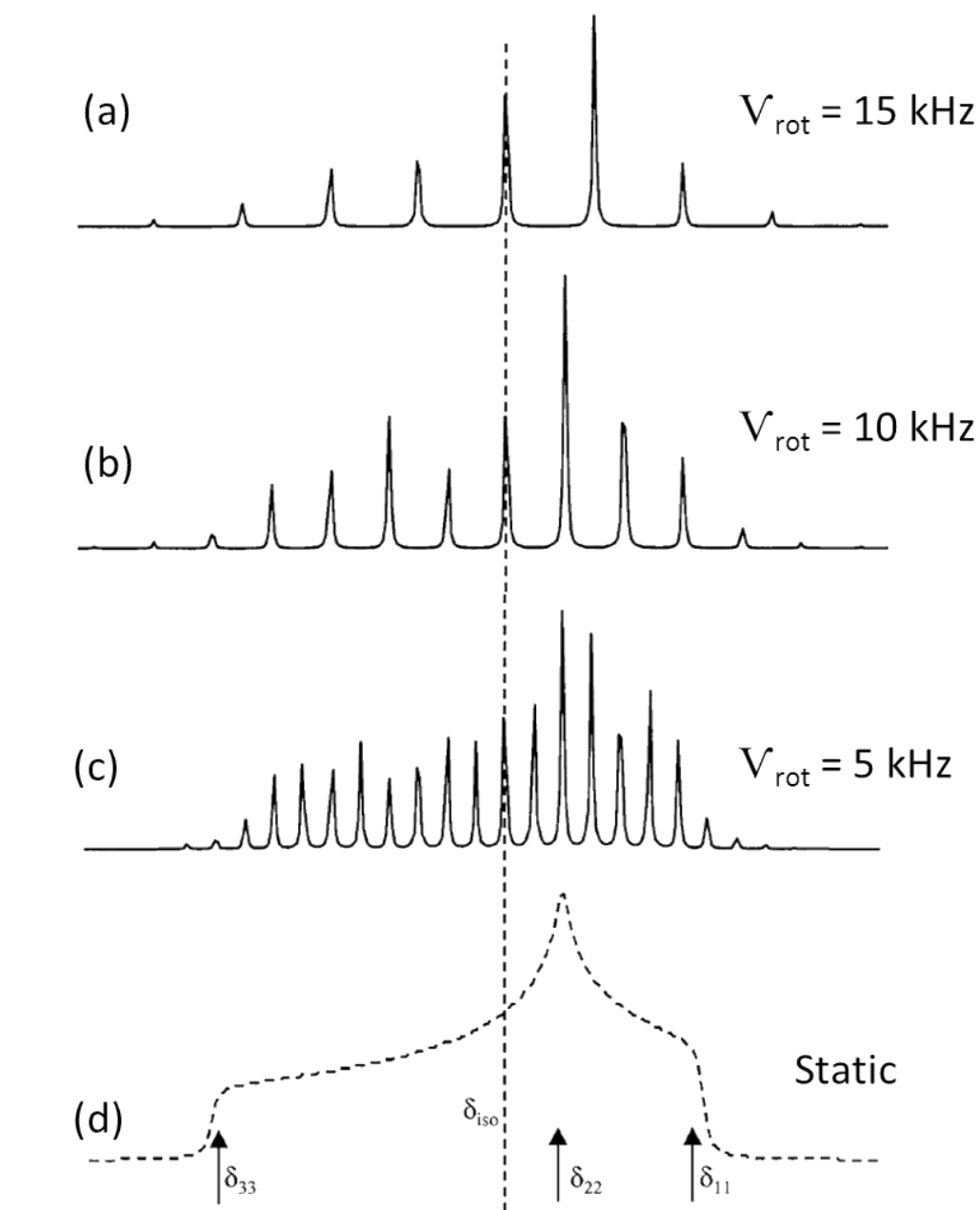


**Figure 2.7** Measured solid-state NMR powder patterns for  $\eta = 0.5$  under (a)-(c) MAS conditions at various spinning rate  $V_{\text{rot}}$  and (d) static conditions.<sup>28</sup>

In this study  $^{119}\text{Sn}$  MAS NMR analysis was conducted to evaluate the coordination of the Sn in zeolite BEA structure. A typical MAS-NMR spectra of hydrated conventional Sn-BEA zeolites is as shown in Figure 2.8. The spectrum of  $^{119}\text{Sn}$  MAS NMR for the hydrated conventional 2Sn-BEA, after calcination and exposure to air, show two bands at  $\delta \approx -690$  and  $-740$  ppm which are within the chemical shift range typical of hydrated  $\text{Sn}^{\text{IV}}$ .<sup>29</sup> It is noteworthy that the spectrum of Sn-BEA zeolite is totally different from that of  $\text{SnO}_2$  or bulk  $\text{SnO}_2$  (Figure 2.8), where only a sharp peak at  $\delta \approx -605$  ppm has been detected. The detected peak for  $\text{SnO}_2$  or bulk  $\text{SnO}_2$  is an attribute of octahedral coordinated Sn in  $\text{SnO}_2$ . A small resonance signal at  $-602$  ppm can be noticed for the Sn-BEA zeolites with the in 2Sn-h\*-BEA showing a clearer signal than 2Sn-Con-BEA, signifying the appearance of some extra-framework Sn species such as  $\text{SnO}_2$ .

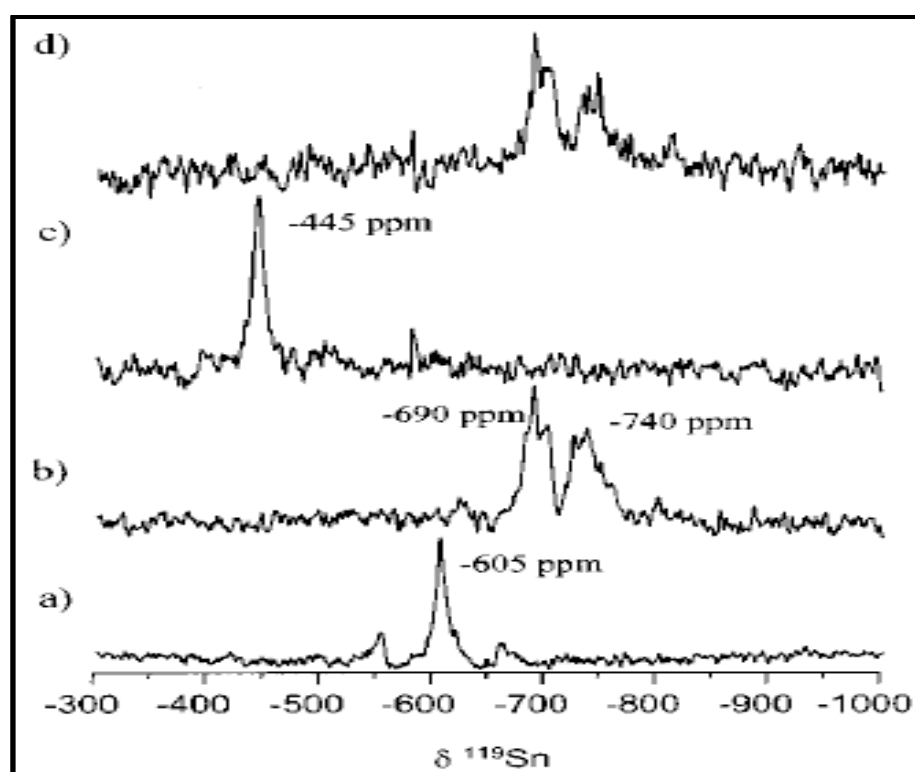


**Figure 2.8**  $^{119}\text{Sn}$  MAS NMR spectra of a)  $\text{SnO}_2$ ; b) hydrated Sn-BEA; c) dehydrated Sn-BEA; and d) rehydrated Sn-BEA.<sup>30</sup>

$^{119}\text{Sn}$  MAS NMR samples in this study were measured under conditions identical to those reported by Bermejo-Deval and co-workers.<sup>30</sup> Non-enriched Sn-BEA samples were measured on both a Varian VNMRS spectrometer, and a Bruker Avance III HD spectrometer with comparable performance.  $^{27}\text{Al}$  MAS-NMR measurements were achieved during this study to identify the extent of dealumination of the zeolite samples upon acid treatment. MAS NMR experiments were performed at Durham University through the EPSRC UK National Solid-State NMR Service. Solid state NMR was utilised to identify the structure of solid and it enabled us to investigate the local environment of the nucleus.

### 2.6.8 Thermogravimetric analysis (TGA)

TGA is an analytical technique for measuring the mass change in a given sample as a function of time or temperature. The TGA equipment is a combination of a furnace connected to an analytical balance so that specimen weight can be assessed as a function of time and temperature. During the analytical process, a highly precise microbalance as well as temperature control are used to monitor the changes in sample-weight as the furnace temperature changes. This analysis is very useful to determine the phase change of a given sample, and to monitor the nature of the evolved effluent like adsorbents, water and gases, all of which correspond to essential mass changes of the specimen. The identification and/or quantification of adsorbent or some other species in the sample can be conducted by matching the mass changes with certain temperatures and reference materials. Thermogravimetric analysis was utilised in this study to investigate the amount of coke deposited on the catalysts. TGA analysis was performed on a Perkin Elmer system.

### 2.6.9 Ultraviolet-Visible spectroscopy (UV-Vis)

Heterogeneous catalysts, particularly those with transition metal ions, can be studied by UV-Vis spectroscopy for oxidation state identification and active site

speciation studies. When the studied material is non-transparent, it undergoes wide-range of scattering and reflection. In this case, the diffuse reflectance spectroscopy (DRS) is a valuable analytic technique to measure the absorption spectrum of opaque solid material. The powdered crystalline surface produces reflection in two ways: (i) a specular reflection which is not transmitted reflective from the surface, and (ii) partially absorbed radiation, which will re-appear to the surface after undergoing several scatterings. The first reflection is minimised by modern spectrometers, so the diffusely reflected radiation is designated as 'reflectance'. DR-UV/Vis spectroscopic technique has become a popular method in the fast assessment of zeolite metal Lewis-acid centres environment. The Beer-Lambert law (equation 2.11) illustrates that the electromagnetic radiation absorbed by the species is proportional to its concentration;

$$A = \epsilon.[c].l \quad 2.11$$

Where; A = absorbance,  $\epsilon$  = molar extinction coefficient, [c] = concentration, and l = path length of the sample cell.

This can be regarded as one of the most important advantages of this technique due to the fact that the intensity of an absorbance is directly related to the concentration of the absorbing species.

At about 200-210 nm, an absorption band, commonly conforming to a charge transfer from  $O^{2-}$  to  $M^{4+}$ , has been directly linked with a framework metal.<sup>31</sup> This band is mostly less defined and wider in Sn-BEA than in Sn-MFI,<sup>32</sup> which tends to be narrower and well-centred. At low energy (240 and 280 nm), the origin of the contribution is not very obvious and could be related to the formation of penta-coordinated species upon water adsorption. However, a more reliable explanation could be the existence of  $SnO_x$  clusters that are bigger sized in comparison with isolated Sn sites.<sup>33</sup> UV/Vis analysis was performed on an Agilent Cary 4000 UV/Visible spectrophotometer in diffuse reflectance mode.

---

## 2.7 References

- 1 C. Horvath, *High-Performance Liquid Chromatography Advances and Perspectives*, Academic Press, INC., New York, 1980.
- 2 K. S. W. Sing, D. H. Everett, R. a. W. Haul, L. Moscou, R. a. Pierotti, J. Rouquérol and T. Siemieniowska, *Pure Appl. Chem.*, 1982, **54**, 2201.
- 3 E. P. Barrett, L. G. Joyner and P. P. Halenda, *J. Am. Chem. Soc.*, 1951, **73**, 373.
- 4 B. C. Lippens, B. G. Linsen and J. H. de Boer, *J. Catal.*, 1964, **3**, 32.
- 5 B. C. Lippens and J. H. de Boer, *J. Catal.*, 1965, **4**, 319.
- 6 J. W. Niemantsverdriet, *Spectroscopy in Catalysis An Introduction*, WILEY-VCH, Third Edit., 2007.
- 7 N. K. Mal, V. Ramaswamy, S. Ganapathy and A. V. Ramaswamy, *Chem. Commun.*, 1994, 1933.
- 8 R. Millini, E. Previde Massara, G. Perego and G. Bellussi, *J. Catal.*, 1992, **137**, 497.
- 9 M. M. J. Treacy and J. B. Higgins, *Elsevier*, 2001, 13.
- 10 C. Baerlocher and L. B. McCusker, *Database Zeolite Struct. 2015*, <http://www.iza-structure.org/databases>.
- 11 S. G. Henderso, R. D. Neuville and R. T. Downs, *Spectroscopic Methods in Mineralogy and Materials Sciences*, 2014.
- 12 G. L. Marra, G. Artioli, A. N. Fitch, M. Milanesio and C. Lamberti, *Microporous Mesoporous Mater.*, 2000, **40**, 85.
- 13 C. A. Hajar, R. M. Jacubinas, J. Eckert, N. J. Henson, P. J. Hay and K. C. Ott, *J. Phys. Chem. B*, 2000, **104**, 12157.
- 14 S. R. Bare, S. D. Kelly, W. Sinkler, J. J. Low, F. S. Modica, S. Valencia, A. Corma and T. L. and Nemeth, *J. Am. Chem. Soc.*, 2005, **127**, 12924.

- 15 S. Calvin, *XAFS for everyone*, CRC Press, 2013.
- 16 F. Zaera, *Chem. Soc. Rev.*, 2014, **43**, 7624.
- 17 A. Drochner, M. Fehlings, K. Krauß and H. Vogel, *Chem. Eng. Technol.*, 2000, **23**, 319.
- 18 G. Busca, *Catal. Today*, 1998, **41**, 191.
- 19 L. M. Kustov, *Top. Catal.*, 1997, **4**, 131.
- 20 J. A. Lercher, C. Grijndling and G. Eder-Mirth, *Catal. Today*, 1996, **27**, 353.
- 21 A. Corma, *Chem. Rev. (Washington, D C )*, 1995, **95**, 559.
- 22 H. Knozinger and S. Huber, *J. Chem. Soc. Faraday Trans.*, 1998, **94**, 2047.
- 23 F. C. Meunier, A. Goguet, S. Shekhtman, D. Rooney and H. Daly, *Appl. Catal. A Gen.*, 2008, **340**, 196.
- 24 G. Ertl, H. Knozinger, F. Schuth and J. Weitkamp, *Handbook of Heterogenous Catalysis*, 2007.
- 25 Y. Lin, J. A. McCarthy, K. R. Poeppelmeier and L. D. Marks, *Applications of Electron Microscopy in Heterogeneous Catalysis*, 2015.
- 26 C. B. Faust, *Modern Chemical Techniques*, 1992.
- 27 M. Hunger, *Catal. Rev.*, 1997, **39**, 345.
- 28 A. P. Guimaraes and I. S. Oliveria, *Magnetism and Magnetic Resonance in Solids*, Wiley, New York, 1998.
- 29 S. J. Hwang, R. Gounder, Y. Bhawe, M. Orazov, R. Bermejo-Deval and M. E. Davis, *Top. Catal.*, 2015, **58**, 435.
- 30 M. Renz, T. Blasco, A. Corma, V. Fornes, R. Jensen and L. Nemeth, *Chem. - A Eur. J.*, 2002, **8**, 4708.
- 31 R. A. Schoonheydt, *Chem. Soc. Rev.*, 2010, **39**, 5051.

- 32 N. K. Mal and A. and V. Ramaswamy, *J. Mol. Catal.*, 1996, **95**, 149.
- 33 P. Y. Dapsens, C. Mondelli and J. Perez-Ramirez, *Chem. Soc. Rev.*, 2015.

# 3

## Identification of Active and Spectator Sn Sites in Sn-BEA Following Solid-State Stannation, and Consequences for Lewis Acid Catalysis

### Abstract

Lewis acidic zeolites are rapidly emerging liquid-phase Lewis acid catalysts. Nevertheless, their inefficient synthesis procedure currently prohibits greater utilization and exploitation of these promising materials, and prohibits greater study of these materials for new types of liquid phase reactions. Herein, the chapter demonstrates that Sn(IV)-containing zeolite BEA can readily be prepared both selectively and extremely rapidly by solid-state incorporation (SSI) method. Through a combination of spectroscopic studies (XRD, UV/Vis, X-ray absorption, magic-angle spinning NMR, and diffuse reflectance infrared Fourier transform spectroscopy), it is unambiguously demonstrated that site-isolated, isomorphously substituted Sn(IV) sites dominate the Sn population up to a loading of 5 wt% Sn. These sites are identical to those found in conventionally prepared Sn-BEA, and result in SSI material exhibiting identical levels of intrinsic activity (that is, turnover frequency) despite the threefold increase in Sn loading, and the extremely rapid and benign nature of preparation methodology. The chapter also identifies the presence of spectator sites, in the form of Sn(IV) oligomers, at higher levels of Sn loading. The consequences of this mixed population with regards to catalysis (Meerwein-Ponndorf-Verley reaction and glucose isomerization) are also identified.

This work contributed to the following papers:

C. Hammond, D. Padovan, A. Al-Nayili, P. P. Wells, E. K. Gibson and N. Dimitratos, *ChemCatChem*, 2015, 7, 3322–3331.

### 3.1 Introduction

Lewis acid catalysts have found widespread applicability for a number of liquid-phase oxidation and isomerization reactions.<sup>1,2</sup> Amongst this class of catalysts are Lewis acidic zeolites, which are important catalysts in the area of sustainable chemistry.<sup>3–5</sup> These crystalline, porous, inorganic Lewis acids possess several major advantages over conventional homogeneous analogues, such as  $\text{AlCl}_3$  and  $\text{ZnCl}_2$ . In addition to the practical benefits of solid catalysts, which simplify downstream processing and various aspects of process intensification, the incorporation of Lewis acidic centres into hydrophobic frameworks inhibits hydrolysis and deactivation of the Lewis acid in the aqueous phase, and thereby allows these promising materials to be utilized as catalysts for a range of emerging aqueous-based reactions.<sup>6</sup>

Of particular interest is Sn-zeolite-BEA. With promising results obtained by many groups for the isomerization of glucose to fructose,<sup>7–12</sup> the Baeyer-Villiger (BV) oxidation of ketones to lactones using  $\text{H}_2\text{O}_2$  as green oxidant,<sup>4,13,14</sup> Meerwein-Ponndorf-Verley (MPV) transfer hydrogenations,<sup>15,16</sup> and various other emerging catalytic transformations,<sup>17–19</sup> the potential of Sn-BEA has attracted significant industrial interest. Nevertheless, some significant practical hurdles currently curtail industrial exploitation, and greater study of the material for new types of reactions. Amongst these limitations are 1) the lengthy and complicated hydrothermal synthesis procedure, 2) the low amount of active metal incorporated per kilogram of final catalyst, resulting in low space-time yield, and 3) the large crystallite sizes obtained via typical hydrothermal synthesis, resulting in mass-transfer issues.

Given the lack of a widely applicable and scalable preparation methodology, significant academic and industrial research has recently focused on the development of new methodologies for preparing Sn-BEA.<sup>19-24</sup> Recently, Hammond and co-workers demonstrated how simple, post-synthetic modifications of commercially available zeolites could readily enhance the availability and practicality of Lewis acidic zeolites for sustainable catalytic transformations.<sup>20</sup> Dealumination of a commercially available BEA zeolite with HNO<sub>3</sub> was found to lead to a highly siliceous framework possessing vacant tetrahedral (T)-sites, into which Sn(IV) could be placed by means of solid-state incorporation (SSI) with Sn(II) acetate. Not only does this approach avoid the long synthesis timescales associated with conventional Sn-BEA synthesis procedures (the total time for mechanochemical and heat-treatment steps is only 8 h), but it also allows for the synthesis of a material with significantly smaller crystallite sizes, increased crystallinity, greater metal content, and improved catalytic performance. Indeed, SSI Sn-BEA was previously found to be up to one order of magnitude more active on a space-time-yield scale than conventionally prepared Sn-BEA both for BV oxidations and the conversion of dihydroxyacetone into ethyl lactate.<sup>20</sup> Furthermore, aqueous/liquid solutions of Sn are also avoided, and complicated/sensitive vapour deposition methods are avoided.

In the original report of this synthesis procedure,<sup>20</sup> characterization of SSI Sn-BEA was investigated by means of UV/Vis and Raman spectroscopy, and preliminary catalytic data focusing on BV oxidation and ethyl lactate synthesis was obtained. However, for a more thorough evaluation of SSI Sn-BEA, and to fully compare its catalytic performance relative to the conventional analogue, further kinetic studies of additional catalytic reactions, such as the isomerization of glucose and MPV transfer hydrogenation, are required. Additionally, advanced characterization of SSI Sn-BEA with more sensitive spectroscopic techniques, such as X-ray absorption spectroscopy (XAS) and solid-state magic-angle spinning (MAS) NMR, is essential. Only by performing these studies can a full comparison between conventional Sn-BEA, and that prepared by SSI, be obtained. This chapter extends the investigations of this particular catalytic

material, and demonstrates both through catalytic and spectroscopic methodologies that SSI Sn-BEA possesses identical site speciation and activity to conventional Sn-BEA at loading up to 5 wt%, which are a factor of three higher than can be obtained by conventional hydrothermal synthesis methods. Nevertheless, some inactive sites are formed at higher loading of Sn. The identity of these spectator sites, and their consequences for Lewis acid catalysis, is rationalized with XAS, MAS NMR, UV/Vis, XRD and diffuse reflectance infrared Fourier transform spectroscopy studies (DRIFTS).

## 3.2 Results and discussion

### 3.2.1 Catalyst synthesis and characterization

According to a modified version of the original synthesis protocol,<sup>20</sup> a range of Sn-BEA catalysts with nominal loadings between 2 and 10 wt% Sn by SSI were prepared. Complete dealumination of Al-BEA (Zeolyst, experimentally determined  $\text{SiO}_2/\text{Al}_2\text{O}_3 = 26.5$ ) was achieved by treatment in  $\text{HNO}_3$  following established literature protocols (13 M  $\text{HNO}_3$ , 100°C, 20 h, 20 mL  $\text{g}^{-1}$ ).<sup>20</sup> In agreement to prior studies, treatment of zeolite BEA with  $\text{HNO}_3$  does not affect the BEA structure, as indicated by the powder XRD (pXRD) pattern (Figure 3.1), and results in a highly siliceous BEA zeolite material ( $\text{SiO}_2/\text{Al}_2\text{O}_3 > 1000$ ) possessing vacant framework sites. Sn(IV) was subsequently introduced into these vacant sites by solid-state incorporation, by mechanochemical treatment of the dealuminated BEA zeolite with the appropriate quantity of Sn(II) acetate for 10 min in a pestle and mortar. Calcination of the resulting homogeneous powder at 550 °C subsequently yielded the final catalytic powder. Figure 3.1 shows the pXRD patterns of Al-BEA, deAl-BEA and various contents of Sn (2, 5, 8, 10 wt %) in BEA zeolite. It can be seen that the crystallinity of BEA zeolite is maintained after dealumination and the deAl-BEA does not show any sign of long-range amorphization or extra lattice crystalline compounds of the zeolite following treatment in  $\text{HNO}_3$ .

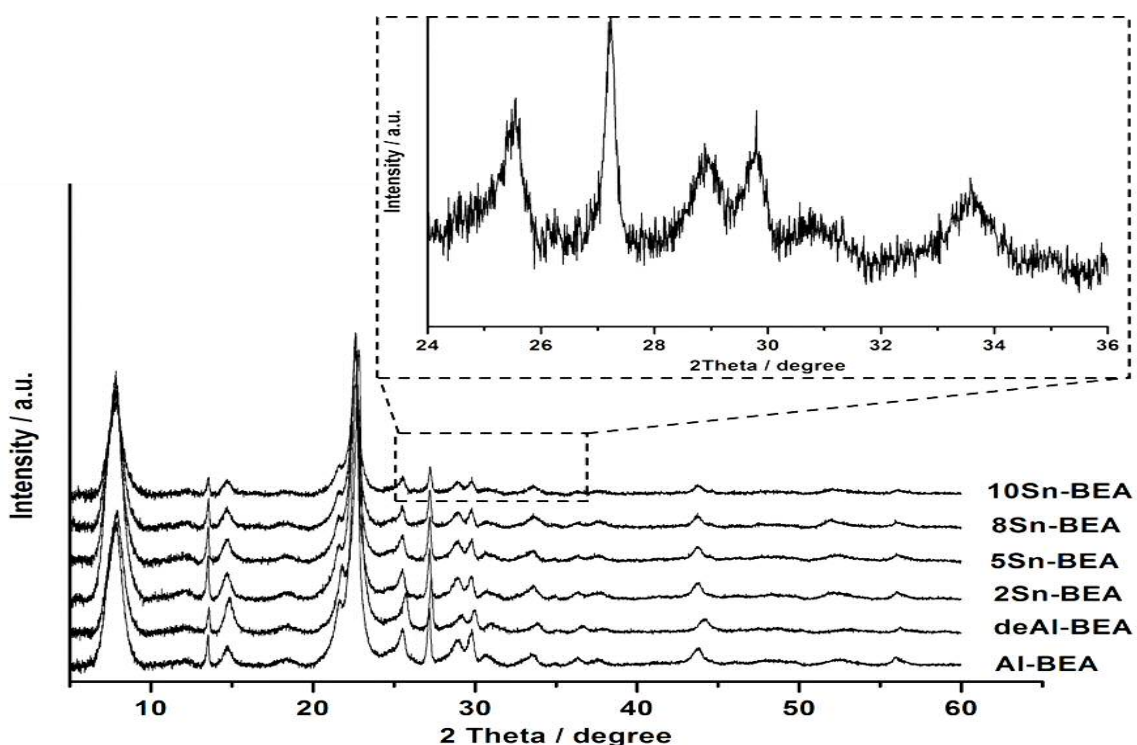


**Figure 3.1** pXRD patterns of various Sn-BEA catalysts prepared by SSI, and containing different Sn contents. The inset gives an enlargement of the indicated spectral region of 10Sn-BEA catalyst.

As described above, the dealumination of Al-BEA leads to no major changes in the pXRD pattern, suggesting that the BEA framework remains fully intact after acidic treatment in  $\text{HNO}_3$ . However, a shift in the calculated d-spacing following dealumination (from  $\pm 3.93$  to  $3.90$  Å for the main reflection in Al-BEA and deAl-BEA, respectively (Figure 3.2)) suggests that there is a contraction in unit cell volume following the removal of Al. Upon incorporation of Sn(IV) into the vacant framework sites of this material by SSI of Sn(II) acetate, no obvious changes in diffraction pattern are observed, although a slight re-expansion of the unit cell volume can be observed (d-spacing of  $3.93$  Å for 2Sn-BEA), which strongly indicates that Sn has occupied the vacant framework sites.

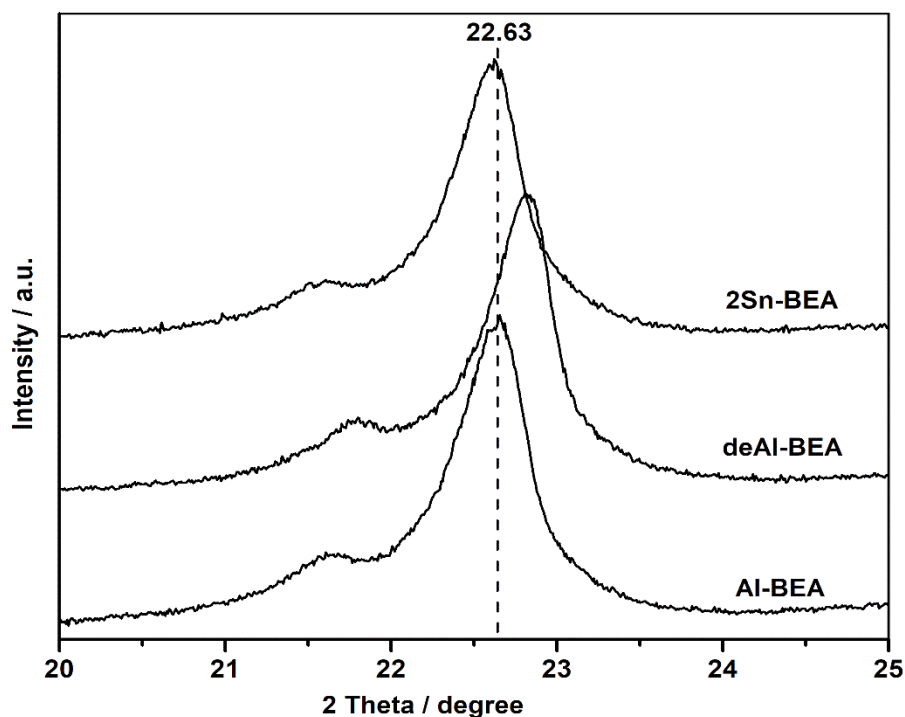


**Figure 3.2** Expansion of the pXRD patterns between 20-25 °2 Theta of the parent, acid treated and 2 wt% Sn-BEA.

SnO<sub>2</sub> produces a very clear pXRD pattern, and can readily be observed by pXRD at levels of < 1 wt% (Figure 3.3). The complete absence of any SnO<sub>2</sub> reflections at 26.7 and 51.8 °2θ in all the catalytic materials (Figure 3.1), even those loaded with 10 wt% Sn, therefore suggests that either SnO<sub>2</sub> is not present in the materials, or that any extraframework Sn domains are so small (<5 nm) and heterogeneous that they do not possess the sufficient long-range order to produce a clear diffraction pattern.

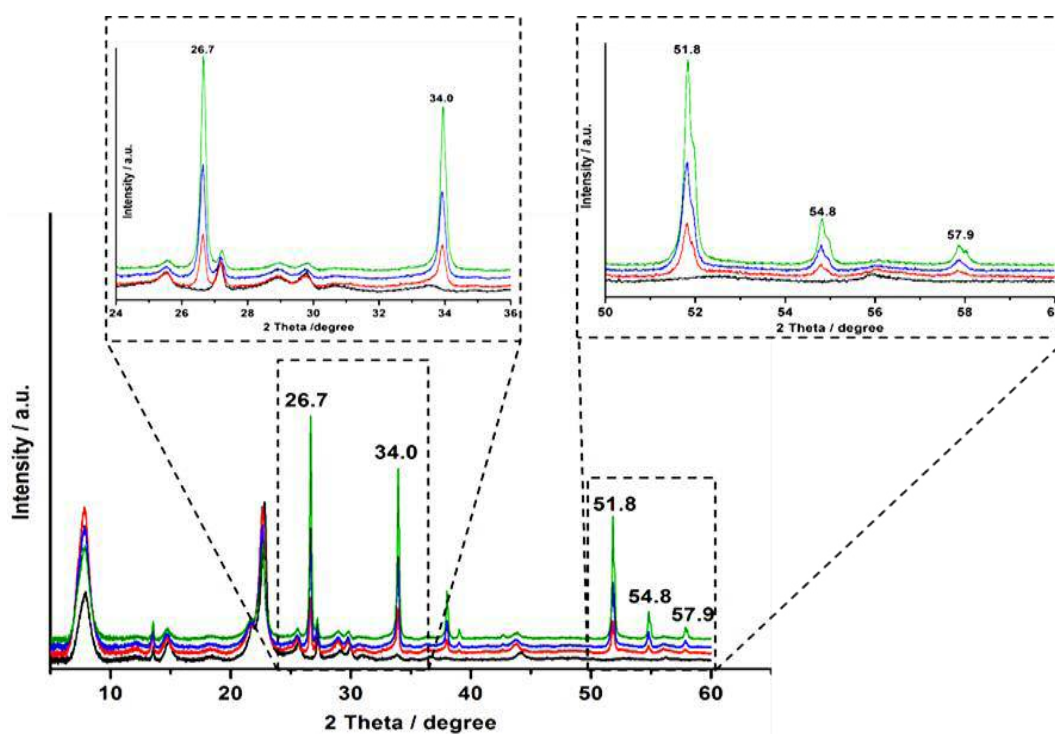


**Figure 3.3** pXRD patterns of various SnO<sub>2</sub>-BEA catalysts, prepared by mechanical mixing of deAl-BEA with various quantities of SnO<sub>2</sub>. Black: deAl-BEA; Red: 2SnO<sub>2</sub>-BEA; Blue: 5SnO<sub>2</sub>-BEA; Green: 10SnO<sub>2</sub>-BEA.

Metal loadings were determined by inductively coupled plasma mass spectrometry (ICP-MS) (Table 3.1), and are consistent within experimental error to the nominal loadings used during preparation.

**Table 3.1** Physical properties of Sn-containing zeolites prepared by SSI

Catalyst	Sn wt % <sup>a</sup> (Si/Sn) <sup>b</sup>
Al-BEA	-
deAl-BEA	-
2 Sn-BEA	1.8 (75)
5 Sn-BEA	4.5 (29)
8 Sn-BEA	7.3 (18)
10 Sn-BEA	9.2 (15)
Conventional Sn-BEA <sup>c</sup>	± 1.5

<sup>a</sup> Determined by ICP-MS; <sup>b</sup> Experimentally determined Si/Sn molar ratio; <sup>c</sup> From Ref.[9]

The N<sub>2</sub> adsorption/desorption isotherms of the Al-BEA and deAl-BEA are shown in Figure 3.4. The isotherm of Al-BEA represents type I, which is characteristic of microporous materials. Dealumination isotherm (deAl-BEA) shows a steep leap and a hysteresis loop at the  $P/P_0$ , which indicates the presence of mesoporosity. The external surface area increases from 91 to 124 m<sup>2</sup> g<sup>-1</sup> with increasing Si/Al ratio (Table 3.2).

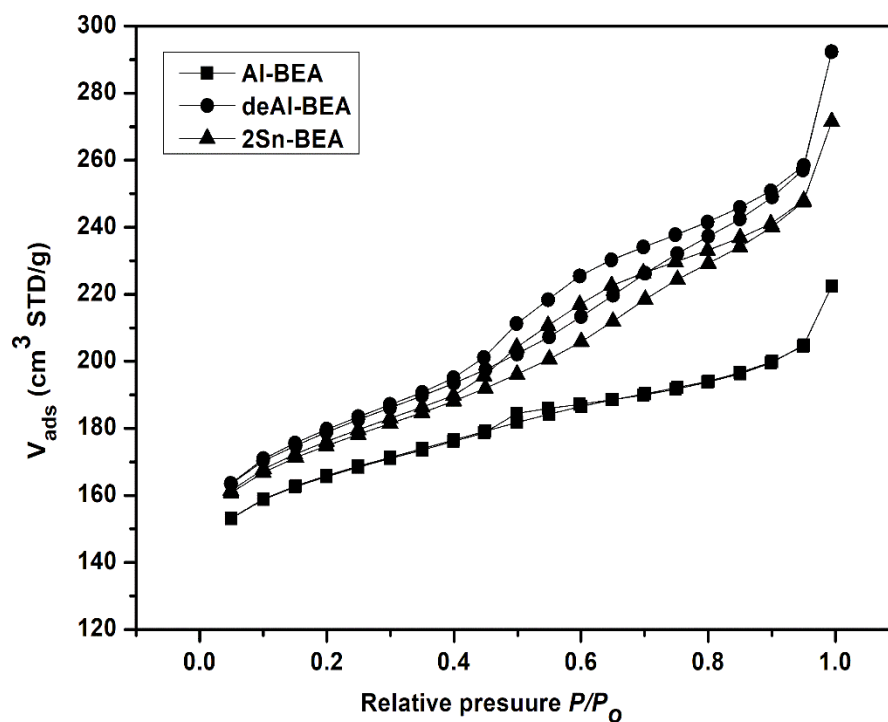


**Figure 3.4** N<sub>2</sub> adsorption/desorption isotherms at 77 K of the parent, acid treated and 2 wt% Sn-BEA.

Porosimetry measurements (Table 3.2) reveal that each of the synthesized materials possesses similar micropore volumes ( $V_{\text{micro}}$ ) to conventional Sn-BEA, although a small but steady decrease in  $V_{\text{micro}}$  is observed as the metal content is increased beyond 5 wt%. Clearly, increased Sn concentrations beyond this point lead to partial pore blockage, and to decreased accessibility of the micropores of zeolite BEA.

**Table 3.2** Porosimetry data obtained for various zeolite BEA materials.

Sample	$S_{\text{BET}}$ ( $\text{m}^2 \text{g}^{-1}$ ) <sup>a</sup>	$S_{\text{external}}$ ( $\text{m}^2 \text{g}^{-1}$ ) <sup>b</sup>	$S_{\text{micro}}$ ( $\text{m}^2 \text{g}^{-1}$ ) <sup>c</sup>	$V_{\text{total}}$ ( $\text{cm}^3 \text{g}^{-1}$ ) <sup>d</sup>	$V_{\text{micro}}$ ( $\text{cm}^3 \text{g}^{-1}$ ) <sup>e</sup>	$V_{\text{external}}$ ( $\text{cm}^3 \text{g}^{-1}$ ) <sup>f</sup>
Al-BEA	587	91	496	0.451	0.230	0.221
de-Al-BEA	541	124	417	0.453	0.229	0.224
2% Sn-BEA	528	115	413	0.421	0.225	0.196
5% Sn-BEA	488	103	384	0.418	0.210	0.208
8% Sn-BEA	440	100	340	0.390	0.186	0.204
10% Sn-BEA	422	94	327	0.359	0.179	0.181

<sup>a</sup> BET surface area ( $S_{\text{BET}}$ ) is calculated from the Brunauer-Emmett-Teller method; <sup>b,c,e</sup> the external surface area ( $S_{\text{external}}$ ), micropore surface area ( $S_{\text{micro}}$ ) and the micropore volume ( $V_{\text{micro}}$ ) are calculated from the t-plot method; <sup>d</sup> the total pore volume ( $V_{\text{total}}$ ) is evaluated at  $P/P_0 = 0.99$ ; <sup>f</sup> the external pore volume ( $V_{\text{external}}$ ) is calculated according to  $V_{\text{total}} - V_{\text{micro}}$ .

Further characterization of the synthesized catalysts was performed with UV/Vis spectroscopy (Figure 3.5). Analysis of the ligand-to-metal charge transfer bands of metal-containing zeolites with diffuse reflectance UV/Vis spectroscopy (DRUV/Vis) provides a great deal of insight of the metal site speciation.<sup>25</sup> The UV/Vis spectra obtained for the synthesized samples (containing between 2 and 10 wt% Sn) all exhibit a sharp maximum at approximately 219 nm, indicative of isolated, tetrahedral Sn(IV) species that are isomorphously substituted into the zeolite framework. Each spectrum is also significantly blue-shifted with respect to bulk SnO<sub>2</sub>, which exhibits a broad, characteristic absorbance at 280 nm, further indicating the presence of site-isolated Sn(IV) sites.<sup>16,20</sup> Although the absorbance maxima remains constant in each material, there is, however, a clear shift in absorbance edge following the incorporation of greater quantities of Sn. The absorbance edge appears to shift from approximately 250 nm/5.0 eV for 2Sn-

BEA, to approximately 282 nm/4.4 eV in 10 Sn-BEA. Although the absorbance edge falls well short of that observed for bulk SnO<sub>2</sub> (approximately 350 nm/3.7 eV), this shift in band edge indicates that at least some extraframework Sn species are present in these samples, although DRUV/Vis is not sufficiently sensitive to provide a quantitative value of their presence, particularly since the extinction coefficients are unknown. However, given the relative sharpness of each peak, any extraframework Sn species are likely to be oligomeric (Sn<sub>x</sub>O<sub>y</sub>) as opposed to oxidic (SnO<sub>2</sub>).

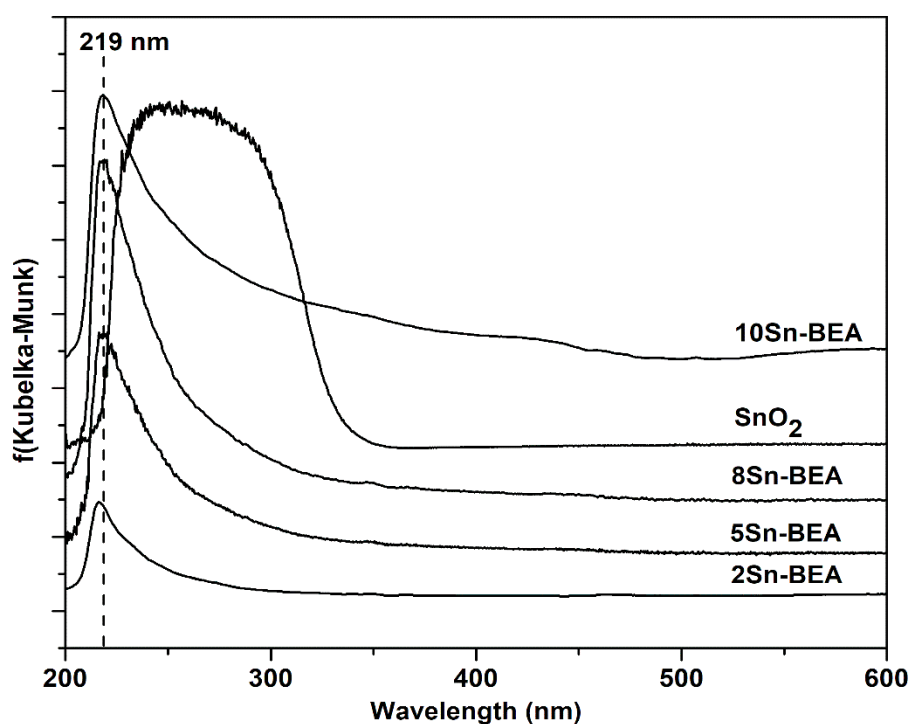


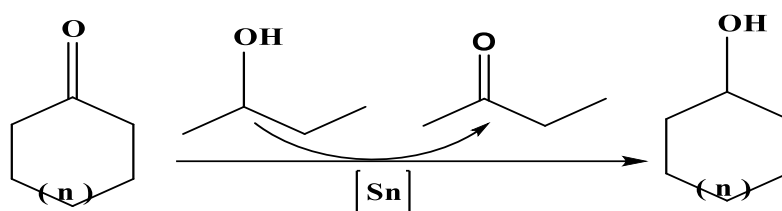
**Figure 3.5** UV-Vis spectra of various Sn-BEA catalysts prepared by SSI, compared to a reference material of bulk SnO<sub>2</sub>.

Porosimetry measurements, powder X-ray patterns and UV-Vis clearly show that the synthesis procedure results in the correct synthesis of Sn-BEA. No clear evidence of bulk SnO<sub>2</sub> could be detected with XRD or UV-Vis spectroscopy, even for very high loadings.

### 3.2.2 Catalytic tests

#### 3.2.2.1 MPV reduction of cyclohexanone

To evaluate the activity of the synthesized catalysts, the chapter focused firstly on the MPV transfer hydrogenation of various cyclic ketones to alcohols (Scheme 3.1), such as cyclohexanone (CyO), as this is key reaction catalyzed by Sn-BEA zeolites and other Lewis acidic analogues. Also, the mechanism is comparable to that reported for glucose isomerization (intramolecular hydrogen transfer see Figure 1.11). Theoretical calculations for the MPV reduction of ketone (cyclohexanone) with alcohol (2-butanol) using Sn-BEA show that the Lewis acid centre is initially coordinated to the carbonyl group of ketone and the alcohol (Figure 3.6).



**Scheme 3.1:** Generalised scheme for the MPV transfer hydrogenation of various ketones.

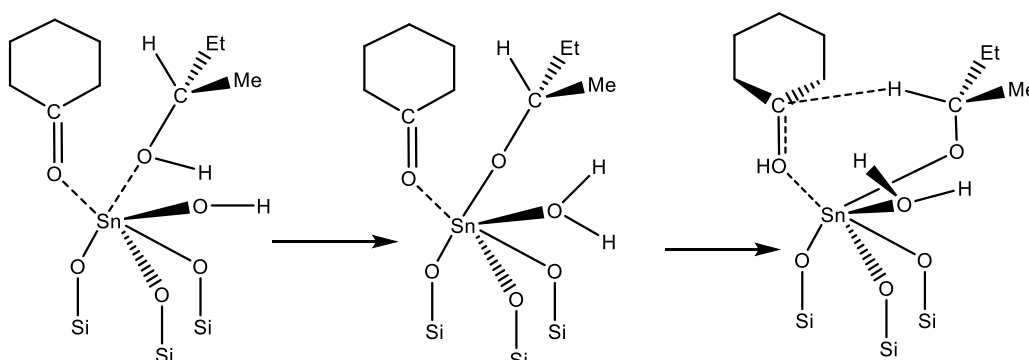


**Figure 3.6** Proposed reaction mechanism for MPV reaction using Sn-BEA as catalyst.

Preliminary kinetic analysis was performed under conditions comparable to those of Corma et al (100 °C, 1 h, CyO/Sn molar ratio of 100).<sup>15</sup> Control experiments performed in the presence of different masses of catalysts confirmed that at 1 mol % Sn, the system was in the kinetic regime (Appendix, Figure 7.15). In Table 3.3, the preliminary catalytic activity of the synthesized catalysts for MPV transfer hydrogenation are presented.

**Table 3.3** Catalytic properties of Sn-containing zeolites prepared by SSI

Catalyst	$X_{\text{CyO}}(\%)^{\text{a}}$
Al-BEA	-
deAl-BEA	0
2 Sn-BEA	100
5 Sn-BEA	100
8 Sn-BEA	95.3
10 Sn-BEA	86.3
Conventional Sn-BEA <sup>b</sup>	95.4

<sup>a</sup> cyclohexanone conversion ( $X_{\text{CyO}}$ ); <sup>b</sup> From Ref. [15]. Reaction conditions: 100 °C, 1 h, 10 mL cyclohexanone in 2-butanol (0.2 M), CyO/Sn molar ratio of 100;.

As revealed in Table 3.3, each of the synthesized catalysts exhibits similar catalytic activity for the MPV transfer hydrogenation of cyclohexanone in terms of cyclohexanone converted in 1 h of reaction time. In all cases, cyclohexanol and 2-butanone were the only products detected, and carbon balances above 95% were obtained, suggesting that any potential byproducts produced below the detectability limit of the analytical instrument are present at a relatively negligible level. With the exception of 10Sn-BEA, each Sn- BEA catalyst prepared by SSI

demonstrated comparable activity and selectivity to conventional Sn-BEA prepared by hydrothermal synthesis, as reported by Corma and co-workers,<sup>15</sup> indicating that the Sn(IV) site speciation in each catalyst is comparable to that of conventional Sn-BEA.

Nevertheless, more detailed kinetic analysis (Figure 3.7) shows this not to be the full picture, and demonstrates that the various catalysts possess markedly different catalytic activity. For these catalytic reactions, an identical quantity of Sn (1 mol% relative to cyclohexanone) was utilized per catalytic experiment by varying the mass of catalyst, to accurately compare specific Sn(IV) site activity. In all cases, cyclohexanol and 2-butanone were the only reaction products, and carbon balances were above 95%, suggesting that Sn(IV) loading does not impact reaction selectivity (that is, product distribution) or any adsorption effects. By examining the full kinetic profile, and particularly the early time course of the reaction, it becomes clear that as the Sn(IV) loading of Sn-BEA is increased systematically from 2 to 10 wt%, and the amount of Sn present in the reactor is kept constant, catalytic activity per mole of Sn decreases. Indeed, 8Sn-BEA and 10Sn-BEA are significantly less active per mole of Sn than 2Sn-BEA and 5Sn-BEA, which are almost identical in catalytic activity. This decrease in activity at elevated loadings strongly suggests that above Sn loading of 5 wt%, inactive, that is, spectator, Sn(IV) sites are produced, effectively decreasing the amount of active Sn present in the reactor, and resulting in decreased catalytic activity. To gain further critical insight into the influence of Sn(IV) loading and catalytic activity, the chapter explored the catalytic activity of Sn-BEA for catalytic glucose isomerization, which is also catalysed by framework Sn(IV) sites in zeolite BEA, reportedly through an intramolecular 1,2-hydride shift mechanism.<sup>8,26,27</sup>

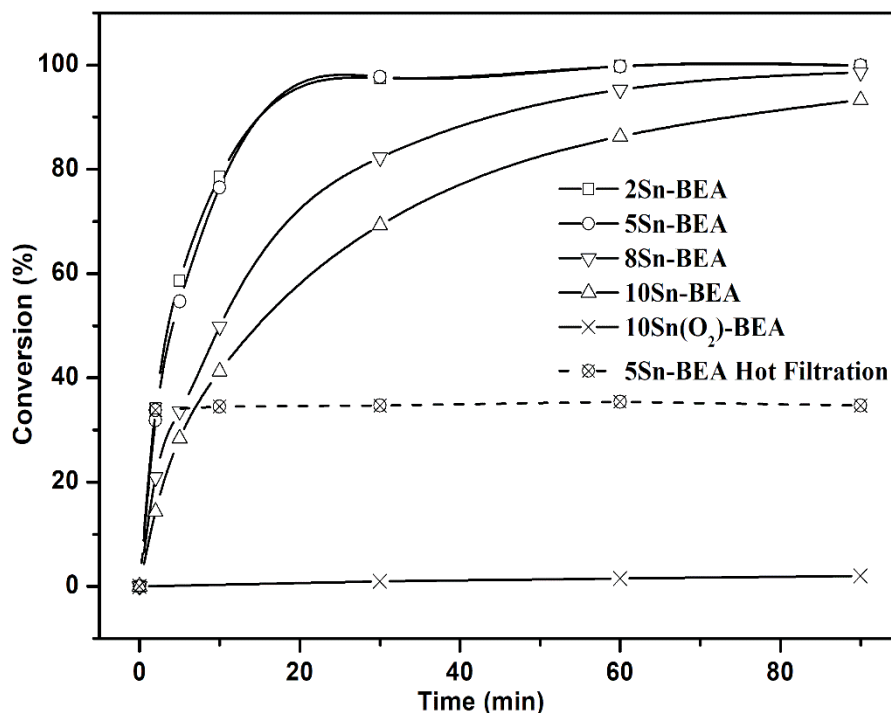
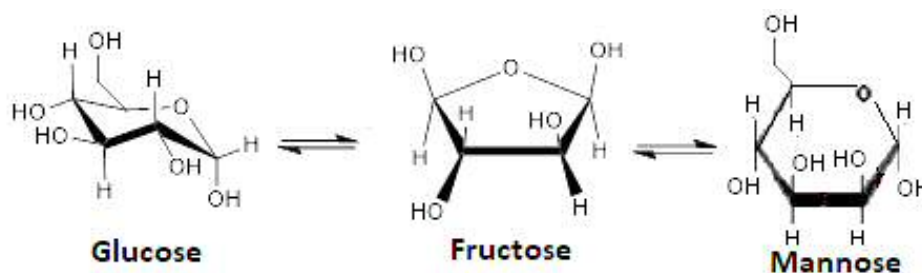


**Figure 3.7** Catalytic activity of Sn-BEA catalysts prepared by SSI, and containing different Sn contents, for MPV hydrogenation of cyclohexanone (CyO). Reaction conditions: 100 °C, 1 h, 10 mL cyclohexanone in 2-butanol (0.2 M), CyO/Sn molar ratio of 100 (1mol% Sn).

### 3.2.2.2 glucose isomerization

An advantage of Lewis acid zeolites is that the metal sites are less liable to poisoning by strong binding species than their homogeneous analogues. The most common example is the water. Although water deactivates most homogeneous Lewis acids by hydrolysis or strong binding, water bound to metal centers in Lewis acid zeolites can be reversibly replaced by reactants.<sup>7</sup> The catalytic activity of Sn-BEA was tested in the isomerization of glucose in aqueous phase. The main products of the isomerization were fructose and mannose (scheme 3.2). The results indicate the glucose isomerization reaction with a Sn-BEA in pure water proceeds by means of an intramolecular hydrogen transfer from C-2 to C-1 and from O-2 to O-1 of an  $\alpha$ -hydroxy aldehyde to create the  $\alpha$ -hydroxy ketone (Figure 1.11).



**Scheme 3.2:** Generalised scheme for glucose isomerization.

Catalytic tests of Sn-BEA in glucose isomerization were carried out in 15 mL thick walled glass vials under autogenous pressure. Control experiments performed in the presence of different masses of catalysts confirmed that at 1 mol % Sn, the system was in the kinetic regime (Appendix, Figure 7.16 (A)). In figure 3.8 the time online kinetic profile for glucose isomerization over the SSI Sn-BEA series is presented.

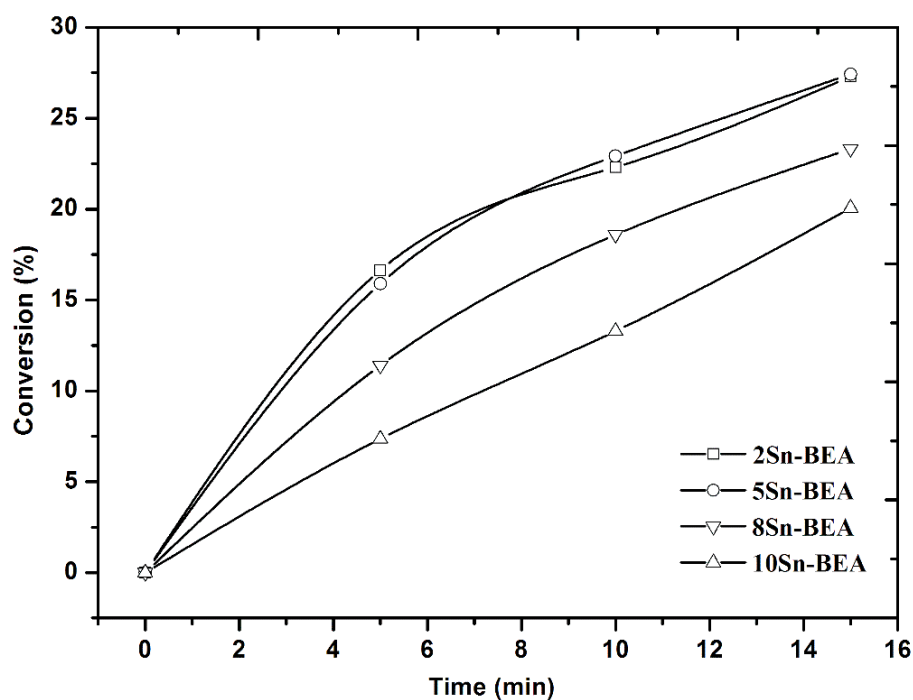


**Figure 3.8** Catalytic activity of various Sn-BEA catalysts prepared by SSI, and containing different Sn contents, for the isomerization of glucose. Reaction conditions: 110 °C, 0.5 h, 10 wt % glucose solution ( $\pm$  0.61 M); glucose/Sn molar ratio of 50.

Table 3.4 shows glucose conversion, fructose and mannose yields, and carbon balance for each catalytic reaction is given at levels close to iso-conversion. Reactions were performed under identical conditions to those described by Roman-Leshkov et al.<sup>9</sup> Only catalytic data up to  $\pm 25\%$  conversion is displayed, as a significant increase in byproduct (humin) formation and a large decrease in carbon balance was observed above this level of conversion. In good agreement to the MPV reaction, both 2Sn-BEA and 5Sn-BEA catalyze the reaction at a similar rate, with  $> 25\%$  conversion readily achieved in 15 min of reaction time under the conditions employed. The initial turnover frequencies (TOF, calculated as moles of substrate converted per mole of Sn, as determined by ICP-MS, per hour) determined in both of these cases (112 and 102 h<sup>-1</sup>, respectively) are almost identical, if not slightly higher, to the value calculated from the original report of Roman-Leshkov et al. (96 h<sup>-1</sup>) (Table 3.4).<sup>9</sup>

**Table 3.4** initial turnover frequencies of Sn-BEA prepared by SSI and hydrothermal synthesis.

Catalyst	Preparation method	TOF <sup>a</sup>	reference
2Sn-BEA	SSI	112	this work
5Sn-BEA	SSI	102	this work
1Sn-BEA	Hydrothermal synthesis	96	[9]

<sup>a</sup>TOF, calculated as moles of substrate converted per mole of Sn, as determined by ICP-MS, per hour.

The almost identical initial TOFs observed for SSI Sn-BEA at loadings of up to 5 wt%, compared to open literature values, indicate that the SSI materials contain an identical active site distribution to that found in the conventional analogue. This is in good agreement with the MPV results and our initial spectroscopic data. Nevertheless, as the loading is elevated to 8 wt% catalytic activity per mole of Sn decrease, and at a loading of 10 wt%, 10Sn-BEA is considerably less reactive, strongly suggesting that spectator sites are a component of these materials at

these loading. Although it was originally proposed that framework and extraframework Sn species could be differentiated by monitoring the epimerization/isomerization ratio if performing the glucose reaction in methanol<sup>10</sup>, more recent studies have shown that the isomerization pathway dominates regardless of solvent choice,<sup>11</sup> and that the modifications in selectivity observed in previous cases was owing to contamination of samples with alkali metal salts, such as Li<sup>+</sup> and K<sup>+</sup>, and not differences in site speciation. Thus, no clear trends between Sn loading and selectivity were identified (Table 3.5) despite the differences in activities observed. In all cases, fructose was the main reaction product, and low levels of mannose formation were also observed. As such, identifying the active site ensembles present in these materials relies upon advanced spectroscopic study.

**Table 3.5** Glucose conversion ( $X$ ), fructose and mannose yield ( $Y$ ), and carbon balance ( $C$ ) obtained during catalytic isomerization with various SSI Sn-BEA samples. Data is presented close to iso-conversion.<sup>a</sup>

Catalyst	Time (min)	$X_{\text{Gluc}}$ (%)	$Y_{\text{Fru.}}$ (%)	$Y_{\text{Man.}}$ (%)	$C_{\text{bal.}}$ (%)
2Sn-BEA	10	22.3	16.4	4.4	98.6
5Sn-BEA	10	22.9	15.1	3.2	95.4
8Sn-BEA	10	20.0	13.1	2.9	96.0
10Sn-BEA	15	20.1	13.8	3.1	96.7

<sup>a</sup> Reaction conditions: 110 °C, 0.5 h, 10 wt% glucose solution ( $\pm$  0.62 M), glucose/Sn molar ratio of 50.

### 3.2.3 Insight into the Sn-BEA activity

To gain further insight into this decrease in activity at elevated Sn content, the initial TOF per mole of Sn in each SSI Sn-BEA catalyst for both catalytic reactions

was calculated. Given the difficulties associated with sampling such rapid catalytic processes at such short time intervals, the experimental errors determined for these samples are considerably higher ( $\pm 10\%$ ) than those experienced during most of our catalytic protocols (typically  $\pm 5\%$ ). Nevertheless, it is clear from Figure 3.9 that as Sn loading increase above  $\pm 5$  wt%, there is a considerable decrease in TOF, strongly indicating that inactive Sn(IV) sites are present in the higher loaded materials. Indeed, as the TOF of the 10 wt% sample in both cases is approximately one half of that of the 5 wt% sample, there are strong indications that potentially all of the additional Sn loading in the higher loaded materials is present in a catalytically inactive, extraframework form, or that the additional Sn loading decreases activity by other means, for example, loss of micropore access, as described above.

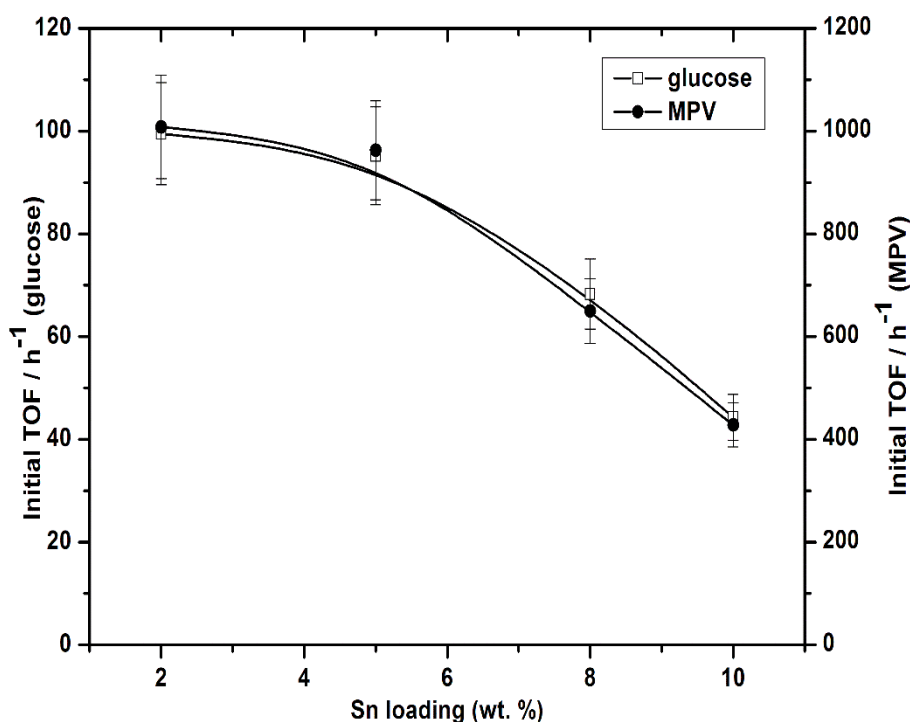


**Figure 3.9** Initial TOF for each Sn-BEA catalyst as a function of total Sn loading for both glucose isomerization (left axis, calculated at 5 min reaction time) and MPV transfer hydrogenation (right axis, calculated at 2 min reaction time). TOF calculated as moles converted per mole Sn per hour.

Noticeably, the relationship between initial activity (TOF) and Sn loading (Figure 3.9) is remarkably similar for both MPV transfer hydrogenation and glucose isomerization experiments. The similar TOF plots obtained strongly indicates that 1) the same active sites and species are responsible for catalytic activity in both reactions and that 2) inactive Sn(IV) sites, possessing lower (or no) Lewis acidity, are formed in Sn-BEA catalysts as the loading is increased substantially beyond 5 wt%. It is thus evident that as the Sn content of SSI Sn-BEA is elevated above 5 wt%, spectator sites are formed during the synthesis process, which negatively impact catalytic activity. It is noted that this is in contrast to the original communication, which had indicated that similar Sn(IV) site activity was observed between 5 and 10 wt% samples. This deviation may be caused by several factors, but likely arises from 1) the modified synthesis procedure (see Experimental Section), which has improved the relative TOFs of the 2 and 5 wt% samples, but may change the overall Sn site speciation at higher loadings; 2) the different reactions undergoing study; and 3) the different source of zeolite precursor utilized.

Clearly the synthesis of Sn-BEA by SSI can lead to a material containing multiple Sn species at very high Sn loading, although catalytic activity and hence Sn site speciation is remarkable similar to that found in the conventional analogue even at significantly higher, that is, a factor of three, loadings ( $\pm 5$  wt%).

Clearly, characterization of the materials with more sensitive techniques, such as XAS and MAS NMR, is required to clarify the presence or absence of extraframework Sn species.

### 3.2.4 Magic-Angle Spinning (MAS) NMR spectroscopy

To further elucidate the nature of Sn species in the SSI samples,  $^{119}\text{Sn}$  MAS NMR spectroscopy was used.  $^{119}\text{Sn}$  MAS NMR spectroscopy is a sensitive technique for probing the Sn species present in Sn-containing zeolites,<sup>10,11</sup> and by now it is well accepted that several important pieces of information can be gained from the

MAS NMR spectral analysis. Hydrated, framework Sn(IV) sites give rise to a clear resonance at  $\delta = -688$  ppm, with this resonance shifting to  $\delta = -440$  ppm upon in situ dehydration. Extraframework  $\text{Sn}_x\text{O}_y$  clusters and  $\text{SnO}_2$  exhibit a major resonance at  $\delta = -602$  ppm. The magnitude of this resonance at  $\delta = -602$  ppm is also dependent upon the degree of  $\text{Sn}_x\text{O}_y$  oligomerization, with  $\text{SnO}_2$  producing a MAS NMR profile with an intense resonance at  $\delta = -602$  ppm, and further, less intense resonances between  $\delta = -500$  and  $-700$  ppm. Despite containing only natural quantities of  $^{119}\text{Sn}$  and thus exhibiting low signal-to-noise ratio, several important pieces of information can be gained from the MAS NMR spectra of 2, 5, and 10Sn-BEA samples (Figure 3.10). As can be seen, both 2Sn-BEA and 5Sn-BEA give similar MAS NMR spectra, suggesting that both materials possess a similar distribution of Sn sites. The major resonance at  $\delta = -688$  ppm demonstrates that hydrated, framework Sn(IV) species predominate in these material, although the small resonances observed at  $\delta = -602$  ppm clearly demonstrates that some  $\text{Sn}_x\text{O}_y$  domains are present in these catalysts. The absence of additional resonance between  $\delta = -550$  and  $-700$  ppm indicates that the  $\text{Sn}_x\text{O}_y$  domains are of low nuclearity. Each of these observations is fully consistent with, and strongly supports, the XAS analysis. As the loading is further increased to 10 %, it is evident that the extraframework Sn component increase in concentration, as evidenced by a significant increase in intensity of the  $\delta = -602$  ppm resonance. At this loading, extraframework Sn apparently constitute a larger percentage of the Sn site speciation, although the current analysis method does not yet allow us to quantify the exact concentration of active and spectator species in this material.

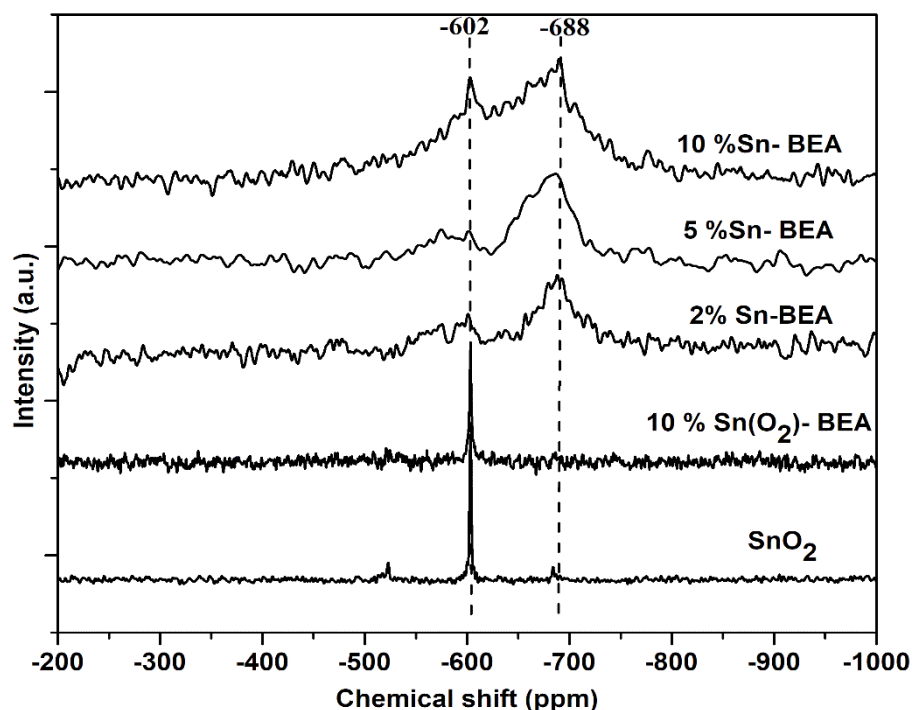


**Figure 3.10**  $^{119}\text{Sn}$  MAS NMR spectra of Sn-BEA samples.

By now it is clear that the Sn site speciation in SSI Sn-BEA catalysts remains relatively uniform up to a loading of 5 wt%, although some minor  $\text{Sn}_x\text{O}_y$  formation is observed at these levels of Sn loading. At higher Sn loadings, increased  $\text{Sn}_x\text{O}_y$  formation is observed, and larger nuclearity clusters, potentially even some  $\text{SnO}_2$ , are also formed.

### 3.2.5 X-ray absorption spectroscopy

To gain further insight into the active site speciation of Sn-BEA as a function of loading, and to gain further insight into the nature of the active and spectator sites present, the chapter subsequently focused upon the characterization of the Sn site speciation of SSI Sn-BEA with a variety of spectroscopic techniques. X-ray absorption fine structure (XAFS) analysis is a powerful technique for determining the local structure of substituted metal sites within framework architectures, with the near-edge structure (XANES) also providing information on the oxidation

state. In Figure 3.11 the normalized Sn k edge XANES data of 2Sn-BEA, 5Sn-BEA, and 10Sn-BEA zeolite samples are shown alongside reference spectra of SnO<sub>2</sub> and Sn foil.<sup>27</sup> The maxima of the first derivative of the XANES data are used to determine the position of the absorption edge. Sn foil and SnO<sub>2</sub> references have edge positions of 29200.0 eV and 29205.1 eV, respectively. All samples have an edge position consistent with that of SnO<sub>2</sub>, suggesting the presence of Sn(IV) after the 550 °C pre-treatment.

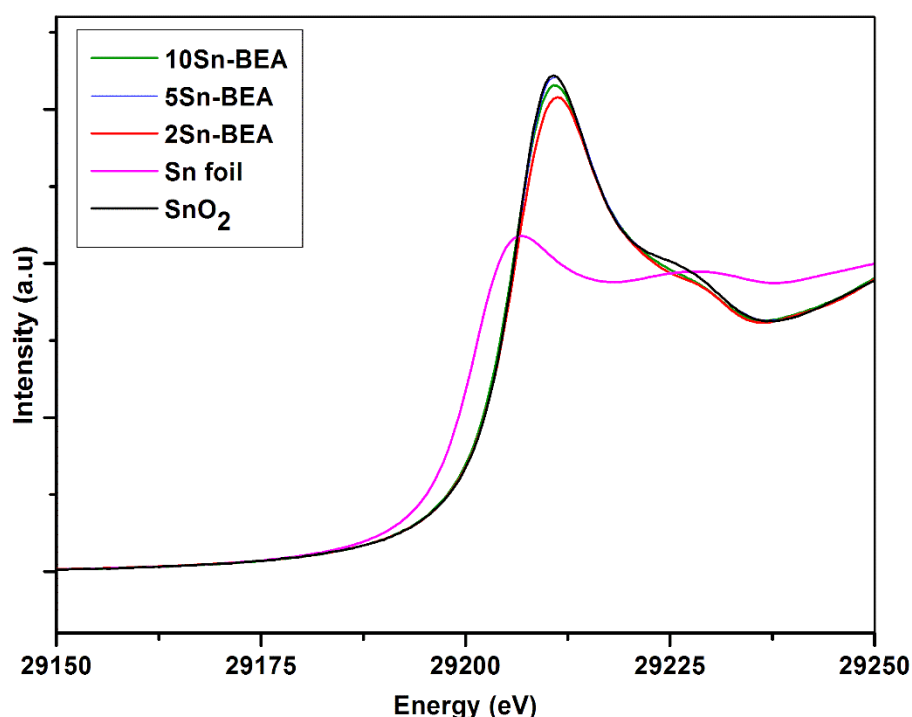


**Figure 3.11** Normalised XANES spectra of 2Sn-BEA(red), 5Sn-BEA(blue), 10Sn-BEA(green). Reference XANES spectra of SnO<sub>2</sub> (black) and Sn foil (pink) are included for a comparison.

The Sn k edge extended X-ray absorption fine structure (EXAFS) technique provides information about the local structure of the Sn within these samples. For completeness and clarity, the SSI Sn-BEA samples were analysed both in the hydrated and dehydrated form. Whilst the majority of EXAFS analysis on metal

substituted zeolites are performed following dehydration (to minimize the influence of water coordination), it is felt that presenting the EXAFS data in both dehydrated and hydrated form is more suitable. The dehydrated data allows a full comparison of the results with the open literature, whilst the hydrated form is more representative of the catalytic material that operates in the liquid/aqueous phase. The EXAFS spectra of dehydrated 5Sn-BEA (our optimal material in terms of loading and TOF) and the SnO<sub>2</sub> reference are shown in Figure 3.12 A, whilst Figure 3.12 B presents the k<sup>3</sup> weighted Fourier Transform spectra of the same two samples.

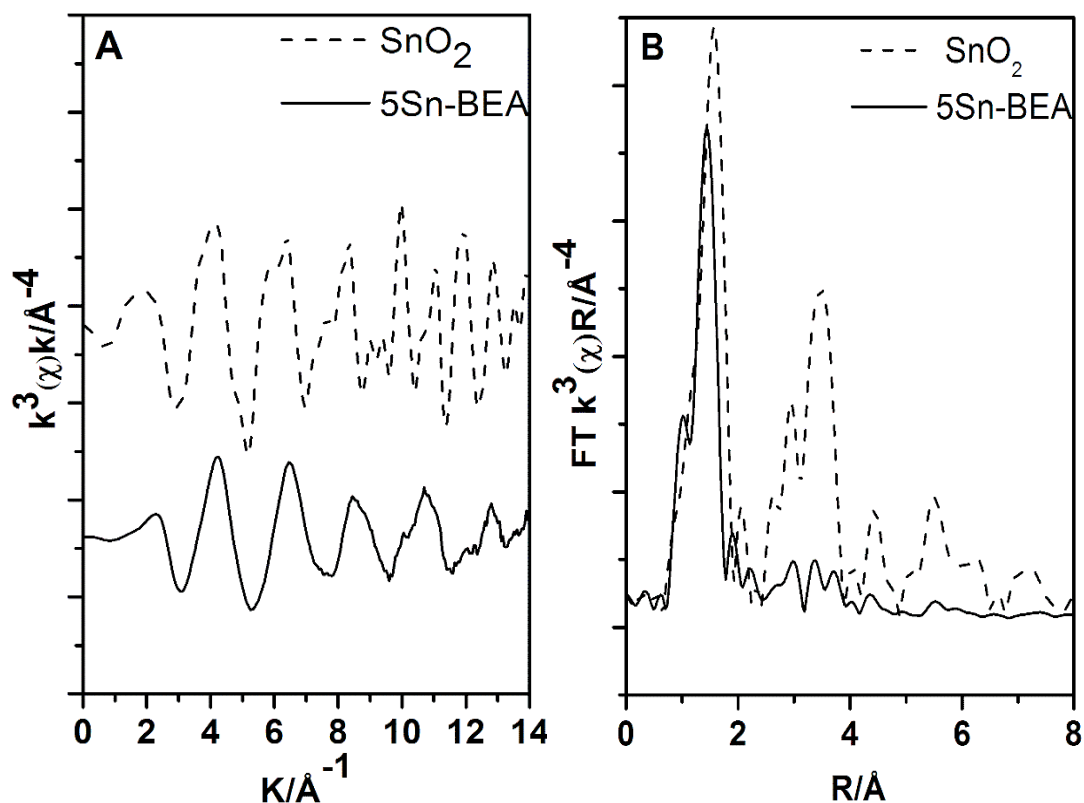


**Figure 3.12** A) EXAFS k<sup>3</sup> weighted X data and B) magnitude of the non-phase corrected Fourier transform, of dehydrated 5Sn-BEA (solid line) and SnO<sub>2</sub>(dash line).

The spectra are of excellent quality up to and beyond a distance of 14 Å<sup>-1</sup>. The first features present in the FT data are assigned to Sn-O scattering interactions,

whilst Sn-Sn scattering paths can be identified by the relatively intense features between 2.5 and 4 Å. SnO<sub>2</sub> is also readily identified by the characteristic splitting of the oscillation around 10 Å<sup>-1</sup> in the EXAFS X data (Figure 3.12 A). Clearly the first peak in the FT spectrum is shifted to a lower radial distance for 5Sn-BEA relative to SnO<sub>2</sub>. This is reflected in change in first-shell oxygen distance (Sn-O) from ± 2.05 Å in SnO<sub>2</sub> to 1.95 Å in 5Sn-BEA, which is fully consistent with a change in geometry from octahedral to tetrahedral. This is also consistent with Sn atoms that are substituted into the vacant sites of the BEA framework.<sup>28</sup> Between 2.5 and 4 Å there are a number of intense scattering peaks arising from Sn-Sn scattering interactions in SnO<sub>2</sub>. Despite their very low level, it is clear that there is a nonnegligible Sn-Sn component in 5Sn-BEA following calcination at 550 °C. This can arise either from the presence of extraframework, oligonuclear Sn clusters present within the zeolite micropores (Sn<sub>x</sub>O<sub>y</sub> species), a bulky SnO<sub>2</sub> component on the external zeolite surface, or potentially through Sn-Sn pairing.<sup>29</sup> Given the complete absence of SnO<sub>2</sub> in all the pXRD patterns (Figure 3.1), the narrow full width at half maximum of the UV/Vis data (Figure 3.5), and the relatively low intensity of the Sn-Sn scattering pattern in the FT spectrum, it is likely that Sn-Sn interactions arise from a minor, but nonnegligible extraframework, oligomeric Sn<sub>x</sub>O<sub>y</sub> component in 5Sn-BEA, although a possible contribution from Sn-Sn pairs cannot be completely excluded. The Sn-Sn coordination numbers, as derived from the EXAFS fitting, are also consistent with this hypothesis (Tables 3.6 and 3.7).

It is noted that the observation of oligomeric Sn<sub>x</sub>O<sub>y</sub> species in Sn-BEA is not unexpected, given that EXAFS and TEM analysis of conventional Sn-BEA revealed that even at low loadings (< 2 wt%), conventionally prepared Sn-BEA contains an extraframework Sn component.<sup>29</sup> Indeed, comparison of our experimental spectra to those presented by Bare et al.<sup>28</sup> for conventional Sn-BEA indicates that an identical Sn site population is present in our material, despite the threefold increase in Sn loading. From this initial analysis, it appears that the majority of the Sn atoms in 5Sn-BEA are substituted into the crystalline zeolite

framework, although a minor fraction of extraframework  $\text{Sn}_x\text{O}_y$  is potentially present in this material.

**Table 3.6** EXAFS fitting data obtained for hydrated SSI Sn-BEA catalysts.<sup>a</sup>

Catalyst	Abs Sc	N	R [Å]	$2\sigma^2$ [Å <sup>2</sup> ]	$E_f$ [eV]	R-factor
2Sn-BEA	Sn-O	3.7 (3)	2.01 (1)	0.002 (2)	8 (1)	0.02
	Sn-O	1.6 (3)	2.15 (2)	0.002 (1)		
	Sn-Sn	0.7 (3)	3.24 (3)	0.005 (2)		
	Sn-Sn	0.8 (4)	3.73 (2)	0.004 (2)		
5Sn-BEA	Sn-O	3.3 (4)	2.00 (1)	0.002 (1)	8(1)	0.02
	Sn-O	2.1 (4)	2.13 (2)	0.002 (2)		
	Sn-Sn	0.6 (3)	3.24 (3)	0.005 (2)		
	Sn-Sn	0.9 (4)	3.74 (2)	0.004 (2)		
10Sn-BEA	Sn-O	3.8 (8)	2.02 (1)	0.002 (2)	8(1)	0.02
	Sn-O	1.4 (9)	2.13 (4)	0.002 (1)		
	Sn-Sn	0.9 (5)	3.23 (4)	0.006 (4)		
	Sn-Sn	1.4 (7)	3.75 (2)	0.003 (1)		

<sup>a</sup> Fitting parameters:  $k = 1$  as deduced by  $\text{SnO}_2$  standard; Fit range  $2.5 < k < 13$ ,  $1 < R < 4$ ; Number of independent points = 19. Values in parenthesis give the experimental error.

The comparable spectroscopic data obtained for the studied material in reference to the benchmark material is in excellent agreement with our observed catalytic data (Figures 3.7, 3.8 and 3.9), which demonstrate that SSI Sn-BEA is equal to conventional Sn-BEA in terms of specific Sn site activity (TOF).<sup>9</sup> The comparable speciation and activity of the studied material compared to the benchmark Sn-BEA material prepared by hydrothermal synthesis highlights the efficacy of our

approach to preparing Sn-BEA, particularly since a much higher Sn loading can be achieved. The  $k^3$  weighted Fourier Transform of hydrated 2, 5, and 10Sn-BEA, along with the simulated fit, is shown in Figure 3.13.

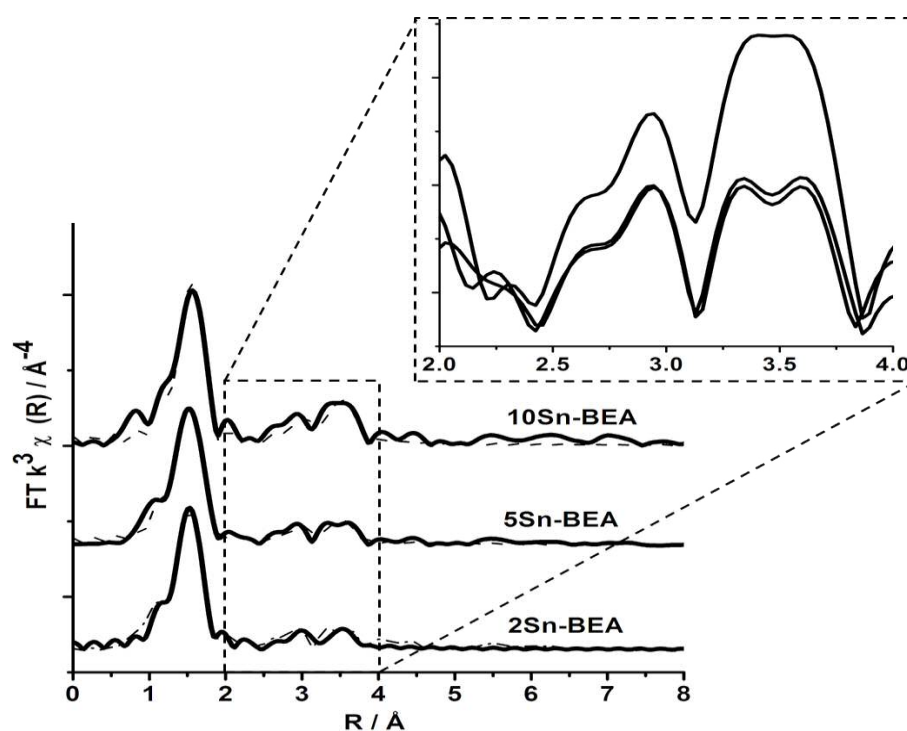


**Figure 3.13** Comparison of the magnitude of the Fourier transform (FT) (solid line) of hydrated Sn-BEA catalyst containing different loading. The fitted data is overlaid onto each spectrum (dash line). The 2-4 Å region of each spectrum is overlaid and magnified in the inset.

The  $X$  data for these samples, with simulated fit is shown in Figure 3.14.  $k^3$  weighted Fourier Transform of dehydrated and hydrated 5 and 10Sn-BEA is in Figure 3.15, along with a comparison in  $k^3$  weighted FT data for dehydrated and hydrated samples.

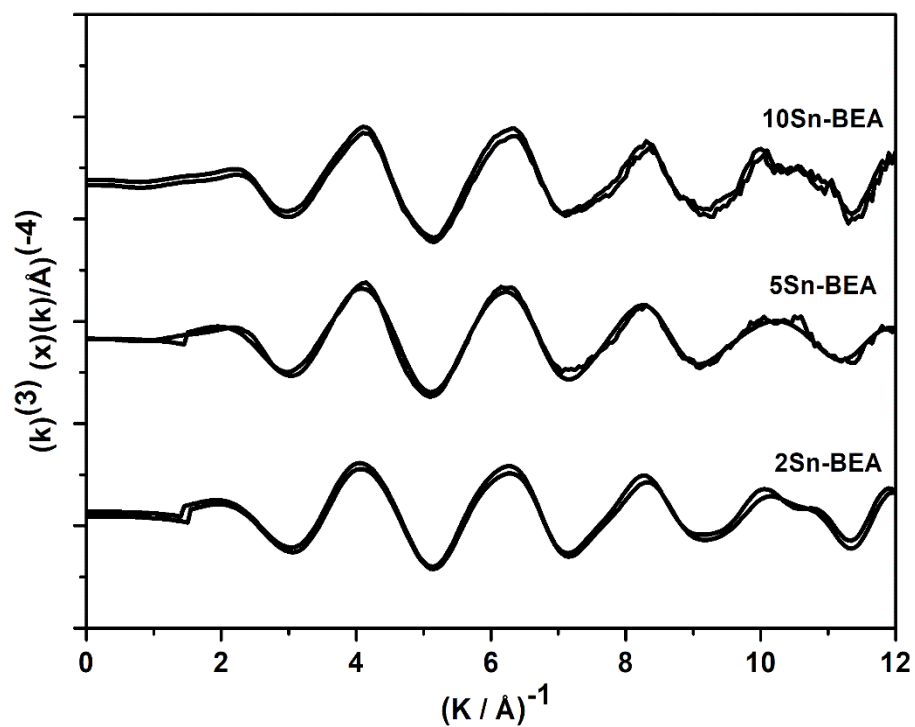


**Figure 3.14** X-data of hydrated Sn-BEA catalysts containing different Sn loading .

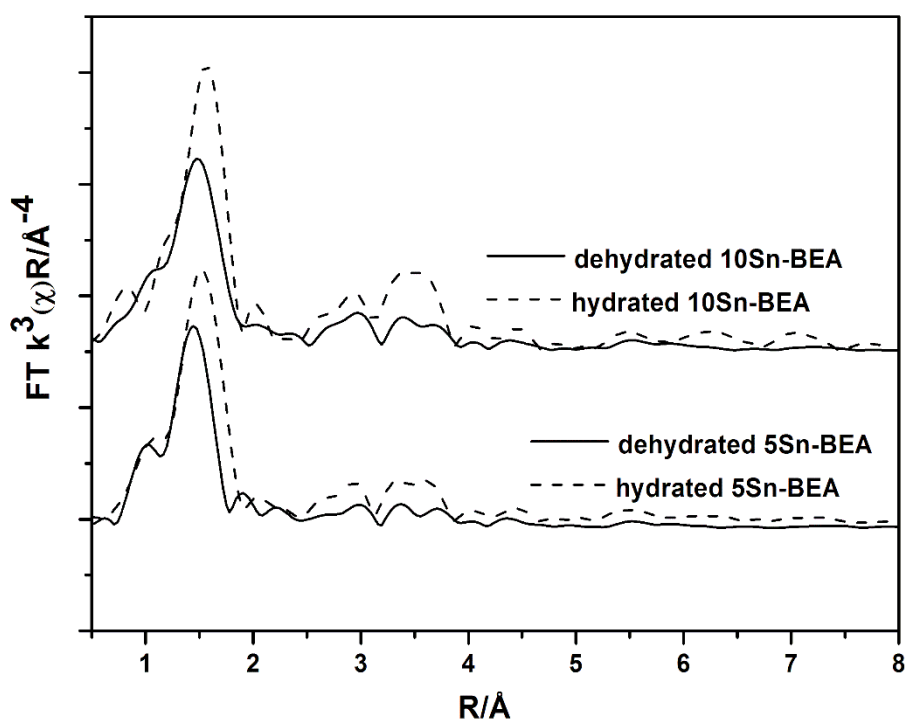


**Figure 3.15** Comparison of the magnitude of the Fourier transform (FT) signal for dehydrated and hydrated Sn-BEA catalyst containing different loading 5Sn-BEA and 10Sn-BEA.

The tabulated fitting parameters for hydrated and dehydrated 2-10Sn-BEA are shown in Tables 3.6 and 3.7, respectively. From Figure 3.15, it is evident that all hydrated samples show the presence of Sn(IV) substituted within the zeolitic framework alongside the co-presence of  $\text{Sn}_x\text{O}_y$  which is present at various levels in each material. Two Sn-O scatters are present in the data. The shortest Sn-O scattering path around 1.9-2.0 Å is assigned to Sn-O scattering interactions arising from Sn substituted into the BEA-zeolite framework. The longer Sn-O scattering path at a distance of 2.1 Å is associated either with Sn-O scattering interactions from  $\text{Sn}_x\text{O}_y$ , or water bound to the Sn within the BEA-zeolite framework. Upon dehydration, there is a clear decrease in intensity for the main peak, and a contraction in the first shell Sn-O distance from 2.0 to 1.95 Å (Figure 3.13). There is also a noticeable decrease in intensity for (or complete elimination of) the second Sn-O distance, and a decrease in the mean square disorder parameter for the oxygen shells upon dehydration. Each of these features indicates that the longer Sn-O scattering path in hydrated SSI Sn-BEA catalysts arises predominantly from water coordination to framework Sn(IV) sites. However, the need for a second Sn-O scattering interaction even following dehydration (Figure 3.11) indicates the co-presence of some  $\text{Sn}_x\text{O}_y$  clusters in all the samples. This is in line with the observed Sn-Sn scattering pattern, and likely confirms that the Sn-Sn scattering path arises predominately from  $\text{Sn}_x\text{O}_y$  oligomers, and less likely from Sn-Sn pairing. However, more sophisticated methods are required to completely eliminate the possibility of extensive Sn-Sn pairing in these materials.

Further information on the degree of Sn-Sn interaction for each sample can be obtained from the Sn-Sn scattering paths at  $\pm 3.2$  and 3.7 Å, and the characteristic splitting of the oscillation around  $10 \text{ \AA}^{-1}$  in the  $k^3$  weighted  $X$  data shown in Figure 3.12 A. The inset of Figure 3.13 shows the overlaid FT data between 2 and 4 Å for 2, 5 and 10Sn-BEA. It is evident that the magnitude of the Sn-Sn scattering path is dependent on the degree of hydration, as much more intense Sn-Sn interactions are observed for the hydrated materials. Despite this, it is still possible to compare the relative intensities between all the hydrated sample. It is

clear that the magnitude of Sn-Sn scattering in 2 and 5Sn-BEA is very similar, and this strongly suggests that both catalysts contain a comparable  $\text{Sn}_x\text{O}_y$  component. This is in agreement with their observed activity, and particularly their very similar TOF values both for glucose isomerization and the MPV reaction. The comparable Sn(IV) site speciation is also indicated by the  $X$  data, which clearly shows that there is only a minor splitting of the  $10 \text{ \AA}^{-1}$  oscillation in these two samples. This further confirms that  $\text{Sn}_x\text{O}_y$  is only a minor component of these materials. It is noted that the extent of splitting, the magnitude of Sn-Sn interactions, and the coordination numbers for Sn-Sn interactions in both samples are almost identical (Table 3.7). This demonstrates that the  $\text{Sn}_x\text{O}_y$  component in both catalysts is of a similar magnitude, and that the  $\text{Sn}_x\text{O}_y$  component in both materials is of comparable nuclearity and composition.

**Table 3.7** EXAFS fitting data obtained for dehydrated SSI Sn-BEA catalysts.<sup>a</sup>

Catalyst	Abs Sc	N	R [ $\text{\AA}$ ]	$2\sigma^2$ [ $\text{\AA}^2$ ]	$E_f$ [eV]	R-factor
2Sn-BEA	Sn-O	2.9 (2)	1.95 (1)	0.002 (1)	7 (1)	0.01
	Sn-O	1.4 (2)	2.11 (2)	0.003 (2)		
	Sn-Sn	0.7 (3)	3.24 (3)	0.007 (2)		
	Sn-Sn	0.4 (3)	3.74 (2)	0.002 (1)		
5Sn-BEA	Sn-O	2.8 (2)	1.95 (1)	0.002 (1)	8(1)	0.01
	Sn-O	1.3 (2)	2.11 (2)	0.002 (2)		
	Sn-Sn	0.4 (2)	3.25 (5)	0.008 (5)		
	Sn-Sn	0.4 (3)	3.74 (4)	0.004 (4)		
10Sn-BEA	Sn-O	2.5 (2)	1.95 (1)	0.002 (2)	8(1)	0.02
	Sn-O	2.0 (2)	2.11 (2)	0.002 (1)		
	Sn-Sn	0.7 (2)	3.25 (4)	0.005 (2)		
	Sn-Sn	0.7 (2)	3.74 (4)	0.002 (1)		
	Sn-O	2.0 (2)	2.11 (2)	0.002 (1)		

<sup>a</sup> Fitting parameters:  $k = 1$  as deduced by  $\text{SnO}_2$  standard; Fit range  $2.5 < k < 13$ ,  $1 < R < 4$ ; Number of independent points = 19. Values in parenthesis are the experimental error value.

As the loading is increased beyond 5 wt%, it is clear that the Sn-Sn interactions, and hence the quantity of extraframework  $\text{Sn}_x\text{O}_y$  species, increases, evidenced by increased Sn-Sn coordination numbers, an increase in the coordination number of the longer Sn-O distance, and an increase in the splitting structure shown in the X data. This indicates that a greater amount of bulkier  $\text{Sn}_x\text{O}_y$  clusters, potentially even  $\text{SnO}_2$ , is formed at elevated loadings, accounting for at least some of the decrease in intrinsic activity observed for this sample. However, the crystallite size of this  $\text{SnO}_2$  must still be below  $\pm 4 - 5$  nm, because of the absence of any  $\text{SnO}_2$  reflections in the pXRD pattern and the position of the absorbance edge in the UV/Vis spectra (Figures 3.1 and 3.5 respectively).

In the absence of full linear combination analysis, precise quantification of the framework/extraframework Sn ratio is not possible. Even so, it is evident that the increase in  $\text{Sn}_x\text{O}_y$  formation at loadings above 5 wt% Sn is not substantial enough to fully account for the significant decrease in observed activity, that is, TOF. It can be reasoned that the discrepancy between the increased level of  $\text{Sn}_x\text{O}_y$  formation in 10Sn-BEA, and the observed TOF decrease (50 %) likely arises from a secondary effect; at a loading of 10 wt%, the micropore volume of Sn-BEA decreases by some 20%, and access to the micropores, and hence the most active Sn atoms, may become somewhat restricted. This would prohibit access to some of the active Sn component, resulting in a greater-than-expected decrease in activity. Thus, not only do  $\text{Sn}_x\text{O}_y$  clusters lead to a decreased number of active sites, but they also prohibit access to the existing active sites in the zeolite.

### 3.2.6 FTIR using a probe molecules

To further determine whether this increased oligomer/oxide formation impacts the Lewis acidity, and hence resulting catalytic activity, of Sn-BEA, the Lewis acidity of the catalysts with in situ DRIFT spectroscopy was subsequently investigated.  $\text{CD}_3\text{CN}$  is a useful molecule for probing the Lewis acid speciation in metal containing zeolites. It has been demonstrated that isolated Lewis acid sites within

the zeolite framework interact with  $\text{CD}_3\text{CN}$ , resulting in a peak in the FTIR spectrum at  $\tilde{\nu} = \pm 2310 \text{ cm}^{-1}$ , which is not observed for extraframework species.<sup>29–33</sup> The adsorption/desorption profile for 2Sn-BEA and 10Sn-BEA is presented in Figure 3.16. Following adsorption of  $\text{CD}_3\text{CN}$ , two major adsorption features are observed, at  $\tilde{\nu} = \pm 2275$  and  $\pm 2311 \text{ cm}^{-1}$ . The first feature at  $\tilde{\nu} = 2275 \text{ cm}^{-1}$  is related to physisorbed  $\text{CD}_3\text{CN}$ , weakly bound to the sample, as evidenced by its very rapid desorption upon heating. The presence of the second feature at  $\tilde{\nu} = 2311 \text{ cm}^{-1}$  in both samples arises from the  $\text{CD}_3\text{CN}$ -Lewis acid site interaction, and demonstrates that Lewis acidic Sn(IV) centers are present in both materials. Upon heating (up to a maximum of  $200 \text{ }^\circ\text{C}$ ), both physisorbed  $\text{CD}_3\text{CN}$  and the  $\text{CD}_3\text{CN}$  coordinated onto the Lewis acidic centers, gradually desorb, although the decrease in intensity for the chemisorbed species is evidently much slower. The comparable rate of desorption in both SSI samples strongly indicates that the active species in both materials possess similar levels of Lewis acid strength.

Despite this, it is evident that the normalized area of the  $\text{CD}_3\text{CN}$ -Lewis feature, that is, the area of  $\text{CD}_3\text{CN}$ -Lewis band divided by wt % Sn, is considerably lower for 10Sn-BEA than for 2Sn-BEA. Despite the semiquantitative nature of this normalization, the large difference in normalized area clearly demonstrates that the  $\text{Sn}_x\text{O}_y$  species identified in 10Sn-BEA by EXAFS and MAS NMR spectroscopy are unable to activate the Lewis base. For 1Sn-BEA, an area of 9.2 a.u was determined, whilst for 2Sn-BEA 5.5 a.u was determined. Thus, they are spectator species to Lewis acid catalysis, and hence decrease the number of Lewis acid sites in the catalyst. Though our spectroscopic methods do not readily allow for quantification of the amount of spectator sites at this time, inactive sites likely account for a significant fraction of the Sn population at loading above 5 wt %, given the significant decreases in overall TOF observed at these Sn loadings (Figure 3.12). This accounts for the lower activity of the higher loaded samples and further clarifies the roles of the active and spectator site. It is noted that the pronounced asymmetry in the  $\tilde{\nu} = 2311 \text{ cm}^{-1}$  band upon desorption, in particular for 2Sn-BEA, may indicate that two possible bands, corresponding to two different Sn active sites with different catalytic properties, may be present in the samples.

Previous FTIR studies have proposed that these may arise from “closed” ( $\tilde{\nu} = 2308 \text{ cm}^{-1}$ ) and “open”/“hydrolysed” ( $\tilde{\nu} = 2316 \text{ cm}^{-1}$ ) Sn species that are still present in the BEA framework. Given that our procedure employs dealuminated BEA zeolite, which evidently contains a high density of networked silanol groups and remaining vacant framework sites, it might be expected that a preference towards “open” Sn species may be present in this material. This may account for the apparent asymmetry of the  $\tilde{\nu} = 2311 \text{ cm}^{-1}$  band. However, further spectroscopic study is required to confirm this effect, particularly as recent work has suggested that the packing structure of  $\text{CD}_3\text{CN}$  may inadvertently lead to the presence of multiple bands in the  $\tilde{\nu} = 2311 \text{ cm}^{-1}$  region.<sup>26</sup>

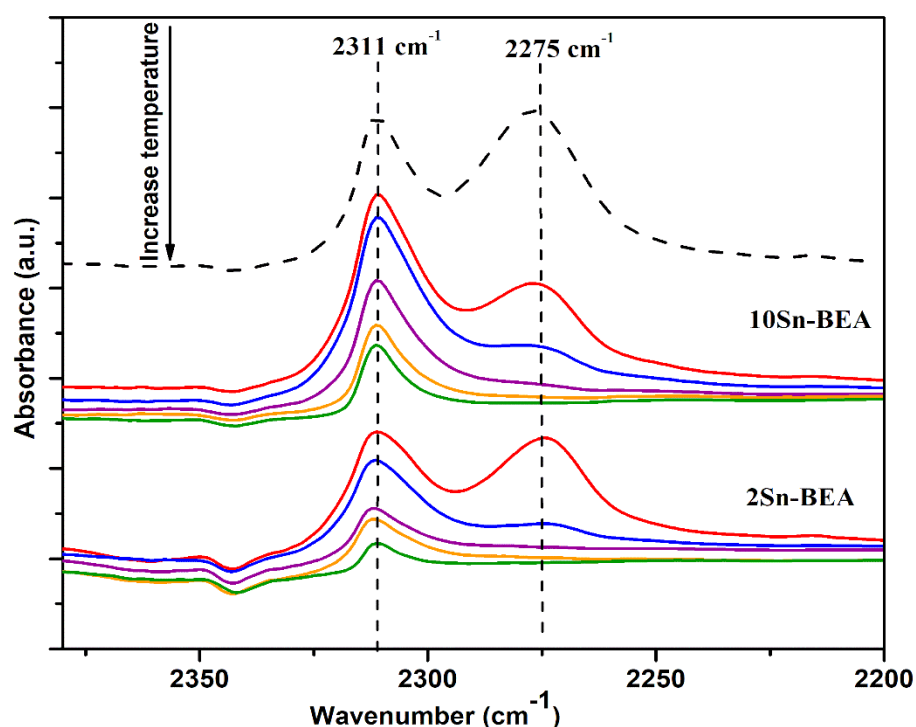


**Figure 3.16** In situ  $\text{CD}_3\text{CN}$  desorption profile for 2Sn-BEA and 10Sn-BEA.  $\text{CD}_3\text{CN}$  was desorbed under a dynamic vacuum at various temperature intervals, increasing from top to bottom (50 (red), 100 (blue), 150 (purple), 200 (yellow) and 250 (green)). All spectra are back-ground-referenced against the dehydrated zeolite sample. A reference spectrum of physisorbed  $\text{CD}_3\text{CN}/2\text{Sn-BEA}$  is provided (dashed line).

---

### 3.3 Conclusions

Sn-BEA is a material of considerable industrial interest, as it has been shown to be an important catalyst for several established and emerging sustainable chemical transformations. In this chapter, it was further demonstrated that solid-state incorporation (SSI) is a suitable alternative methodology for preparing highly active Sn-BEA catalysts. Not only are the resulting catalysts identical in activity to the conventional analogues, but they are prepared very rapidly, very cleanly (without, for example, solvent) and very selectively.

In this chapter, both catalytic and spectroscopic studies were combined to demonstrate that isolated, framework Sn(IV) sites dominate the Sn population of these materials, even at loadings of up to 5 wt%, which is a loading approximately two-to-three times greater than can be obtained by conventional hydrothermal methods. Identical catalytic activity to the established material is also observed, even at these significantly elevated loadings. This consequently leads to significant increases in the space-time yield of each catalyst, that is, the productivity per gram of catalyst. At higher levels of Sn loading (8-10 wt%), spectator sites in the form of Sn oligomers, and likely some SnO<sub>2</sub>, are also formed. Though they do not participate in the main catalytic reactions or competitive side reactions, these Sn oligomers decrease the effective concentration of active Sn in the material, and result in a catalytic powder exhibiting lower values of TOF. Spectroscopic analysis with a variety of sophisticated methods, including extended X-ray absorption fine structure, magic-angle spinning NMR, and diffuse reflectance infrared Fourier transform spectroscopy, allowed obtaining an overview of the active site distribution, and further allowed rationalizing the observed catalytic trends.

At this stage of the study, it was observed that the catalytic performance of Lewis acid catalysts in liquid phase can be inhibited by slow molecular diffusion in their microporous structures, especially when bulky molecules are used. Hence, the next chapter focuses on the generation of a novel hierarchical stannosilicate

zeolite with improved diffusional properties that overcome the limitations common to almost all microporous zeolites.

## 3.4 Experimental

### 3.4.1 Catalyst synthesis and pre-treatment

Commercial zeolite Al-BEA (Zeolyst, NH<sub>4</sub>-form, SiO<sub>2</sub>/Al<sub>2</sub>O<sub>3</sub> = 25) was dealuminated by treatment in HNO<sub>3</sub> solution (13 M HNO<sub>3</sub>, 100 °C, 20 h, 20 mL g<sup>-1</sup> zeolite). The dealuminated powder was washed extensively with water (± 500 mL g<sup>-1</sup> catalyst), and dried overnight at 110 °C. SSI was performed by a modified procedure of Refs.[16], by grinding the appropriate amount of Sn(II) acetate with the necessary amount of dealuminated zeolite for 10 min in a pestle and mortar. Following this procedure, the sample was heated in a combustion furnace (Carbolite MTF12/38/400) to 550 °C (10 °C min<sup>-1</sup> ramp rate) first in a flow of N<sub>2</sub> (3h) and subsequently air (3h) for a total of 6 h. Gas flow rates of 60 mL min<sup>-1</sup> were employed at all times. The sample was held horizontally in an alumina combustion boat (10 mL capacity), and a quartz tube was used to seal the sample environment and permit gas flow.

### 3.4.2 Catalyst characterization

Specific surface area was determined from nitrogen adsorption using the BET equation, and microporous volume was determined from nitrogen adsorption isotherms using the t-plot method. Porosymmetry measurements were performed on a Quantachrome Autosorb, and samples were degassed prior to use (275 °C, 3h). Adsorption isotherms were obtained at 77 K. Powder X-ray diffraction analysis was performed on a PANalytical X'PertPRO X-ray diffractometer, with a Cu K $\alpha$  radiation source (40 kV and 40 mA). Diffraction patterns were recorded between 5-55 °2 $\theta$  at a step size of 0.0167° (time/step = 150 s, total time = 1h). UV/Vis analysis was performed on an Agilent Cary 4000 UV/Visible

spectrophotometer in diffuse reflectance mode. Samples were scanned between 190 and 900 nm at a scan rate of 600 nm min<sup>-1</sup>.

MAS NMR experiments were performed at Durham University through the EPSRC UK National Solid-State NMR Service. Samples were measured under conditions identical to those reported by Bermejo-Deval and co-workers.<sup>11</sup> Nonenriched Sn-BEA samples were measured on both a Varian VNMRS spectrometer, and a Bruker Avance III HD spectrometer with comparable performance. Both spectrometers possess operating frequencies of 400 and 149 MHz for <sup>1</sup>H and <sup>119</sup>Sn, respectively. Approximately 60-100 mg of sample was packed into a 4 mm rotor. Measurements were performed in direct excitation mode (spin-echo 90x-t-180y), with a recycle delay of 2 s. Samples were spun at ±12000 Hz, and approximately 50000 repetitions were typically employed for each sample. Sn k-edge XAFS studies were performed on the B18 beamline at the Diamond Light Source, Didcot, UK. Measurements were performed using a QEXAFS setup with a fast-scanning Si (311) double crystal monochromator. The time resolution of the spectra reported herein was 2 min/spectrum ( $k_{\max} = 14$ , step size 0.5 eV), on average three scans were acquired to improve the signal-to-noise level of the data for transmission measurements. All solid reference samples were diluted with cellulose and pressed into pellets to optimize the effective edge-step of the XAFS data and measured in transmission mode using ion chamber detectors. All Sn-substituted zeolite samples were prepared as undiluted pellets, with the amount of sample optimized to yield a suitable edge step and measured in transmission mode using ion chamber detectors. All XAFS spectra were acquired concurrently with the appropriate foil placed between  $I_t$  and  $I_{ref}$ . XAFS data processing was performed using IFEFFIT<sup>34</sup> with the Horae package<sup>35</sup> (Athena and Artemis). The amplitude reduction factor,  $S_0$ , was derived from EXAFS data analysis of a known reference compound, SnO<sub>2</sub>, (with known coordination numbers which were fixed during analysis) to be 1.0, which was used as a fixed input parameter. DRIFT spectroscopy was performed in a Harrick praying mantis cell. The spectra were recorded on a Bruker Tensor spectrometer over a range of 4000-650 cm<sup>-1</sup> at a resolution of 2 cm<sup>-1</sup>. In situ CD<sub>3</sub>CN

measurements were performed on pretreated zeolite powders (550 °C, 1h under flowing air, 60 mL min<sup>-1</sup>) as follows: following pretreatment, the sample was dosed with CD<sub>3</sub>CN vapour at room temperature for 5 min, and one spectrum was recorded. The sample chamber was subsequently evacuated under dynamic vacuum (approximately 10<sup>-4</sup> mbar), and spectra were recorded at 25, 50, 100, 150, and 200 °C. All spectra were background subtracted against the pretreated zeolite.

### 3.4.3 Kinetic evaluation and analytical methods

Batch MPVO reactions were performed in a 50 mL round bottom flask equipped with a reflux condenser, which was thermostatically controlled by immersion in a silicon oil bath. The vessel was charged with a 10 mL solution of cyclohexanone in 2-butanol (0.2 M), which also contained an internal standard (biphenyl, 0.01 M), and was subsequently heated to the desired temperature (100 °C internal temperature). The reaction was initiated by addition of an appropriate amount of catalyst, corresponding to 1 mol% Sn relative to cyclohexanone. The solution was stirred at 800 rpm with an oval magnetic stirrer bar. Aliquots of reaction solution were taken periodically for analysis, and were centrifuged prior to injection into a GC (Agilent 7820, 25 m CP-Wax 52 CB). Reactants were quantified against a biphenyl internal standard.

D-glucose isomerization experiments were performed in 15 mL thick-walled glass reactors (Ace pressure tube, Sigma-Aldrich) that were heated in a temperature-controlled oil bath. The reactor was charged with 5 mL of an aqueous solution of glucose (10 wt%, 0.61 M) and an appropriate amount of catalyst corresponding to a 1:50 metal/glucose molar ratio. Once the oil had reached the desired temperature (110 °C), the reaction was initiated by vigorous stirring with a magnetic stirrer bar (600 rpm). The reactor was stirred for an appropriate length of time, and time online samples were obtained by periodically quenching the reaction by rapidly cooling the reactor in an ice bath. Aliquots of solution were extracted with a syringe, centrifuged to remove solid particulates, and were

subsequently analysed by HPLC (Agilent 1220). The compounds were separated with a Ca Hi-Plex column (6.5x300 mm, 8  $\mu$ m particle size, Agilent), which was isothermally held at 60 °C. Ultrapure water was used as the mobile phase, at a flow rate of 0.3 mL min<sup>-1</sup>. The compounds were detected by use of diode array and refractive index detectors.

### 3.5 References

- 1 Y. Roman-Leshkov and M. E. Davis, *ACS Catal.*, 2011, **1**, 1566.
- 2 M. Moliner, *Dalt. Trans.*, 2014, **43**, 4197.
- 3 S. Bordiga, F. Bonino, A. Damin and C. Lamberti, *Phys. Chem. Chem. Phys.*, 2007, **9**, 4854.
- 4 A. Corma, L. T. Nemeth, M. Renz and S. Valencia, *Nature*, 2001, **412**, 423.
- 5 C. Hammond, R. L. Jenkins, N. Dimitratos, J. A. Lopez-Sanchez, M. H. Ab Rahim, M. M. Forde, A. Thetford, D. M. Murphy, H. Hagen, E. E. Stangland, J. M. Moulijn, S. H. Taylor, D. J. Willock and G. J. Hutchings, *Chem. - A Eur. J.*, 2012, **18**, 15735.
- 6 R. Gounder, *Catal. Sci. Technol.*, 2014, **4**, 2877.
- 7 M. Moliner, Y. Román-Leshkov and M. E. Davis, *Proc. Natl. Acad. Sci.*, 2010, **107**, 6164.
- 8 R. Bermejo-Deval, R. S. Assary, E. Nikolla, M. Moliner, Y. Roman-Leshkov, S.-J. Hwang, A. Palsdottir, D. Silverman, R. F. Lobo, L. A. Curtiss and M. E. Davis, *Proc. Natl. Acad. Sci.*, 2012, **109**, 9727.
- 9 Y. Román-Leshkov, M. Moliner, J. A. Labinger and M. E. Davis, *Angew. Chemie - Int. Ed.*, 2010, **49**, 8954.
- 10 R. Bermejo-Deval, R. Gounder and M. E. Davis, *ACS Catal.*, 2012, **2**, 2705.

- 
- 11 R. Bermejo-Deval, M. Orazov, R. Gounder, S. J. Hwang and M. E. Davis, *ACS Catal.*, 2014, **4**, 2288.
  - 12 G. Li, E. A. Pidko and E. J. M. Hensen, *Catal. Sci. Technol.*, 2014, **4**, 2241.
  - 13 M. Boronat, A. Corma, M. Renz, G. Sastre and P. M. Viruela, *Chem. - A Eur. J.*, 2005, **11**, 6905.
  - 14 M. Renz, T. Blasco, A. Corma, V. Fornes, R. Jensen and L. Nemeth, *Chem. - A Eur. J.*, 2002, **8**, 4708.
  - 15 A. Corma, M. E. Domine, L. Nemeth and S. Valencia, *J. Am. Chem. Soc.*, 2002, **124**, 3194.
  - 16 P. Wolf, C. Hammond, S. Conrad and I. Hermans, *Dalt. Trans.*, 2014, **43**, 4514.
  - 17 M. S. Holm, S. Saravanamurugan and E. Taarning, *Science (80-. )*, 2010, **328**, 602.
  - 18 W. R. Gunther, Y. Wang, Y. Ji, V. K. Michaelis, S. T. Hunt, R. G. Griffin and Y. Román-Leshkov, *Nat. Commun.*, 2012, **3**, 1109.
  - 19 B. Tang, W. L. Dai, G. J. Wu, N. J. Guan, L. D. Li and M. Hunger, *ACS Catal.*, 2014, **4**, 2801.
  - 20 C. Hammond, S. Conrad and I. Hermans, *Angew. Chemie - Int. Ed.*, 2012, **51**, 11736.
  - 21 W. N. P. Van Der Graaff, G. Li, B. Mezari, E. A. Pidko and E. J. M. Hensen, *ChemCatChem*, 2015, **7**, 1152.
  - 22 J. Dijkmans, D. Gabriëls, M. Dusselier, F. de Clippel, P. Vanelderren, K. Houthoofd, A. Malfliet, Y. Pontikes and B. F. Sels, *Green Chem.*, 2013, **15**, 2777.
  - 23 C.-C. Chang, H. J. Cho, Z. Wang, X. Wang and W. Fan, *Green Chem.*, 2015, **17**, 2943.

- 
- 24 P. Y. Dapsens, C. Mondelli, J. Jagielski, R. Hauert and J. Pérez-Ramírez, *Catal. Sci. Technol.*, 2014, **4**, 2302.
- 25 C. Hammond, N. Dimitratos, J. A. Lopez-Sanchez, R. L. Jenkins, G. Whiting, S. A. Kondrat, M. H. Ab Rahim, M. M. Forde, A. Thetford, H. Hagen, E. E. Stangland, J. M. Moulijn, S. H. Taylor, D. J. Willock and G. J. Hutchings, *ACS Catal.*, 2013, **3**, 1835.
- 26 R. S. Assary and L. A. Curtiss, *J. Phys. Chem. A*, 2011, **115**, 8754.
- 27 S. Bordiga, E. Groppo, G. Agostini, J. A. Van Bokhoven and C. Lamberti, *Chem. Rev.*, 2013, **113**, 1736.
- 28 S. R. Bare, S. D. Kelly, W. Sinkler, J. J. Low, F. S. Modica, S. Valencia, A. Corma and T. L. and Nemeth, *J. Am. Chem. Soc.*, 2005, **127**, 12924.
- 29 C. M. Osmundsen, M. S. Holm, S. Dahl and E. Taarning, *Proc. R. Soc. A Math. Phys. Eng. Sci.*, 2012, **468**, 2000.
- 30 S. Roy, K. Bakhmutsky, E. Mahmoud, R. F. Lobo and R. J. Gorte, *ACS Catal.*, 2013, **3**, 573.
- 31 M. Boronat, P. Concepcion, A. Corma, M. T. Navarro, M. Renz and S. Valencia, *Phys. Chem. Chem. Phys.*, 2009, **11**, 2794.
- 32 M. Boronat, P. Concepción, A. Corma, M. Renz and S. Valencia, *J. Catal.*, 2005, **234**, 111.
- 33 J. Chen, J. M. Thomas and G. Sankar, *J. Chem. Soc. Faraday Trans.*, 1994, **90**, 3455.
- 34 M. Newville, *J. Synchrotron Radiat.*, 2001, **8**, 322.
- 35 B. Ravel and M. Newville, *J. Synchrotron Radiat.*, 2005, **12**, 537.

# 4

## Hierarchically porous BEA stannosilicates as unique catalysts for bulky ketone conversion and continuous operation.

### Abstract

Pore size limitations typically limit the applicability of Lewis acidic zeolites, such as titano- and stannosilicates to catalytic processes based on small-to-mid sized substrates, and increase their rates of deactivation, prohibiting further exploitation. Herein, this study demonstrates that Sn-containing zeolites possessing modified hierarchical BEA matrices can be prepared by a modified version of solid state incorporation, the methodology optimised in Chapter 3. These hierarchical stannosilicates are able to mediate the catalytic conversion of bulky ketone substrates, a pertaining challenge in the field that purely microporous analogues are unable to mediate. Deactivation studies in the continuous regime also demonstrate the exceptional stability of hierarchical Sn-BEA compared to purely microporous Sn-BEA, with <20% loss of activity observed over 700 h on stream. In contrast, the purely microporous analogue lost  $\pm 70\%$  activity in only 200 h. To the best of our knowledge, this is the first time a stannosilicate with a beneficial hierarchical BEA framework has been prepared, and the first evidence of cyclododecanone valorisation with stannosilicate catalysts.

---

This work contributed to the following papers:

A. Al-Nayili, K. Yakabi and C. Hammond, *J. Mater. Chem. A*, 2016, 4, 1373.

## 4.1 Introduction

Lewis acid catalysts have been widely used for a range of essential catalytic transformations, including biomass valorisation. Of particular interest are crystalline, porous inorganic materials, such as zeolites, which contain encapsulated Lewis acidic centres, such as Al, Sn, Ti and Zr.<sup>1-4</sup> These materials combine the advantages of molecular catalysts, such as site isolation and high intrinsic activity, along with the practical advantages of heterogeneous catalysts, which simplify downstream processing. Amongst these materials, Sn-BEA, a medium pore zeolite possessing isolated Sn(IV) sites and BEA topology, has garnered tremendous levels of academic and industrial interest. Over the last decade, it has been demonstrated that this material possesses an exceptional ability to catalyse various transformations involving carbonyl compounds, such as the Baeyer-Villiger oxidation (BVO) of ketones,<sup>5-7</sup> the Meerwein-Ponndorf-Verley (MPV) transfer hydrogenation of ketones to alcohols,<sup>8-11</sup> and the isomerization of renewable sugars, such as glucose,<sup>12-15</sup> amongst several others.

In addition to high levels of activity, microporous crystalline zeolites, such as Sn-BEA, also provide excellent levels of hydrothermal stability, high surface area, and molecular sieving capability due to the uniform nature of their micropores. Possessing a microporous structure, Sn-BEA is, however, very susceptible to the limitations associated with this particular degree of confinement, such as (i) internal mass transfer limitations hindering catalytic performance through slow molecular diffusion, (ii) restricted diffusion of bulkier reactants, which limits their scope of reactivity, and (iii) increased rates of deactivation through pore blocking (cf. fouling). These limitations are, unfortunately, common to almost all microporous zeolites. Indeed, it was recently demonstrated that despite exhibiting high levels of stability during steady state (continuous) operation, microporous Sn-BEA slowly deactivates with extended time on stream through fouling of the micropores with reaction products and higher molecular weight carbonaceous residue.<sup>16</sup>

Over the years, several approaches have been followed in order to alleviate these limitations, such as (i) the synthesis of extra-large pore zeolites,<sup>17-19</sup> (ii) the

development of ordered mesoporous materials (e.g. MCM-41)<sup>20</sup> and related composites,<sup>21</sup> (iii) the preparation of nano-sized zeolite particles,<sup>22</sup> and (iv) the development of 2D materials.<sup>23–28</sup> Indeed, several of these approaches have been attempted for a range of zeolite materials, including silicates, aluminosilicate, titanosilicate, and more recently, stannosilicate. Nevertheless, each of these alternative materials experience particular disadvantages when it comes to catalytic activity, and several hurdles and challenges remain to be tackled. Decreased levels of specific active site activity (e.g. turnover frequency), poorer levels of hydrothermal stability and increased production costs (through the use of costly surfactant templates) are just three of the known disadvantages of each of the alternative materials that have been prepared to date.

Hierarchical zeolites are those that possess levels of mesoporosity imprinted upon the conventional microporous structure. In principle, these materials retain the advantages of purely microporous materials, such as increased intrinsic reactivity and (hydro)thermal stability, whilst also improving the particular disadvantages associated with overly confined materials, such as retarded diffusion and increased rates of deactivation.<sup>29–31</sup> Consequently, these materials have experienced an explosion of interest in recent years. Most of this attention has focused upon the generation of hierarchical aluminosilicate materials, unsurprising given their widespread use throughout the petrochemical industry.<sup>32,33</sup> Desilication, a top down approach involving the treatment of a parent zeolite in an alkaline medium under mild conditions, has been shown to be a particular efficient method of generating hierarchy.<sup>34–36</sup> The role of the base is to remove silicon atoms from the framework of the material (Figure 4.1), thus resulting in partial destruction of the micropores, and leading to the appearance of mesoporosity. Under optimised conditions, this can lead to the generation of a hierarchical material without causing excessive destruction, i.e. collapse, of the zeolite framework.

Given their emerging status as sustainable heterogeneous catalysts, it is unsurprising that attention is being turned to the generation of stannosilicates with improved diffusional properties.<sup>37–39</sup> To date, however, focus has primarily been on the synthesis of stannosilicates with a hierarchical MFI-type topology, and very

little attention<sup>40</sup> has been devoted to the synthesis of other hierarchical stannosilicates. Furthermore, in all of these previous cases, catalytic studies have only focused upon the conversion of relatively small substrates that do not present a significant hindrance for conventional medium pore zeolites, such as zeolite BEA. Examples include the isomerisation of dihydroxyacetone (C<sub>3</sub>) and the catalytic conversion of glucose (C<sub>6</sub>). As such, full appreciation of the potential advantages of hierarchical stannosilicates has yet to be realised.

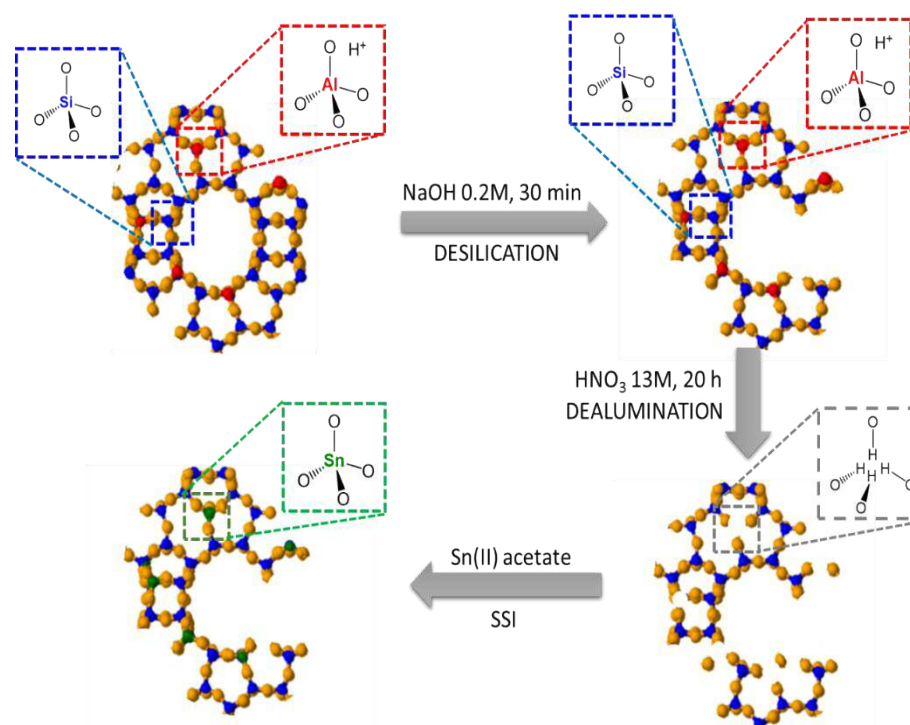


**Figure 4.1** Postsynthetic desilication procedure for mesopores creation in the zeolite BEA using NaOH as desilication agent (step 1) and subsequent formation of stannosilicate via solid state stannation (step 2 and 3).

Motivated by this research challenge, this work demonstrates that hierarchically-modified zeolite BEA, doped with 2 wt% Sn through solid-state stannation, is an effective catalyst for the catalytic conversion of bulky ketones, such as cyclododecanone. These ketones are far too large to be catalytically converted in the micropores of even medium pore zeolites, and thus offer an ideal challenge for their hierarchical matrices. Kinetic and spectroscopic methodologies reveal

that the active sites present in the hierarchical matrix are comparable to those found in the conventional microporous Sn-BEA despite the modified porosity, and that the hierarchical material demonstrates significantly higher levels of activity than ordered mesoporous analogues, such as Sn-MCM-41. Furthermore, deactivation studies in continuous mode also demonstrate the supreme advantage of the hierarchical analogue when it comes to extended steady state operation, with high levels of activity observed even after 700 h on stream. To the best of our knowledge, this is the first time a stannosilicate with a hierarchical BEA framework has been prepared, and the first evidence of cyclododecanone valorisation with stannosilicate catalysts.

## 4.2 Results and discussion

### 4.2.1 Generation of hierarchical zeolite BEA

The typical solid-state stannation methodology involves the remetallation of dealuminated (deAl-) BEA with Sn(II) acetate (Figure 4.1). Accordingly, the first focus is upon the desilication (deSi) of a pre-dealuminated (deAl) sample of H-BEA (denoted [deAl,deSi]-BEA), which was previously prepared by dealumination in HNO<sub>3</sub>. It is noted here that for materials with multiple pretreatment steps, the nomenclature used follows the order of treatment, i.e. [deAl,deSi]-BEA indicates dealumination, followed by desilication. The subsequent desilication protocol employed was based on a modified protocol published by the group of Perez-Ramirez.<sup>34</sup> The optimised protocol involves treatment of the dealuminated solid in an aqueous solution of NaOH (0.2 M) for 0.5 h at 45 °C. Although only minor changes to the textural properties of H-BEA were observed after the first step i.e. dealumination (Table 4.1, Entry 2), desilication of the already dealuminated material ([deAl,deSi]-BEA) resulted in complete structural collapse, as evidenced by the porosimetry data (Table 4.1, Entry 3) and XRD analysis (Figure 4.2). Clearly, the presence of framework Al in the zeolite is essential for desilication to proceed without complete destruction of the framework, in line with previous research.<sup>41</sup>

**Table 4.1** Textural properties of sample used in this work.

Entry	Sample	$S_{\text{BET}}^{\text{a}}$ ( $\text{m}^2 \text{g}^{-1}$ )	$S_{\text{external}}^{\text{b}}$ ( $\text{m}^2 \text{g}^{-1}$ )	$S_{\text{micro}}^{\text{b}}$ ( $\text{m}^2 \text{g}^{-1}$ )	$V_{\text{total}}^{\text{c}}$ ( $\text{cm}^3 \text{g}^{-1}$ )	$V_{\text{micro}}^{\text{b}}$ ( $\text{cm}^3 \text{g}^{-1}$ )	$V_{\text{meso}}^{\text{d}}$ ( $\text{cm}^3 \text{g}^{-1}$ )
1	Parent H-BEA	498	61	437	0.35	0.23	0.11
2	deAl-BEA	541	124	417	0.53	0.23	0.22
3	[deAl,deSi]-BEA	243	197	47	0.40	0.0	0.40
4	deSi-BEA	805	483	323	0.95	0.19	0.76
5	[deSi,deAl]- BEA(h*BEA)	691	458	233	0.84	0.15	0.61
6	2Sn-h*BEA	614	356	259	0.67	0.15	0.52
7	2Sn-BEA	528	115	412	0.42	0.23	0.20
8	2Sn-MCM-41	832	832	0	0.85	0	0.85

<sup>a</sup> Brunauer-Emmett-Teller surface area ( $S_{\text{BET}}$ ) was calculated from BET method. <sup>b</sup> External and micropore surface area ( $S_{\text{ext}}$  and  $S_{\text{micro}}$ ) and micropore volume ( $V_{\text{micro}}$ ) derived from the t-plot method. <sup>c</sup> Total pore volume ( $V_{\text{total}}$ ) was evaluated at  $P/P_0 = 0.99$ . <sup>d</sup> Meso pore volume ( $V_{\text{meso}}$ ) was calculated according to  $V_{\text{T}} - V_{\text{micro}}$ .

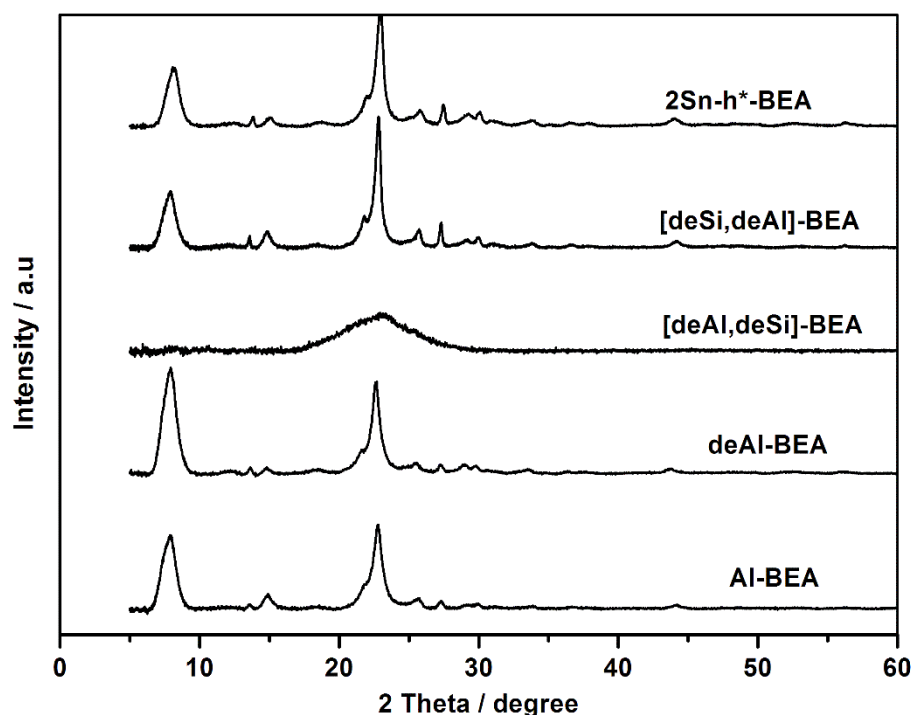


**Figure 4.2** XRD patterns of the commercial zeolite BEA upon various treatments.

The preparation procedure was subsequently reversed, and first desilicated the parent zeolite directly (deSi-BEA, Table 4.1 Entry 4). The desilication procedure employed leads to several changes in the properties of the parent zeolite. Substantial increases in BET surface area ( $S_{\text{BET}}$ ), external surface area ( $S_{\text{ext}}$ ), and total pore volume ( $V_{\text{total}}$ ) are accompanied by decreased micropore surface area ( $S_{\text{micro}}$ ), and micropore volume ( $V_{\text{micro}}$ ). More crucially, however, is the retained crystalline structure (Figure 4.2) and the substantial increase in mesopore volume ( $V_{\text{meso}}$ ) following the desilication procedure. Having generated a clearly hierarchical structure, the material in line with the previous chapter was subsequently dealuminated, in order to generate the vacant framework sites required for the incorporation of Sn ([deSi,deAl]-BEA, Table 4.1 Entry 5).

Despite the dealumination protocol being able to induce some mesopore formation and increasing  $S_{\text{BET}}$  and  $S_{\text{ext}}$  on its own (Table 4.1, Entry 2), dealumination of the desilicated structure ([deSi,deAl]-BEA, henceforth h<sup>+</sup>-BEA) leads to minor decreases in each of these parameters (Table 4.1, Entry 5) compared to desilication alone (Table 4.1, Entry 4). The complete absence of Al

from the dealuminated material confirms that extra-framework Al species are not present and are therefore not partially blocking the pores (Table 4.2). Accordingly, this unexpected result was attributed to a slight relaxation of the framework upon removal of the isomorphously substituted framework atoms.

**Table 4.2** EDX analysis for element quantification.

Sample	O (Wt. %)	Si (Wt. %)	Al (Wt. %)	Sn (wt. %)
Parent zeolite BEA	54.8	43.4	1.8	0
deSi, deAl-BEA	65.3	34.7	0	0
2Sn-h <sup>*</sup> -BEA	54.1	43.7	0	2.1
2Sn-BEA	55.5	42.5	0	2.0

EDX analysis condition: Uncoated samples using a Silicon detector and accelerating voltage of 25 kV.

Physical adsorption in micropores, such as those found in the zeolites in this study, occurs at relative pressures substantially lower than in case of adsorption in mesopores. Therefore, it is noted that adsorption measurements with N<sub>2</sub> at 77.4 K do not directly provide information on the microporosity of the samples. However, it remains an extremely useful methodology for gaining insight into the mesoporosity of the materials, which is clearly a key parameter for hierarchical materials. Type I isotherms, as observed for purely microporous zeolites, exhibit a large plateau region at relative pressures above values of approximately 0.1, whereas mesoporous materials, which display Type IV character, typically experience adsorption at intermediate relative values. Although missing the low relative pressure region (vide supra), the N<sub>2</sub> adsorption isotherm obtained for Al-BEA is clearly reminiscent of a Type I isotherm, and Type IV character is clearly gained following dealumination (deAl-BEA, open triangles), or more extensively by the [deSi, deAl] treatment (h<sup>\*</sup>-BEA, open circles). This clearly demonstrates the formation of mesopores, which is more readily visualised from the BJH data. In line with its microporous structure, no mesopores are evident in Al-BEA. For deAl-BEA and h<sup>\*</sup>-BEA, the presence of new mesopores with pore diameters of

approximately 7-8 nm are evident. These values are in excellent agreement to previous work with hierarchical zeolites.<sup>30</sup> The more extensive adsorption observed for h\*-BEA indicates that the extent of mesopores formation increases substantially with the added desilication step. It can also be observed that the dealumination step alone is able to introduce some minor mesoporosity, although to a substantially lower degree than desilication (Figure 4.3).

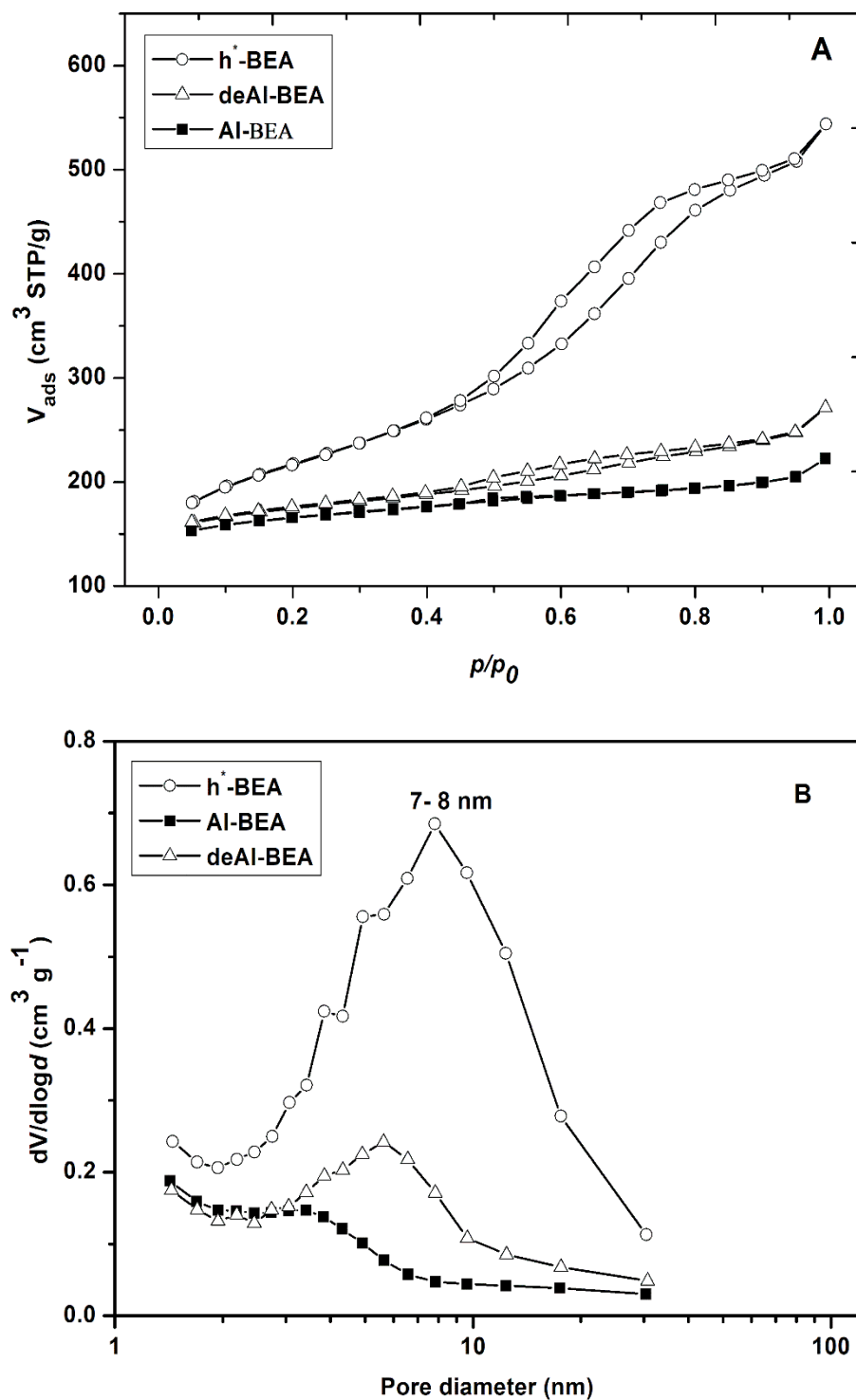


**Figure 4.3** A) Nitrogen adsorption-desorption isotherms, (B) pore size distribution of commercial zeolite BEA (black/squares), deAl-BEA (hollow/ tringles), and [deSi, deAl]-BEA (h\*-BEA) (hollow/circles).

Powder X-ray diffractions and surface area techniques clearly show the design and synthesis of the hierarchical materials upon alkaline and acid treatment of BEA zeolites.

The activity of both zeolite materials, *i.e.* 2Sn-h\*-BEA and 2Sn-BEA, were compared to an authentic sample of Sn-MCM-41, an amorphous but ordered, mesoporous Sn-containing silicate containing 2 wt% Sn. The textural characterisation of this material was investigated by N<sub>2</sub> adsorption/desorption isotherms (Figure 4.4). Sn-MCM-41 exhibited Type IV adsorption isotherms, typical of mesoporous MCM-41 materials, with a hysteresis loop in the  $P/P_0$  range of 0.4-0.5. The pore size distributions were calculated from the desorption branch of the isotherm using the Barrett-Joyner-Halenda (BJH) method. This materials were chosen in order to gain insight into and rationalise the effect of mesopores type and strength of acid sites.

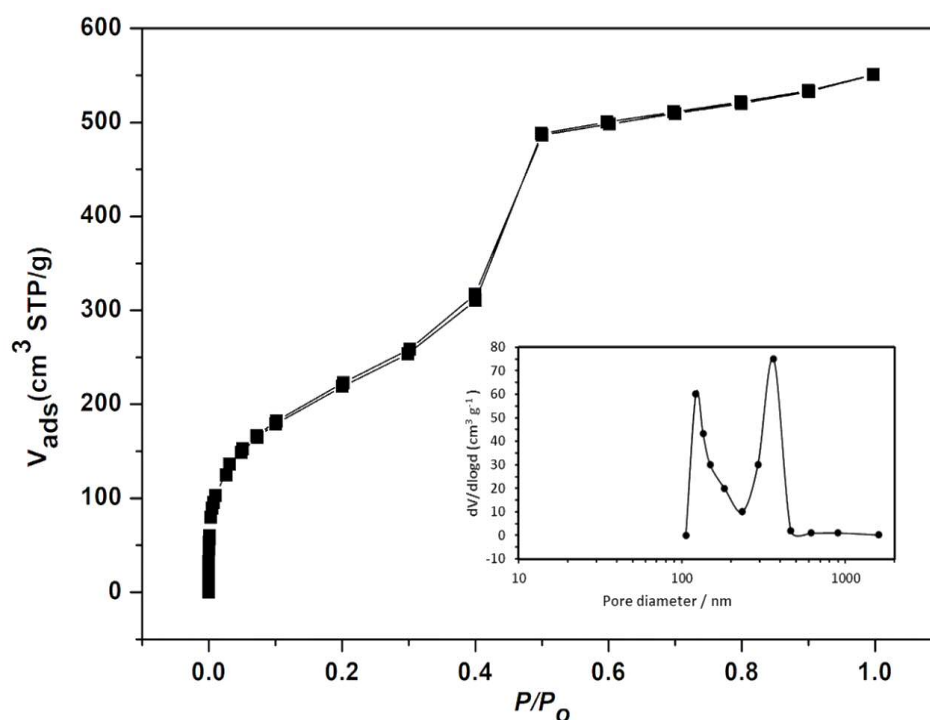


**Figure 4.4** N<sub>2</sub> adsorption/desorption isotherms for 2Sn-MCM-41, the isotherms were measured at 77 K. Insert: The pore size distribution curve for 2Sn-MCM-41.

Scanning Electron Microscopy analysis of the final catalysts, i.e. hierarchical and microporous Sn-BEA, demonstrated that neither the deAl protocol (in the case of the microporous Sn-BEA) nor the [deSi, deAl] protocol (as for the hierarchical material) overly modified the zeolite crystals (Figure 4.5 A-C). No significant changes in terms of crystal morphology or size are observed. Spherical crystals shape were maintained after the post-synthetic treatments. Although the samples experience some beam damage, preliminary TEM studies confirmed the absence of any major mesopores in deAl-BEA, and confirms the presence of mesopores (5-10 nm) in the h<sup>\*</sup>-BEA material. The absence of major bulk SnO<sub>2</sub> (vide infra) domains is also evident from this analysis. The SEM image for 2Sn-MCM-41 is shown in Figure (4.5 D).

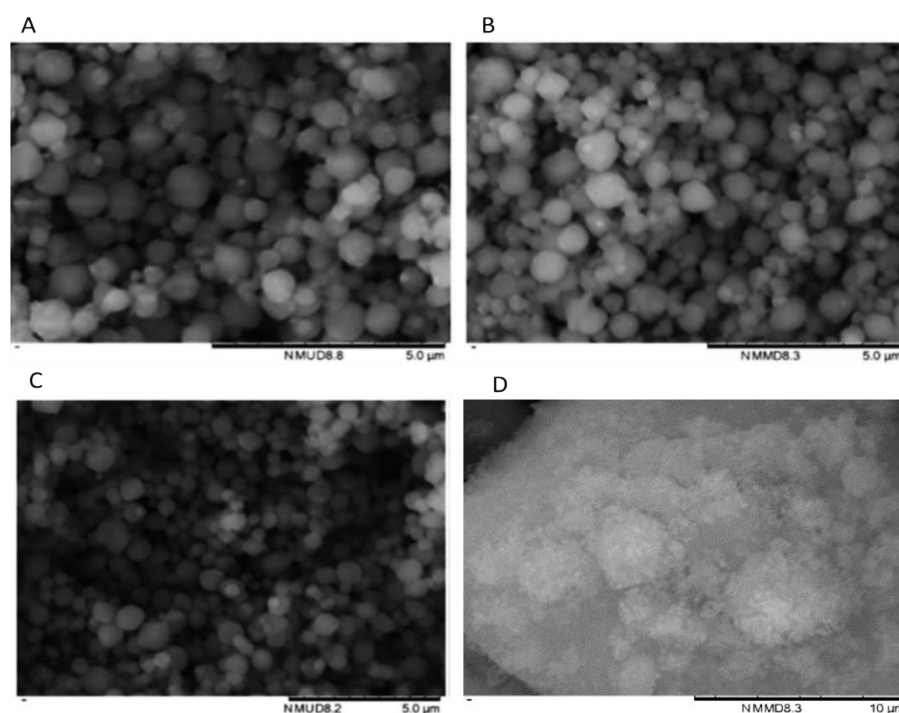


**Figure 4.5** SEM images of (A) commercial zeolite BEA, (B) 2Sn-BEA, (C) 2Sn-h<sup>\*</sup>-BEA, and (D) 2Sn-MCM-41.

Transmission electron microscopy (TEM) analysis of the dealuminated and hierarchical BEA zeolite samples (Figures 4.6 and 4.7 respectively). Figure 4.7 B shows resemble perforated crystals, indicating furthermore evidences a high

degree of mesoporosity in the alkaline treated sample, in agreement with the N<sub>2</sub> adsorption results. Since TEM does not supply information on the presence of Lewis acid site, more detailed assessment of Lewis acid species will be accomplished by DRIFT, MAS NMR and XPS spectroscopy.

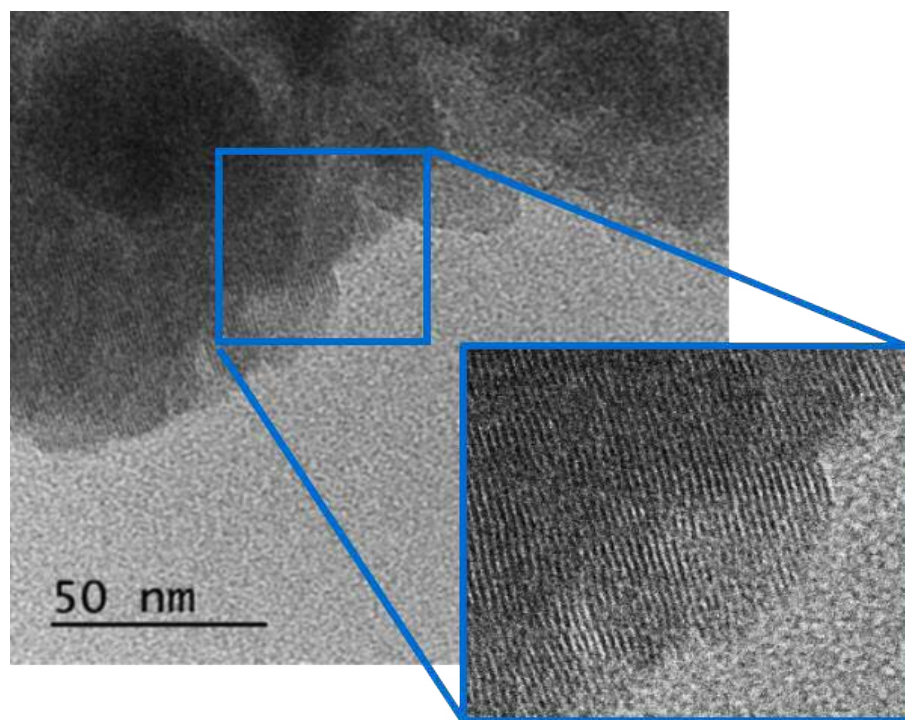


**Figure 4.6** TEM image of dealuminated zeolite BEA.

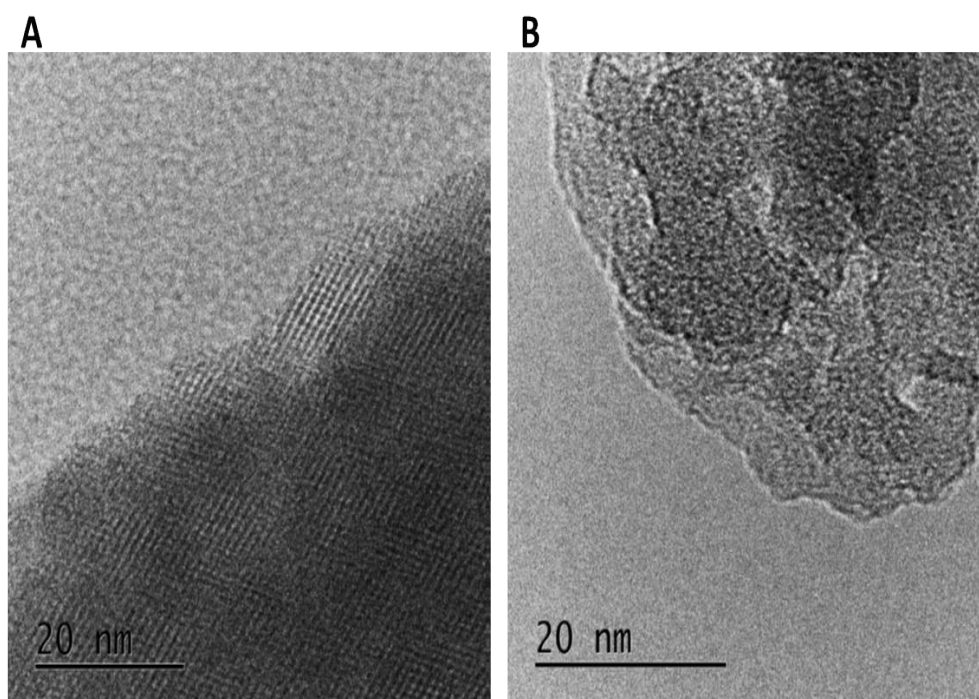


**Figure 4.7** TEM image of (A) deAl-BEA and (B) 2Sn-h<sup>\*</sup>-BEA.

#### 4.2.2 Preparation and characterisation of 2Sn-h<sup>\*</sup>BEA, following solid state stannation.

Subsequently, the study focused upon the solid-state incorporation of Sn(IV) into the vacant tetrahedral framework sites of h<sup>\*</sup>-BEA, according to the solid-state stannation methodology described in Chapter 3. The preparation typically involves the dealumination of zeolite BEA with HNO<sub>3</sub>, prior to remetallation with Sn. In this case, the typical solid-state stannation procedure was preceded by the desilication step (Figure 4.1). In contrast to approaches whereby pre-synthesised stannosilicates are converted into hierarchical matrices, incorporating Sn post-synthetically into a pre-modified hierarchical structure ensures the presence of accessible Sn(IV) sites in the mesopores, in line with the observations of Dapsens et al.<sup>37</sup>

Sn(IV) was introduced via a Sn(II) acetate precursor. In line with our recent work in Chapter 3, this chapter focused upon the preparation of materials with a high degree of site isolation, and consequently incorporated 2 wt% of Sn into the

material, as this is a loading which was shown to lead to the highest levels of intrinsic activity, i.e. TOF per Sn atom. The materials are henceforth denoted as 2Sn-BEA (microporous) and 2Sn-h\*-BEA (hierarchical). A multitude of spectroscopic techniques (XAS, MAS NMR, DRIFTS) were subsequently employed to verify the speciation of the incorporated Sn(IV) atoms, and to deduce whether Sn(IV) had incorporated into the vacant framework sites of h\*-BEA. A control sample of microporous 2Sn-BEA was also prepared, whereby 2 wt% Sn was incorporated into a dealuminated (but not desilicated) material. Chapter 3 has recently benchmarked the activity, selectivity and Sn site speciation of this control sample in depth.

In situ DRIFT spectroscopy with CD<sub>3</sub>CN probe was first used to verify the presence of Lewis acidic, framework Sn(IV) sites in both 2Sn-BEA and 2Sn-h\*-BEA. CD<sub>3</sub>CN is an extremely useful probe molecule for Lewis acidic zeolites since it can interact with the framework heteroatoms,<sup>42,43</sup> resulting in an acid-base adduct that displays an intense absorbance at 2311 cm<sup>-1</sup>. This particular feature is not observed for extra-framework Sn species nor SnO<sub>2</sub>, and its appearance can thus confirm the presence of framework Sn(IV) atoms. As can be seen (Figure 4.8 A), upon dosing 2Sn-h\*-BEA with CD<sub>3</sub>CN, two intense features are observed in the DRIFTS spectrum.<sup>44,45</sup> The first (2275 cm<sup>-1</sup>) arises from physisorbed CD<sub>3</sub>CN, which is readily desorbed from the sample upon heat treatment (see desorption profile temperature increasing from top (50 °C) to bottom (200 °C)). The second feature (2311 cm<sup>-1</sup>), arises from the CD<sub>3</sub>CN molecules interacting with framework Sn(IV) atoms, and clearly demonstrates the presence of isomorphously substituted Sn atoms in the hierarchical material, in excellent agreement to the prior chapter. The comparative spectra of purely microporous 2Sn-BEA are also displayed in Figure 4.8 B. The presence of Lewis acidic Sn heteroatoms is also evident in this material. Similar observations are found in the DRIFT spectra of CD<sub>3</sub>CN-dosed 2Sn-MCM-41 (Figure 4.8 C).

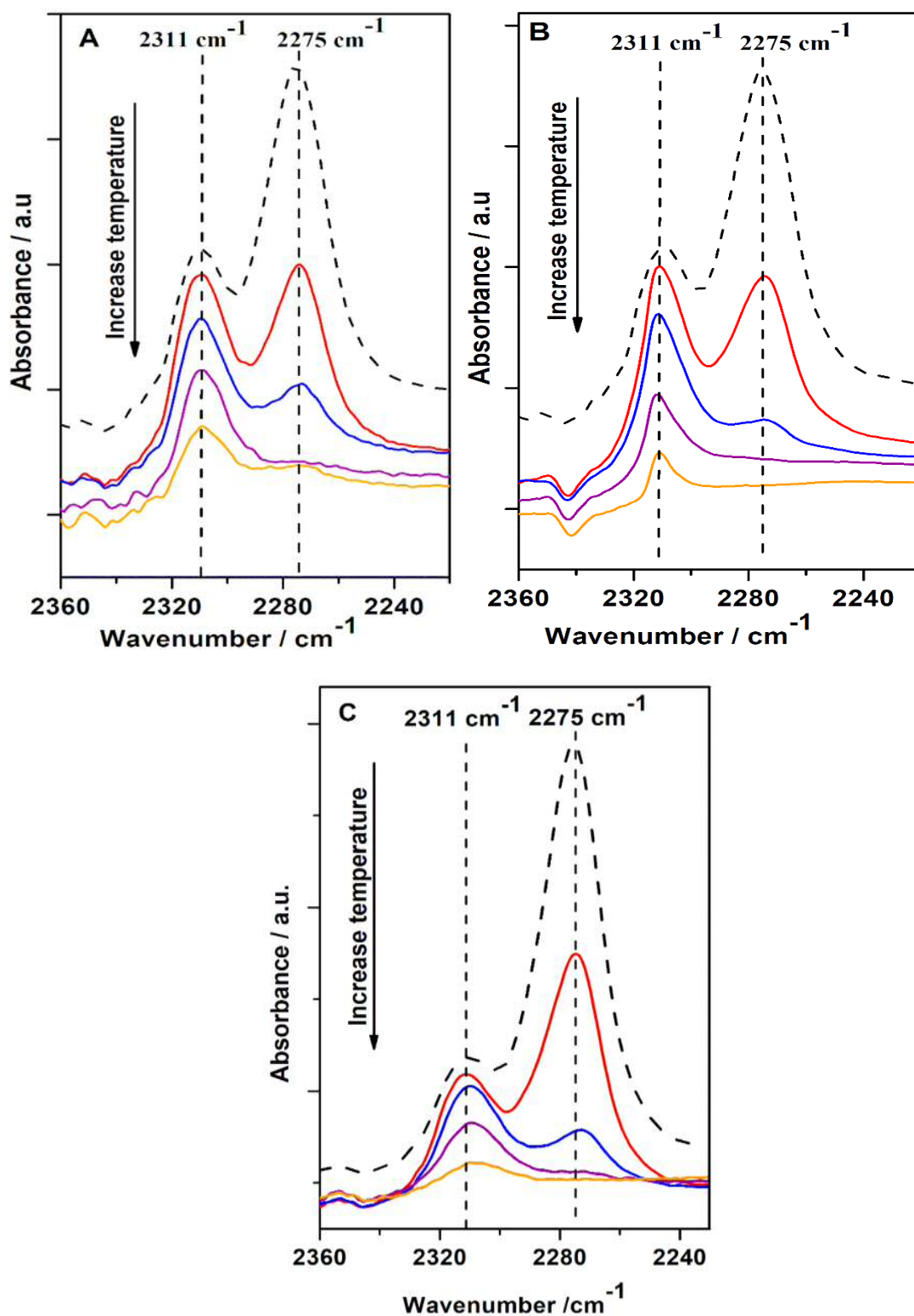


**Figure 4.8** In situ DRIFT spectra of (A) 2Sn-h\*-BEA, (B) 2Sn-BEA, and (C) 2Sn-MCM-41, following (dashed line) 10 minute treatment with CD<sub>3</sub>CN at room temperature. Various desorption temperatures (50 (red), 100 (blue), 150 (purple) and 200 (yellow) °C) from top to bottom are also displayed.

---

Although there are some minor differences in absorbance intensity and desorption rate for both of these samples, DRIFT spectroscopy is not sufficiently quantitative to differentiate between the total number of Lewis acidic (framework) and spectator sites (extra-framework) in each of these materials. Accordingly, attention was turned into spectroscopic techniques that provide more detailed insight of the Sn site speciation, , such as Magic Angle Spinning (MAS) NMR and X-ray Absorption Spectroscopy (XPS).

#### 4.2.3 Magic-Angle Spinning (MAS) NMR spectroscopy

Despite the low signal to noise (S/N) ratio due to the fact materials were prepared with naturally abundant  $^{119}\text{Sn}$ , the ambient temperature and pressure MAS NMR spectra of 2Sn-BEA and 2Sn-h\*-BEA primarily consists of an intense resonance at -688 ppm, which is indicative of framework Sn(IV) species in their hydrated state, in excellent agreement with the prior chapter (Figure 4.9). The absence of a substantial resonance at -602 ppm in the spectrum of 2Sn-BEA indicates that extra-framework Sn species are a very minor component of this catalytic material, in line with the detailed MAS NMR and XAFS studies of this material presented in Chapter 3. The presence of a shoulder at -602 ppm does, however, indicate that a minor quantity of extra-framework Sn is present in this material, both in line with chapter three, and that of Bare and co-workers focusing on conventional, i.e. hydrothermally prepared, Sn-BEA.<sup>46</sup>

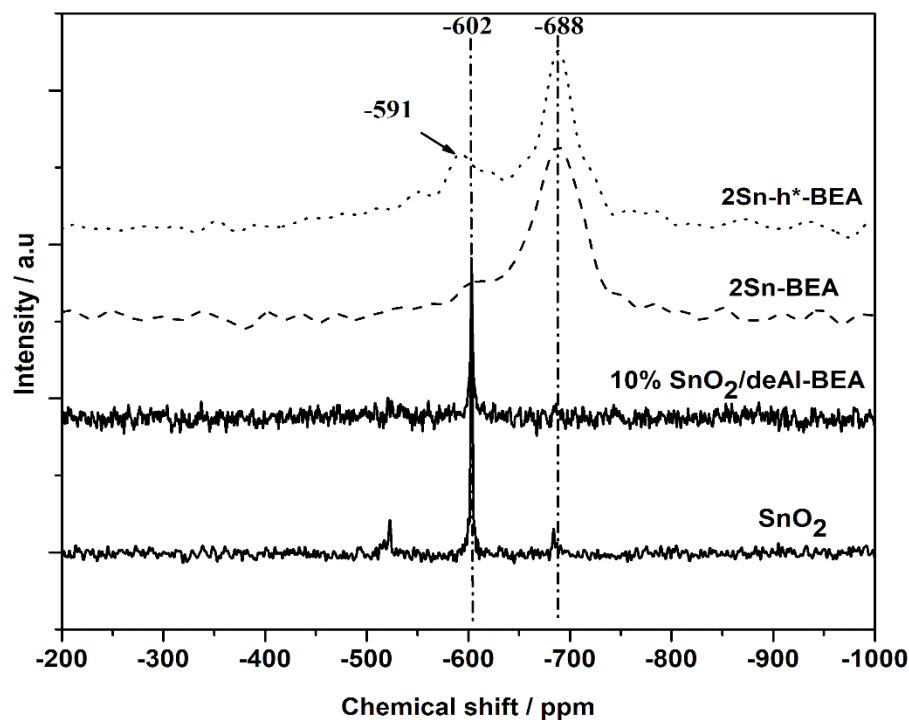


**Figure 4.9** MAS NMR spectra of SnO<sub>2</sub>, 10% SnO<sub>2</sub>/deAl-BEA (physical mixture), 2Sn-BEA and 2Sn-h\*-BEA from bottom to top.

In good agreement to the spectrum of 2Sn-BEA, the MAS NMR spectrum of 2Sn-h\*-BEA is also dominated by a resonance at -688 ppm, indicative of Sn being primarily present within the zeolite framework.<sup>47,13,48</sup> In contrast to the spectrum of 2Sn-BEA, however, at least one additional resonance at -591 ppm is present. The chemical shift of this resonance overlaps with the resonance observed for extra-framework Sn sites, such as SnO<sub>2</sub> (-602 ppm), but with a +11 ppm shift. This shift, coupled with the pronounced asymmetry of the resonance, causes some ambiguity as to whether this resonance is associated with a minor contribution of extra-framework Sn species, or isolated Sn sites present in a different geometrical position or hydrated state to those typically found in Sn-BEA. Given the XAS analysis (*vide infra*) and the observation that a dehydration/rehydration protocol did not affect the intensity or position of this resonance, it was tentatively attributed to extra-framework Sn sites in a slightly perturbed environment. Even so, the MAS NMR data obtained for the hierarchical material is in excellent agreement to that obtained for microporous Sn-BEA at

---

similar metal loadings, and indicates that Sn(IV) is primarily present in the zeolite framework.

#### 4.2.4 X-ray absorption spectroscopy

To verify the presence of extra-framework Sn species in these samples, it was also probed the Sn site speciation with X-ray Absorption Spectroscopy. Various elements of the EXAFS spectra of 2Sn-h\*-BEA and the conventional microporous analogue are shown in Figure 4.10 A and B. The spectra are of excellent quality up to a distance of  $14 \text{ \AA}^{-1}$ . The first feature present arises from Sn-O scattering interactions, whilst the second feature ( $2.5 - 4 \text{ \AA}$ ) arises from Sn-Sn scattering interactions, which are indicative of (i) extra-framework Sn atoms that are oligomeric or oxidic in nature, and/or (ii) Sn-Sn pairing.<sup>44</sup> It is clear from this analysis neither material possesses a substantial quantity of extra-framework Sn, given the relatively minor scattering intensity observed between  $2.5$  and  $4 \text{ \AA}$ , particularly when compared to a reference sample of SnO<sub>2</sub>. However, the intensity of the second shell region clearly differs between both the microporous and hierarchical analogues, with Sn-Sn scattering interactions clearly being more intense in the hierarchical material. It was concluded that this confirms the presence of an extra-framework Sn component in the hierarchical matrix, suggesting that the modified porosity following the generation of mesopores leads to a very slight increase in difficulty for incorporating Sn into the framework successfully. This is in full agreement to the MAS NMR analysis of 2Sn-BEA and 2Sn-h\*-BEA.

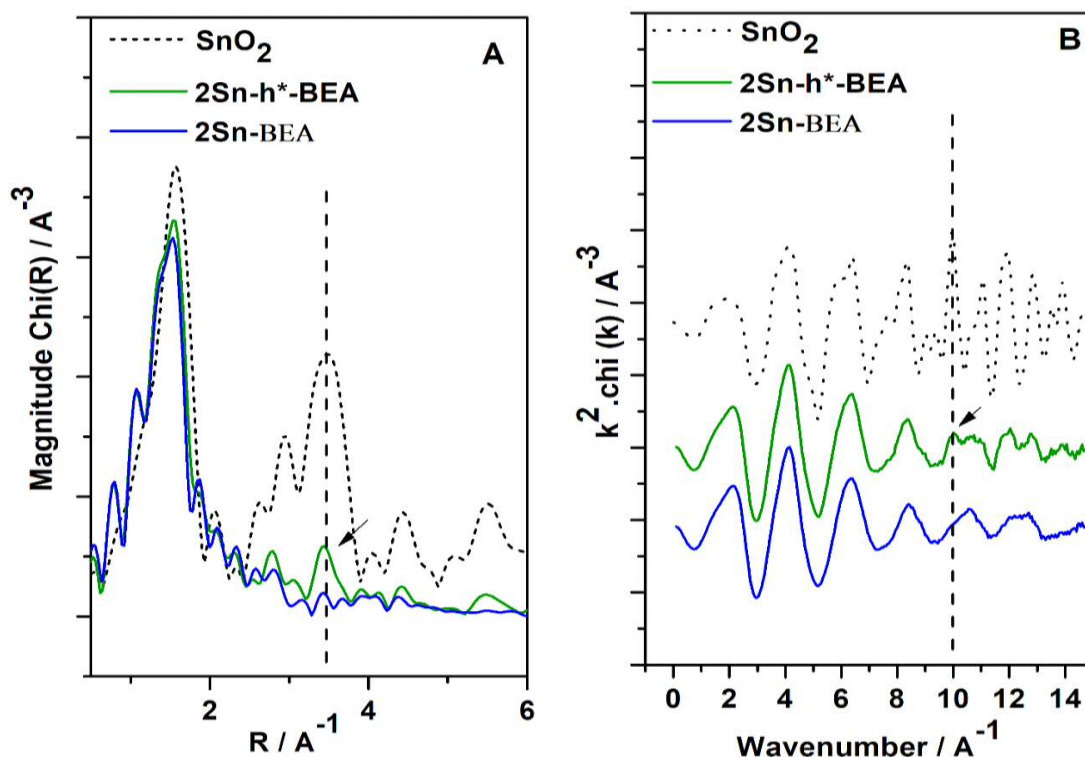


**Figure 4.10** (A) Magnitude of the Fourier transform spectra, and (B) EXAFS  $k^3$ -weighted  $\chi$  data, of 2Sn-BEA, (blue) and 2Sn-h\*-BEA (green). The corresponding spectra of SnO<sub>2</sub> (black dots) are also displayed.

In summary, the spectroscopic study undertaken indicates that Sn(IV) is almost exclusively incorporated into the vacant framework sites of h\*-BEA, although a non-negligible fraction of extra-framework Sn species appear to be present at very low concentrations. The fraction of extra-framework Sn appears to be somewhat larger in the hierarchical Sn-BEA than for purely microporous Sn-BEA, that the modified hierarchical topology has some impact on the solid-state stannation step. Nevertheless, the relatively low quantity of extra-framework Sn observed in both materials, as observed spectroscopically and through TEM analysis (Figure 4.7 B), agrees both with our previous studies,<sup>11</sup> and those published for conventional Sn-BEA, and provides two suitable materials from which the benefit(s) of a hierarchical topology may be studied.

### 4.2.5 Catalytic tests

To probe the catalytic properties of the hierarchical stannosilicates, particularly in reference to purely microporous Sn-BEA, the study focused upon the Meerwein-Ponndorf-Verley (MPV) transfer hydrogenation of various cyclic ketones to alcohols. This probe reaction was chosen for two main reasons; (i) it was shown in Chapter 3 to be an excellent model reaction for Sn-BEA catalysis, matching the TOF trends observed for other Sn-BEA catalysed reaction, such as the isomerisation of glucose to fructose,<sup>11</sup> (ii) in contrast to several other Sn-BEA catalysed reactions (e.g. glucose-fructose isomerisation, BVO), the MPV process is an intermolecular reaction, which requires coordination of both the ketone substrate and the alcohol solvent. It is, therefore, a very sterically challenging reaction, and provides an excellent case study for the hierarchical materials.

To fully evaluate the performance of 2Sn-h\*-BEA and 2Sn-BEA, and to determine the positive (or negative) impact of the hierarchical matrix, the MPV transfer hydrogenation of various cyclic ketones, containing between 6 and 12 carbon atoms (i.e. cyclohexanone to cyclododecanone) was performed. To date, only C<sub>6</sub> substrates have been efficiently converted by MPV transfer hydrogenation under the mediation of purely microporous Sn-BEA, with diffusion limitations largely accounting for the poor activity observed for bulkier substrates. Indeed, whilst cyclohexanone (kinetic diameter, 6.0 Å, relative diameter 1.0) is on the borderline of being able to freely diffuse in the pores of zeolite BEA (free diffusion limit of a sphere, 5.95 Å),<sup>49</sup> cyclooctanone (relative diameter 1.1) and cyclododecanone (1.4) should be too large to freely diffuse through the micropores of zeolite BEA (geometry structures of C<sub>6</sub>-C<sub>8</sub> are shown in the (Appendix, Figure 7.18)), even before the need for solvent molecule coordination is considered (*vide supra*). The three substrates therefore provide a useful span of molecular sizes to truly evaluate the performance of the hierarchical material. The chapter first focused upon the MPV transfer hydrogenation of cyclohexanone (Figure 4.11), which can be effectively catalysed by purely microporous Sn-BEA. The initial reaction conditions chosen for this reaction were identical to those recently described in Chapter 3.

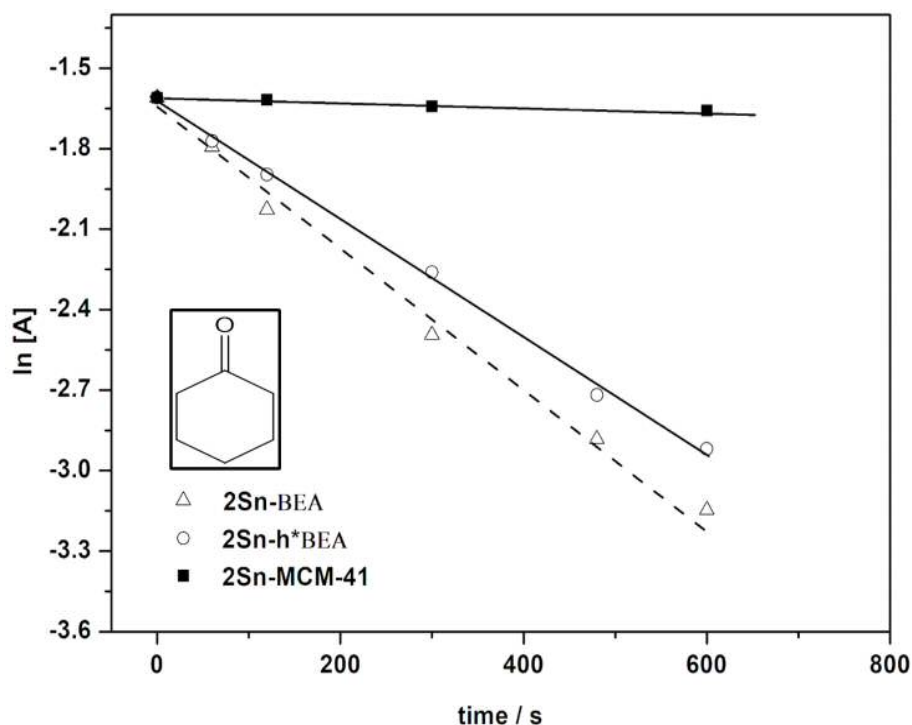


**Figure 4.11** Catalytic activity for 2Sn-BEA (open triangles), 2Sn-h\*-BEA (open circles) and 2Sn-MCM-41 (filled squares) for the MPV reduction of cyclohexanone.

Initial rate data was used to accurately compare the intrinsic activity of each catalytic material without excessive influence from (product induced) deactivation. Tests were performed at a CyO/Sn molar ratio of 100, consistent with experiments in chapter 3, and ensuring the reaction is in the kinetic regime (Figures 4.12) and (Appendix, 7.15).

Figure 4.11 shows that the pseudo-first order rate constants for the MPV transfer hydrogenation of cyclohexanone are extremely similar for both 2Sn-BEA ( $2.5 \times 10^{-3} \text{ s}^{-1}$ ) and 2Sn-h\*-BEA ( $2.2 \times 10^{-3} \text{ s}^{-1}$ ), although there is a minor decrease in activity for the hierarchical material. This minor decrease in activity was attributed to the presence of additional extra-framework Sn species in this material, which decreases the relative amount of active Sn per gram of catalyst. Nevertheless, the comparable catalytic rates obtained over these two materials indicates that (a) the generation of a hierarchical structure does not excessively impact the intrinsic activity of the isomorphously substituted Sn atoms within the matrix, a key result given the decreased intrinsic activity observed in other reports (*vide*

*supra*), and (b) that increased micropore accessibility is not essential for enhanced catalytic rates to be observed for C<sub>6</sub> substrates. This is in line with the previous observation that the C<sub>6</sub> reaction experiences no internal mass transfer limitations (Figure 4.12).

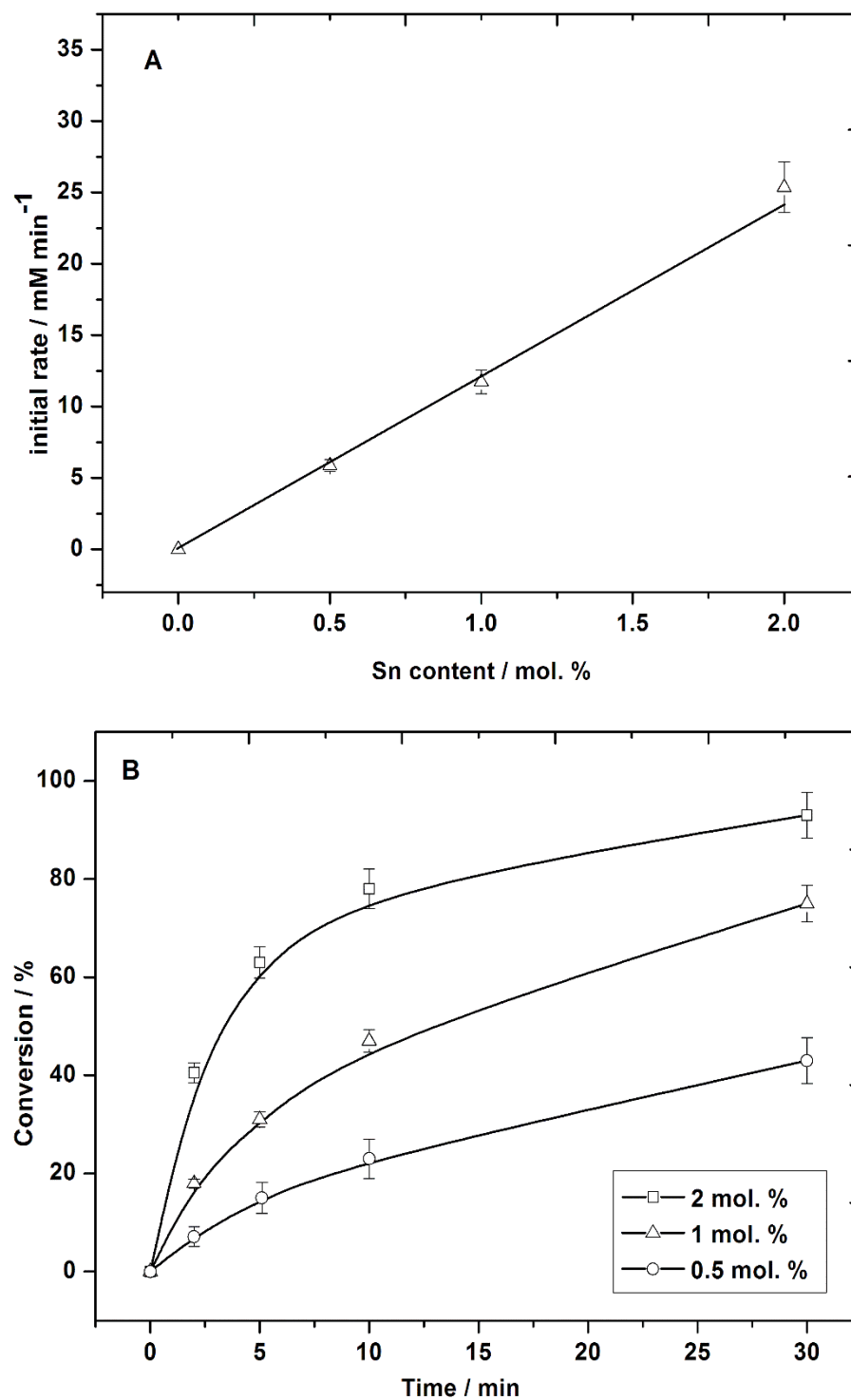


**Figure 4.12** Catalytic activity of 2Sn-BEA for the MPV hydrogenation of cyclohexanone as a function of catalyst loading. Sn content was varied by changing the mass of 2Sn-BEA present in the reactor. Both the initial rate data (A) and the time online analysis as a function of Sn content within the reactor (B) are presented.

However, as the size of the cyclic ring is increased beyond six carbon atoms, the significant advantages of the hierarchical BEA framework become apparent. For the MPV reduction of cyclooctanone (Figure 4.13), the hierarchical material is by far the most active catalyst, demonstrating a catalytic rate ( $1.4 \times 10^{-4} \text{ s}^{-1}$ ) over one order of magnitude greater than that observed over the conventional microporous analogue ( $1.6 \times 10^{-5} \text{ s}^{-1}$ ), and also the mesoporous material 2Sn-MCM-41 ( $1.2 \times 10^{-5} \text{ s}^{-1}$ ).

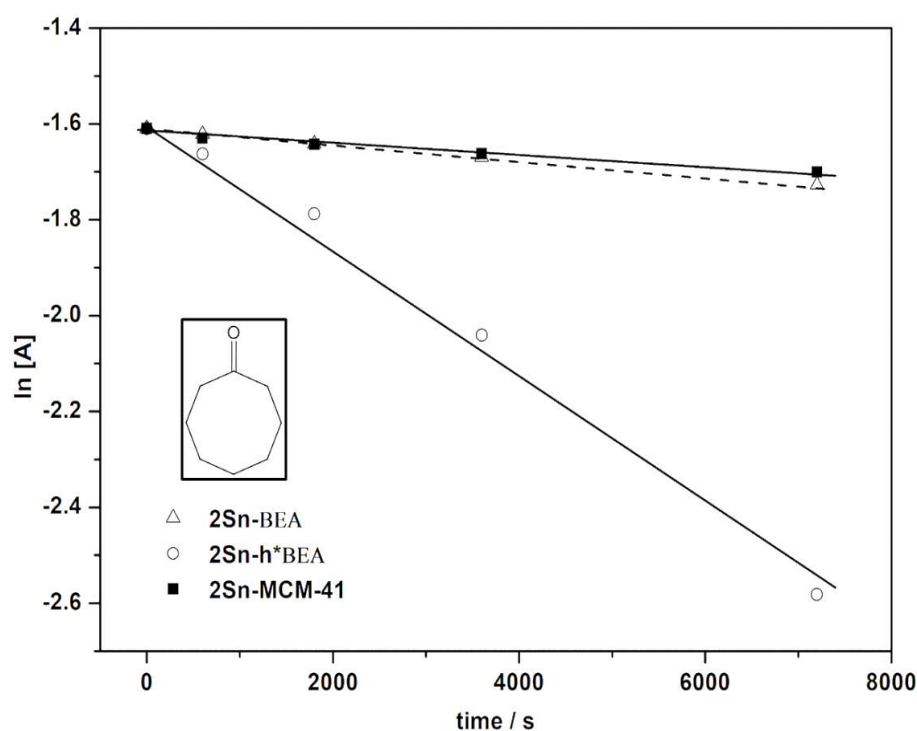


**Figure 4.13** Catalytic activity for 2Sn-BEA (open triangles), 2Sn-h\*BEA (open circles) and 2Sn-MCM-41 (filled squares) for the MPV reduction of cyclooctanone.

Increasing the carbon chain length of the ketone substrate is highly detrimental to catalysis in the microporous analogue, demonstrating that pore size limitations are a major disadvantage of the conventional BEA framework structure when bulkier substrates are undergoing study. To further evaluate the performance of these three materials, the study also examined the comparative performance of each catalyst as a function of conversion and selectivity against time. The

superior performance of the hierarchical analogue for the larger substrate is clearly evident, particularly at extended reaction times (Table 4.3). In line with Chapter 3, neither deAl-BEA, nor SnO<sub>2</sub> dispersed upon deAl-BEA behave as suitable catalysts for these reactions.

**Table 4.3** Catalytic performances of microporous and hierarchical Sn-BEA, and Sn-MCM-41, for the MPV hydrogenation of cyclohexanone and cyclooctanone

Catalyst	Cyclohexanone converted (cyclohexanol selectivity) <sup>a</sup>	Cyclooctanone converted (cyclooctanol selectivity) <sup>b</sup>
2Sn-BEA	97.5 (>95)	17.9 (90)
2Sn-h*-BEA	93.9 (>95)	83.4 (94)
2S-MCM-41	8.2 (49)	12.5 (45)
deAl-BEA	0.8 (26)	1.1 (29)
2SnO <sub>2</sub> /deAl-BEA	1.2 (10)	1.0 (24)

<sup>a</sup> Reaction conditions: cyclohexanone (0.2 M) in 2-butanol, 10 mL; 100°C; 1.0 mol% Sn relative to CyO; 750 rpm; 30 minutes. <sup>b</sup> Reaction conditions: cyclooctanone (0.2 M) in 2-butanol, 10 mL; 100°C; 1.0 mol% Sn relative to cyclooctanone; 750 rpm; 240 minutes.

To further probe this, the study also explored the MPV reduction of cyclododecanone (Figure 4.14). In this case, the catalytic rate of 2Sn-h\*-BEA ( $1.0 \times 10^{-4} \text{ s}^{-1}$ ) is again over one order of magnitude greater than that observed over the microporous material ( $8.5 \times 10^{-6} \text{ s}^{-1}$ ) and 2Sn-MCM-41 ( $6.9 \times 10^{-6} \text{ s}^{-1}$ ). To the best of our knowledge, this is the first time that an efficient heterogeneous catalyst for the catalytic valorisation of cyclododecanone in the liquid phase has been reported, a key result given that this substrate is a precursor to lauro lactam and hence, polyamide 12. This clearly demonstrates that the presence of a hierarchical structure significantly improves the general applicability of Sn-BEA, is extremely beneficial to Sn-mediated catalysis in general.

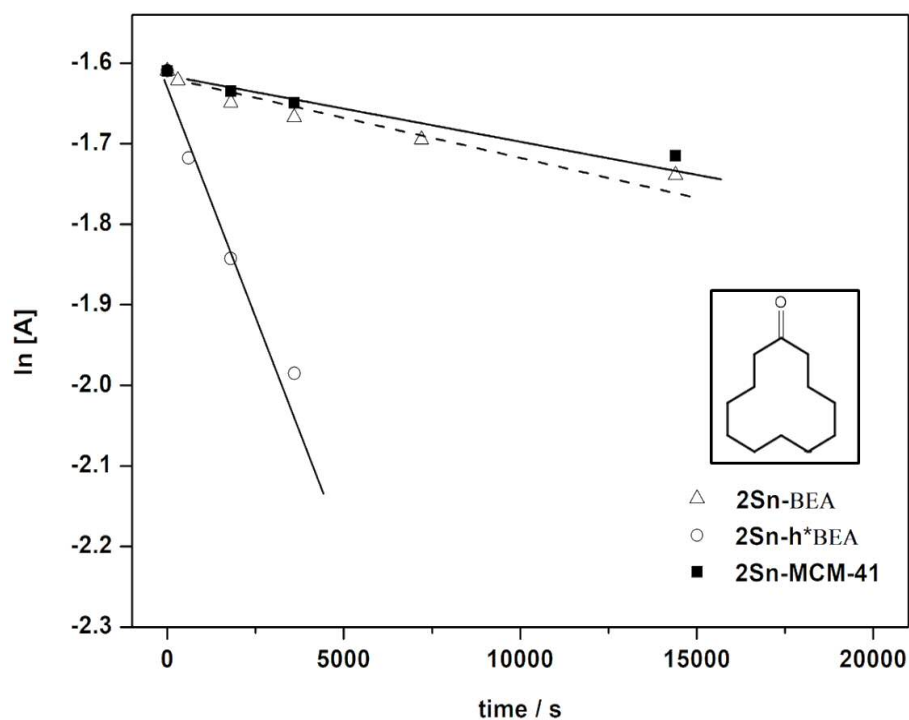


**Figure 4.14** Initial rate data for 2Sn-BEA (open triangles), 2Sn-h\*-BEA (open circles) and 2Sn-MCM-41 (filled squares) for the MPV reduction of cyclododecanone.

In all cases, the ordered mesoporous analogue, Sn-MCM-41, is the least active catalyst for these catalytic transformations, although its performance relative to microporous Sn-BEA improves substantially as the carbon chain length is increased. This lower activity of 2Sn-MCM-41 relative to the hierarchical material is likely due to the lower levels of Lewis acidity exhibited by heteroatoms when buried in the amorphous walls. It is noted that for both zeolitic materials, the selectivity to the primary MPV product (alcohol) remains largely constant at above 90% regardless of the size of the substrate. However, the selectivity observed for 2Sn-MCM-41 is substantially lower, typically <50%, thus indicating the further favourability of the hierarchical material over the purely mesoporous analogue. At this time, the study also draws attention to surprising activity exhibited by microporous Sn-BEA for the transfer hydrogenation of cyclododecanone (Figure 4.15). The conversion of this bulky substrate by this microporous material indicates that a certain fraction of Sn-BEA catalysis must occur on the external

surface of the material, potentially as a consequence of external enrichment of the zeolite crystals, which is known to occur for these materials.<sup>50</sup>

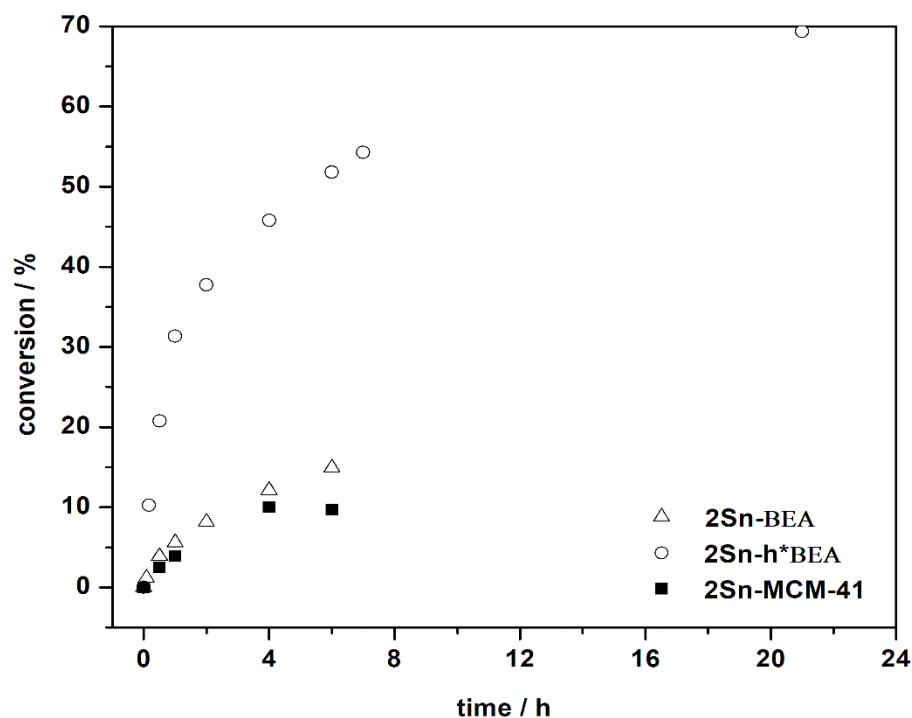


**Figure 4.15** Catalytic activity for 2Sn-BEA (open triangles), 2Sn-h\*-BEA (open circles) and 2Sn-MCM-41 (filled squares) for the MPV reduction of cyclododecanone as a function with time.

#### 4.2.6 Deactivation studies

Operational lifetime is a critical, but often overlooked, key performance indicator for a heterogeneous catalyst.<sup>51</sup> Due to their microporous structure, zeolites, such as Sn-BEA are particularly prone to some deactivation events, such as fouling, which can significantly impact their commercial feasibility. As it was recently demonstrated, Sn-BEA possesses high levels of stability during Lewis acid catalysis (MPV transfer hydrogenation), but steadily deactivates over the course of steady state operation. The spectroscopic and kinetic analysis revealed that product absorption and coking were largely responsible for this slow but steady decrease in catalytic activity, causing fouling i.e. blocking, of the micropores.<sup>16</sup> At

this stage, it was hypothesised that the improved diffusional properties of the hierarchical matrix would not only allow the study of new reactions with bulky substrates, but may also lead to decreased rates of deactivation through fouling. Consequently, the study examined the steady state activity of both 2Sn-h\*-BEA and 2Sn-BEA for the MPV transfer hydrogenation of cyclohexanone in continuous flow.

Continuous Plug Flow Reactors (PFR) (Figure 1.16) offer major advantages over slurry reactors, including (1) improved safety and process control,<sup>52</sup> (2) higher levels of mass- and heat-transfer, (3) improved rates of reaction, (4) smaller reactor volumes, and (5) scalability. In addition, by operating under steady state conditions they allow detailed evaluation of catalyst stability.<sup>53-55</sup> The performance of these catalysts, are compared in terms of activity (TOF, equation 4.1), stability (relative performance, equation 4.2).<sup>53</sup> It is noted here that the contact time ( , equation 4.3) in the first two reactions was adjusted so that both catalysts exhibited a similar level of substrate conversion. Moreover, experiments were performed at flow rates at, or above, those consistent with a kinetic regime, where external mass transfer limitations were absent (Appendix, Figure 7.19).

$$\text{TOF} = \frac{\text{moles}_{(\text{CyO converted})}}{\text{mol}_{(\text{Sn})} \text{min}^{-1}} \quad 4.1$$

$$\text{Relative performance} = \frac{\text{TOF}_{\text{h*}}}{\text{TOF}_{\text{BEA}}} \quad 4.2$$

$$\text{Contact time} = \frac{V_{\text{reactor}}}{F} \quad 4.3$$

Figure 4.16 demonstrates the steady state activity of 2Sn-h\*-BEA and 2Sn-BEA for the MPV transfer hydrogenation of cyclohexanone over a 700 h period. The contact time for each catalyst was optimised so that similar levels of conversion (80% for 2Sn-h\*-BEA and 92% for 2Sn-BEA) were achieved, in order to allow accurate comparison of lifetime. As can be seen, the hierarchical analogue possess substantially improved lifetime compared to the microporous analogue. Whereas the conversion obtained over 2Sn-BEA decreases from 92% to 33%

over a 200 h period, 2Sn-h\*-BEA retains over 80% of its original activity over 420 h on stream. With a single regeneration procedure under the conditions employed during the final calcination step (3 h, 550 °C, 60 mL min<sup>-1</sup> air), 2Sn-h\*-BEA is able to catalyse the MPV reaction at >80% of its initial activity for over 700 h on stream, a remarkable improvement in long-term stability. Although periodic regeneration can also restore activity of 2Sn-BEA, increasing the time between essential regenerations provides added benefits for both reactor design and process economics. It was noted here that both the selectivity to CyOH and the carbon balance remained >95% throughout for both catalysts during steady state operation.

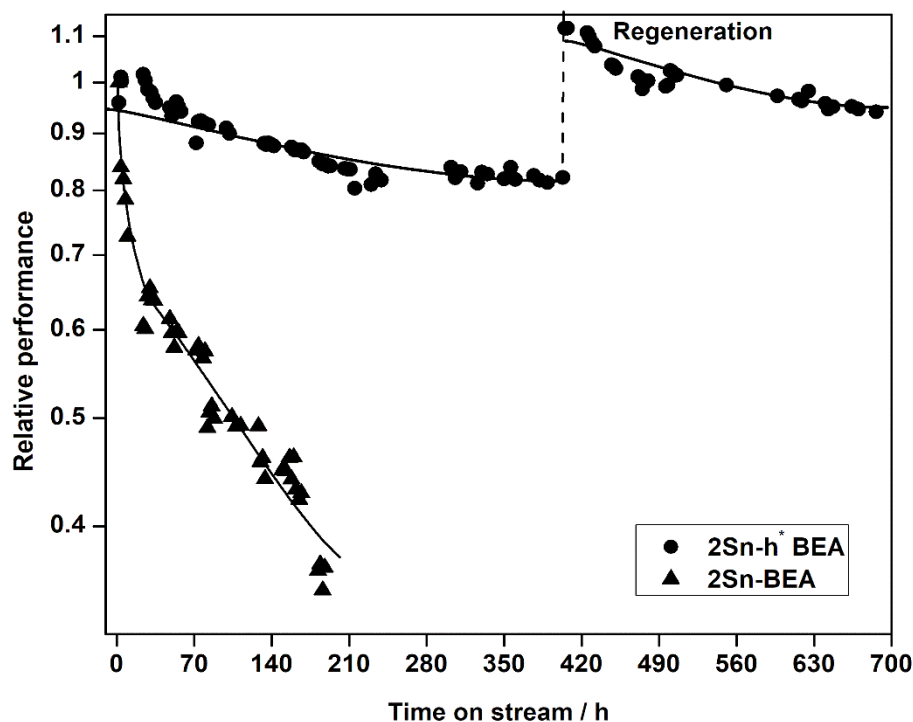


**Figure 4.16** Catalytic activity for 2Sn-BEA and 2Sn-h\*-BEA for the MPV reduction of cyclohexanone in the continuous regime.

The activity of the catalyst decreases as the catalyst is used. Sometimes this drop is rapid; sometimes it is slow. The kinetic of the 2Sn-BEA and 2Sn-h\*-BEA deactivation is analysed using Krishnaswamy and Kittrell equation (4.6)<sup>56,57</sup>,

which describes the variation of conversion with time for a first order reaction in an isothermal plug flow reactor.

$$\ln(\ln(1/(1-X))) = \ln(k' T') - k_d t \quad 4.6$$

Where  $X$  = conversion,  $k'$  = reaction rate constant,  $T'$  = reactor performance,  $k_d$  = rate constant for the deactivation of catalyst and  $t$  = time (s).

$k_d$  is the so-called deactivation constant, which determines the rate of deactivation,  $k_d$  can be obtained from the slop of the plot of  $\ln(\ln(1/(1-X)))$  versus time.

The deactivation profiles for conventional and hierarchical zeolites with time of operation presented in Figure 4.17. The deactivation rate of micropore 2Sn-BEA ( $k_d = 0.026 \text{ hr}^{-1}$ ) is more than hierarchical 2Sn-h\*-BEA ( $k_d = 0.011 \text{ hr}^{-1}$ ), which is mostly related to significant deactivation of the catalyst. This deactivation is usually reported to the fouling, which becomes more harmful when the physical transport of cyclohexanone is bad due to, for instance, longer micropore diffusion path lengths or narrow pores. Interestingly, the hierarchical catalyst showed a lower deactivation ( $k_d = 0.0014 \text{ hr}^{-1}$ ) even after 200 h compared to micropore catalyst ( $k_d = 0.0114 \text{ hr}^{-1}$ ). The suppressed deactivation can be attributed to the enhanced physical transport of cyclohexanone and cyclohexanol in the shortened micropores of the hierarchical catalyst. The intracrystalline mesopores assist access of cyclohexanone to the intrapore active sites, thus forwarding more efficient utilize of the catalyst volume.

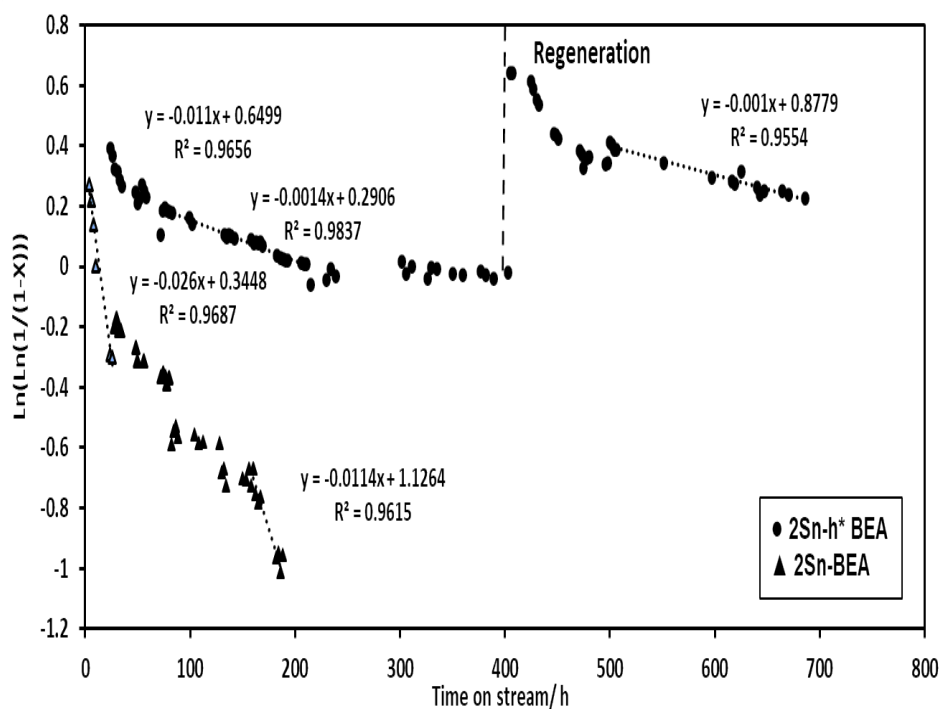


**Figure 4.17** Plot  $\text{Ln}(\text{Ln}(1/(1-X)))$  versus time on stream of 2Sn-BEA and 2Sn-h\*-BEA for the MPV reduction of cyclohexanone in the continuous regime.

### 4.3 Conclusions

Lewis acidic zeolites have rapidly emerged as unique heterogeneous catalysts for a range of sustainable liquid phase, catalytic applications. However their microporous structure means that they lack general applicability (typically they may only be used for reactions involving small to medium sized substrates), and makes them particularly prone to deactivation through fouling. This chapter shows that hierarchically porous BEA stannosilicates are able to mediate the catalytic conversion of bulky ketone substrates that purely microporous analogues are unable to catalyse. Deactivation studies in the continuous regime also demonstrate the exceptional stability of hierarchical Sn-BEA compared to purely microporous Sn-BEA, with limited (<20%) activity loss observed over 700 h on stream. In contrast, microporous Sn-BEA lost  $\pm 70\%$  activity in only 200 h on stream. To the best of our knowledge, this is the first time a stannosilicate with a hierarchical BEA topology has been prepared, the first evidence of condensed

phase cyclododecanone valorisation with stannosilicates, and the first full study of condensed phase deactivation kinetics for hierarchical zeolite materials.

Due to the increasing demand for energy and fine chemicals, more research efforts were conducted in the conversion of renewable resource into fuels and chemicals for a sustainable economy. Hence, the work of the next chapter focuses on the development of a Lewis acid heterogeneous catalysis to produce a renewable platform chemical as a useful biodiesel additive, mainly furanic ethers at high levels of activity, selectivity and stability. The work will build on our ability to functionalise zeolite frameworks with Lewis acid heteroatoms, as optimised in Chapter 3, and to probe the continuous performance of catalysts, as optimised in Chapter 4.

## 4.4 Experimental

### 4.4.1 Catalyst synthesis

#### 4.4.1.1 Synthesis 2Sn-h\*-BEA

Commercial zeolite Al-BEA (Zeolyst, NH<sub>4</sub>-form, SiO<sub>2</sub>/Al<sub>2</sub>O<sub>3</sub> = 38) was dealuminated by treatment in HNO<sub>3</sub> solution (13 M HNO<sub>3</sub>, 100 °C, 20 h, 20 mL g<sup>-1</sup> zeolite). The dealuminated powder was washed extensively with water (±500 mL g<sup>-1</sup> catalyst), and dried overnight at 110 °C. Desilicated-dealuminated zeolite BEA ([deSi, deAl]-BEA, referred to as h\*-BEA throughout the chapter) was prepared as follows: commercial Al-BEA zeolite (CP814E, NH<sub>4</sub>-form, SiO<sub>2</sub>/Al<sub>2</sub>O<sub>3</sub> = 38, Zeolyst International) was first converted into protonic form by calcination in static air at 550 °C (5 °C min<sup>-1</sup>) for 5 h. The H-form zeolite was subsequently suspended in an aqueous solution of NaOH (0.2 M, 318 k, 0.5 h, 30 mL g<sup>-1</sup> zeolite) to obtain a desilicated zeolite BEA (deSi-BEA). The reaction was stopped immediately by cooling the container in an ice bath. The remaining solid product was filtered, thoroughly washed with deionized water until neutral pH was attained, and finally dried at 373 k overnight. Subsequently, deSi-BEA was dealuminated following the same procedure described above. After filtering and

drying the sample, the sample was reconverted into  $\text{NH}_4$ -form *via* ion exchange in a solution of  $\text{NH}_4\text{NO}_3$  (1 M, 2 h, 85 °C, 30 mL solution per g (catalyst)).

Solid-state stannation of both dealuminated zeolite BEA (deAl-BEA) and [deSi,deAl]-BEA ( $h^*$ -BEA) was performed the procedure reported in ref. 11 and 52, by grinding the appropriate amount of Sn(II) acetate with the necessary amount of dealuminated or desilicated-dealuminated zeolite for 10 minutes in a pestle and mortar. Following this procedure, the sample was heated in a combustion furnace (Carbolite MTF12/38/400) to 550 °C (10 °C  $\text{min}^{-1}$ ) first in a flow of  $\text{N}_2$  (3h) and subsequently air (3h) for a total dwell time of 6 h. Gas flow rates of 60 mL  $\text{min}^{-1}$  were employed at all times.

#### 4.4.1.2 Synthesis 2Sn-MCM-41

An aqueous solution of hexadecyltrimethyl-ammonium bromide ( $\text{C}_{16}\text{TMABr}$ ), tetramethylammonium hydroxide solution (25%, Sigma-Aldrich) and Sn(IV) chloride pentahydrate were mixed under continuous stirring. After homogenisation, fumed silica was slowly added and the gel was further homogenised for 2 h. The final molar composition was  $1\text{SiO}_2$ :  $0.08\text{C}_{16}\text{TABr}$ :  $0.08\text{C}_4\text{TAOH}$ :  $0.26\text{TMAOH}$ :  $0.02\text{SnCl}_4$ :  $24.3\text{H}_2\text{O}$ . The homogeneous gel was transferred to a stainless steel autoclave (125 mL capacity) and crystallized at 135 °C for 24 h. The organic template was removed by heating at 540 °C for 1 h in  $\text{N}_2$  flow, followed by 6 h in air.

#### 4.4.2 Plug flow reactor conditions

Continuous reactions were performed in a plug flow, stainless steel, tubular reactor connected to an HPLC pump in order to regulate the reactant flow. The catalyst was mixed with a diluent material (SiC) to minimise backmixing and excessive pressure drop, and placed between two plugs of quartz wool. The diluted sample was densely packed into a  $\frac{1}{4}$  stainless steel tube (4.1 mm internal diameter), and a frit of 0.5  $\mu\text{m}$  was placed at the end of the catalytic bed in order to avoid any loss of materials. The reactor was subsequently immersed in a thermostatted oil bath at the desired reaction temperature. Pressure in the system

was controlled by means of a backpressure regulator, and the pressure drop was determined by comparison of the HPLC pump pressure to the outlet pressure measured by a pressure gauge. An overpressure of 5 bar was typically employed. Aliquots of the reaction solution were taken periodically from a sampling valve placed after the reactor column. Catalyst regeneration was performed heating the whole reactor in a combustion furnace (Carbolite MTF12/38/400) to 550 °C (10 °C min<sup>-1</sup>) in air (3h).

#### 4.4.3 Catalyst characterisation

A PANalytical X'PertPRO X-ray diffractometer was employed for powder XRD analysis. A Cu K $\alpha$  radiation source (40 kV and 40 mA) was utilised. Diffraction patterns were recorded between 5-55 °2 $\theta$  (step size 0.0167°, time/step = 150 s, total time = 1 h). Porosimetry measurements were performed on a Quantachrome Autosorb, and samples were degassed prior to use (277 °C, 6 h), Adsorption isotherms were obtained at 77 k and various analysis methods were employed (see Table 4.1). SEM Images of the catalysts were obtained using a Hitachi TM3030Plus, at 15 kV and at EDX observation conditions. The EDX tool was utilised to analyse the elemental composition and distribution. TEM images were obtained using JEOL JEM-1200EX at an operating voltage 200 kV. The samples were prepared by deposited a few droplets of zeolites suspension in high purity ethanol using ultra-sonication on a copper grid, followed by evaporation at room temperature. A Bruker Tensor spectrometer equipped with a Harrick praying mantis cell was utilised for DRIFT measurements. Spectra were recorded between 4000-650 cm<sup>-1</sup> at a resolution of 2 cm<sup>-1</sup>. CD<sub>3</sub>CN measurements were performed on pre-treated zeolite powders (550 °C, 1 h under flowing air, 60 mL min<sup>-1</sup>) according to the method described in ref. 10. MAS NMR experiments were performed at Durham University through the EPSRC UK National Solid-state NMR Service. Samples were measured under conditions identical to those reported by Bermejo-Deval et al.,<sup>47</sup> X-ray absorption spectroscopy measurements were performed on the B18 beamline at the Diamond Light Source. Spectra were recorded at the Sn K-edge in transmission mode. Sn k-

edge XAS data was collected by the methods described in detail elsewhere, those described in Chapter 3.

#### 4.4.4 Kinetic evaluation and analytical methods

MPV reactions with cyclohexanone were performed in a 100 mL round bottom flask equipped with a reflux condenser, which was thermostatically controlled by immersion in a silicon oil bath. The vessel was charged with a 10 mL solution of cyclohexanone in 2-butanol (0.2 M), which also contained an internal standard (biphenyl, 0.01 M), and was subsequently heated to the desired temperature (100 °C internal temperature). The reaction was initiated by addition of an appropriate amount of catalyst, corresponding to 1 mol% Sn relative to cyclohexanone. The solution was stirred at 800 rpm with an oval magnetic stirrer bar. MPV reactions with cyclooctanone were performed with the same methodology and conditions. MPV reactions with cyclododecanone were performed in a 15 mL thick walled glass reactor, which was thermostatically controlled by immersion in a silicon oil bath. The vessel was charged with a 5 mL solution of cyclododecanone in 2-butanol (0.2 M), which also contained an internal standard (biphenyl, 0.01 M). The appropriate amount of catalyst, corresponding to 2.5 mol% Sn relative to cyclododecanone, was also added. The reactor was subsequently heated to the desired temperature (130 °C internal temperature), and the reaction was initiated by stirring at  $\pm 750$  rpm with an oval magnetic stirrer bar. Aliquots of both reaction solutions were taken periodically for analysis, and were centrifuged prior to injection into a GC (Agilent 7820, 25m CP-Wax 52 CB). Reactants were quantified against a biphenyl internal standard.

---

## 4.5 References

- 1 Y. Roman-Leshkov and M. E. Davis, *ACS Catal.*, 2011, **1**, 1566.
- 2 P. Y. Dapsens, C. Mondelli, B. T. Kusema, R. Verel and J. Pérez-Ramírez, *Green Chem.*, 2014, **16**, 1176.
- 3 P. Y. Dapsens, C. Mondelli and J. Pérez-Ramírez, *Chem. Soc. Rev.*, 2015, **44**, 7025.
- 4 M. Moliner, *Dalt. Trans.*, 2014, **43**, 4197.
- 5 A. Corma, L. T. Nemeth, M. Renz and S. Valencia, *Nature*, 2001, **412**, 423.
- 6 C. Hammond, S. Conrad and I. Hermans, *Angew. Chemie - Int. Ed.*, 2012, **51**, 11736.
- 7 Z. Kang, X. Zhang, H. Liu, J. Qiu and K. L. Yeung, *Chem. Eng. J.*, 2013, **218**, 425.
- 8 A. Corma, M. E. Domine, L. Nemeth and S. Valencia, *J. Am. Chem. Soc.*, 2002, **124**, 3194.
- 9 A. Corma, M. E. Domine and S. Valencia, *J. Catal.*, 2003, **215**, 294.
- 10 P. Wolf, C. Hammond, S. Conrad and I. Hermans, *Dalton Trans.*, 2014, **43**, 4514.
- 11 C. Hammond, D. Padovan, A. Al-Nayili, P. P. Wells, E. K. Gibson and N. Dimitratos, *ChemCatChem*, 2015, **7**, 3322.
- 12 J. Dijkmans, D. Gabriels, M. Dusselier, F. de Clippel, P. Vanelderen, K. Houthoofd, A. Malfliet, Y. Pontikes and B. F. Sels, *Green Chem.*, 2013, **15**, 2777.
- 13 R. Bermejo-Deval, M. Orazov, R. Gounder, S. J. Hwang and M. E. Davis, *ACS Catal.*, 2014, **4**, 2288.
- 14 Y. Román-Leshkov, M. Moliner, J. A. Labinger and M. E. Davis, *Angew. Chemie - Int. Ed.*, 2010, **49**, 8954.
- 15 M. Moliner, Y. Román-Leshkov and M. E. Davis, *Proc. Natl. Acad. Sci.*,

- 2010, **107**, 6164.
- 16 D. Padovan, C. Parsons, M. Simplicio Grasina and C. Hammond, *Green Chem.*, 2016, **18**, 5041.
- 17 J. Jiang, J. Yu and A. Corma, *Angew. Chemie - Int. Ed.*, 2010, **49**, 3120.
- 18 C. C. Freyhardt, M. Tsapatsis, R. F. Lobo, K. J. Balkus and M. E. Davis, *Nature*, 1996, 381, 295.
- 19 A. Corma, M. J. Diaz-Cabanas, J. Martinez-Triguero, F. Rey and J. Rius, *Nature*, 2002, **418**, 514.
- 20 C. Perego and R. Millini, *Chem. Soc. Rev.*, 2013, **42**, 3956.
- 21 P. S. Niphadkar, A. C. Garade, R. K. Jha, C. V. Rode and P. N. Joshi, *Microporous Mesoporous Mater.*, 2010, **136**, 115.
- 22 L. Tosheva and V. P. Valtchev, *Chem. Mater.*, 2005, **17**, 2494.
- 23 M. Choi, K. Na, J. Kim, Y. Sakamoto, O. Terasaki and R. Ryoo, *Nature*, 2009, **461**, 246.
- 24 K. Na, C. Jo, J. Kim, K. Cho, J. Jung, Y. Seo, R. J. Messinger, B. F. Chmelka and R. Ryoo, *Science (80-. )*, 2011, **333**, 328.
- 25 A. Corma, V. Fornes, S. B. Pergher, T. L. M. Maesen and J. G. Buglass, *Nature*, 1998, **396**, 353.
- 26 L. Ren, Q. Guo, P. Kumar, M. Orazov, D. Xu, S. M. Alhassan, K. A. Mkhoyan, M. E. Davis and M. Tsapatsis, *Angew. Chemie - Int. Ed.*, 2015, **54**, 10848.
- 27 X. Ouyang, S. J. Hwang, D. Xie, T. Rea, S. I. Zones and A. Katz, *ACS Catal.*, 2015, **5**, 3108.
- 28 H. Y. Luo, L. Bui, W. R. Gunther, E. Min and Y. Román-Leshkov, *ACS Catal.*, 2012, **2**, 2695.
- 29 K. Li, J. Valla and J. Garcia-Martinez, *ChemCatChem*, 2014, **6**, 46.
- 30 J. Pérez-Ramírez, C. H. Christensen, K. Egeblad, C. H. Christensen and J. C. Groen, *Chem. Soc. Rev.*, 2008, **37**, 2530.

- 
- 31 M. Hartmann, *Angew. Chemie - Int. Ed.*, 2004, **43**, 5880.
- 32 M. S. Holm, E. Taarning, K. Egeblad and C. H. Christensen, *Catal. Today*, 2011, **168**, 3.
- 33 T. C. Keller, J. Arras, S. Wershofen and J. Perez-Ramirez, *ACS Catal.*, 2015, **5**, 734.
- 34 J. C. Groen, L. A. A. Peffer, J. A. Moulijn and J. Pérez-Ramírez, *Microporous Mesoporous Mater.*, 2004, **69**, 29.
- 35 M. S. Holm, M. K. Hansen and C. H. Christensen, *Eur. J. Inorg. Chem.*, 2009, 1194.
- 36 L. Sommer, D. Mores, S. Svelle, M. Stöcker, B. M. Weckhuysen and U. Olsbye, *Microporous Mesoporous Mater.*, 2010, **132**, 384.
- 37 P. Y. Dapsens, C. Mondelli, J. Jagielski, R. Hauert and J. Pérez-Ramírez, *Catal. Sci. Technol.*, 2014, **4**, 2302.
- 38 H. J. Cho, P. Dornath and W. Fan, *ACS Catal.*, 2014, **4**, 2029.
- 39 J. C. Groen, S. Abelló, L. A. Villaescusa and J. Pérez-Ramírez, *Microporous Mesoporous Mater.*, 2008, **114**, 93.
- 40 J. Jin, X. Ye, Y. Li, Y. Wang, L. Li, J. Gu, W. Zhao and J. Shi, *Dalton Trans.*, 2014, **43**, 8196.
- 41 J. C. Groen, L. A. A. Peffer, J. A. Moulijn and J. Pérez-Ramírez, *Chem. - Eur. J.*, 2005, **11**, 4983.
- 42 M. Boronat, P. Concepción, A. Corma, M. Renz and S. Valencia, *J. Catal.*, 2005, **234**, 111.
- 43 S. Roy, K. Bakhmutsky, E. Mahmoud, R. F. Lobo and R. J. Gorte, *ACS Catal.*, 2013, **3**, 573.
- 44 A. G. Pelmenschikov, R. A. Van Santen, J. Janchen and E. Meijer, *J. Phys. Chem.*, 1993, **97**, 11071.
- 45 J. Chen, J. M. Thomas and G. Sankar, *J. Chem. Soc., Faraday Trans.*, 1994, **90**, 3455.

- 
- 46 S. R. Bare, S. D. Kelly, W. Sinkler, J. J. Low, F. S. Modica, S. Valencia, A. Corma and T. L. and Nemeth, *J. Am. Chem. Soc.*, 2005, **127**, 12924.
- 47 R. Bermejo-Deval, R. Gounder and M. E. Davis, *ACS Catal.*, 2012, **2**, 2705.
- 48 W. R. Gunther, V. K. Michaelis, M. A. Caporini, R. G. Griffin and Y. Román-Leshkov, *J. Am. Chem. Soc.*, 2014, **136**, 6219.
- 49 C. Baerlocher and L. B. McCusker, *Database Zeolite Struct. 2015*, <http://www.iza-structure.org/databases>.
- 50 S. Tolborg, A. Katerinopoulou, D. D. Falcone, I. Sadaba, C. M. Osmundsen, R. J. Davis, E. Taarning, P. Fristrup and M. S. Holm, *J. Mater. Chem. A*, 2014, **2**, 20252.
- 51 I. Sádaba, M. L. Granados, A. Riisager and E. Taarning, *Green Chem.*, 2015, **17**, 4133.
- 52 C. Liebner, J. Fischer, S. Heinrich, T. Lange, H. Hieronymus and E. Klemm, *Process Saf. Environ. Prot.*, 2012, **90**, 77.
- 53 C. Hammond, *Green Chem.*, 2017, **19**, 2711.
- 54 G. M. Lari, P. Y. Dapsens, D. Scholz, S. Mitchell, C. Mondelli and J. Pérez-Ramírez, *Green Chem.*, 2016, **18**, 1249.
- 55 J. P. Lange, *Angew. Chemie - Int. Ed.*, 2015, **54**, 13187.
- 56 J. D. Lewis, S. Van De Vyver, A. J. Crisci, W. R. Gunther, V. K. Michaelis, R. G. Griffin and Y. Román-Leshkov, *ChemSusChem*, 2014, **7**, 2255.
- 57 O. Levenspiel, *Chemical Reaction Engineering*, John Wiley & Sons, Third Edit., 1999.

# 5

## Bifunctional Lewis and Brønsted acidic zeolites permit the continuous production of bio-renewable furanic ethers

### Abstract

The catalytic valorisation of bio-renewable feedstock often relies upon multi-stage processing of highly-functionalised substrates, resulting in selectivity and process engineering challenges, in addition to the requirement of multifunctional catalytic systems. Herein, this chapter demonstrates that a bifunctional zeolitic material, containing both Lewis and Brønsted acid sites in a single catalytic material, permits the continuous production of bio-renewable furanic ethers, such as (butoxy)methyl furan, which possess potential as fuel additives. In contrast to mono-functional catalysts and physical mixtures thereof, the bifunctional Sn- and Al-containing BEA zeolite results in uniquely-high levels of activity, selectivity and stability. Optimal results were obtained over a bifunctional catalyst containing 2 wt% Sn and 0.5 wt% Al, prepared by modified solid state incorporation, which was highly selective (>75%) to the desired ether for over 100 h on stream, and for over 3000 substrate turnovers.

---

This work contributed to the following papers:

D. Padovan, A. Al-Nayili and C. Hammond, *Green Chemistry*, 2017, 19, 2846.

## 5.1 Introduction

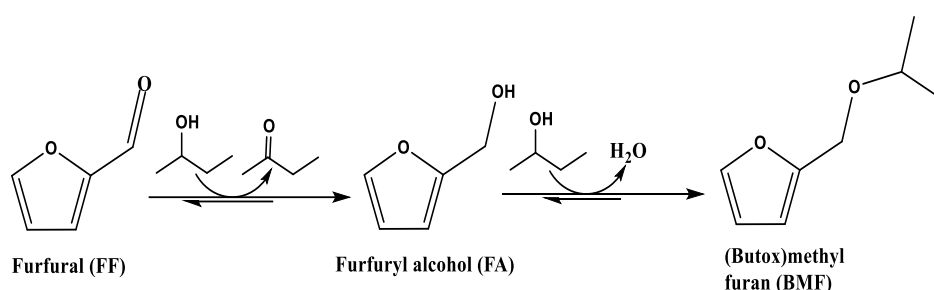
The depletion of fossil feedstock, coupled with the need for more environmentally sustainable chemical processing, drives the contemporary chemical community towards the sustainable utilisation of, preferably, renewable raw materials. The quest to employ such resources also relates to increasing population growth and to climate change. Lignocellulose, a complex mixture of lignin, cellulose and hemicellulose, is the most abundant bio-renewable feedstock inedible to humans. Consequently, the valorisation of lignocellulose, or derivatives thereof, represents a key target of contemporary research. Amongst several methods of lignocellulose valorisation, catalytic methods employing heterogeneous materials offer greatest potential.<sup>1–5</sup>

Unfortunately, the chemical nature of lignocellulose and its derivatives differs greatly from traditional petrochemical feedstock. Lignocellulose-derived feedstock is highly functionalised, typically highly oxygenated, and exhibits poor levels of volatility and thermal stability. Consequently, traditional heterogeneous catalytic methodologies are unsuitable for its valorisation.<sup>6</sup> Accordingly, the development of more sustainable chemical processes requires the co-development of new catalytic methods and materials.

An emerging approach undergoing an intensive period of research involves the liquid-phase valorisation of so-called platform molecules, obtained through controlled depolymerisation and separation of lignocellulose and its key building blocks through e.g. hydrolysis.<sup>7</sup> Amongst such feedstock, the catalytic valorisation of C<sub>5</sub>- and C<sub>6</sub>- based furanics, such as 5-hydroxymethyl furfural (HMF) and furfural (FF), has received widespread attention.<sup>8–10</sup> Indeed, the catalytic conversion of furfural can produce a variety of useful products, and furfuryl alcohol and its ethers are intermediates for the synthesis of  $\gamma$ -valerolactone (GVL), and its ethers also possess particular promise as fuel additives.<sup>11–13</sup> Although a wide range of materials, conditions and approaches have been explored for furfural valorisation, few works have truly demonstrated high levels of selectivity and stability. In fact, obtaining high selectivity to a single product is a major challenge during all biomass-to-chemicals research, given the

highly functionalised nature of the reactive substrates. Although terms, such as “useful product selectivity” are now routinely employed, the cost of separation in catalytic processes is sufficient that high selectivity to a single product must be attained. Moreover, catalyst stability under rigorous, continuous conditions also requires significant attention.

Ethers of furfural and its derivatives (Scheme 5.1) hold particular promise as fuel additives.<sup>11</sup> Whilst ethers are typically obtained through Brønsted acid catalysis, recent studies have indicated that Lewis acid-only systems may show good levels of activity and selectivity for such processes, with Lewis acidic silicates, such as Sn- and Hf-containing zeolite BEA, showing significant potential.<sup>14–17</sup>



**Scheme 5.1** Catalytic formation of furanic ethers from furfural.

However, little is known about how Lewis acids catalyse such reactions, or what role adventitious Brønsted acidity possible exhibits. Moreover, although catalyst stability has been probed, high selectivity to ethers of furfural and 5-HMF has only been observed at relatively low turnover numbers (<250 turnovers), and the intermediate alcohol species are typically observed as major products after a particular period of operation.<sup>16</sup> Given their notorious ability to polymerise and subsequently deactivate heterogeneous catalysts, the generation of such alcohols at high selectivity is far from desirable. Moreover, up to 35% loss in conversion over the same number of turnovers was also observed in previous studies.<sup>16</sup> Motivated by these observations, the major target of this work is to develop a catalytic system capable of selectively producing furanic ethers at high levels of selectivity, activity and stability, whilst exploring the potential of bifunctional Lewis and Brønsted acidic zeolites.

---

In this chapter, the dealumination protocol employed in Chapter 3 for SSI, was optimized, by varying the time and hence extent, of dealumination to leave some residual Brønsted acid sites (Al) in the framework prior to SSI with Sn. The prepared materials, thus containing both Sn and Al were used as bifunctional Lewis and Brønsted acidic catalysis for one-pot multistep conversion of furfural to the bio-renewable furanic ethers.

## 5.2 Result and discussion

### 5.2.1 Lewis acid-only system

As described above, Lewis acidic silicates have previously demonstrated promising levels of activity, selectivity and stability for a range of biomass valorisation reactions, including transfer hydrogenation and etherification.<sup>18–20</sup> Accordingly, the study focused upon the tandem transfer hydrogenation and etherification of furfural, a platform molecule obtained through the isomerisation and dehydration of xylose. Under conditions adapted from the transfer hydrogenation of various carbonyl compounds,<sup>21</sup> where 2-butanol is employed as H-donor, the catalytic performance of two stannosilicates containing different amounts of Sn(IV) (2 and 10 wt%) in batch reactors (100 °C, 1h, 10 mL furfural in 2-butanol (0.2 M), Fur/Sn molar ratio of (1 mol% Sn)) was first evaluated.<sup>22</sup> Both materials were prepared by solid-state incorporation, a two-step methodology requiring dealumination of an alumionsilicate precursor, followed by remetallation of the material with Sn(IV) as described in depth in Chapter 3. Metal contents, porosity data and XRD patterns of these materials are included in the Table 5.1 and Figure 5.1.

**Table 5.1** Metal content and porosity data for various aluminosilicate and stannosilicate materials.

Entry	Catalyst	<sup>a</sup> Al wt. %	<sup>b</sup> Sn wt. %	<sup>c</sup> S <sub>BET</sub> (m <sup>2</sup> g <sup>-1</sup> )	<sup>d</sup> V <sub>micro</sub> (cm <sup>3</sup> g <sup>-1</sup> )
1	H-BEA-38	2.30	-	551	0.210
2	deAl-BEA-38	<0.05	-	596	0.221
3	2Sn-BEA	<0.05	1.7	563	0.191
4	10Sn-BEA	<0.05	9.4	525	0.193

<sup>a</sup> Al content determined by ICP-MS. <sup>b</sup> Sn content determined by EDX spectroscopy. <sup>c</sup> Brunauer-Emmett-Teller surface area (S<sub>BET</sub>) was calculated from BET method and <sup>d</sup> Micropore volume (V<sub>micro</sub>) derived from the t-plot method.

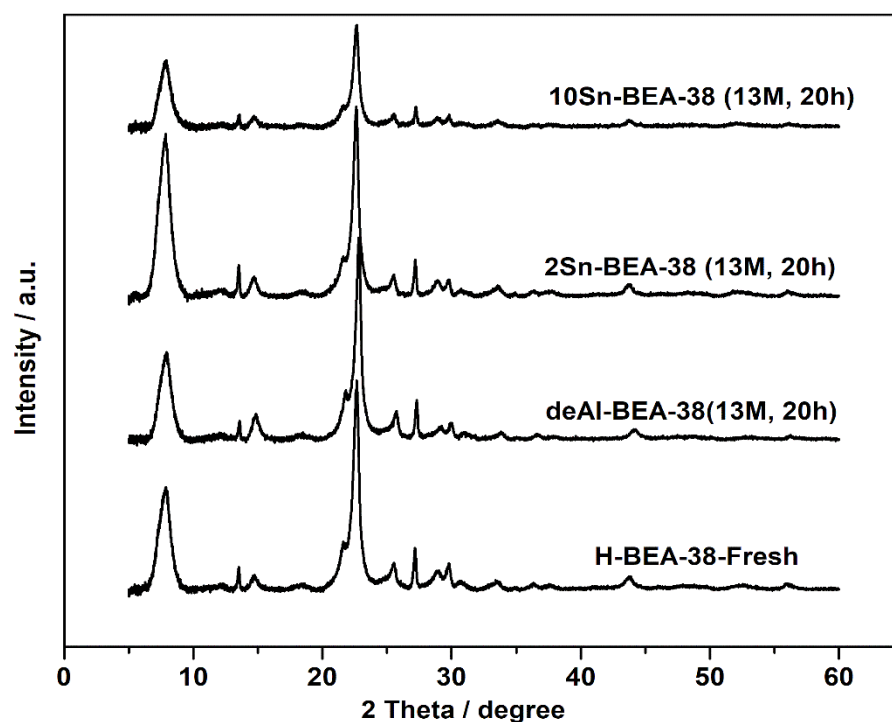


**Figure 5.1** XRD analysis of different aluminosilicate and stannosilicate catalysts, including (from bottom to top) zeolite H-BEA (SiO<sub>2</sub>/Al<sub>2</sub>O<sub>3</sub> =38), dealuminated zeolite BEA, 2Sn-BEA and 10Sn-BEA.

Under identical reaction conditions, including substrate/metal ratio (FF/Sn = 100), it is clear that 2Sn-BEA and 10Sn-BEA are both active for the transfer hydrogenation/etherification reaction, with up to 70% conversion being obtained in 90 minutes (Figure 5.2 A). In good agreement to our recent studies in chapter 3, 2Sn-BEA is approximately 30% more active on a TOF basis (234 vs. 173 h<sup>-1</sup>), indicating that 10Sn-BEA possesses a greater number of inactive Sn sites, as described in Chapter 3. Despite their comparable activity, tremendous differences in selectivity are observed between both catalytic materials (Figure 5.2 B).

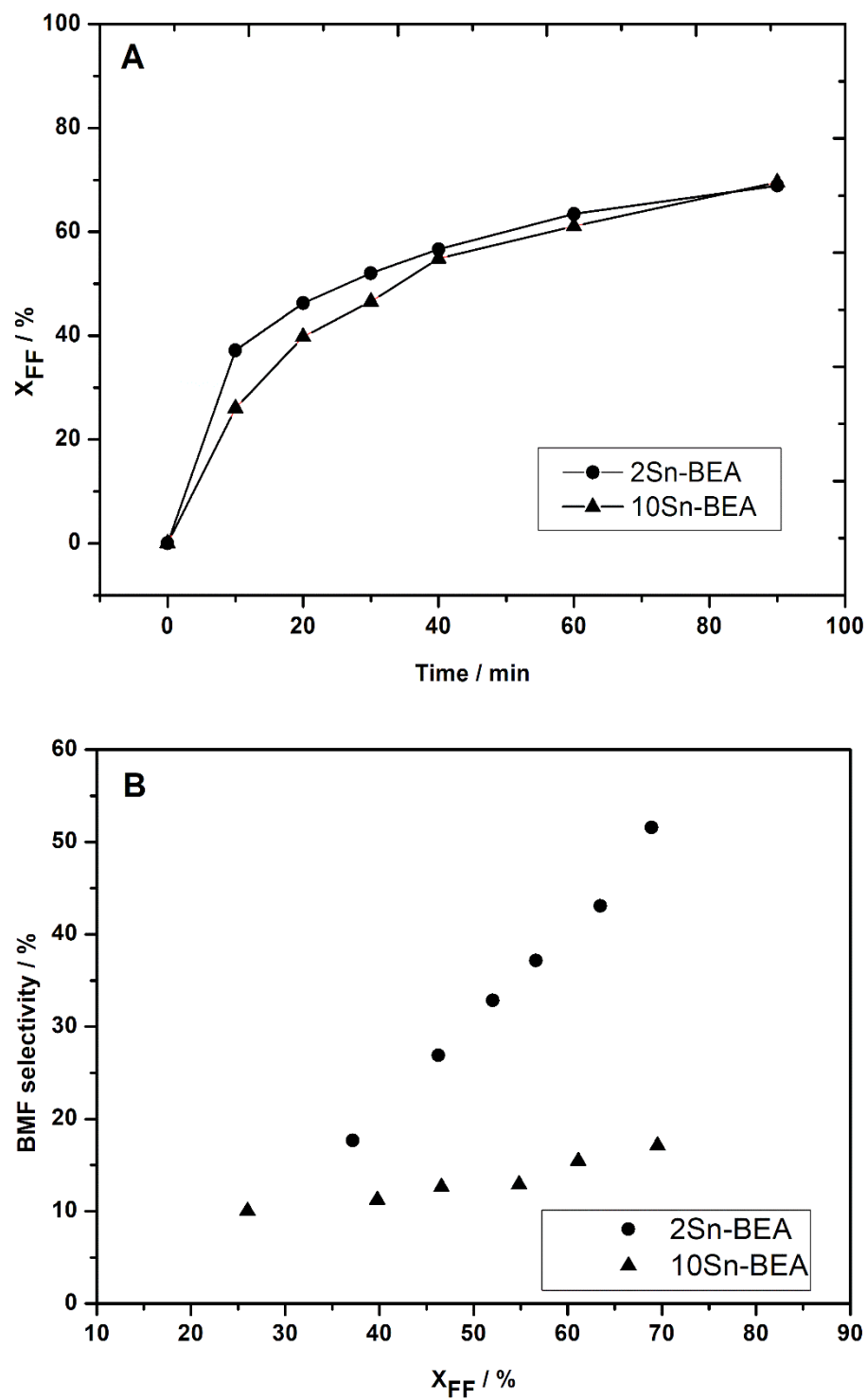


**Figure 5.2** (A) Rate of furfural conversion ( $X_{FF}$  %) over Sn-containing BEA zeolites, and (B) selectivity to BMF as a function of furfural conversion ( $X_{FF}$  %).

Whilst FA is the major reaction product obtained over 10Sn-BEA, 2Sn-BEA exhibits substantially higher selectivity to BMF at all levels of conversion. Although both catalysts exhibit slightly different levels of Lewis activity in terms of rate of FF conversion, the differences in intrinsic activity are not sufficient to solely explain the improved levels of selectivity, particular at all levels of conversion. Since 2Sn-BEA contains a greater fraction of silanol nests, present from the dealumination of the parent aluminosilicate as indicated by FTIR analysis (Figure 5.3),<sup>23–25</sup> we hypothesises that contribution from these Brønsted sites may aid the etherification process to some extent.<sup>26</sup>

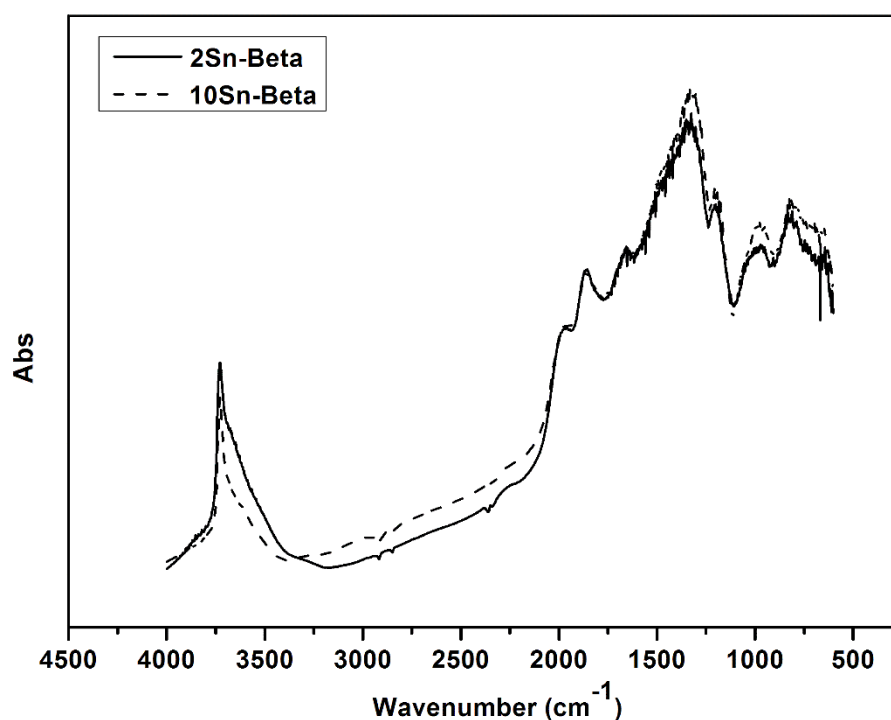


**Figure 5.3** FTIR analysis of 2Sn-BEA and 10Sn-BEA following outgassing at 550 °C.

Having obtained the intrinsic kinetic and selectivity data, the study subsequently set about exploring the activity and stability of 2- and 10Sn-BEA in continuous flow reactors.<sup>27</sup> 2- and 10Sn-BEA exhibit substantial differences in performance in the continuous regime (Figure 5.4). Firstly, 2Sn-BEA is substantially more active under comparable conditions, with its TOF being approximately 2.5 times

---

larger than that observed for 10Sn-BEA. In addition, 2Sn-BEA is also substantially more stable, with less than 20 % loss in performance observed over 1000 turnovers, equivalent to 10 batch reactions under typical literature conditions.<sup>14-17</sup> In contrast, 10Sn-BEA loses almost 50% of its original activity after 700 turnovers.

In addition to higher degrees of activity and stability, 2Sn-BEA is also more selective to (butoxy)methyl furan than 10Sn-BEA, particularly at extended periods of operation. However, whilst 2S-BEA is more selective than 10Sn-BEA, neither catalyst exhibits high selectivity to (butoxy)methyl furan at an extended period of operation. Indeed, after approximately 300 turnovers, furfural alcohol becomes the major reaction product for 2Sn-BEA, and the decrease in selectivity as a function of TON is even more dramatic for 10Sn-BEA, where (butoxy)methyl furan selectivity rapidly diminishes to < 20 %. It is noted here that in both cases, the selectivity balance is fully accounted for by furfural alcohol and (butoxy)methyl furan. Accordingly, deactivation of the etherification process occurs more rapidly than for the hydrogenation process (Scheme 5.1). Thus, even if Lewis acid sites alone are capable of catalysing the two step process, they are not able to do so with sufficient levels of activity and stability to be particularly interesting for continuous operation.

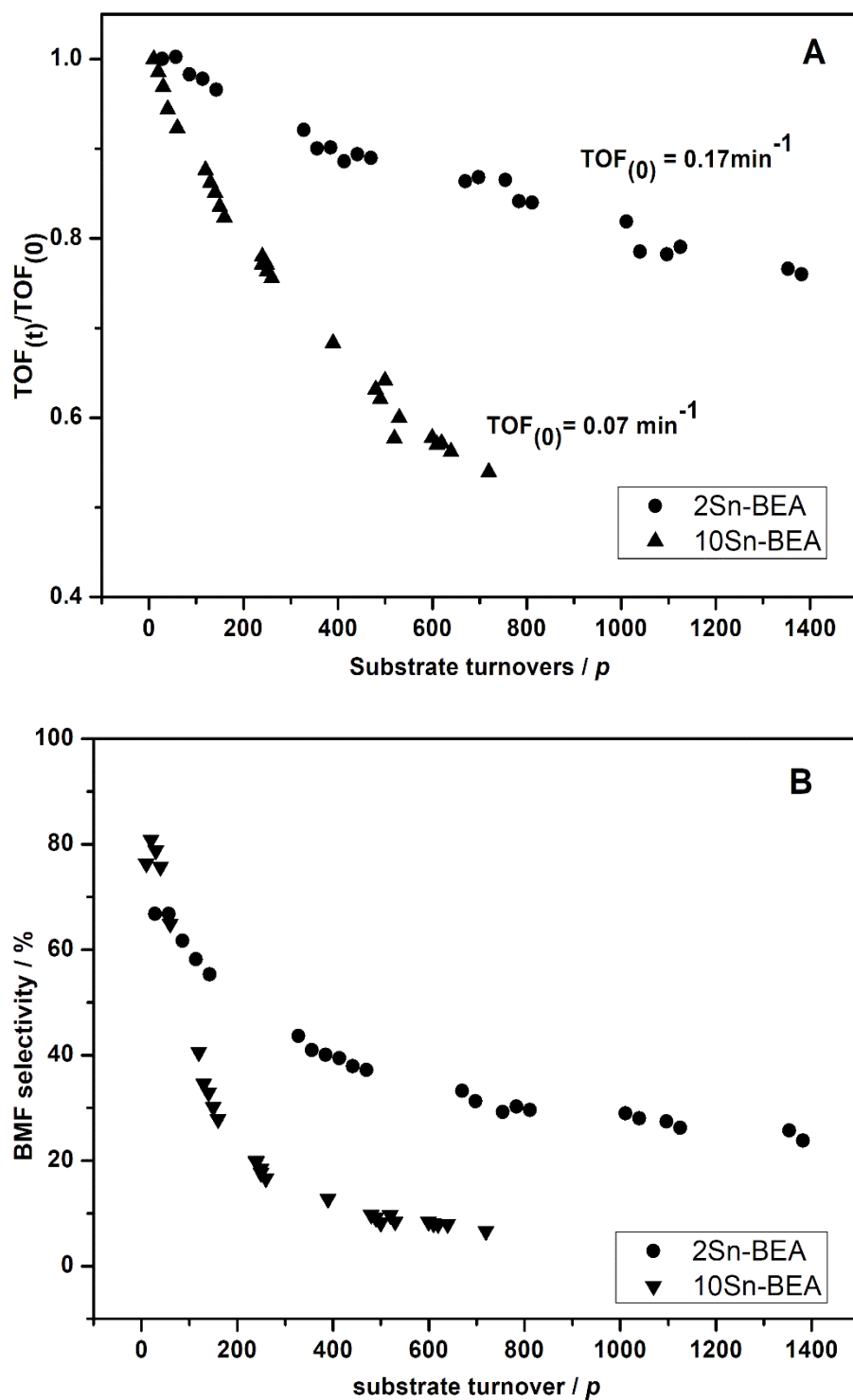


**Figure 5.4** (A) Relative performance and (B) BMF selectivity displayed by 2- and 10Sn-BEA, as a function of substrate turnover.

### 5.2.2 Catalytic etherification

To develop a selective and stable catalytic system, catalytic studies of the etherification reaction alone were performed, where furfural alcohol was employed as substrate (100 °C, 1h, 10 mL furfural alcohol in 2-butanol (0.2 M), Fur/Sn molar ratio of (1 mol% Sn)). In good agreement with the initial results, 2Sn-BEA is clearly more active for etherification than 10Sn-BEA, reaching a maximum conversion of 50% in 90 minutes. To evaluate the potential role of silanol nests, dealuminated zeolite BEA was also evaluated. Despite exhibiting lower levels of activity than the Sn-containing analogues, the contribution of this activity can readily explain the differences in selectivity of 2- and 10-Sn-BEA, strongly indicating that a combination of Lewis and Brønsted acid sites may be a more effective catalytic system.

A variety of Brønsted acidic zeolites and mineral acids were thus screened (Figure 5.5), with a FA/H<sup>+</sup> ratio of 100 employed. Clearly, such catalysts are far more suitable for etherification catalysis, with H-BEA (SiO<sub>2</sub>/Al<sub>2</sub>O<sub>3</sub> = 300, henceforth H-BEA (300)) exhibiting the best levels of activity under the initial reaction conditions. Indeed, the activity of this catalyst was so high that mass transfer limitations were found to influence the rate of reaction at a FA/H<sup>+</sup> ratio of 100.

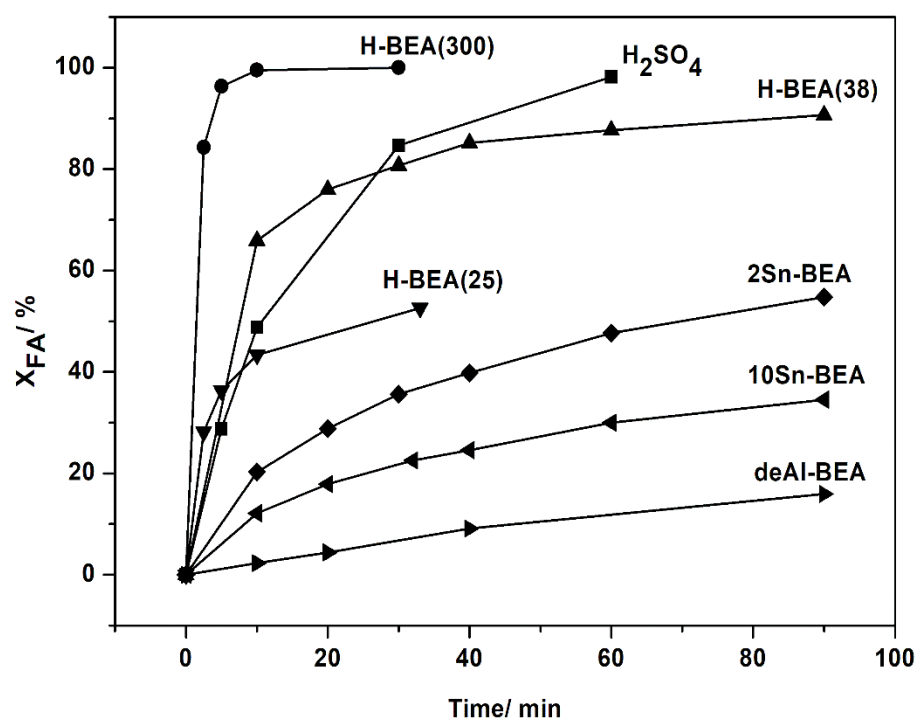


**Figure 5.5** Rate of FA conversion as a function of time over a variety of Brønsted and Lewis acid catalysts.

Decreasing the amount of catalyst to reach the true kinetic regime (Figure 5.6) revealed the initial activity of H-BEA (300) to be  $4009 \text{ h}^{-1}$ . In contrast to  $119 \text{ h}^{-1}$  for 2S-BEA alone. Accordingly, it is evident that a combination of Lewis and Brønsted acidity offers the best opportunity of achieving high yields and selectivity to (butoxy)methyl furan. Amongst mineral acids,  $\text{H}_2\text{SO}_4$  was found to be the most active. However, the selectivity to BMF was much lower in this case than when the reaction was catalysed by H-BEA; whilst H-BEA always exhibits a BMF selectivity of  $> 80 \%$ , reactions catalysed by  $\text{H}_2\text{SO}_4$  resulted in high selectivity to butyl levulinate (Figure 5.7).

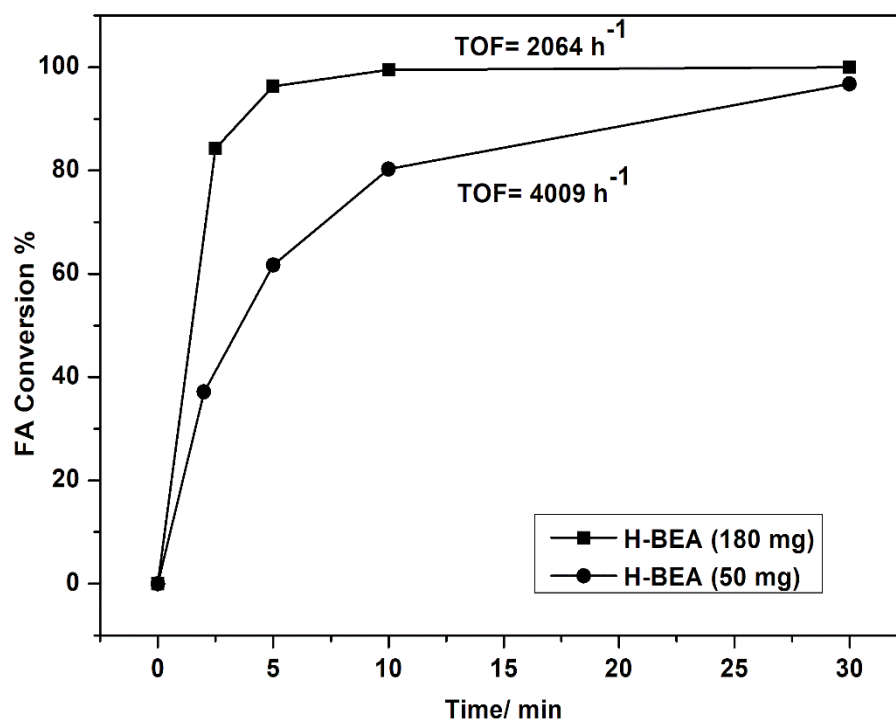


**Figure 5.6** Conversion of FA to BMF as a function of time using H-BEA (300) at different mass loading. Initial TOF is displayed for the two different loading.

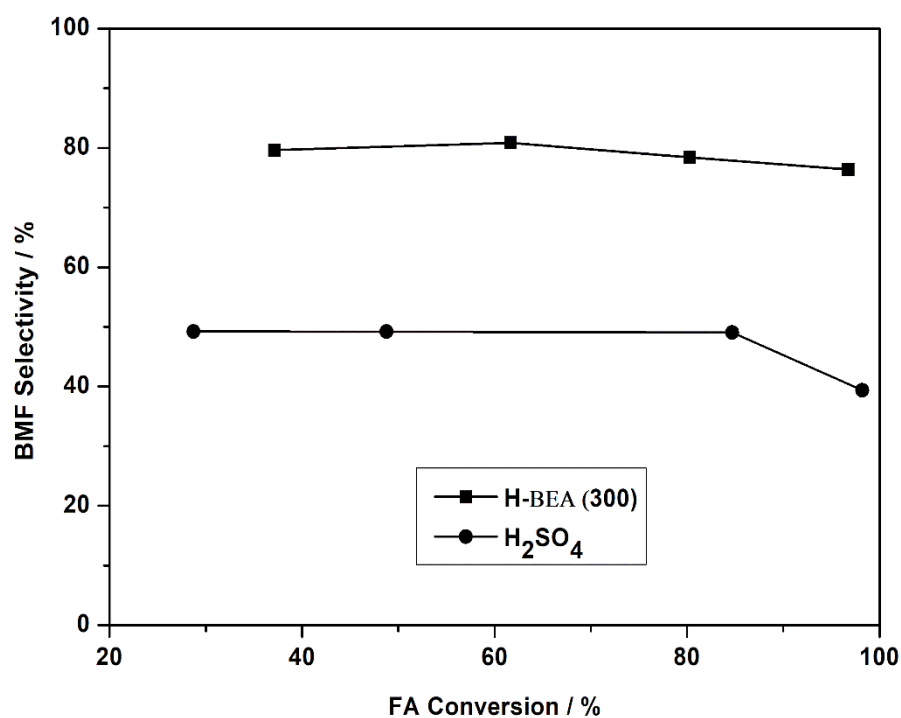


**Figure 5.7** BMF selectivity as a function of FA conversion for H-BEA (300) and sulfuric acid.

### 5.2.3 Bifunctional catalytic systems

In order to obtain both Lewis acid and Brønsted acid capability, we first explored a hybrid catalytic system, comprising of a solid Lewis acid (2Sn-BEA) and a continuous feed of mineral acid ( $\text{H}_2\text{SO}_4$ ). Such a hybrid approach, where Sn-BEA is employed in combination with a mineral acid, has previously shown to be effective for the production of 5-HMF from glucose, a two-step reaction that proceeds via Lewis-catalysed isomerisation and Brønsted-catalysed dehydration.<sup>28</sup> Unfortunately, this results primarily in the formation of butyl levulinate, and was not studied further

Given the efficacy and selectivity of H-BEA (300) for the etherification reaction, we instead focused upon developing bifunctional, heterogeneous catalytic systems based on BEA zeolite. Two approaches were considered including (1) the utilisation of simple physical mixtures of 2Sn-BEA and H-BEA (300), and (2) the preparation of a bifunctional Sn- and Al-containing BEA zeolite, in a similar manner to Dijkmas et al.<sup>29</sup> Such bifunctional materials, where both active components are hosted in one matrix, have shown unanticipated advantages for some multistep catalytic transformations, particularly where equilibrium or internal diffusion plays a role.<sup>30,31</sup>

The following section first describes optimisation of the physical mixture composition, prior to describing the synthesis and characterisation of bifunctional Sn- and Al-containing BEA zeolite.

### 5.2.4 Optimisation of physical mixture

Physical mixtures of solid Lewis and Brønsted acids have previously been employed for multi-step catalytic processes, such as the conversion of glucose to 5-HMF, and the conversion of furfural to  $\gamma$ -valerolactone.<sup>32,33</sup> Based on the etherification results, a combination of 2Sn-BEA and H-BEA(300) was chosen. We first explored the potential of the physical mixture in batch reactors, in order to optimise the ratio of Lewis/Brønsted acidity. Unfortunately, the catalytic activity of 2Sn-BEA in terms of TH capability is somewhat compromised by the co-

presence of H-BEA (300), given that the rate of FF conversion decreases slightly (Figure 5.8). Notably, the decrease in rate correlates to the increase in H-BEA (300) loading.

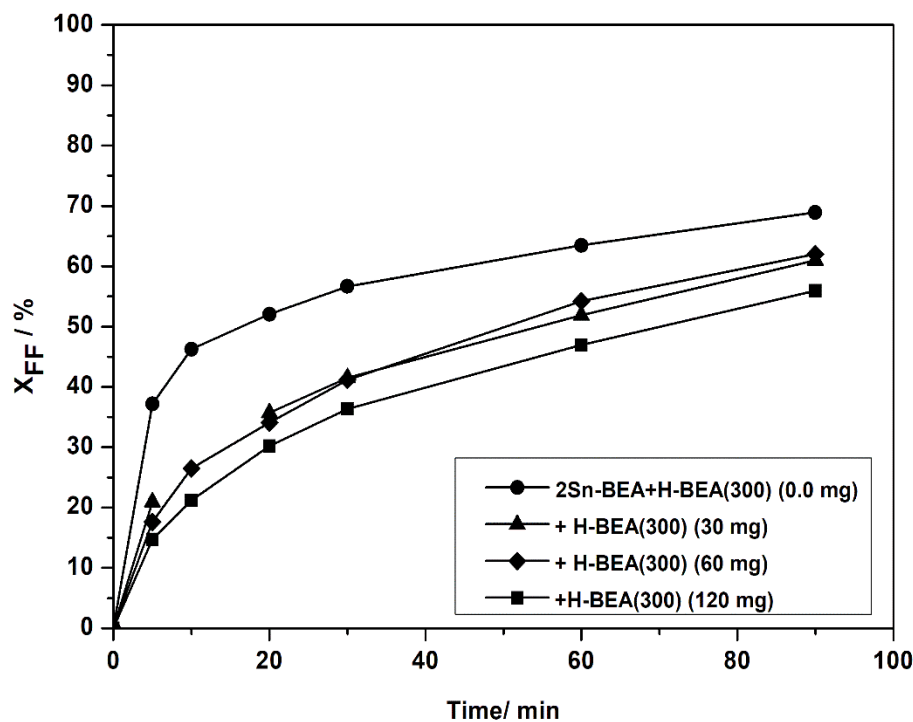


**Figure 5.8** Rate of FF conversion, over 2Sn-BEA in the co-presence varies masses (0, 30, 60, 120) mg of H-BEA (300) as a function of time.

However, dramatic improvements in the selectivity of the reaction are observed, with BMF observed as the major reaction product in the presence of H-BEA (300) (Figure 5.9). Optimal selectivity trends were observed at a H-BEA(300) mass charge of 30 mg, which resulted in 77% selectivity to BMF at a FF conversion of  $\pm 65\%$ . When greater amounts of H-BEA (300) were employed, a decrease in BMF selectivity was also observed, due to undesired ring opening. Given the decrease in TH rate and the increase in BMF ring opening at increasing H-BEA (300) masses, the optimal mass ratio of 2Sn-EA to H-BEA(300) is 4:1.

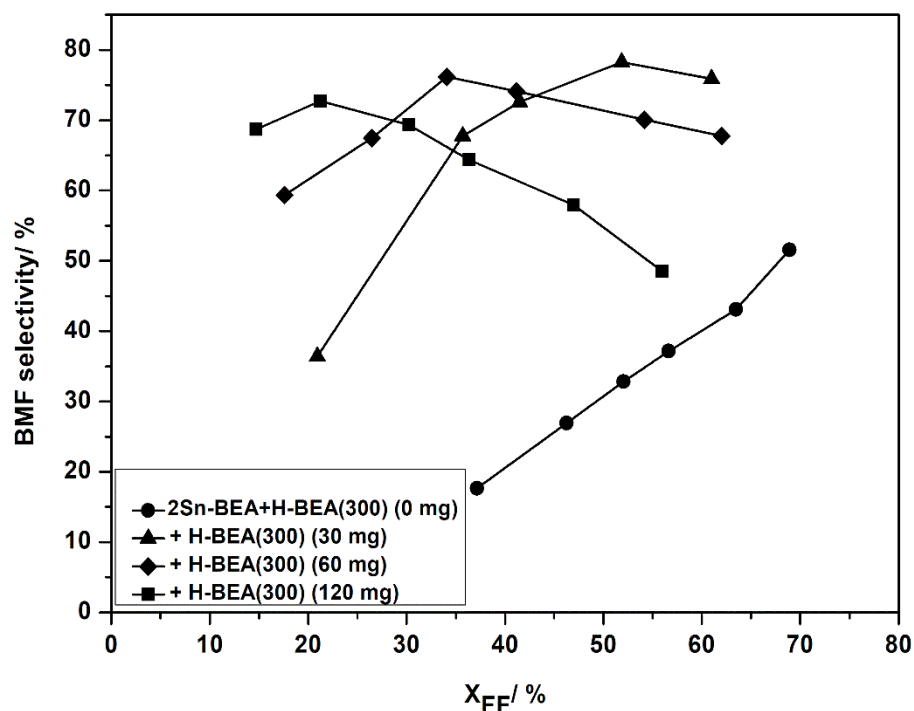


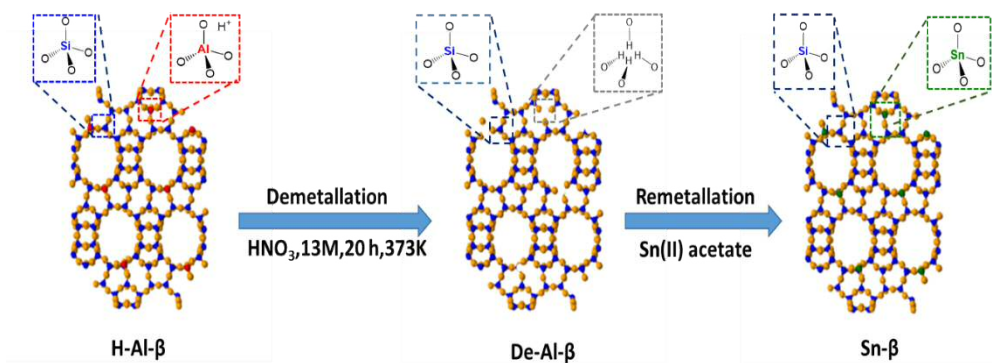
**Figure 5.9** BMF selectivity as a function of FF conversion, over 2Sn-BEA in the co-presence varies masses (0, 30, 60, 120) mg of H-BEA (300).

### 5.2.5 Preparation and characterisation of bifunctional [Sn, Al]-BEA.

As described in Chapter 3, solid state stannation requires dealumination of a parent aluminosilicate material, prior to the solid state incorporation of Sn(IV) with Sn(II)acetate (Scheme 5.2).<sup>34</sup> By only partially dealuminating the zeolite, one can theoretically prepare a material containing both Lewis acidity from Sn(IV), and Brønsted acidity from residual Al(III) in the zeolite framework. Such an approach was elegantly employed by Dijkmans *et al.* in order to prepare a bifunctional Sn- and Al-containing BEA zeolite.<sup>29</sup> In that case, the bifunctional catalyst was employed for the catalytic conversion of dihydroxyacetone to ethyl lactate in batch reactors, and Sn(IV) was incorporated through grafting of SnCl<sub>4</sub>·5H<sub>2</sub>O in dry isopropanol.

Following the approach of Dijkmans *et al.*, partial dealumination of H-BEA (38) was achieved by treatment in 13 M HNO<sub>3</sub> for various periods of time. Amongst a range of times, treatment of H-BEA (38) for (1 and 10) h, resulted in a material

containing (0.16 and 0.05) wt% Al as determined by ICP-MS. In agreement with the full dealumination studies (see Chapter 3), the crystalline structure of the BEA zeolite was unaffected by this treatment (Figure 5.10), with no impurities or an amorphous phase spotted in the patterns. Metal contents of these materials are included in the Table 5.2.



**Scheme 5.2** Schematic of solid state incorporation.

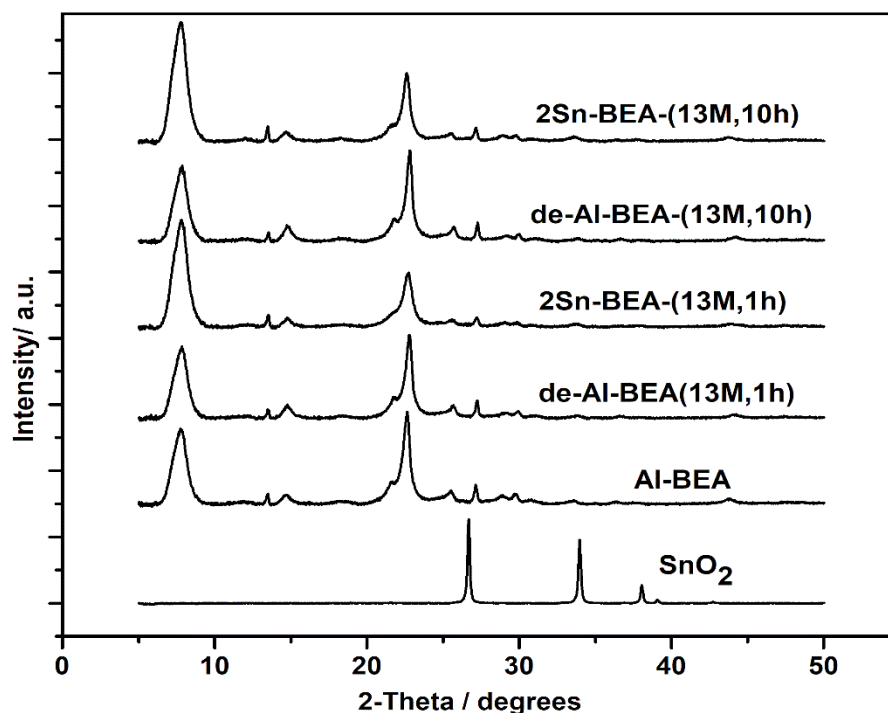


**Figure 5.10** XRD patterns of zeolites treated at different conditions. The dealumination time and concentration are in parentheses. From top to bottom: 2Sn-BEA-38(13M, 10h), deAl-BEA-38(13M, 10h), 2Sn-BEA-38(13M, 1h), deAl-BEA-38(13M, 1h), Al-BEA and SnO<sub>2</sub>.

**Table 5.2** Metal content for various aluminosilicate and stannosilicate materials.

Catalyst	<sup>a</sup> Al wt. %	<sup>b</sup> Sn wt. %
H-BEA	2.30	-
deAl-BEA(20h)	<0.05	-
2Sn-BEA(20h)	<0.05	1.78
deAl-BEA(1h)	0.16	-
2Sn-BEA(1h)	0.16	1.63
deAl-BEA(10h)	0.05	-
2Sn-BEA(10h)	0.05	2.09

<sup>a</sup> Al content determined by ICP-MS. <sup>b</sup> Sn content determined by EDX spectroscopy

Given the poor sensitivity of DRIFTS studies with pyridine as a probe molecule, and the very low Al(III) content, verification of the presence of Brønsted acid sites

was obtained by  $^{27}\text{Al}$  MAS NMR (Figure 5.11). This technique is powerful method of probing the geometrical environment of Al(III) in zeolites. Typically two resonances at 54.3 and 0.13 ppm are observed. The first is attributed to tetrahedrally coordinated Al(III) in the framework, giving rise to exchange capability and hence, Brønsted acidity. The second feature is typically assigned to octahedrally coordinated Al(III), typically in extra-lattice sites. This clearly demonstrated that the residual Al(III) content was present within the zeolite framework, hence giving rise to Brønsted acid sites, which are directly related to tetrahedrally-coordinated framework Al species, indicated by a peak in the  $^{27}\text{Al}$  MAS NMR (Figure 5.11) spectrum of zeolite at 54.3 ppm.

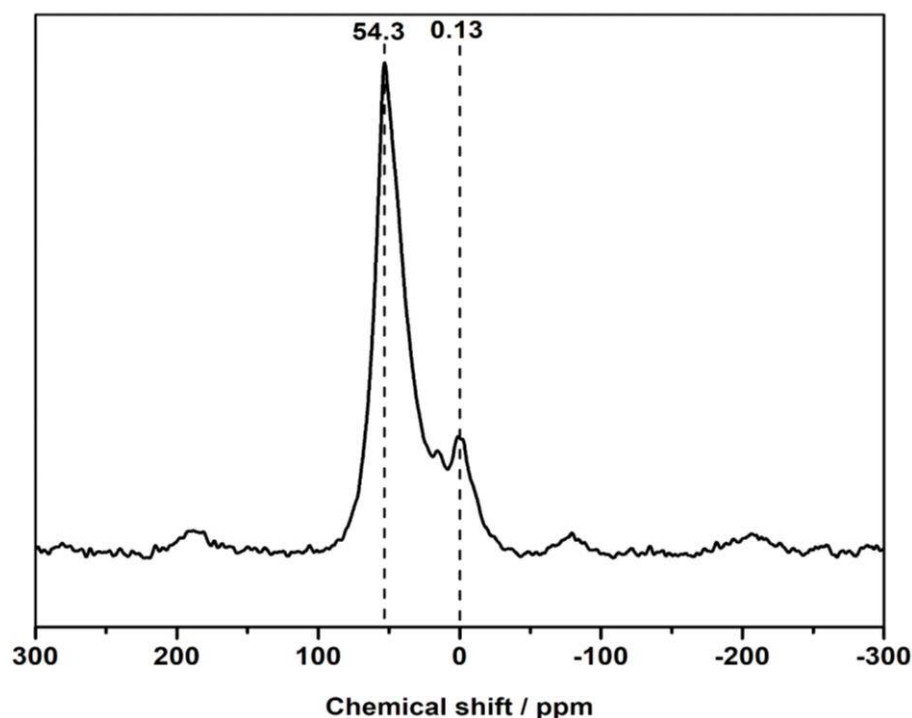


**Figure 5.11**  $^{27}\text{Al}$  MAS NMR spectrum of [2Sn,0.16Al]-BEA.

Subsequently, Sn(IV) was incorporated into the partially dealuminated framework at a loading of 2 wt%, consistent with a loading possessing the most uniform amount of active Sn species, as evidenced in Chapter 3. In line with the characterisation studies in Chapters 3 and 4, verification of the Lewis acidic

nature of the Sn(IV) content was achieved by DRIFTS studies with  $\text{CD}_3\text{CN}$  as probe molecule, where the characteristic stretch  $2309\text{ cm}^{-1}$  was present (Figure 5.12).<sup>35</sup>

No asymmetry, potentially indicative of open- or closed-Sn(IV) sites<sup>36</sup> was observed even following desorption at  $200\text{ }^\circ\text{C}$ . Accordingly, Lewis acidity is present from Sn (2 wt%) and Brønsted acidity present from residual Al(III) ( $\pm 0.16$  wt%). The catalyst is henceforth described as  $[\text{2Sn},0.16\text{Al}]\text{-BEA}$ .

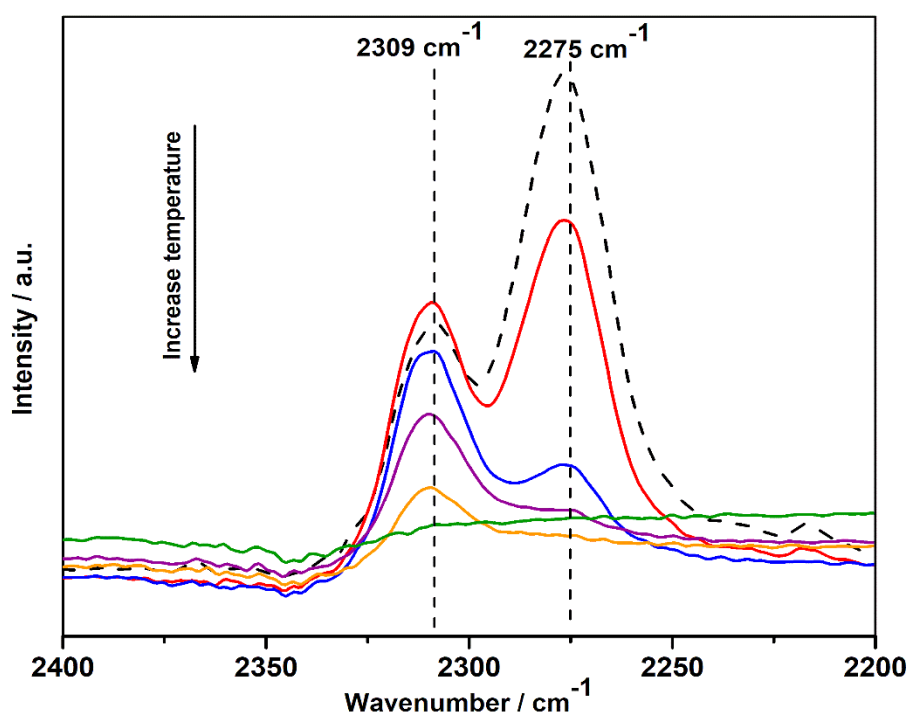


**Figure 5.12** In situ DRIFT spectra of  $[\text{2Sn},0.16\text{Al}]\text{-BEA}$ , following (dashed line) 10 minute treatment with  $\text{CD}_3\text{CN}$  at room temperature. Various desorption temperatures (50 (red), 100 (blue), 150 (purple), 200 (yellow) and 250 (green)  $^\circ\text{C}$ ) from top to bottom are also displayed.

### 5.2.6 Meerwein-Ponndorf-Verley Reduction of Furfural by Bifunctional ([2Sn, Al]-BEA).

The catalytic performances of bifunctional Lewis and Brønsted acid containing [2Sn, 0.16Al]-BEA and [2Sn, 0.05Al]-BEA were evaluated for the coupled transfer hydrogenation/etherification of furfural, using 2-butanol as H-donor and etherification reagent, to produce furfuryl alcohol (FA) by transfer hydrogenation and (butoxy)methyl furan (BMF) by consecutive etherification. The performance of these materials was also compared to that. Under identical reaction conditions, including substrate/metal ratio (FF/Sn = 100), it is clear that, of the three catalysts investigated, Lewis acidic 2Sn-BEA exhibited the highest conversion of furfural with 78% conversion being obtained with this catalyst in 90 minutes. The activity of the bifunctional analogues was somewhat lower with bifunctional [2Sn,0.05Al]-BEA and [2Sn,0.16Al]-BEA converting 73% and 64% of the initial furfural concentration, respectively (Figure 5.13 A). Despite their comparable levels of catalytic activity, tremendous differences in selectivity are observed. [2Sn-0.16Al-BEA] exhibits substantially higher selectivity to (butoxy)methyl furan at all levels of conversion than [2Sn-0.05Al]-BEA and 2Sn-BEA (Figure 5.13 B). The influence of Al ratio in the three catalysts increase the activity of 2Sn-BEA and selectivity of [2Sn-0.16Al]-BEA. The Al ratio of < 0.05 showed the highest furfural conversion and lowest selectivity. The remaining Al content leads to 5–15% drop of the furfural conversion. Hence, the concentration of the Brønsted acid had a strong influence on conversion; particularly when Sn/Al tetrahedral ratios were increased. However, a greater effect on reaction selectivity is evident, with increasing Al(III) content resulting in significantly improved selectivity to the desired ether at all overlapping levels of conversion.

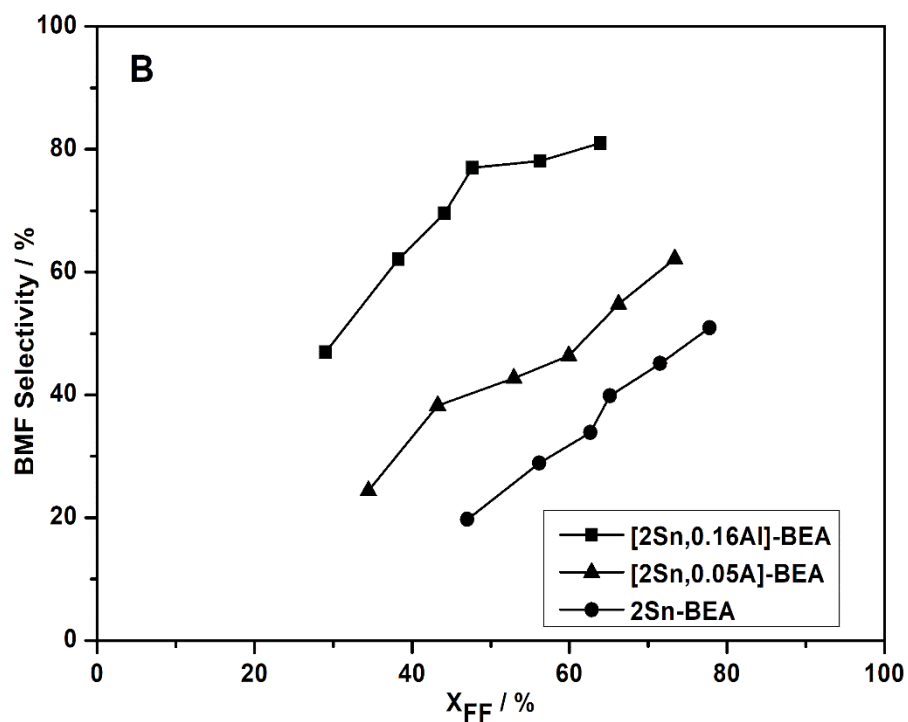
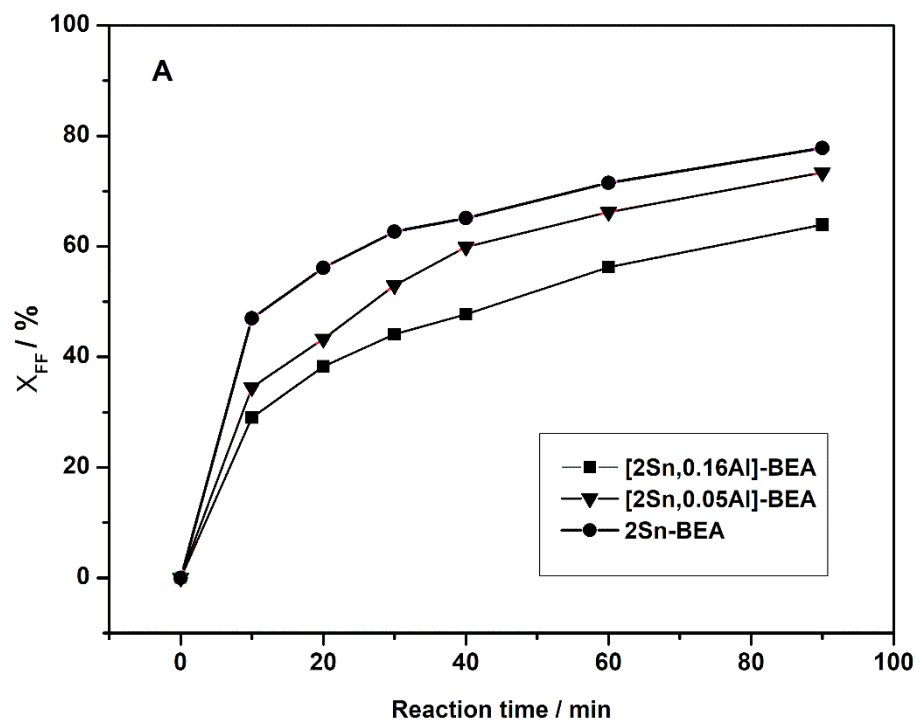


**Figure 5.13** (A) Rate of FF conversion and (B), BMF selectivity as a function of FF conversion, over [2Sn,0.16Al]-BEA, [2Sn,0.05Al]-BEA and 2Sn-BEA.

Clear that Lewis acid only display different activity and selectivity as a function of loading; but, best performance with bifunctional, with [2Sn, 0.16Al]-BEA displaying best level of performance.

Furfural conversion, yield and selectivity of the reaction media at different reaction temperatures were assessed with bifunctional [2Sn, 0.16Al]-BEA catalyst as being the most selective catalyst to the desired ether product. Figure 5.14 presents the impact of the reaction temperatures, as a function of time, on the conversion of furfural and the yield of furfuryl alcohol and (butoxy)methyl furan. Furfural is converted at high levels only if the applied reaction temperature is increased from 100 up to 120°C. The furfural conversion was 64% at 100°C, while the conversion reached 87% at 120°C in 90 min. However, the assessment performed under various temperature conditions results in different yields towards furfuryl alcohol and (butoxy)methyl furan. Thus, the former appears as the minor product only at low temperatures 100 °C ( Figure 5.14), reaching a product yield of 5%, for a substrate conversion of 64% after 90 min of reaction. Under the impact of these conditions, 49% of the starting furfural is converted into the (butoxy)methyl furan. Increasing the reaction temperature up to 110 °C improves the yield of the target product, gaining a (butoxy)methyl furan yield (53%) higher than that achieved at 100 °C, while the amount of produced furfuryl alcohol is much lower (0.9%). As the reaction temperature is increased, the yield to (butoxy)methyl furan is decreased from 53% at 110 °C to 44.5% at 120 °C. Increasing the temperature to 120 °C decreases the yield of (butoxy)methyl furan ,could be attributed to the formation of heavy by-products from the self-etherification of the substrates at 120 °C. The yield to this by-product is significantly influenced by the reaction temperature, so that low temperatures have to applied to keep its production at low levels.

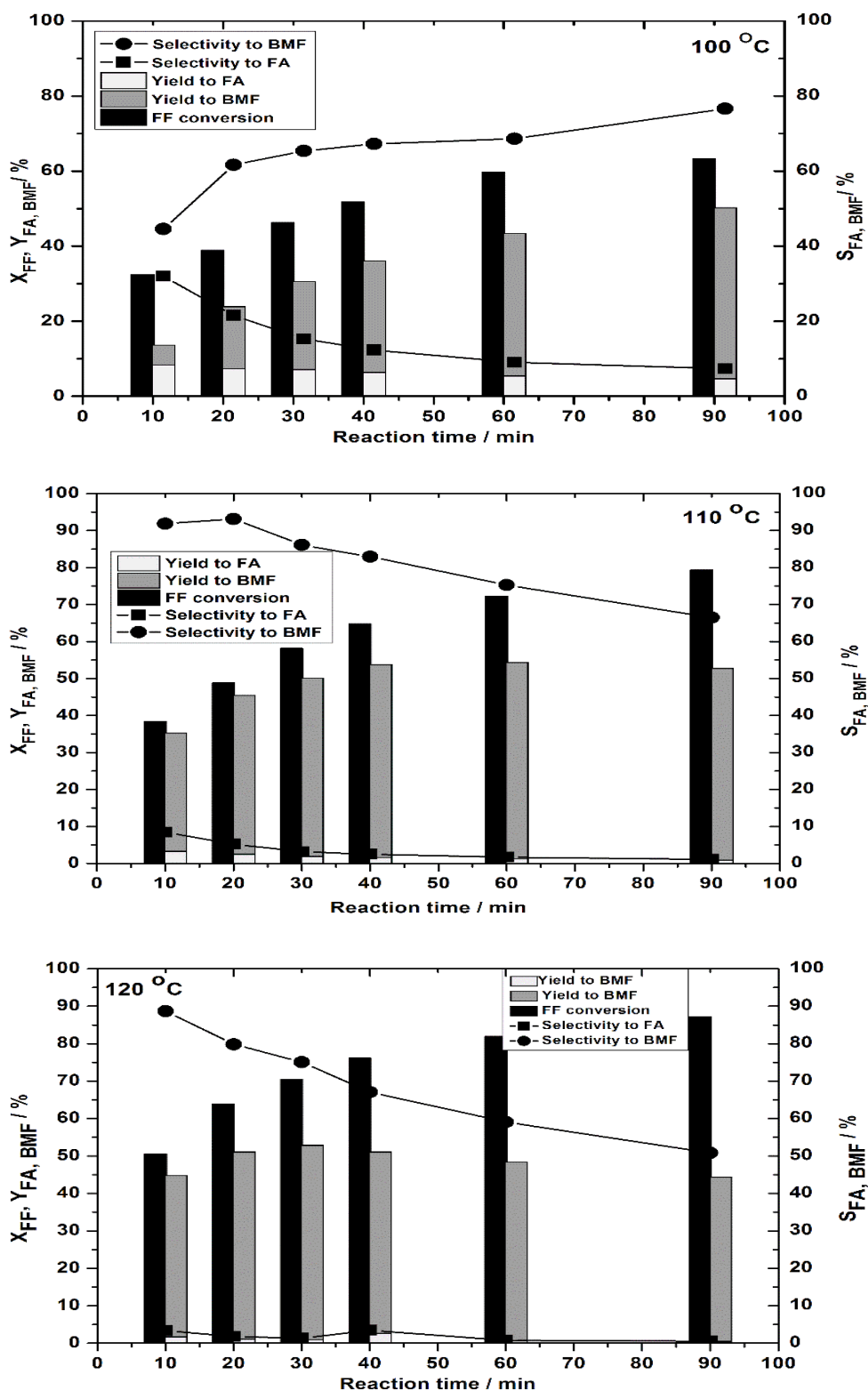


**Figure 5.14** Influence of the reaction temperature on MPV reduction of furfural with 2-butanol in presence of [2Sn, 0.16Al]-BEA. MPV reaction conditions, 90 min, 10 mL furfural in 2-butanol (0.2 M), FF/Sn ratio of 100. (X= Substrate conversion; Y= Product yield; S= Selectivity towards the product).

All catalysts are white powders in their as-prepared (Figure 5.15 A) form, but they change their colour clearly after reaction to become light grey or grey, depending on the reaction temperature (see Figure 5.15 B, C and D). This colour change is most likely due to furfural and furfural alcohol oligomerization in which one or both polymerize under reaction conditions,<sup>37,38</sup> changing the colour of the catalyst. Thermogravimetric analysis (TGA) of the spent catalyst indicates that the TGA traces show no differences in their shape (Figure 5.16). More specifically, the trace of the spent [2Sn, 0.16Al]-BEA, at different temperatures, has carbon species that are thermally more combust and stable.

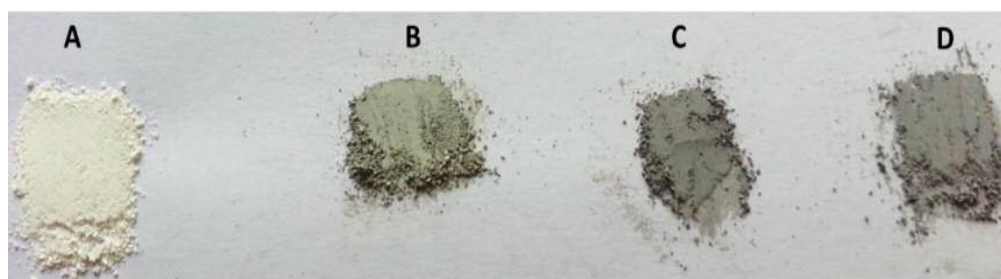


**Figure 5.15** (A) fresh [2Sn, 0.16Al]-BEA and (B, C and D) spent [2Sn, 0.16Al]-BEA catalyst at (100, 110 and 120) °C respectively.

Thermogravimetric analysis of the [2Sn, 0.16Al]-BEA catalyst (Figure 5.16) shows three distinct temperature regions; region 1, at temperature below 400 k, region 2 at temperatures between 400-600 k and region 3 at temperatures between 600-900 k. The peaks in region 1 around 400k corresponds to the loss of water and volatile species, while the peaks in region 2 and 3 correspond to desorption of coke. The coke desorbed in region 2 at temperature 430 k is made up of oxygenated polyaromatic hydrocarbons while the coke in region 3 at temperature between 600-800 k is made up of less oxygenated polyaromatic compounds.<sup>39</sup> The change in colour of the used catalyst, and in TGA curves suggests that polymerization phenomenon contribute to the observed deactivation.

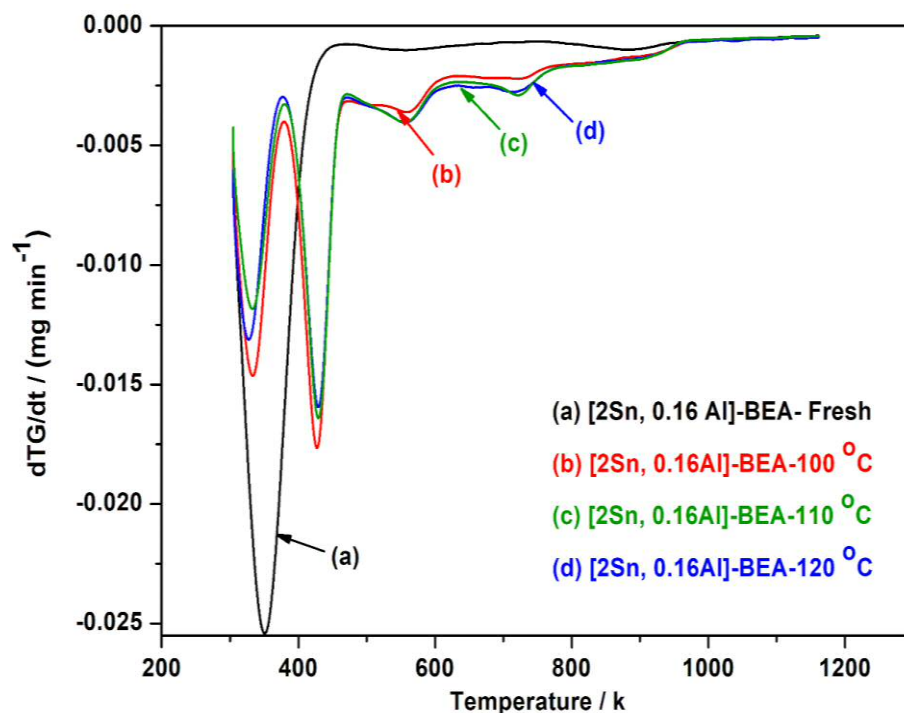


**Figure 5.16** Thermogravimetric analysis of fresh [2Sn, 0.16Al]-BEA and spent catalyst at different temperatures. Analysis was performed in air at a heat rate of  $10 \text{ k min}^{-1}$ .

### 5.2.7 Continuous performance of physical mixtures and bifunctional catalysts

2Sn-BEA/H-BEA(300) and [2Sn,0.16Al]-BEA were subsequently evaluated as bifunctional catalytic systems for the combined hydrogenation/etherification of furfural to (butoxy)methyl furan, and compared to the reference sample of purely Lewis acidic 2Sn-BEA. The contact time in each case was adjusted so that a similar stage of the reaction coordinate, in terms of furfural conversion, was probed.

The performance of these catalysts, are compared in terms of activity (TOF, equation 5.1), stability (relative performance, equation 5.2) and selectivity ( $S_{\text{BMF}}$ , equation 5.3), all as a function of number of substrate turnovers ( $p$ , equation 5.4). Comparing activity as a function of TON as opposed to time on stream allows true comparison of catalysts of disparate activity in terms of the amount of product produced.<sup>40</sup> It is noted here that the contact time ( , equation 5.5) in the reactions

was adjusted so that all catalysts exhibited a similar level of substrate conversion, in order to probe similar parts of the reaction coordinate, which is particularly important when comparing (butoxy)methyl furan selectivity. Moreover, experiments were performed at flow rates at, or above, those consistent with a kinetic regime, where external mass transfer limitations were absent (Appendix, Figure 7.19).

$$\text{TOF} = \frac{\text{moles}_{(\text{FF converted})}}{\text{mol}_{(\text{Sn})} \text{min}^{-1}} \quad 5.1$$

$$\text{Relative performance} = \frac{\text{TOF}_{\text{catalyst}}}{\text{TOF}_{\text{reference}}} \quad 5.2$$

$$S_{(\text{BMF})} = \frac{\text{moles}_{(\text{BMF})}}{\text{moles}_{(\text{FF})}} \quad 5.3$$

$$= \frac{\text{moles}_{(\text{BMF})}}{\text{moles}_{(\text{FF})}} \quad 5.4$$

$$\text{Contact time} = \left( \frac{\text{moles}_{(\text{FF})}}{\text{moles}_{(\text{FF converted})}} \right) \times \text{TOF} \quad 5.5$$

As can be seen (Figure 5.17), each of the catalytic systems is relatively stable in terms of hydrogenation capability, with the relative performance decreasing by 10 – 30 % over approximately 600 substrate turnovers. However, bifunctional [2Sn,0.16Al]-BEA appears to exhibit slightly higher levels of deactivation, indicating it to be a poorer Lewis acid catalyst. Further indication of this is observed from the initial activity of each catalytic system. Indeed, whilst the initial rate of conversion over 2Sn-BEA and 2Sn-BEA/H-BEA(300) are 0.17 and 0.19 min<sup>-1</sup>, respectively, the rate observed over [2Sn,0.16Al]-BEA was only 0.08 min<sup>-1</sup>, close to that of 10Sn-BEA (Figure 5.4), which is a material known to contain inactive, extra-framework SnO<sub>x</sub> species.<sup>22</sup>

Despite slightly poorer performance in terms of hydrogenation catalysis, dramatic improvements in ether selectivity are obtained for the bifunctional solid catalyst. Indeed, after approximately 700 substrate turnovers, (butoxy)methyl furan selectivity is still close to 75%. In contrast, the (butoxy)methyl furan selectivity

observed over 2Sn-BEA and 2Sn-BEA/H-BEA(300) at the same number of substrate turnovers is dramatically lower ( $\pm 30\%$ ). Clearly, hosting both Lewis and Brønsted acidic active sites in the same matrix results in substantial improvements in (butoxy)methyl furan selectivity.

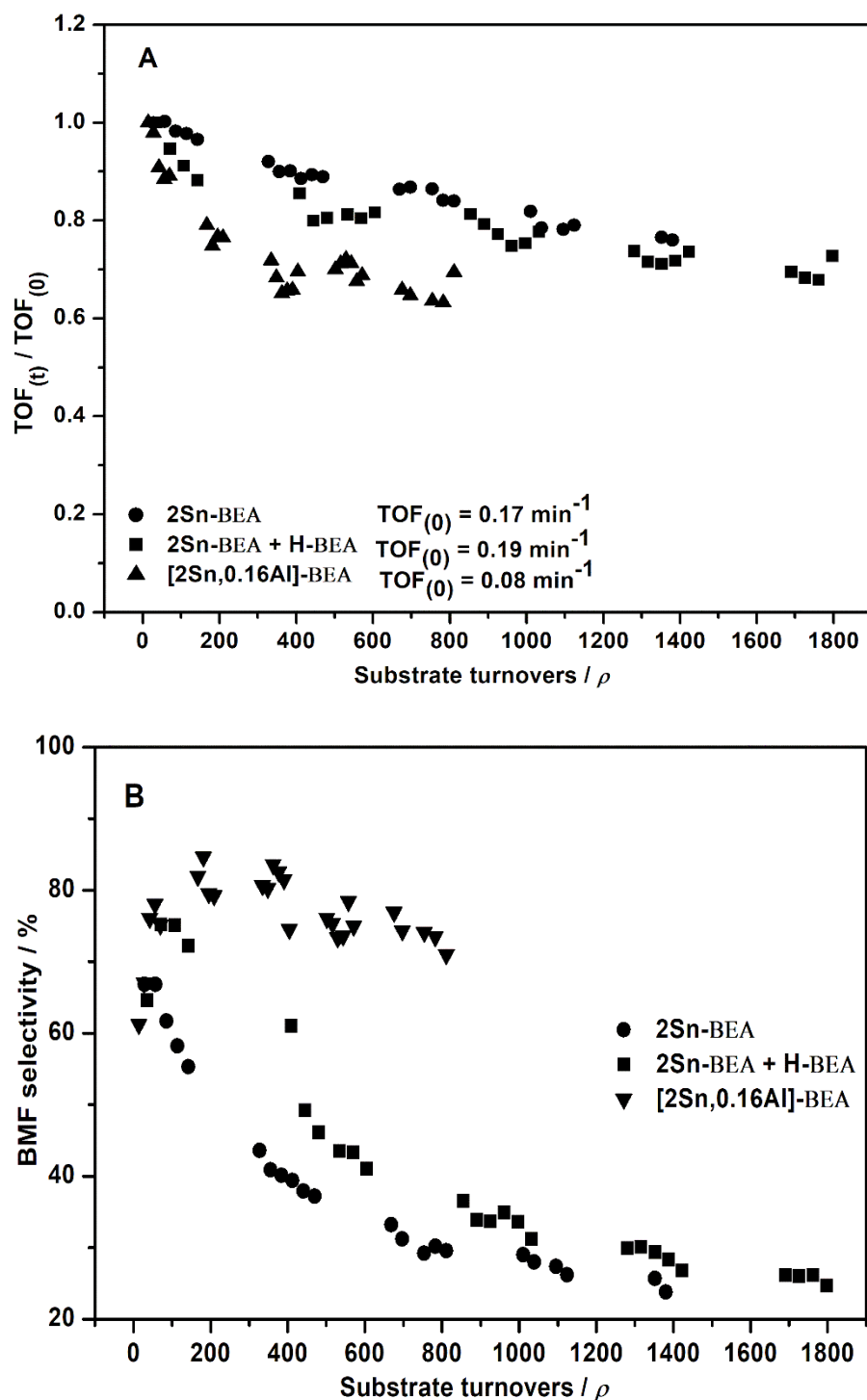


**Figure 5.17** (A) Relative performance and (B) BMF selectivity displayed by 2Sn-BEA, 2Sn-BEA/H-BEA(300) and [2Sn,0.16Al]-BEA, as a function of substrate turnover.

To account for the significant improvement in etherification stability, a variety of characterisation studies, such as TGA and porosimetry, were performed on the

*ex-reactor* samples of 2Sn-BEA/H-BEA(300) and [2Sn,0.16Al]-BEA. However, no major differences in the used catalytic materials were observed (Figure 5.18). Whilst etherification activity is lost for the physical mixture of 2Sn-BEA/H-BEA(300), the selectivity to FA compensates for the loss of selectivity, *i.e.* the potential formation of an undesirable by-product does not occur. Accordingly, no clear differences between the used bifunctional catalytic beds can be observed, despite the vast differences in etherification activity after extended operation.

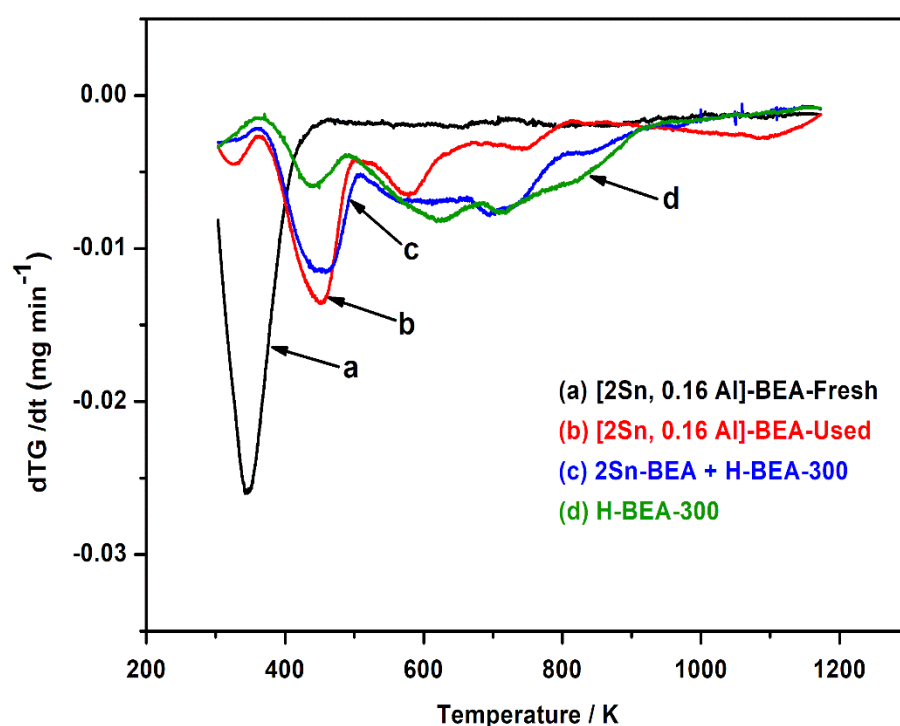


**Figure 5.18** Thermogravimetry analysis of different used catalysts in continuous regime compared against a fresh sample: (a) 2Sn-BEA(1h)-fresh, (b) 2Sn-BEA(1h)-used after FF MPV/etherification, (c) physical mixture used after FF MPV/etherification and (d) H-BEA 300 used after FA etherification only.

Given the known sensitivity of furfural alcohol to polymerise and form undesirable by-products, leading to the deactivation of heterogeneous catalysts,<sup>37,41</sup> the study hypothesises that hosting both Sn and Al in the same framework may lead to more facile conversion of furfural alcohol to (butoxy)methyl furan than found over

the physical mixture, where diffusion of furfuryl alcohol out of the crystallites of 2Sn-BEA, and subsequently into the crystallites of H-BEA, needs to occur. Accordingly, deactivation may be related to the decreased steady state concentration of furfuryl alcohol throughout the reaction period, by having close proximity of the Lewis and Brønsted acid sites of the catalyst.

### 5.2.8 Bifunctional [Sn, Al]-BEA prepared by solid state incorporation

To understand why [2Sn,0.16Al]-BEA exhibits poorer levels of Lewis acid activity than the fully dealuminated analogues,  $^{119}\text{Sn}$  MAS NMR measurements were performed. As can be seen, at the same Sn loading, i.e. 2 wt%, a larger amount of extra-framework  $\text{SnO}_x$  species ( $\delta = -602$  ppm) are observed in [2Sn,0.16Al]-BEA than in fully dealuminated 2Sn-BEA (note that isomorphously-substituted Sn(IV) sites in their hydrated form are characterised by a resonance at -690 ppm). In fact, it is evident that a greater amount of inactive  $\text{SnO}_x$  species is observed when there is a greater amount of residual Al(III) in the framework (Figure 5.19). Unfortunately, this clearly indicates that incorporating Sn(IV) into a partially dealuminated framework by solid state incorporation is hindered by the co-presence of residual Brønsted acid sites.

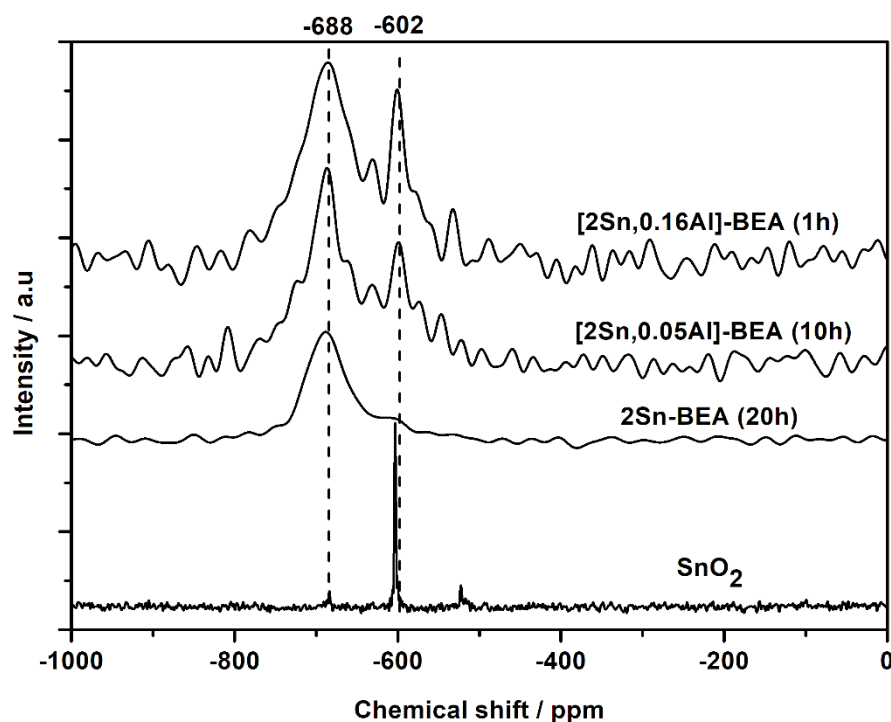


**Figure 5.19**  $^{119}\text{Sn}$  MAS NMR spectra of bifunctional samples of Sn and Al-containing BEA zeolites. Each sample contains 2 wt% Sn, and the time of dealumination for each sample is added in parenthesis.

To overcome this, this study explored an alternative synthesis strategy, involving the incorporation of both Sn(IV) and Al(III) into a fully dealuminated zeolite framework.<sup>42</sup> Accordingly, the solid state incorporation method was modified so that a suitable Al precursor (in this case Al(III)acetyl acetonate) was present alongside Sn(II) acetate during the preparation process.<sup>43</sup> A material with a Sn loading of 2 wt% and an Al(III) loading of 0.5 wt% was subsequently prepared, and is denoted as [2Sn,0.5Al]-BEA.

To verify that Al(III) was reincorporated into the framework, and hence verify the presence of both Lewis and Brønsted acid sites in [2Sn,0.5Al]-BEA,  $^{27}\text{Al}$  MAS NMR was performed. As can be seen (Figure 5.20), Al(II) is almost exclusively present as tetrahedral Al(III), characteristic of isomorphously substituted Al(III). DRIFTS studies with pyridine as probe molecule were also performed, in order to verify the bifunctionality of the material.<sup>44</sup> Despite the low Al(III) loading of [2Sn,0.5Al]-BEA, the presence of both Lewis and Brønsted acid sites in all the

spectra (even those heated to 200 °C) is evident (Figure 5.21). Absorption bands at 1643 and 1540  $\text{cm}^{-1}$  correspond to Brønsted sites, whilst those at 1595 and 1450  $\text{cm}^{-1}$  correspond to the interaction between pyridine and Lewis acid sites. Accordingly, it is clear that a bifunctional catalyst consisting of both Lewis and Brønsted acidity has been prepared by modified solid state incorporation.

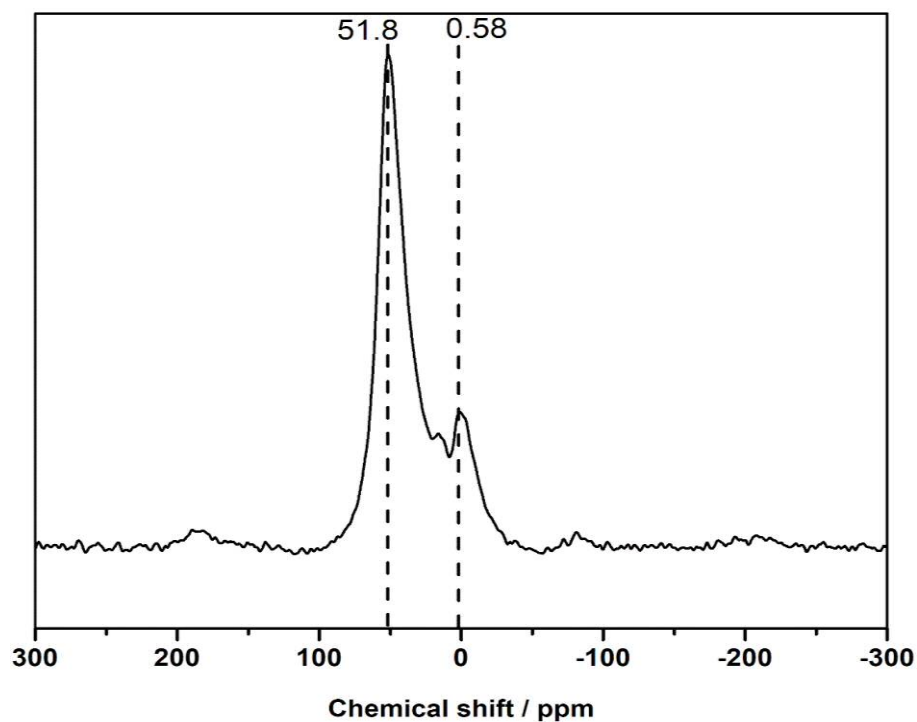


**Figure 5.20**  $^{27}\text{Al}$  MAS NMR spectrum of  $[\text{2Sn},\text{0.5Al}]\text{-BEA}$ .

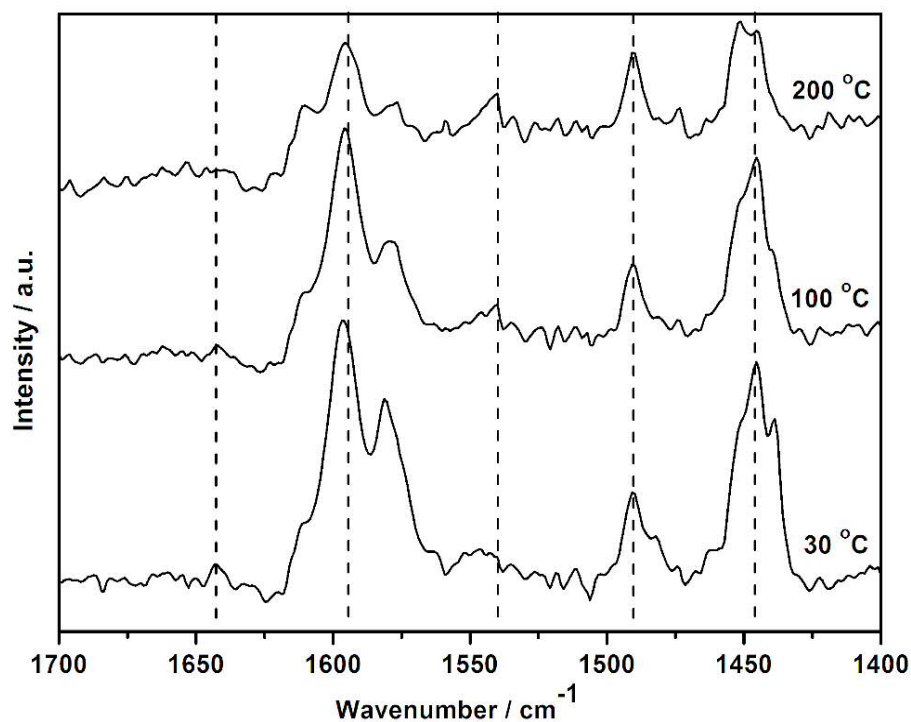


**Figure 5.21** DRIFT studies of [2Sn,0.5Al]-BEA with pyridine as probe molecule.

The catalytic properties of [2Sn,0.5Al]-BEA were subsequently evaluated in the continuous regime (Figure 5.22). In contrast to [2Sn,0.16Al]-BEA, which exhibited lower rates of conversion due to the presence of extra-framework SnO<sub>x</sub> species, the initial activity of [2Sn,0.5Al]-BEA is no lower than that exhibited by Lewis acidic 2Sn-BEA when both are tested at 100 °C. This indicates that the Lewis acidity of these materials is comparable. Moreover, the (butoxy)methyl furan selectivity obtained over [2Sn,0.5Al]-BEA is also comparable to [2Sn,0.16Al]-BEA, and substantially higher at a given number of turnovers than 2Sn-BEA. This indicates that the realumination strategy is more suitable for the introduction of Brønsted acidity than the partial dealumination approach. These observations confirm that modified solid state incorporation is a more suitable method of preparing bifunctional Lewis and Brønsted acidic Sn, Al-BEA than the partial dealumination approach.

The reaction conditions in the presence of the optimal bifunctional catalyst, [2Sn,0.5Al]-BEA, were subsequently optimised. Operating the reactor at elevated

temperatures (120 °C) was found to increase both the productivity (initial TOF of 0.33 min<sup>-1</sup>), and the (butoxy)methyl furan selectivity, which was held above 70% even after >2000 substrate turnovers (corresponding to 80 h on stream) during an initial operational cycle. In addition to long term (butoxy)methyl furan selectivity, the initial activity (0.33 mol converted min<sup>-1</sup>) and number of turnovers achieved by the optimised catalytic system (2300 during the initial period) are an order of magnitude higher than previously reported in the literature for similar reactions.<sup>16</sup>

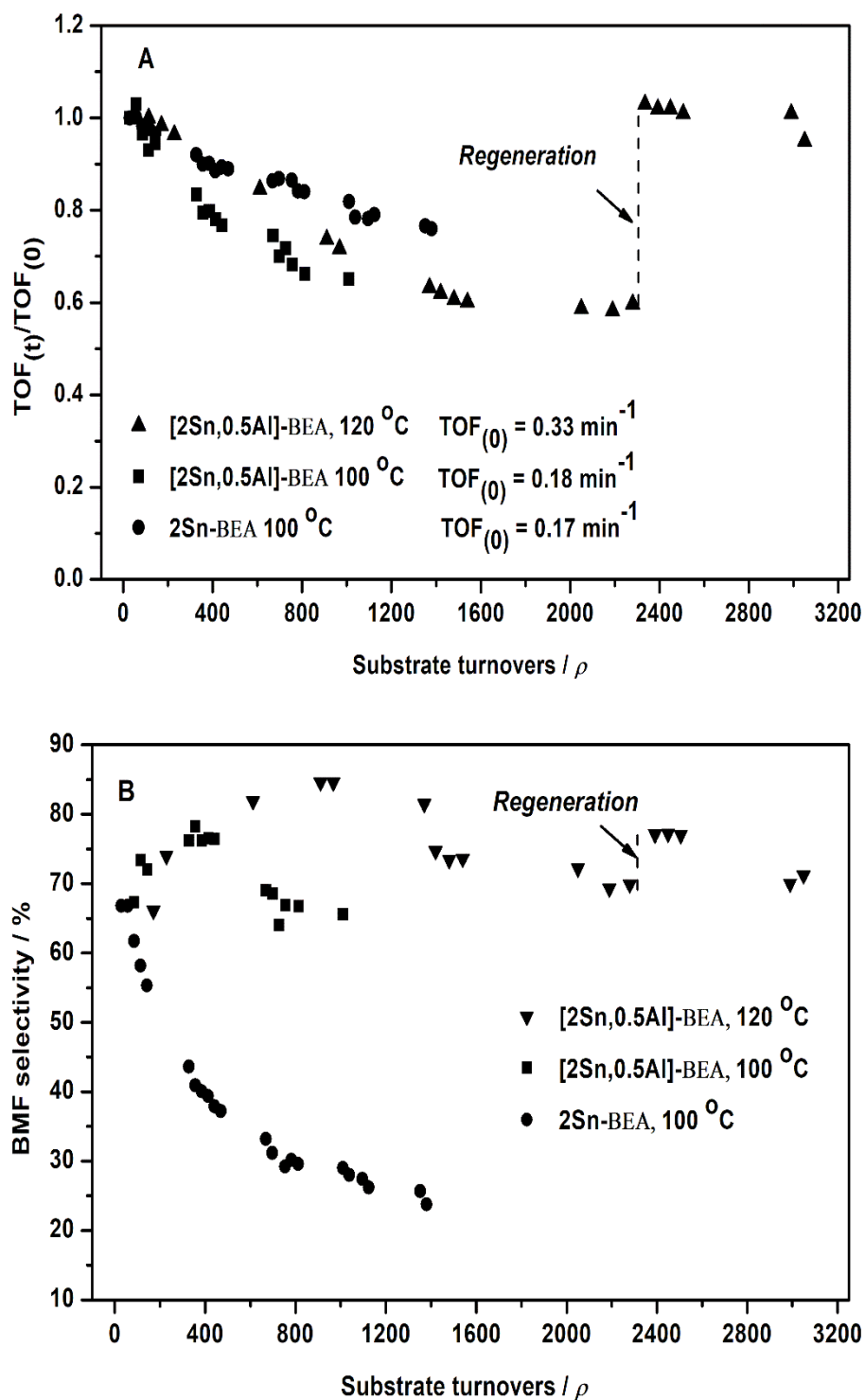


**Figure 5.22** (A) Relative performance and (B) BMF selectivity displayed by 2Sn-BEA and [2Sn, 0.5Al]-BEA at 100 and 120 °C as a function of substrate turnover. Regeneration conditions (550 °C, 3h, 60 mL min<sup>-1</sup> air)

To investigate the potential mechanisms of deactivation, *ex reactor* characterisation of the used catalytic materials was performed. This revealed that the long-range order of all the catalytic materials was maintained even after extended operation (Figure 5.23), but that loss in porosity occurred (Table 5.3). In fact, after 2300 turnover the surface area and micropore volume of [2Sn,0.5Al]-BEA decreased by 43% and 49%, respectively (Table 5.3). Notably, the loss in porosity correlates very closely to the loss in performance (<40%) over the initial period. This strongly indicates that fouling of the micropores occurs during extended operation. Given that fouling is typically non-permanent, the potential suitability of regeneration protocols was investigated. Full performance of the system – in terms of activity *i.e.* conversion, and (butoxy)methyl furan selectivity, could be restored following simple heat treatment of the catalyst in air at 550 °C. Accordingly, over 3000 substrate turnovers (107 h time on stream) at a (butoxy)methyl furan selectivity >70% could be achieved with only one regeneration procedure being employed.

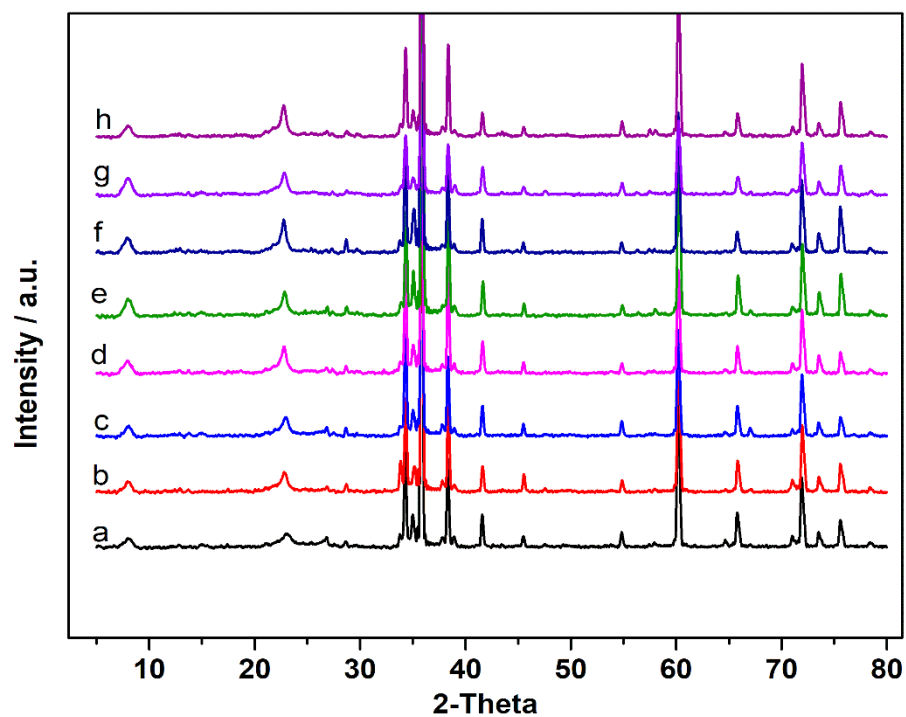


**Figure 5.23** XRD patterns for different fresh and used zeolite catalysts (20 wt.%) mixed with SiC (80 wt.%). From bottom to top: (a) 2Sn(1h)-BEA fresh, (b) 2Sn(1h)-BEA used, (c) 2Sn(10h)-BEA fresh, (d) 2Sn(10h)-BEA used, (e) 2Sn(20h)+H-BEA(300) fresh, (f) 2Sn(20h)+H-BEA used, (g) 2Sn-0.5Al-BEA fresh and (h) 2Sn-0.5Al-BEA used.

**Table 5.3** Porosity data of various fresh, used and regenerated alumina-and stannosilicate catalysts.

Catalyst	<sup>a</sup> S <sub>BET</sub> (m <sup>2</sup> g <sup>-1</sup> )	<sup>b</sup> V <sub>micro</sub> (cm <sup>3</sup> g <sup>-1</sup> )
Al-BEA-38	550.38	0.247
[2Sn,0.5Al]-undiluted	560.71	0.245
[2Sn,0.5Al]-BEA (1:4 by weight physical mixture with SiC.	<i>53.43</i> (after reaction) <u>93.48</u> (after reaction + regeneration)	<i>0.022</i> (after reaction) <u>0.043</u> (after reaction + regeneration)

<sup>a</sup> Brunauer-Emmett-Teller surface area (S<sub>BET</sub>) calculated from BET method, <sup>b</sup> micropore volume (V<sub>micro</sub>) derived from the t-plot method. Values in italic and underlined correspond to measurements made on used (*i.e* ex reactor) and regenerated catalyst mixtures, respectively.

### 5.3 Conclusions

The catalytic conversion of furfural to (butoxy)methyl furan was studied in the batch and continuous regime. Optimisation of a bifunctional zeolite material, possessing both Brønsted and Lewis acid sites from Al(III) and Sn(IV), resulted in a catalytic system more selective, active and stable than monofunctional analogues or physical mixtures thereof. A maximum (butoxy)methyl furan selectivity of 87% was obtained for a catalyst consisting of 2 wt% Sn and 0.5 wt% Al, which was prepared by modified solid state incorporation of a dealuminated BEA zeolite precursor, and which operated at 120 °C. Continuous operation for over 3000 turnover (107 h on stream) was achieved. The high activity, selectivity and durability of this catalytic material are over an order of magnitude higher than observed in comparable system, and demonstrates that high selectivity to a single product can be obtained during biomass upgrading, despite the highly functionalised nature of the substrate and its products.

---

## 5.4 Experimental

### 5.4.1 Catalyst synthesis

Commercial zeolite Al-BEA (Zeolyst, NH<sub>3</sub>-form) was dealuminated by treatment in HNO<sub>3</sub> solution (13 M HNO<sub>3</sub>, 100 °C, 20 mL g<sup>-1</sup> zeolite, 20 hours if not specified differently in the text). Solid-state stannation of dealuminated zeolite BEA was performed by the procedure optimised in Chapter 3, grinding the appropriate amount of Sn(II) acetate with the necessary amount of dealuminated zeolite for 10 minutes in a pestle and mortar. Following this procedure, the sample was heated in a combustion furnace (Carbolite MTF12/38/400) to 550 °C (10 °C min<sup>-1</sup> ramp rate), first in a flow of N<sub>2</sub> (3 h) and subsequently air (3 h) for a total of 6 h. Gas flow rates of 60 mL min<sup>-1</sup> were employed at all times. Bifunctional Al/Sn-BEA was made by solid state incorporation of Sn(II) acetate and Al(III) acetylacetonate pentahydrate into a dealuminated zeolite BEA following the same procedure described above. Proton form from the NH<sub>4</sub>-form of the Al-BEA zeolites (H-BEA) was obtained after a treatment at 550 °C in a tubular furnace for 3 h under air flow.

### 5.4.2 Catalyst characterisation

A PANalytical X'PertPRO X-ray diffractometer was employed for powder XRD analysis. A Cu K $\alpha$  radiation source (40 kV and 40 mA) was utilised. Diffraction patterns were recorded between 6-55 °2 $\theta$  (step size 0.0167°, time/step = 150 s, total time = 1 h). Specific surface area was determined from nitrogen adsorption using the BET equation, and microporous volume was determined from nitrogen adsorption isotherms using the t-plot method. Porosymmetry measurements were performed on a Quantachrome Quadrasorb, and samples were degassed prior to use (277°C, 6 h, nitrogen flow). Adsorption isotherms were obtained at 77 K. DRIFT spectroscopy was performed in a Harrick praying mantis cell. The spectra were recorded on a Bruker Tensor spectrometer over a range of 4000-650 cm<sup>-1</sup> at a resolution of 2 cm<sup>-1</sup>. *In situ* CD<sub>3</sub>CN and Pyridine measurements were performed on pre-treated zeolite powders (550 °C, 1 h under flowing air, 60 mL

min<sup>-1</sup>) as follows: following pre-treatment, the sample was dosed with the probe molecule vapour at room temperature for 5 minutes, and one spectrum was recorded. The sample chamber was subsequently evacuated under dynamic vacuum (approximately 10<sup>-4</sup> mbar), and spectra were recorded at 30, 100 and 200 °C. MAS NMR experiments were performed at Durham University through the EPSRC UK National Solid-state NMR Service. Samples were measured under conditions identical to those reported by Bermejo-Deval et al.,<sup>45</sup> and Hammond and co-workers.<sup>46</sup> TGA analysis was performed on a PerkinElmer system. Samples were held isothermally at 30 °C for 30 minutes, before being heated to 550 °C (10 °C min<sup>-1</sup> ramp rate) in air.

### 5.4.3 Kinetic evaluation and analytical methods

Batch TH and etherification reactions with furfural (or furfuryl alcohol) were performed in a 100 mL round bottom flask equipped with a reflux condenser, which was thermostatically controlled by immersion in a silicon oil bath. The vessel was charged with a 10 mL solution of FF (or FA) in 2-butanol (0.2 M), which also contained an internal standard (biphenyl, 0.01 M). The solution was subsequently heated to the desired temperature (98 °C internal temperature). The reaction was initiated by addition of an appropriate amount of catalyst, typically corresponding to 1 mol% Sn (or Al) relative to the reactant. The solution was stirred at ±800 rpm with an oval magnetic stirrer bar.

Continuous transfer hydrogenation reactions were performed in a plug flow, stainless steel, tubular reactor. The reactor was connected to an HPLC pump in order to regulate the reactant flow and allow operation at elevated pressures. The catalyst was mixed with a diluent material (SiC (particle size of 63-75 µm)), and the catalytic bed placed in between two plugs of quartz wool. The diluted sample was densely packed into a ¼ stainless steel tube (4.1 mm internal diameter), and a frit of 0.5 µm was placed at the reactor exit. The reactor was subsequently immersed in a thermostatted oil bath at the desired reaction temperature. Pressure in the system was controlled by means of a backpressure regulator, and the pressure drop was determined by comparison of the HPLC pump

pressure to the outlet pressure measured by a pressure gauge. An overpressure of 5-10 bar was typically employed, depending on reactant flow rate and column length, and this allowed operation above the boiling temperature of the solvent (2-butanol, 98 °C). The reaction feed was identical to that one used for batch reactions. Aliquots of the transfer hydrogenation reaction solutions were taken periodically from a sampling valve placed after the reactor. Periodic catalyst regeneration was performed heating the whole reactor in a combustion furnace (Carbolite MTF12/38/400) to 550 °C (10 °C min<sup>-1</sup>) in air (3h). All reactants and products during TH were analysed by GC (Agilent 7820, 25 m CP-Wax 52 CB column), and quantified against a biphenyl internal standard.

---

## 5.5 References

- 1 J.-P. Lange, *Biofuels, Bioprod. Biorefining*, 2007, **1**, 39.
- 2 I. Delidovich, K. Leonhard and R. Palkovits, *Energy Environ. Sci.*, 2014, **7**, 2803.
- 3 T. Ennaert, J. Van Aelst, J. Dijkmans, R. De Clercq, W. Schutyser, M. Dusselier, D. Verboekend and B. F. Sels, *Chem. Soc. Rev.*, 2016, **45**, 584.
- 4 C. O. Tuck, E. Perez, I. T. Horvath, R. A. Sheldon and M. Poliakoff, *Science (80-. )*, 2012, **337**, 695.
- 5 P. Y. Dapsens, C. Mondelli and J. Pérez-Ramírez, *ACS Catal.*, 2012, **2**, 1487.
- 6 I. Sádaba, M. López Granados, A. Riisager and E. Taarning, *Green Chem.*, 2015, **17**, 4133.
- 7 M. J. Climent, A. Corma and S. Iborra, *Green Chem.*, 2014, **16**, 516.
- 8 T. D. Swift, H. Nguyen, Z. Erdman, J. S. Kruger, V. Nikolakis and D. G. Vlachos, *J. Catal.*, 2016, **333**, 149.
- 9 J. M. R. Gallo, D. M. Alonso, M. A. Mellmer, J. H. Yeap, H. C. Wong and J. A. Dumesic, *Top. Catal.*, 2013, **56**, 1775.
- 10 R. Mariscal, P. Maireles-Torres, M. Ojeda, I. Sádaba and M. López Granados, *Energy Environ. Sci.*, 2016, **9**, 1144.
- 11 J. P. Lange, E. Van Der Heide, J. Van Buijtenen and R. Price, *ChemSusChem*, 2012, **5**, 150.
- 12 X. Zhang, K. Wilson and A. F. Lee, *Chem. Rev.*, 2016, **116**, 12328.
- 13 H. P. Winoto, B. S. Ahn and J. Jae, *J. Ind. Eng. Chem.*, 2016, **40**, 62.
- 14 A. Corma and M. Renz, *Angew. Chemie - Int. Ed.*, 2007, **46**, 298.
- 15 M. Koehle and R. F. Lobo, *Catal. Sci. Technol.*, 2016, **6**, 3018.

- 
- 16 J. D. Lewis, S. Van De Vyver, A. J. Crisci, W. R. Gunther, V. K. Michaelis, R. G. Griffin and Y. Román-Leshkov, *ChemSusChem*, 2014, **7**, 2255.
- 17 J. Jae, E. Mahmoud, R. F. Lobo and D. G. Vlachos, *ChemCatChem*, 2014, **6**, 508.
- 18 M. Moliner, *Dalt. Trans.*, 2014, **43**, 4197.
- 19 P. Y. Dapsens, C. Mondelli and J. Pérez-Ramírez, *Chem. Soc. Rev.*, 2015, **44**, 7025.
- 20 H. Y. Luo, J. D. Lewis and Y. Román-Leshkov, *Annu. Rev. Chem. Biomol. Eng.*, 2016, **7**, 663.
- 21 A. Corma, M. E. Domine, L. Nemeth and S. Valencia, *J. Am. Chem. Soc.*, 2002, **124**, 3194.
- 22 C. Hammond, D. Padovan, A. Al-Nayili, P. P. Wells, E. K. Gibson and N. Dimitratos, *ChemCatChem*, 2015, **7**, 3322.
- 23 P. Hoffmann and J. A. Lobo, *Microporous Mesoporous Mater.*, 2007, **106**, 122.
- 24 T. Kawai and K. Tsutsumi, *J. Colloid Interface Sci.*, 1999, **212**, 310.
- 25 P. Wu, T. Komatsu and T. Yashima, *J. Phys. Chem.*, 1995, **99**, 10923.
- 26 P. Lanzafame, K. Barbera, S. Perathoner, G. Centi, A. Aloise, M. Migliori, A. MacArio, J. B. Nagy and G. Giordano, *J. Catal.*, 2015, **330**, 558.
- 27 D. Padovan, C. Parsons, M. Simplicio Grasina and C. Hammond, *Green Chem.*, 2016, **18**, 5041.
- 28 E. Nikolla, Y. Román-Leshkov, M. Moliner and M. E. Davis, *ACS Catal.*, 2011, **1**, 408.
- 29 J. Dijkmans, M. Dusselier, D. Gabriëls, K. Houthoofd, P. C. M. M. Magusin, S. Huang, Y. Pontikes, M. Trekels, A. Vantomme, L. Giebel, S. Oswald and B. F. Sels, *ACS Catal.*, 2015, **5**, 928.
- 30 H. Li, Z. Fang, R. L. Smith and S. Yang, *Prog. Energy Combust. Sci.*,

- 2016, **55**, 98.
- 31 M. J. Climent, A. Corma, S. Iborra and M. J. Sabater, *ACS Catal.*, 2014, **4**, 870.
- 32 L. Bui, H. Luo, W. R. Gunther and Y. Román-Leshkov, *Angew. Chemie - Int. Ed.*, 2013, **52**, 8022.
- 33 C. M. Lew, N. Rajabbeigi and M. Tsapatsis, *Ind. Eng. Chem. Res.*, 2012, **51**, 5364.
- 34 C. Hammond, S. Conrad and I. Hermans, *Angew. Chemie - Int. Ed.*, 2012, **51**, 11736.
- 35 S. Roy, K. Bakhmutsky, E. Mahmoud, R. F. Lobo and R. J. Gorte, *ACS Catal.*, 2013, **3**, 573.
- 36 M. Boronat, P. Concepción, A. Corma, M. Renz and S. Valencia, *J. Catal.*, 2005, **234**, 111.
- 37 T. Kim, R. S. Assary, C. L. Marshall, D. J. Gosztola, L. A. Curtiss and P. C. Stair, *ChemCatChem*, 2011, **3**, 1451.
- 38 A. Gandini and M. N. Belgacem, *Prog. Polym. Sci.*, 1997, **22**, 1203.
- 39 S. K. Sahoo, N. Viswanadham, N. Ray, J. K. Gupta and I. D. Singh, *Appl. Catal. A Gen.*, 2001, **205**, 1.
- 40 C. Hammond, *Green Chem.*, 2017, **19**, 2711.
- 41 S. Bertarione, F. Bonino, F. Cesano, A. Damin, D. Scarano and A. Zecchina, *J. Phys. Chem. B*, 2008, **112**, 2580.
- 42 A. Omegna, M. Vasic, J. Anton van Bokhoven, G. Pirngruber and R. Prins, *Phys. Chem. Chem. Phys.*, 2004, **6**, 447.
- 43 M. M. Antunes, S. Lima, P. Neves, A. L. Magalhães, E. Fazio, A. Fernandes, F. Neri, C. M. Silva, S. M. Rocha, M. F. Ribeiro, M. Pillinger, A. Urakawa and A. A. Valente, *J. Catal.*, 2015, **329**, 522.
- 44 J. W. Harris, M. J. Cordon, J. R. Di Iorio, J. C. Vega-Vila, F. H. Ribeiro

- and R. Gounder, *J. Catal.*, 2016, **335**, 141.
- 45 R. Bermejo-Deval, M. Orazov, R. Gounder, S. J. Hwang and M. E. Davis, *ACS Catal.*, 2014, **4**, 2288.
- 46 A. Al-Nayili, K. Yakabi and C. Hammond, *J. Mater. Chem. A*, 2016, **4**, 1373.

# 6

## Conclusions, Outlooks and pertaining challenges

### 6.1 Conclusions

This work is dedicated to handle one of the greatest challenges in Lewis acid catalysts; namely seeking novel routes to design Sn-BEA whose potentials attracted significant industries. In spite of the high activity and selectivity of hydrothermally-synthesized high-silica Sn-containing BEA zeolite due to its hydrophobicity, placement of its metal centres and well-defined nature, it still has some disadvantages that limit the large scale of its industrial production, such as its need for HF in its preparation method and the low amount of active metal that can be inserted into the framework of zeolite BEA. Therefore, the pivotal aim of this doctoral work is to develop i) more industrially-applicable post-synthetic modification to prepare Lewis-acid catalysts, ii) intracrystalline mesoporosity Lewis-acid zeolites via desilication (framework silicon extraction) in order to demonstrate a more efficient utilization of the Lewis-acid zeolite volume by enhanced shorter diffusion path lengths and accessibility, and iii) prepare highly active, selective and stable Lewis-acid catalysts for the production of biofuels chemicals.

Chapter three of this thesis elucidates that solid-state incorporation (SSI) is a convenient alternative method for preparing high active and selective Sn-BEA catalysts. The resulting catalysts from this method are not only as active as conventional analogues, but they have cleaner, more selective and highly rapid synthesising process. In this chapter, catalytic and spectroscopic studies were combined to show that isolated, framework Sn(IV) sites predominate the Sn population of these materials at loading of up to 5 wt %, which is a loading

approximately 2- to -3 times more than what can be gained from conventional methodologies. These highly elevated loadings lead to significant increase in the space-time yield of the catalyst which would in turn increase the productivity per gram of catalyst. However, at higher loading of Sn (8-10 wt %), the effective concentration of active Lewis acid sites decreases due to the formation of Sn oligomers and likely some SnO<sub>2</sub>, which results in showing lower values of TOF in catalytic powder. Beside the MPV transfer hydrogenation of carbonyl compounds such as cyclohexanone (CyO), this chapter focuses on exploring the catalytic activity of Sn-BEA for catalytic glucose isomerization. This application of Sn-BEA can improve the potential economics of high-fructose corn syrup production.

In chapter four of this thesis, a novel route for preparing a stannosilicate with a beneficial hierarchical BEA framework was successfully applied for the first time. Prior to this work, the microporous size of Lewis acidic BEA zeolites limits their general applicability to the small- and medium- sized substrates and makes them particularly prone to deactivation through fouling. In this chapter, alkaline treatment of zeolites was investigated as a method to introduce mesoporosity in view of increasing the diffusion of the reactants/products to/from the active centres. Subsequently, dealumination of the material, in line with chapter three, was adopted in order to generate the vacant framework sites required for the incorporation of Sn. The lifetime of Sn- hierarchical BEA was investigated in MPV transfer hydrogenation of cyclohexanone on continuous flow reactor and it showed a remarkable improvement in long-term stability. Finally, this chapter provides for the first time, to the best of known works, the preparation of a stannosilicate with a hierarchical BEA topology, the first evidence of condensed phase cyclododecanone valorisation with stannosilicates, and the first full study of condensed phase deactivation kinetics for hierarchical zeolite materials.

Chapter five concludes that a bifunctional zeolite, containing both Lewis and Brønsted acid sites in a single catalyst permits the production of the bio-renewable furanic ether (butoxy)methyl furan, which has the potential as fuel additive, in both the batch and continuous regime. Different catalytic zeolites which contain modified versions of zeolite BEA including Al were prepared from commercially available microcrystalline zeolite BEA via post-synthesis partial

dealumination followed by solid-state ion-exchange. Contrary to mono-functional catalysts and physical mixtures therefrom, the bifunctional Sn- and Al-containing BEA zeolite results in distinctively high levels of activity, durability and selectivity. Notably, conventional methods would not be prepare such as material due to the differing rates of incorporation of Sn(IV) and Al(III). Hence, this provides added evidence of the unique ability of SSI to prepare active and highly desirable Lewis acidic silicates.

## 6.2 Outlooks and pertaining challenges

Though this study has increased our understanding of Lewis acid zeolites, there are still many challenges before we can synthesis commercially-suitable heterogeneous Lewis acid catalysts.

*Simple and scalable synthesis:* In this work, a simpler and greener method for the synthesis of Lewis acidic Sn-BEA zeolite is depicted, consisting of the post-synthetic incorporation of Sn atoms into dealuminated BEA-zeolite by solid-state-ion-exchange (chapter 3). The low loading of Sn (2-5 wt %) showed similar to higher activity and selectivity in comparison with Sn-BEA prepared by hydrothermal synthesis. However, high loading of Sn ( 8-10 wt %) showed unexpected results because the effective concentration of active Lewis acid sites decreases due to the formation of Sn oligomers and likely some SnO<sub>2</sub>, which leads to a catalytic material exhibiting lower values of TOF and consequently low levels of catalyst productivity and space-time-yield. Future work in the synthesis field should provide to prepare high loading Sn by changing synthesis conditions, such as temperature, incorporation time, and metal precursor. In addition, understanding the incorporation mechanisms and its impact on the catalyst's behaviour represents a very crucial point in the improvement of the catalyst activity to design perfect protocol for incorporating the active metal at higher levels of loading.

*Decrease deactivation:* Hierarchical Lewis acid zeolites, which have levels of mesoporosity and reduced diffusion limitations, have been used to reduce

deactivation by coking. The catalytic results (chapter 4) demonstrate the exceptional stability of hierarchical Lewis acid compared to purely microporous Lewis acid, with limited (<20%) activity loss observed over 700 h on stream. However, in contrast to the purely microporous material, the TOF is decreased by  $\pm 10\%$ . This loss in TOF can be explained by a slight decrease in zeolite crystallinity and high defect concentration but most likely results from local changes to the metal sites. In addition, the current method of introducing mesoporosity with NaOH as desilication agent has no control over the level of mesoporosity. Consequently, developing improved materials that combine the supreme advantages of the hierarchical material, without its disadvantages, is a challenge that should be tackled.

Towards this challenge, some preliminary studies were performed to investigate the continuous performance of two other classes of zeolites containing improved diffusional properties. Specifically:

A) Nanocrystalline Sn-BEA prepared by solid-state incorporation of Sn(II) into the vacant framework sites of nanocrystalline zeolite BEA, was evaluated as a catalyst for the MPV reduction of cyclohexanone under continuous conditions. Whilst the nano-crystalline material did not show any improvement in rates of deactivates (Figure 6.1), preliminary characterisation revealed the crystallite sizes of the initial nanocrystalline BEA were not substantially smaller than those of the conventional micrometer-sized zeolite BEA, potentially accounting for their comparable rates of deactivation. It may therefore be that further optimizing studies to get lower size of crystals will still result in improved continuous performance.

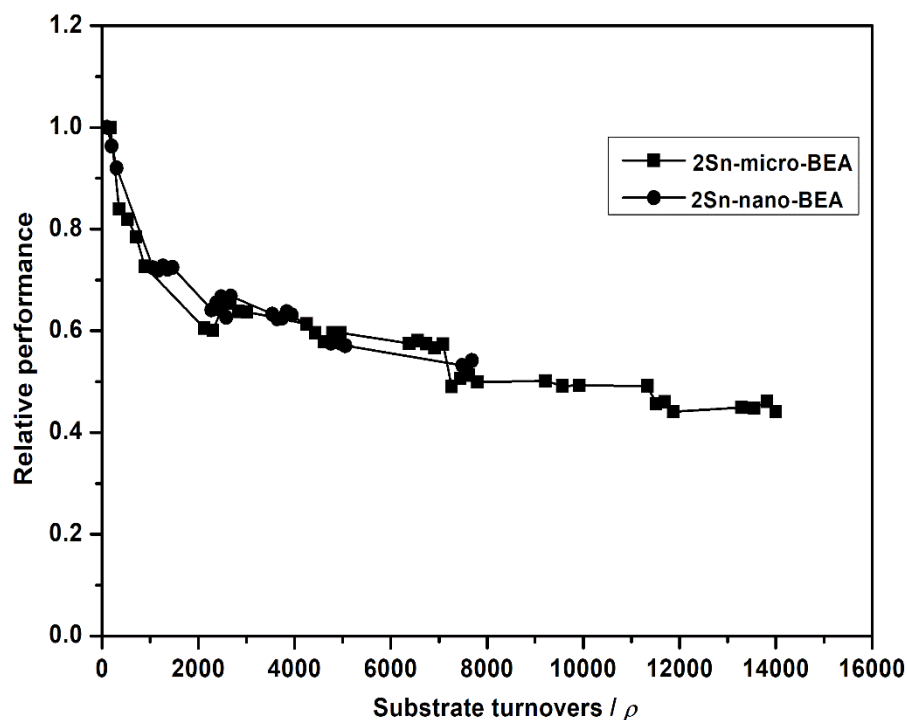


**Figure 6.1** Catalytic activity for 2Sn-micro-BEA and 2Sn-nano-BEA for the MPV reduction of cyclohexanone in the continuous regime.

B) Two-dimensional zeolites are those in which the three-dimensional structure is curtailed in one dimension. Accordingly, they offer extreme potential as continuous liquid phase catalysts, as their active sites are not constrained in a full three-dimensional structure, potentially alleviating deactivation through fouling. Two-dimensional zeolites can be prepared via bottom-up and top-down methods. In bottom-up methods, a surfactant consisting of a hydrophilic head and a paraffinic hydrophobic tail containing di-quaternary amines spaced at regular intervals is used as organic structure directing agent (SDA). The long chain tail inhibits crystal growth in one spatial dimension while the diammonium head group direct the forming of the zeolite topology. This method to create nanosheets results in highly crystalline and highly dispersed nanosheets without supplementary post-synthetic treatment. In top-down approaches, a suitable precursor material, such as MCM-22, is delaminated by sonochemical treatment. Preliminary work towards achieving deactivation-resistant Lewis acid catalysis focused upon the production of a two-dimensional zeolite via conversion of MCM-

22, as this is the simple method of synthesis. Whilst the X-ray diffraction patterns of as-synthesized and calcined samples of MCM-22 zeolites are not presented here, both samples were found to have poor levels of crystallinity precluding their use as catalysts for liquid phase processing.

Future work have to focus on the direct synthesis of hierarchical zeolite materials by using a single supramolecular template that can direct the formation of zeolite structures on the microporous and mesoporous length scales simultaneously. Moreover, the future studies of Lewis-acid zeolites should provide a more rigorous analysis of the stability of these materials in the liquid phase. The relative influence of temperature, substrate properties, solvent polarity and framework geometry on deactivation requires more research emphasis.

As noted throughout this study, a single characterization technique cannot show a perfect understanding of the active sites in a given catalysts, nor a full explanation of catalyst or adsorbent behaviour. Many of the characterization techniques used in this study require vacuum conditions, which may not be translatable to operational conditions. Hence, more characterization techniques continue to develop and the impact of their applications will influence the zeolitic systems. For instance, Scanning Transmission Electron Microscopy (STEM) technique used perfectly for imaging individual Pt atoms dispersed on a catalyst support. Applying this technique for imaging the location of metal sites in a zeolite is supposed to follow. Connecting this with other techniques enables the possibility of identifying the location of metal clusters in the zeolite channels. The mobility of metal atoms under the electron beam as well as the beam sensitivity of zeolites turn this into a particularly difficult and challenging experiment. Despite all the difficulties and challenges in this and other processes, the catalytic uses of zeolites will continue to develop toward greater conversion and higher selectivity for each reaction in which they are employed, and this requires the co-development of new catalytic methods and materials

## 7

## Appendix

## 7.1 GC chromatograms

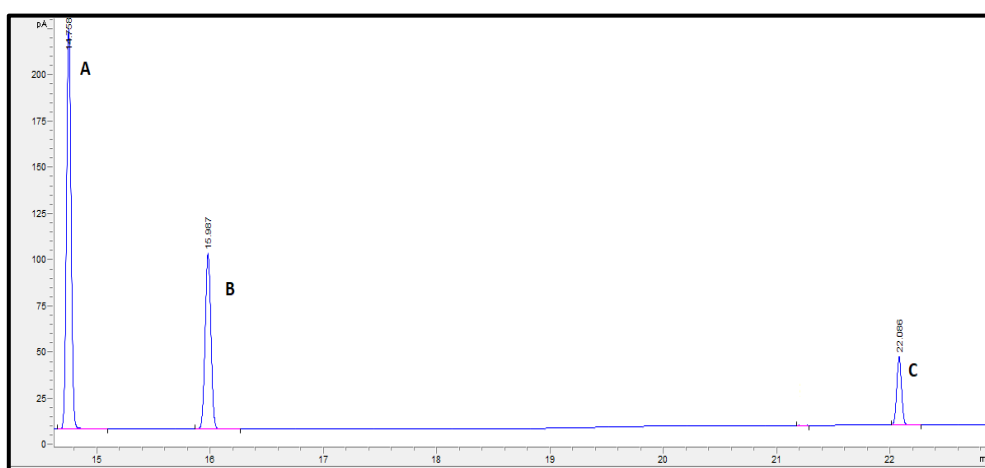


**Figure 7.1** A sample gas chromatogram of reactant and product (A) Cyclohexanone, (B) Cyclohexanol and (C) Biphenyl.

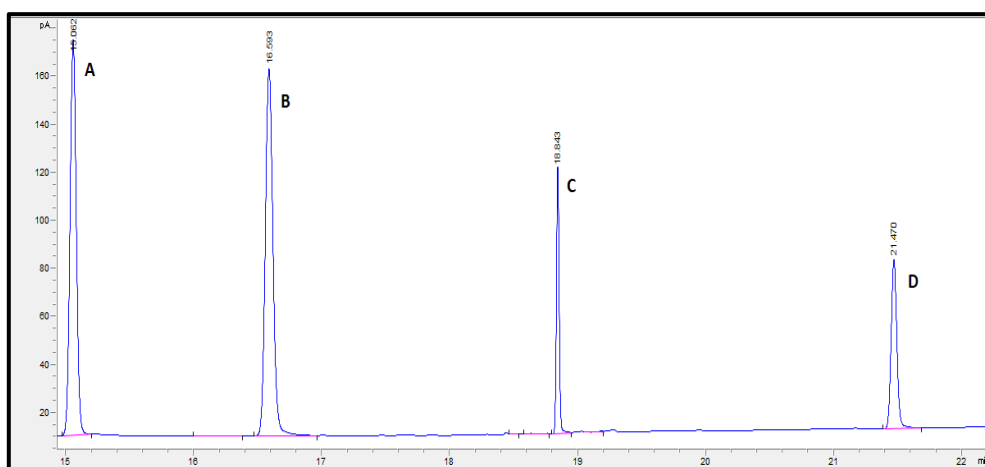


**Figure 7.2** A sample gas chromatogram of reactant and products (A) (butoxy)methyl furan, (B) Furfural, (C) Furfuryl alcohol and (D) Biphenyl.

## 7.2 HPLC chromatogram

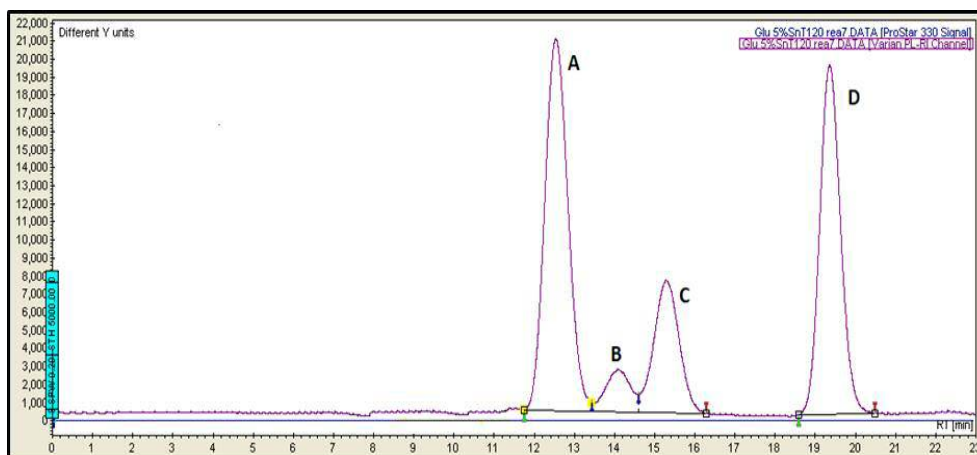


**Figure 7.3** A sample HPLC chromatogram of reactant and products (A) Glucose, (B) Mannose, (C) Fructose and (D) mannitol.

## 7.3 Calibration curves

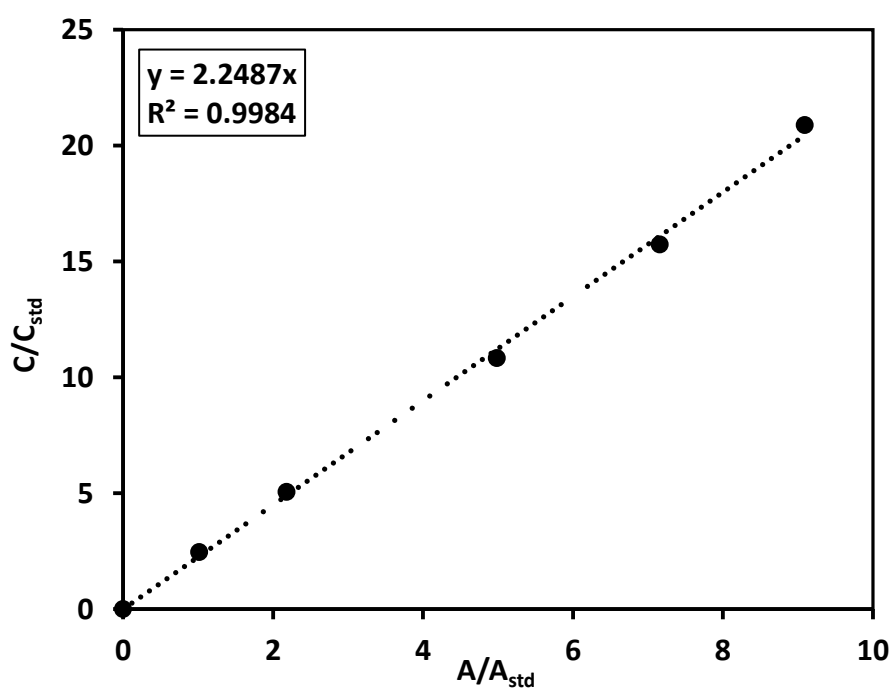


**Figure 7.4** GC calibration curve of cyclohexanone with biphenyl.

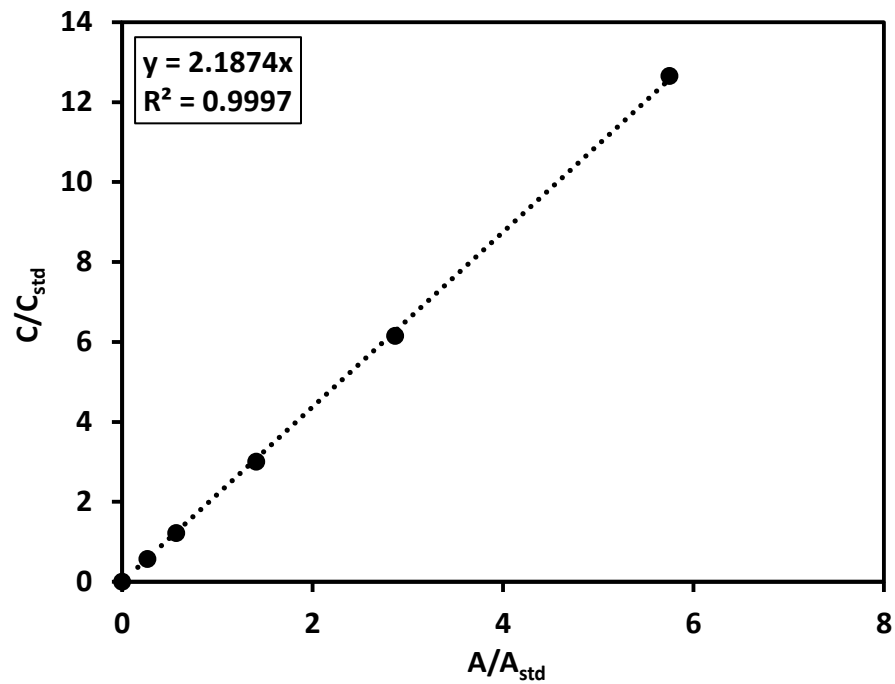


**Figure 7.5** GC calibration curve of cyclohexanol with biphenyl.

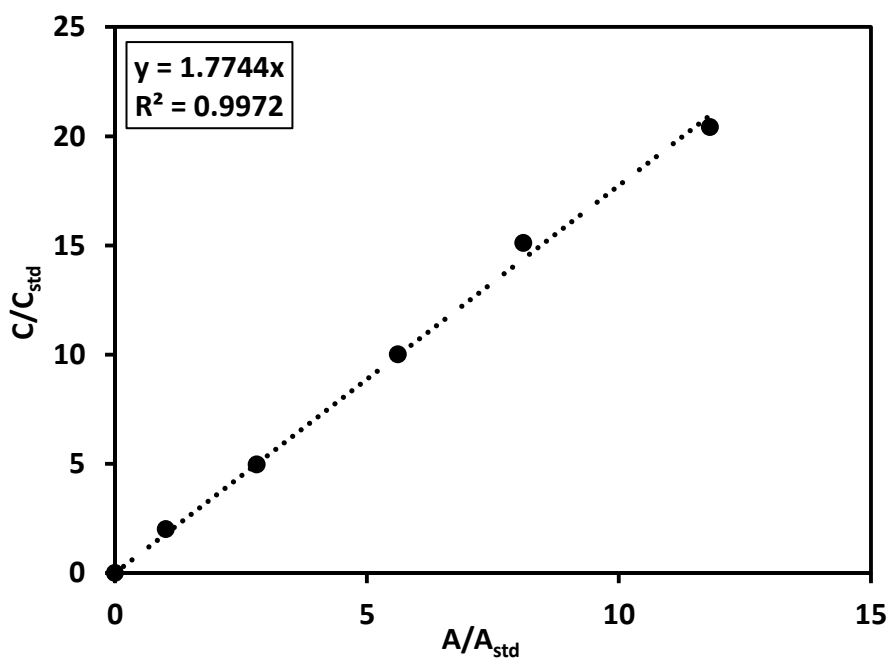


**Figure 7.6** GC calibration curve of cyclooctanone with biphenyl.

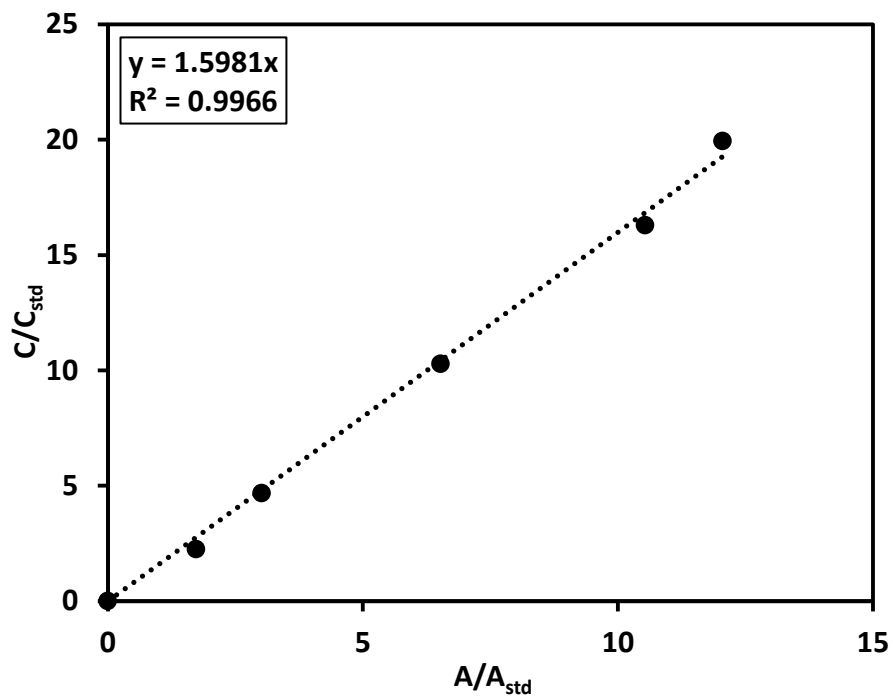


**Figure 7.7** GC calibration curve of cyclooctanol with biphenyl.

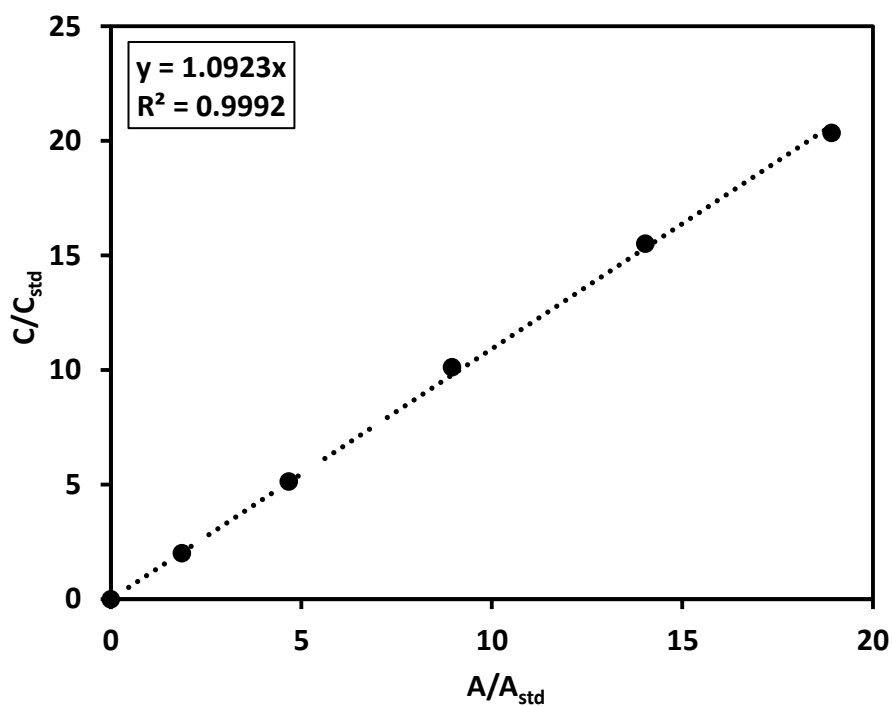


**Figure 7.8** GC calibration curve of cyclododecanone with biphenyl.

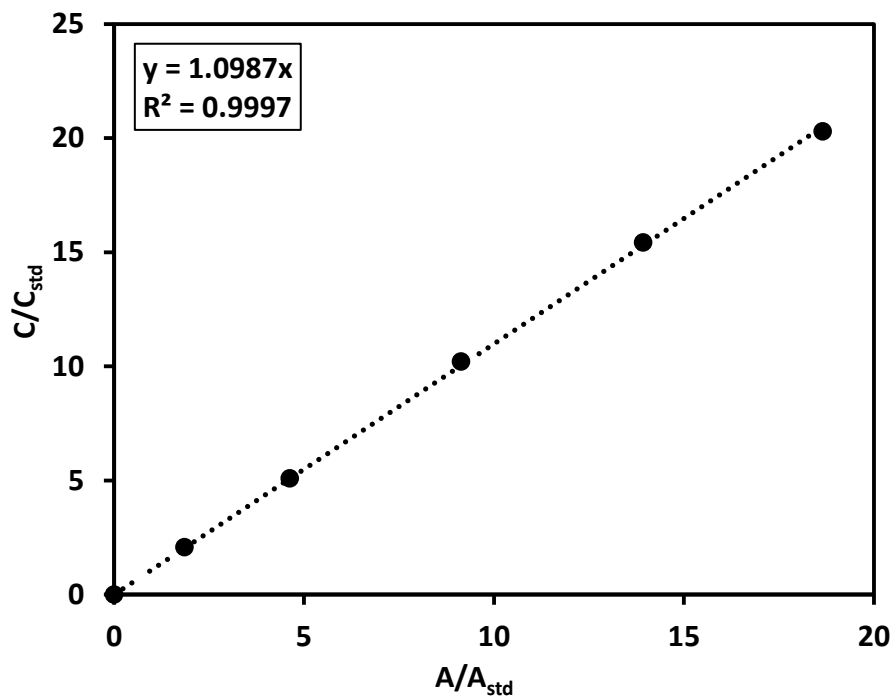


**Figure 7.9** GC calibration curve of cyclododecanol with biphenyl.

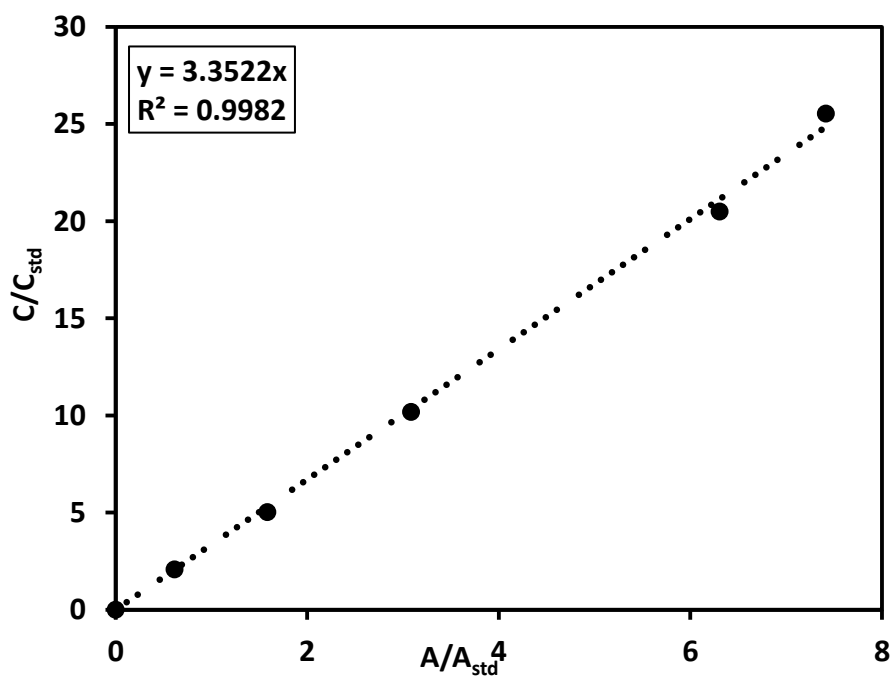


**Figure 7.10** GC calibration curve of furfural with biphenyl.

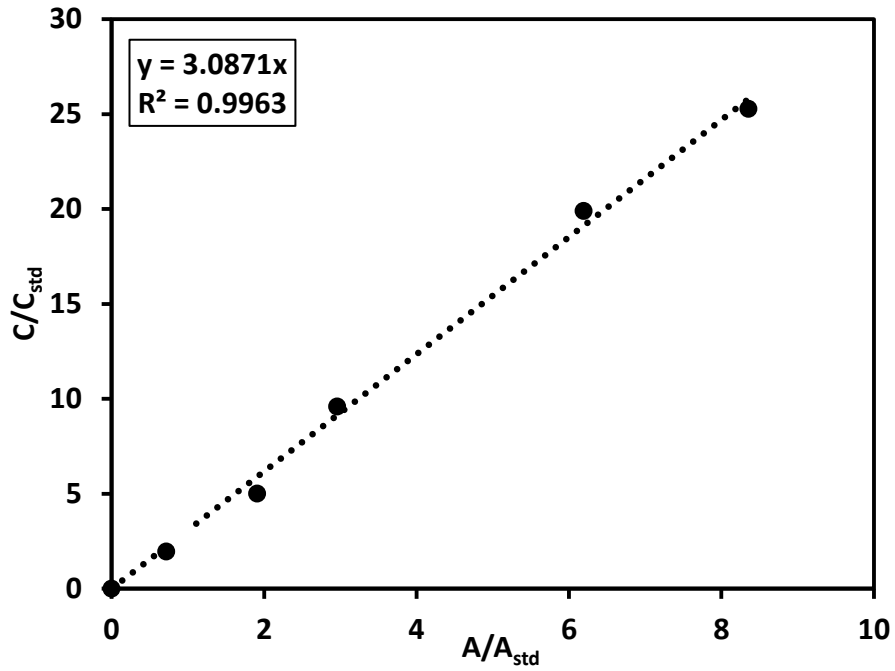


Figure 7.11 GC calibration curve of furfuryl alcohol with biphenyl.

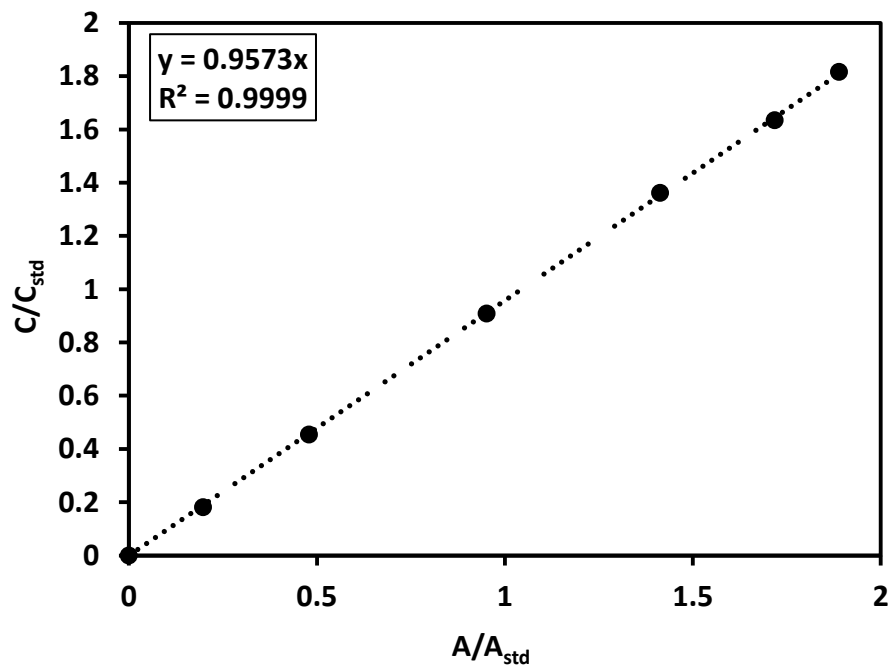
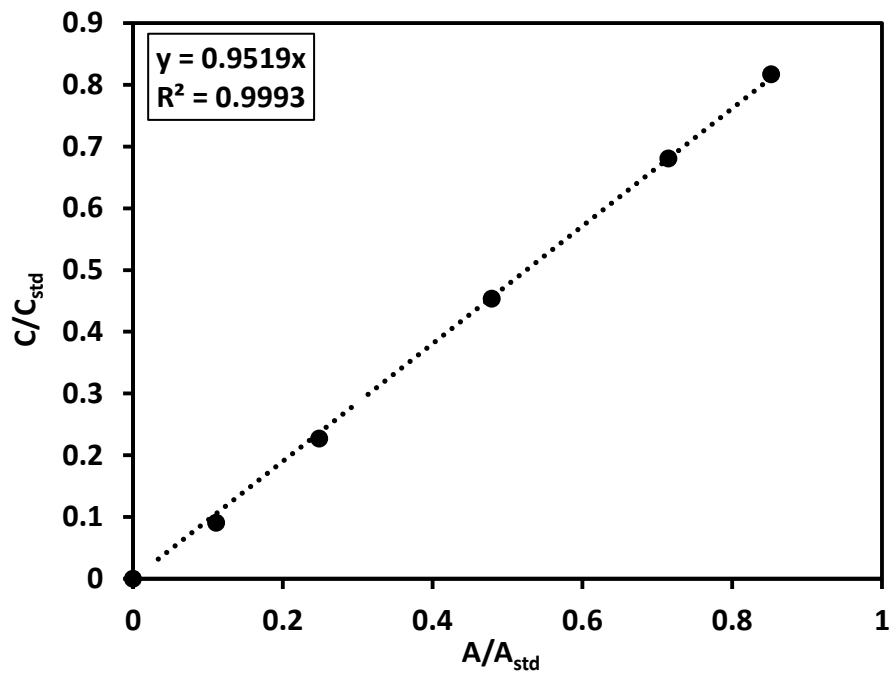
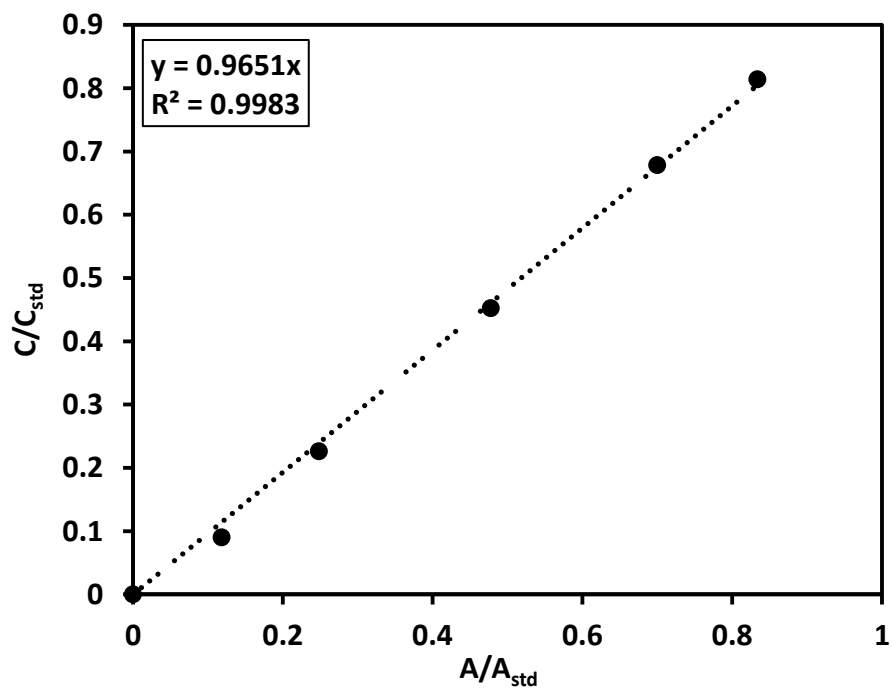


Figure 7.12 HPLC calibration curve of D-(+)-Glucose with D-Mannitol.



**Figure 7.13** HPLC calibration curve of D-(-) Fructose with D-Mannitol.



**Figure 7.14** HPLC calibration curve of D-(+) Mannose with D-Mannitol.

## 7.4 Experimental data for chapter 3

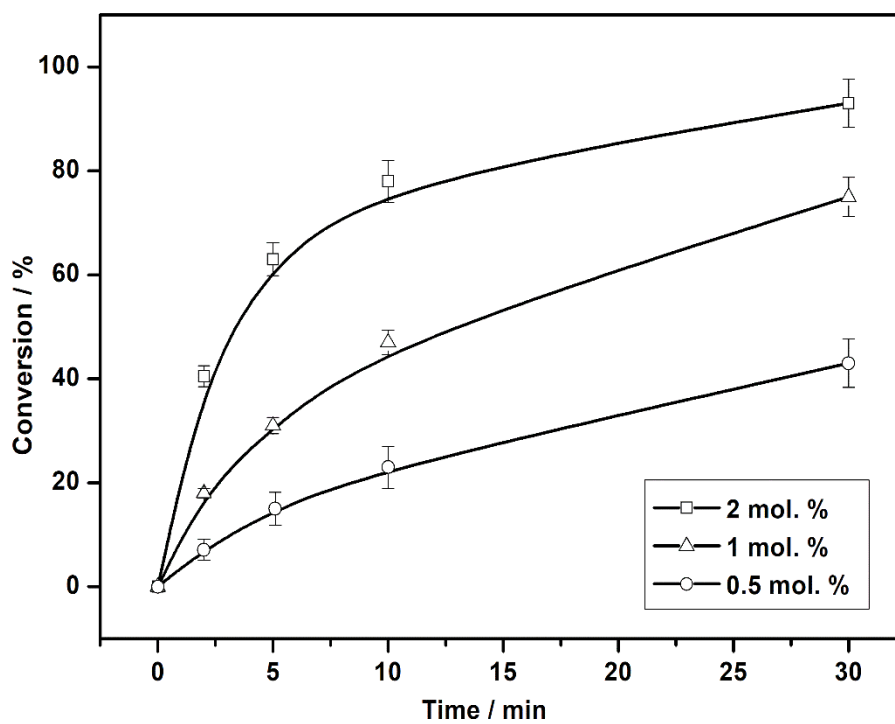


**Figure 7.15** Catalytic activity of 2Sn-BEA for the MPV hydrogenation of cyclohexanone as a function of time.

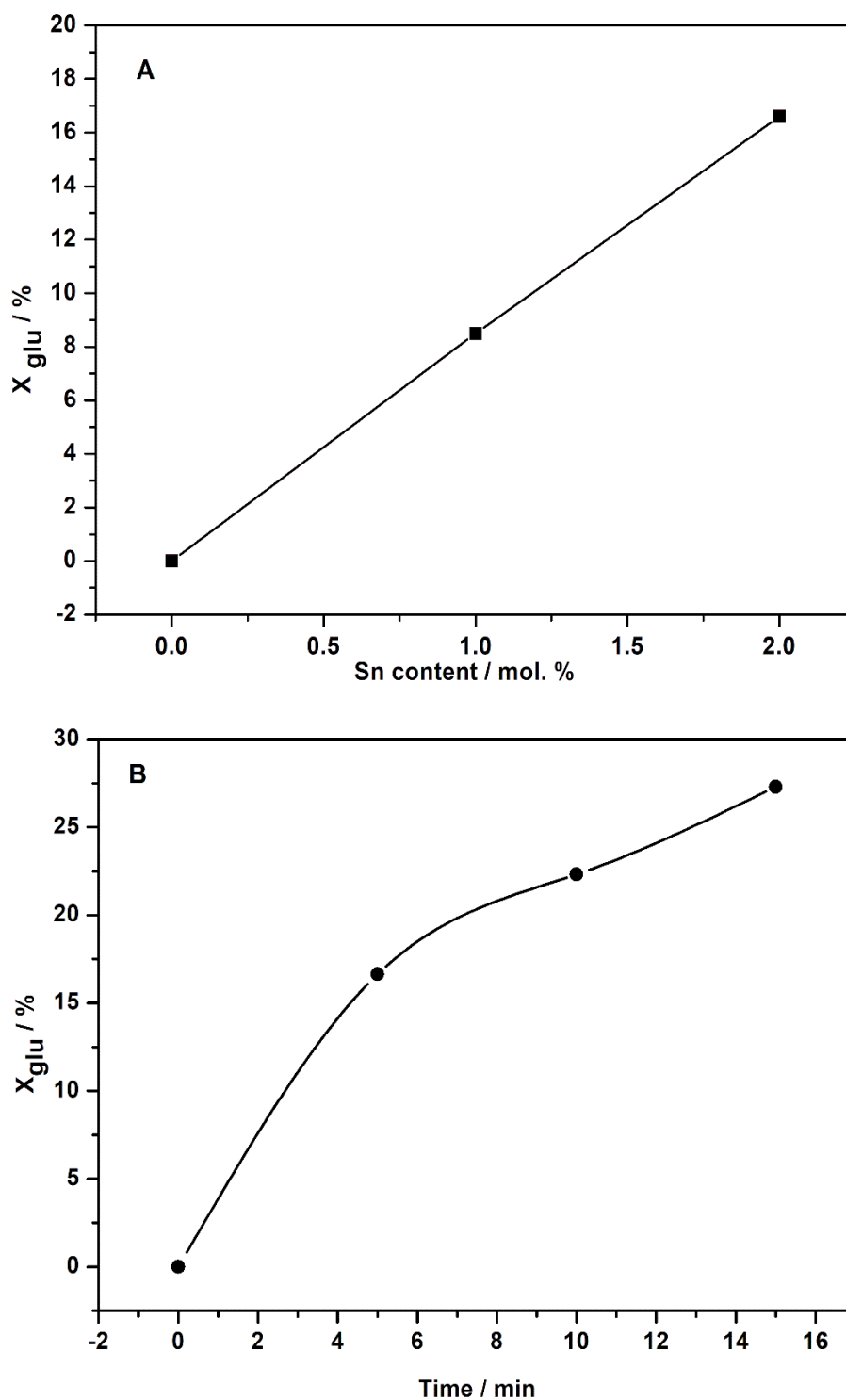


**Figure 7.16** (A) Catalytic activity ( $X_{\text{glu}} \%$ ) at 5 min. of 2Sn-BEA for glucose isomerization at 1 mol. % Sn (glucose/Sn = 100) as a function of catalyst loading (Sn content was varied by changing the mass of 2Sn-BEA present in the reactor), (B) Catalytic activity ( $X_{\text{glu}} \%$ ) of 2Sn-BEA for glucose isomerization at 2 mol. % Sn (glucose/Sn = 50) as a function of time online analysis.

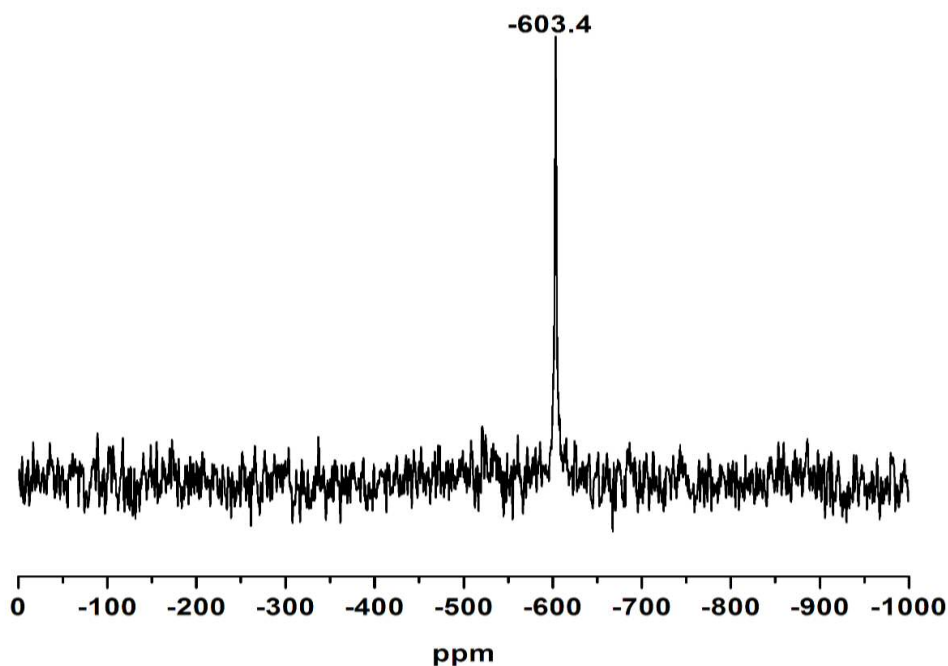


**Figure 7.17**  $^{119}\text{Sn}$  MAS-NMR signal of  $10\text{SnO}_2\text{-BEA}$  (containing naturally abundant  $^{119}\text{Sn}$ ).

## 7.5 Experimental data for chapter 4

Figure 7.2 shows the geometry optimised structures of  $\text{C}_6\text{-C}_8$  ketones and table 7.1 shows the relative values of diameter calculated by a combination of theoretical and experimental values. The estimated effective diameter was calculated by taking the distance between the centre of two carbon atoms along the largest direction of the carbon ring ( $r$ , indicated on the molecules), and adding the two atomic radii of the same carbon atoms, leads to the following calculated sizes: 4.4, 5.0 and 6.1 Å. Although this underestimates the actual kinetic diameter, it provides a useful “relative value” that can be compared to known literature values.<sup>1</sup>

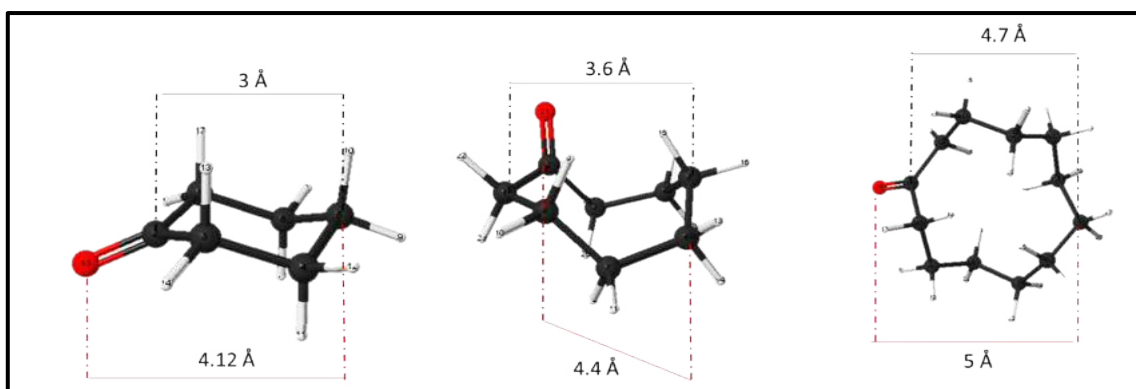


**Figure 7.18** Geometry optimised structures of C<sub>6</sub>-C<sub>8</sub> ketones.

**Table 7.1** Relative values diameter of C<sub>6</sub>-C<sub>8</sub> ketones.

Entry	Known kinetic diameter (Å)	Calculated molecular volume (Å <sup>3</sup> molecule <sup>-1</sup> )	Diameter based on molecular volume	Relative diameter based on molecular volume	Estimated effective diameter from calculation (B3LYP)(Å)	Relative effective diameter from calculation (B3LYP)(Å)	Approximate kinetic diameter (relative to cyclohexanone)
C <sub>6</sub> =O	6.0	101.06	5.8	1	4.4	1	6.0
C <sub>8</sub> =O	-	133.97	6.3	1.1	5.0	1.1	6.6
C <sub>12</sub> =O	-	-	-	-	6.1	1.4	8.4

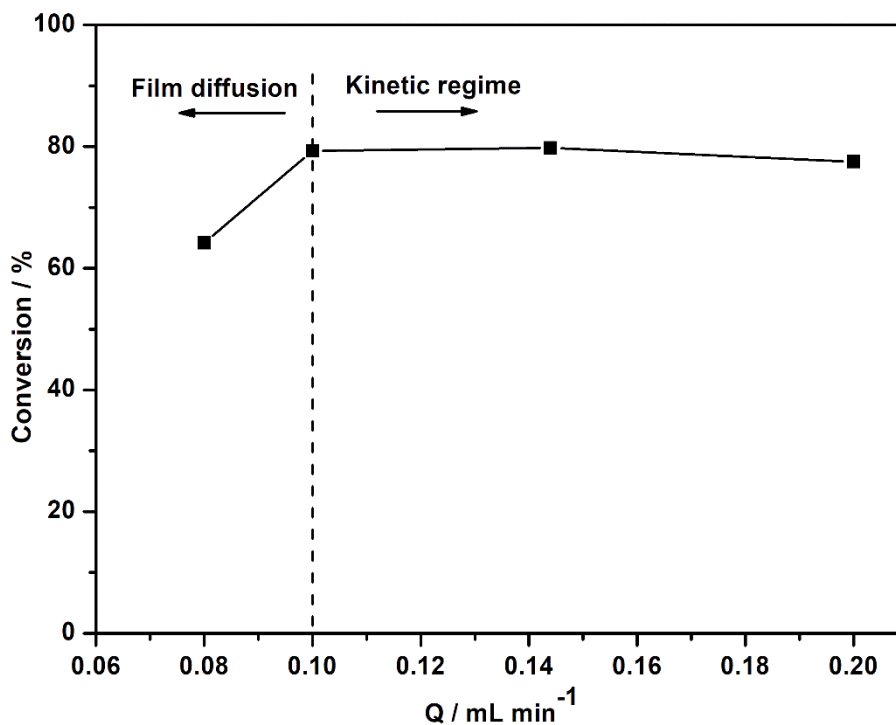


**Figure 7.19** Effect of linear velocity in terms of mL min<sup>-1</sup>, on the conversion of cyclohexanone observed over 2Sn-BEA during MPV transfer hydrogenation.

## 7.6 Conference contributions

May. 2015 Poster presentation at Chemistry conference, Cardiff University, UK.

Sep. 2015 Poster presentation at Applied Catalysis and Biocatalysis Reaction Engineering, University of Bath, UK.

Jan. 2016 Poster presentation at CCI conference, Cardiff University, UK.

May. 2016 Poster presentation at Chemistry conference, Cardiff University, UK.

## 7.7 References

- 1 C. E. Webster, R. S. Drago and M. C. Zerner, *J. Am. Chem. Soc.*, 1998, **120**, 5509.